Optimal Topology and Critical Evaluation of Slip Synchronous Permanent Magnet Wind Generator

by

Johannes H. J. Potgieter

Dissertation presented for the degree of
Doctor of Philosophy in Electrical Engineering
in the Faculty of Engineering at Stellenbosch University

Promoter: Prof. Maarten J. Kamper

April 2014

Declaration

By submitting this thesis electronically, I declare that the entirety of the work contained therein is my own, original work, that I am the sole author thereof (save to the extent explicitly otherwise stated), that reproduction and publication thereof by Stellenbosch University will not infringe any third party rights and that I have not previously in its entirety or in part submitted it for obtaining any qualification.

Date: 2014/02/20 ....

Abstract

Optimal Topology and Critical Evaluation of Slip Synchronous Permanent Magnet Wind Generator

J. H. J. Potgieter

Dissertation: PhDEng (Elec)
April 2014

In this study the recently proposed slip-synchronous permanent magnet generator (SS-PMG), is considered as an alternative to other wind generator topologies. The SS-PMG is connected directly to the grid without the need for a power electronic converter and it can also be connected directly to the turbine without a gearbox. Due to the SS-PMG requiring no gearbox or power electronic converter it is evident that this type of generator have a significant advantage regarding reduced maintenance and operation costs. The SS-PMG consist of two integrated permanent magnet generating units, a directly turbine connected slip permanent magnet generator (slip-PMG) and a directly grid connected permanent magnet synchronous generator (PMSG). In this, study many of the implementation aspects of the SS-PMG are addressed. It is found that the short-circuit torque and current profiles of both the slip-PMG and PMSG are significantly influenced by the end-winding inductance and PM end-effects. A new analytical method is proposed for the calculation of the end-winding inductance in this study and a new approach is devised to take the PM end-effects into account. A very important aspect considered in this thesis, is the stability of the SS-PMG connected directly to the grid regarding turbine, generator and grid voltage disturbances, which influences the design of the PMSG and slip-PMG units. Furthermore, it is important that the final SS-PMG design comply to the relevant grid code specifications. For both the PMSG and slip-PMG an extensive design optimisation is done, with several novel wind generator concepts introduced. In this study the dynamic behaviour, grid connection aspects and operational principles of the SS-PMG are verified by means of practical tests in the laboratory and for the SS-PMG interfaced with an existing 15 kW wind turbine system in the field.

Uittreksel

Optimale Topologie en Kritiese Evaluering van ’n Glip Sinchroon Permanent Magneet Wind Generator

(“Optimal Topology and Critical Evaluation of Slip Synchronous Permanent Magnet Wind Generator”)

J. H. J. Potgieter

Proefskrif: PhDEng (Elek)

April 2014

In hierdie studie word die onlangs voorgestelde, glip-sinchroon permanent magneet generator (GS-PMG), oorweeg as ’n alternatief vir ander wind generator topologieë. Die GS-PMG word direk aan die netwerk gekonnekteer sonder die nodigheid van ’n drywingselektroniese omsetter en dit kan ook direk aan die turbine gekoppel word sonder ’n ratkas. Omdat die GS-PMG geen ratkas of drywingselektroniese omsetter benodig nie, is dit duidelik dat hierdie tipe generator ’n geweldige voordeel het rakende verminderde onderhoud en operasionele kostes. Die GS-PMG bestaan uit twee geïntegreerde permanent magneet generator eenhede, ’n direkte turbine gekoppelde glip permanent magneet generator (glip-PMG) en ’n direkte netwerk gekonnekteerde permanent magneet sinchroon generator (PMSG). In hierdie studie word baie van die implementerings aspekte van die SS-PMG aangeraak. Daar word gevind dat die kortsluit draaimoment en stroom profiele van beide die glip-PMG en PMSG geweldig deur die end-wikkeling induktansie en PM randeffekte beïnvloed word. Dus, word ’n nuwe analitiese metode voorgestel vir die uitwerk van die end-wikkeling induktansie in hierdie studie en ’n nuwe benadering word voorgestel om die PM randeffekte in ag te neem. ’n Baie belangrike aspek om te oorweeg in hierdie tesis, is die stabiliteit van die GS-PMG direk aan die netwerk gekoppel rakende turbine, generator en netwerkspanning steurnisse, wat die ontwerp van die PMSG en glip-PMG eenhede beïnvloed. Dit is ook belangrik dat die finale SS-PMG ontwerp voldoen aan die relevante netwerkkode spesifikasies. Vir beide die PMSG en glip-PMG word ’n deeglike ontwerpsoptimering gedoen, met talle nuwe wind generator konsepte voorgestel. In hierdie studie word die dinamiese gedrag, netwerk konneksie aspekte en operasionele kenmerke van die GS-PMG geverifieer met behulp van praktiese toetse in die laboratorium en vir die SS-PMG geïntegreer met ’n bestaande 15 kW wind turbine stelsel in die veld.

Acknowledgements

I would like to express my sincere gratitude to the following people and organisations. If I neglect to mention anyone, please accept my apology and sincerest thanks.

My promoter Prof. Maarten Kamper, for all of his guidance and contributions throughout my studies.

The National Research Foundation (NRF) and Technology Innovation Agency (TIA) for the financial support that contributed to this study.

Will Esterhuise and Mateo Schroeder for their help in the assembly of the numerous prototype generators.

Chris Vorster and Eddy Howard, for the mechanical designs of the prototype generator topologies.

Jos Weerdenburg from SMD for the several manufactured prototype generators.

David Groenewald for all of his help with the variable speed drive control and laboratory measurements.

Ernie Aylward and Gregg Walker from SWET for the manufacturing of the final SS-PMG prototype.

Murray Jumat, André Swart and Pietro Petzer from the SED workshop.

All of the members of the Electrical Machines Laboratory, thank you for a memorable experience.

Finally all of my friends and family, whom I have neglected so much during the writing of this thesis, thank you so much for your understanding.

List of Conference Proceedings and Publications

Local Conferences

J. H. J. Potgieter, A. N. Lombard, R-J Wang and M. J. Kamper, “Evaluation of a permanent magnet excited induction generator for renewable energy applications,” *Southern African Universities Power Engineering Conference (SAUPEC)*, Stellenbosch, South Africa, 2009.

J. H. J. Potgieter, “Evaluation and application of a slip-synchronous permanent magnet wind generator,” *Centre for Renewable and Sustainable Energy Studies (CRSES)* 3^{rd} *Postgraduate Research Symposium*, Stellenbosch, South Africa, 2012.

J. H. J. Potgieter and M. J. Kamper, “Design considerations in the implementation of an electromagnetic brake for a 15 kW PM wind generator,” *Southern African Universities Power Engineering Conference (SAUPEC)*, Potchefstroom, South Africa, 2013.

International Conferences

R. Vermaak, J. H. J. Potgieter and M. J. Kamper, “Grid-connected VSC-HVDC wind farm system and control using permanent magnet induction generators,” *IEEE International Conference on Power Electronics and Drive Sytems (PEDS)*, Tapei, Taiwan, 2009.

J. H. J. Potgieter and M. J. Kamper, “Cogging torque sensitivity in design optimisation of low cost non overlap winding PM wind generator,” *International Conference on Electrical Machines (ICEM)*, Rome, Italy, 2010.

J. H. J. Potgieter and M. J. Kamper, “Design of new concept permanent magnet induction wind generator,” *IEEE Energy Conversion Congress & Exposition (ECCE)*, Atlanta, GA, USA, 2010.

P. Bouwer, J. H. J. Potgieter, and M. J. Kamper, “Modelling and dynamic performance of a direct-drive direct-grid slip permanent magnet wind generator,” *IEEE International Electric Machines & Drives Conference (IEMDC)*, Niagara Falls, ON, Canada, 2011.

M. J. Kamper, J. H. J. Potgieter, J. A. Stegmann and P. Bouwer, “Comparison of air-cored and iron-cored non-overlap winding radial flux permanent magnet direct drive wind generators,” *IEEE Energy Conversion Congress & Exposition (ECCE)*, Phoenix, AZ, USA, 2011.

J. H. J. Potgieter and M. J. Kamper, “Evaluation of calculation methods and the effect of end-winding inductance on the performance of non-overlap winding PM machines,” *International Con-*

ference on Electrical Machines (ICEM), Marseilles, France, 2012.

J. H. J. Potgieter and M. J. Kamper, "Optimum design and technology evaluation of slip permanent magnet generators for wind energy applications," *IEEE Energy Conversion Congress & Exposition (ECCE)*, Raleigh, NC, USA, 2012.

J. H. J. Potgieter and M. J. Kamper, "Design specifications and optimisation of a directly grid-connected PM wind generator," *IEEE Energy Conversion Congress & Exposition (ECCE)*, Denver, CO, USA, 2013.

Journal Publications

J. H. J. Potgieter and M. J. Kamper, "Torque and voltage quality in design optimisation of low cost non-overlap single layer winding permanent magnet wind generator," *IEEE Trans. on Industrial Electronics*, vol. 59, no. 5, pp. 2147 - 2156, 2012.

J. H. J. Potgieter and M. J. Kamper, "Design of new concept gearless direct-grid connected slip-synchronous permanent magnet wind generator," *IEEE Trans. on Industry Applications*, vol. 48, no. 3, pp. 913 - 922, 2012.

J. H. J. Potgieter and M. J. Kamper, "Modelling and stability analysis of a direct-drive-direct-grid slip-synchronous permanent magnet wind generator," *in print IEEE Trans. on Industry Applications*, vol. PP, no. PP, pp. 1 - 1, 2013.

J. H. J. Potgieter and M. J. Kamper, "Calculation methods and effects of end-winding inductance and permanent magnet end-flux on performance prediction of non-overlap winding permanent magnet machines," *in print IEEE Trans. on Industry Applications*, vol. PP, no. PP, pp. 1 - 1, 2014.

J. H. J. Potgieter and M. J. Kamper, "Optimum design and comparison of slip permanent magnet couplings with wind energy as case-study application," *in print IEEE Trans. on Industry Applications*, vol. PP, no. PP, pp. 1 - 1, 2014.

Patents

Split Permanent Magnet Machine, M. J. Kamper, J. H. J. Potgieter and J. N. Stander Ref. No: PCT/IB2011/001812, Year: 08/2011

Awards

The Electrical Machines Committee of the IEEE Industry Applications Society Best Paper Award, First Prize, Raleigh, North Carolina, USA, 2012

Dedicated to Thelana
You were taken so suddenly and violently,
but the love we once shared
shall echo in eternity....

Contents

List of Figures

List of Tables

Nomenclature

Abbreviations

1G	One stage gearbox
2G	Two stage gearbox
3G	Three stage gearbox
2D	Two dimensional
3D	Three dimensional
AC	Alternating current
BDC	Brushless-DC
BDFIG	Brushless doubly-fed induction generator
CVT	Continuous variable transmission
DC	Direct current
DD	Direct drive
DFIG	Doubly-fed induction generator
DL	Double layer
ECC	Eddy-current coupling
EESG	Electrically excited synchronous generator
FE	Finite element
FG	Function generator
FL	Full-load
HVDC	High voltage direct current
IEC	International electrotechnical commission
IG	Induction generator
IM	Induction motor
LCC	Line commutating converter
LVRT	Low voltage ride through
MMF	Magneto motive force
NL	No-load
NO	Non overlap
O&M	Operation and maintenance
PCC	Point of common coupling
PM	Permanent magnet

PMIG	Permanent magnet induction generator
PMSG	Permanent magnet synchronous generator
RMS	Root mean square
SANAE IV	South African national Antarctic research base
SG	Synchronous generator
SL	Single layer
SLR	Series line reactance
slip-PMC	Slip permanent magnet coupling
slip-PMG	Slip permanent magnet generator
SSC	Solid-state converter
SS-PMG	Slip synchronous permanent magnet generator
VSC	Voltage source converter
VSD	Variable speed drive
WSG	Wound synchronous generator

Variables

a, b, c	Dimensional parameters used in the calculation of $L_{e(123)}$	[mm]
A_e	PM end-flux fringing area	[m^2]
A_t	Gain or attenuation of disturbance signal	
b_r	Frictional coefficient of slip-PMG unit	
b_s	Frictional coefficient of PMSG unit	
B	Flux density	[T]
B_m	PM work point flux density	[T]
B_r	PM remanence flux density	[T]
$B_{r1,2}$	Variation of PM remanence flux density with demagnetisation	[T]
C_p	Power factor correcting capacitance	[μF]
d	Refers to d-axis in dq-reference frame	
$\mathbf{D_g}$	Grid disturbance input function generator	
D_i	Machine inside diameter	[mm]
D_o	Machine outside diameter	[mm]
$\mathbf{D_r}$	slip-PMG torque ripple disturbance input function generator	
$\mathbf{D_s}$	PMSG torque ripple disturbance input function generator	
$\mathbf{D_t}$	Turbine torque disturbance input function generator	
e_{qr}	Transient q-axis induced voltage of slip-PMG	[V]
e_{qs}	Transient q-axis induced voltage of PMSG	[V]
E_{qr}	Steady-state q-axis induced voltage of slip-PMG	[V]
E_{qs}	Steady-state q-axis induced voltage of PMSG	[V]
E_r	Per phase slip-PMG induced voltage	[V]
E_s	Per phase PMSG induced voltage	[V]

$f_{1,2,3,4}$	Sub-functions in the calculation of k_2	
f_d	Disturbance input frequency	[Hz]
f_s	Grid electrical frequency	[Hz]
f_{sl}	Slip-PMG electrical slip frequency	[Hz]
f_r	Torque ripple frequency	[Hz]
f_t	Turbine mechanical frequency	[Hz]
F_s	Nominal grid electrical frequency	[Hz]
h_c	Conductor height	[mm]
$h_{f(t)}$	Grid frequency function	[Hz]
h_g	Airgap height	[mm]
$h_{LV(t)}$	Grid voltage LVRT function	[V]
h_m	Permanent magnet height	[mm]
h_{ry}	PM-rotor yoke height	[mm]
h_s	Slot height	[mm]
h_{sy}	Stator or slip-rotor yoke height	[mm]
H	Normalized inertia constant	[MWs/MVA]
H_i	Magnetic field intensity	[kA/m]
H_c	PM coercivity	[kA/m]
H_m	PM work point magnetic field intensity	[kA/m]
h_{ry}	PM-rotor yoke height	[mm]
i_{abc}	Transient three phase grid currents	[A]
i_{dr}	Transient d-axis current of slip-PMG	[A]
i_{ds}	Transient d-axis current of PMSG	[A]
i_{qr}	Transient q-axis current of slip-PMG	[A]
i_{qs}	Transient q-axis current of PMSG	[A]
I_{br}	Steady-state bar current of slip-PMG	[A]
I_{dr}	Steady-state d-axis current of slip-PMG	[A]
I_{ds}	Steady-state d-axis current of PMSG	[A]
I_{qr}	Steady-state q-axis current of slip-PMG	[A]
I_{qs}	Steady-state q-axis current of PMSG	[A]
I_m	Magnetising current	[A]
I_r	Per phase slip-PMG current	[A]
I_s	Per phase PMSG current	[A]
j	Complex operator	
J_g	Inertia of gearbox and driving motor	[kg.m^2]
J_i	Inertia of slip-rotor	[kg.m^2]
J_m	Inertia of common PM-rotor	[kg.m^2]
J_r	Slip-PMG current density	[A/mm^2]
J_s	PMSG current density	[A/mm^2]

J_t	Turbine and slip-rotor inertia	[kg.m^2]
k	Simulation procedure counter	
k_1, k_2	End-winding inductance calculation constants as given in Appendix A	
K	$K = k_1 - k_2$	
K_r	Slip-PMG machine constant as used in brushless-DC modelling	
k_w	Winding factor	
K_f	Permanent magnet end-flux fringing factor	
K_M	End-winding mutual per phase cross-coupling factor	
K_p	External permeability factor	
$\mathbf{K_p}$	Park transformation	
$\mathbf{K_p}^{-1}$	Inverse park transformation	
l	Axial stack length	[mm]
l_e	Average end-winding length	[mm]
l_g	Distance of end-winding from stack	[mm]
L_{br}	Slip-PMG per bar inductance component	[H]
L_{cs}	Series compensating inductance	[H]
L_{cp}	Power factor correction inductance	[H]
L_{er}	Slip-PMG end-winding inductance component	[H]
L_{es}	PMSG end-winding inductance component	[H]
$L_{e(1,2,3)}$	Different analytical end-winding inductance calculation methods	[H]
L_{dr}	d-axis inductance of slip-PMG	[H]
L_{ds}	d-axis inductance of PMSG	[H]
L_{qr}	q-axis inductance of slip-PMG	[H]
L_{qs}	q-axis inductance of PMSG	[H]
L_r	Slip-PMG per phase inductance	[H]
L_s	PMSG per phase inductance	[H]
m	Indicates number of bars conducting current	
M_c	Mutual phase end-winding cross-coupling	[%]
M_C	Conductor mass	[kg]
M_{Fe}	Steel mass	[kg]
M_{PM}	Magnet mass	[kg]
M_{Top}	Total SS-PMG tower-top mass	[kg]
M_{Tot}	Total active mass	[kg]
n	Harmonic index	
n_a	Number of parallel circuits	
n_g	Gearing ratio	
n_s	Rotational speed of common PM-rotor	[r/min]
n_t	Rotational speed of turbine	[r/min]
N_c	Number of turns per coil	

N	Maximum harmonic index	
p	Number of poles	
P_{cue}	Frequency dependent eddy-current copper loss component	[W]
P_{cur}	Copper loss component of slip-PMG unit	[W]
P_{cus}	Copper loss component of PMSG unit	[W]
P_{ecr}	Core loss component of slip-PMG unit	[W]
P_{ecs}	Stator core loss component of PMSG unit	[W]
P_{ecm}	PM-rotor core and PM eddy-losses	[W]
PF	Power factor	
P_{Loss}	Total loss component	[W]
P_r	Output power of slip-PMG unit	[kW]
P_s	Electrical output power of PMSG unit	[kW]
P_t	Mechanical turbine input power	[kW]
P_{wfr}	Wind and friction losses of slip-PMG unit	[W]
P_{wfs}	Wind and friction losses of PMSG unit	[W]
q	Number of coils per phase or indicates q-axis in dq-reference frame	
Q_s	Reactive power component	[kVAr]
r	Optimisation counter	
r_c	Average coil radius	[mm]
R_b	Electromagnetic braking resistance	[Ω]
R_{br}	Slip-PMG resistance per bar	[Ω]
R_e	Conductor eddy current loss resistance	[Ω]
R_c	Core loss resistance	[Ω]
R_r	Per phase slip-PMG resistance	[Ω]
R_s	Per phase PMSG resistance	[Ω]
s	Slip or Laplace operator in the frequency domain	
s_b	Slip value at which T_b occurs	
S	Number of slots	
t	Time	[s]
t_{off}	Time duration for current not being conducted	[s]
t_{on}	Time duration for current being conducted	[s]
t_{sl}	Electrical slip-PMG period	[s]
$T_{1,2}$	Transformer notations	
T_b	Maximum breakdown torque amplitude	[Nm]
T_{dr}	Slip-PMG torque ripple disturbance torque input amplitude	[Nm]
T_{ds}	PMSG torque ripple disturbance torque input amplitude	[Nm]
T_{dt}	Turbine disturbance torque input amplitude	[Nm]
THD	Total harmonic distortion	[%]
T_m	PM temperature	[°C]

T_r	Steady-state torque of slip-PMG unit	[Nm]
T_s	Steady-state torque of PMSG unit	[Nm]
T_t	Steady-state mechanical turbine input torque	[Nm]
v_{abc}	Transient three phase grid voltages	[V]
v_{ds}	Transient d-axis terminal voltage of PMSG	[V]
v_{qs}	Transient q-axis terminal voltage of PMSG	[V]
v_w	Wind speed	[m.s^{-1}]
V_{abc}	Nominal three phase grid voltages	[V]
V_{ds}	Steady-state d-axis terminal voltage of PMSG	[V]
V_{qs}	Steady-state q-axis terminal voltage of PMSG	[V]
V_s	Per phase grid or PMSG terminal voltage	[V]
w_c	Conductor or slot width	[mm]
w_e	End-winding width	[mm]
w_t	Average tooth width	[mm]
$W_{p1,2}$	Indication of different work points on PM BH-curves	
W_s	Number of winding sections	
x	Indicates x-axis direction	
$\mathbf{X}$	Dimensional input parameters, $[\mathbf{X}] = [x_1, x_2, ...x_n]$	
X_l	Line reactance	[Ω]
X_m	Magnetising reactance	[Ω]
X_r	Per phase slip-PMG reactance	[Ω]
X_s	Per phase PMSG reactance	[Ω]
X_{cs}	Series compensating reactance	[Ω]
X_{cp}	Power factor correction compensating reactance	[Ω]
y	Indicates y-axis direction	
$\mathbf{Y}$	Machine output performance parameters, $[\mathbf{Y}] = [y_1, y_2, ...y_n]$	
Z_l	Grid line impedance	[Ω]
α_r	Slip-PMG current angle	[°]
α_s	PMSG current angle	[°]
β	Parameter used in the calculation of k_1	
δ	Parameter used in the calculation of k_2	
Δ_s	PMSG power angle	[°]
$\Delta\tau_L$	Peak to peak load torque ripple	[%]
$\Delta\tau_{NL}$	Peak to peak no load cogging torque	[%]
η_r	Efficiency of slip-PMG unit	[%]
η_s	Efficiency of PMSG unit	[%]
η_t	Total system efficiency	[%]
$\lambda_{1,2}$	Notations used in flux linkage calculations for brushless-DC slip-PMG	[wb.t]
λ_{abc}	Three phase flux linkages	[wb.t]

λ_e	End-winding flux linkage	[wb.t]
λ_{mr}	slip-PMG permanent magnet flux linkage	[wb.t]
λ_{ms}	PMSG permanent magnet flux linkage	[wb.t]
λ_{dr}	d-axis flux linkage of slip-PMG	[wb.t]
λ_{ds}	d-axis flux linkage of PMSG	[wb.t]
λ_{qr}	q-axis flux linkage of slip-PMG	[wb.t]
λ_{qs}	q-axis flux linkage of PMSG	[wb.t]
λ_s	Per phase PMSG flux linkage	[wb.t]
θ_d	Disturbance input signal mechanical angle	[°]
θ_m	Mechanical angle of PM-rotor	[°]
θ_p	Pole pitch angle	[°]
θ_{PM}	Magnet pitch angle	[°]
θ_r	Slip-PMG power factor angle	[°]
θ_s	PMSG power factor angle	[°]
θ_S	Average slot pitch angle	[°]
θ_t	Slot pitch angle	[°]
θ_w	Slot width angle	[°]
σ_m	Magnet pitch to pole pitch ratio	
σ_t	Slot pitch to average slot pitch ratio	
σ_w	Slot width to average slot pitch ratio	
τ_{dr}	Slip-PMG torque ripple disturbance input	[Nm]
τ_{ds}	PMSG torque ripple disturbance input	[Nm]
τ_{dt}	Turbine torque disturbance input	[Nm]
τ_m	Transient torque response of common PM-rotor	[Nm]
τ_r	Transient torque response of slip-PMG unit	[Nm]
τ_s	Transient torque response of PMSG unit	[Nm]
τ_t	Transient torque response of turbine	[Nm]
ψ	Parameter used in the calculation of k_2	
ω	Angular speed	[rad/s]
ω_b	Electrical angular speed at which T_b occur	[rad/s]
ω_d	Disturbance input signal mechanical angular speed	[rad/s]
ω_e	PM rotor electrical angular speed	[rad/s]
ω_m	PM rotor mechanical angular speed	[rad/s]
ω_s	Electrical grid angular speed	[rad/s]
ω_{sl}	Mechanical slip angular speed	[rad/s]
ω_{sle}	Electrical slip angular speed	[rad/s]
ω_t	Turbine mechanical angular speed	[rad/s]
ω_{te}	Turbine electrical angular speed	[rad/s]

Chapter 1

Introduction

Although wind power is currently one of the renewable energy resources being harnessed on the largest scale, several challenges still exist to make this energy resource more competitive with regard to conventional energy sources. Some of these challenges include, reducing the initial capital cost, increasing the efficiency, improving the grid compliance of wind generator systems and increasing the reliability to reduce the operation and maintenance (O&M) costs of the system. In this study, the focus is on the improvement of the drive-train of the wind turbine system with special emphasis to the electrical generator part.

1.1 Background on Wind Generation

Regarding power output wind turbine systems can be divided into broad categories such as, small and micro-scale, medium-scale, utility-size onshore and utility size offshore. Fig. 1.1 show the cumulatively installed total worldwide wind capacity, with a significant growth observed within the last few years. Although the total installed capacity of offshore wind power is still very small compared to onshore wind turbine systems, the number of installed offshore systems are growing at a fast pace as shown in Fig. 1.2. Less information is available regarding small scale installations, with Fig. 1.3 showing the cumulatively installed small wind power generation capacity estimated until 2020. Interesting is that the projected installation of small wind power systems in 2020 is about as much as the current installed offshore wind power capacity.

Although there are many definitions for the power ranges of small scale wind turbines, small-scale systems are mostly considered as anything below 100 kW, with around more or less 1 kW and less considered as micro or pico wind power generation. The range between more or less 100 kW and 500 kW and maybe even up to 1 MW is considered as medium-scale wind power generation. Small wind turbines have been around for a very long time and its market share is growing significantly as shown Fig. 1.3, due to feed in tariffs and government rebates. Also for rural and mini grid applications, small and medium scale wind generators are anticipated to play a much more significant role. It is estimated in [21] that almost 1.5 billion people worldwide are without electricity, almost 600 million in Africa alone. Many of these grids as explained in [21] consist of a diesel gen-set, with renewables utilised to supplement the power in the mini-grid and offset the diesel usage. It is furthermore, mentioned in [22] that wind can be a viable solution for these grids. A significant challenge is, however, operation and maintenance for these wind turbines and the availability of spare parts and skilled technicians in remote regions. Furthermore, due to the distributed installation of small wind turbines in general, maintenance is, thus, a very

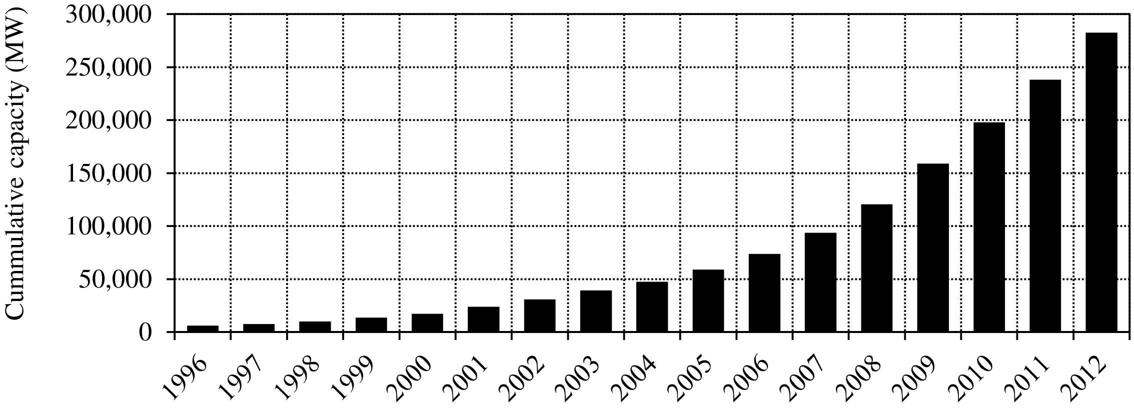

Figure 1.1: Cumulatively installed total wind power capacity [1].

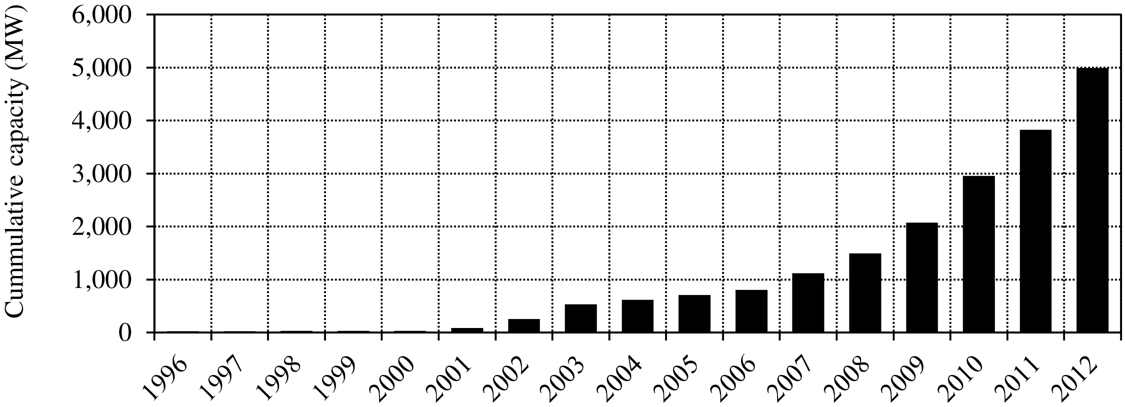

Figure 1.2: Cumulatively installed offshore wind power capacity [2].

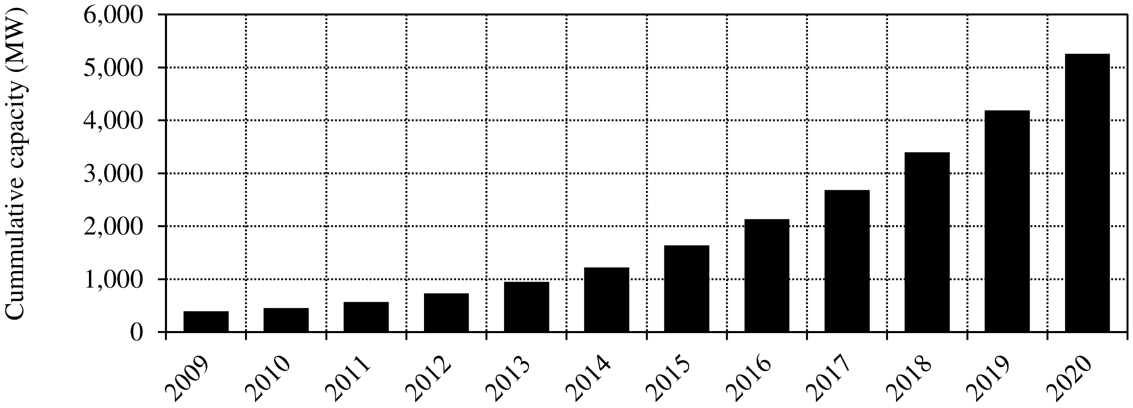

Figure 1.3: Cumulatively installed small wind power capacity (estimated from 2012 onwards) [3].

important aspect. Although there are clear indications regarding the growth in market share, not many research studies exist on the improvement of the technology of small wind turbine systems compared to utility scale systems. Significant advances are, thus, required in the technology of small wind power systems in order to improve their performance, reduce the cost and increase the reliability of these systems. As the wind generator technologies being considered in this study are being demonstrated at the small scale level it is important to obtain an idea of the design requirements and implementation issues regarding these systems.

Above 1 MW is considered as utility scale, with the average rating of wind turbines currently being installed about 2.5 to 3 MW and the largest currently installed prototype rated at 7.5 MW [23]. Although most existing wind farms are onshore, in the last few years offshore wind energy installations have gained significant interest due to a shortage of land in many countries, and due to offshore wind turbine installations having the advantage of a much higher capacity factor. This means that offshore wind turbines have a much higher theoretical energy yield for the same size turbine installed onshore [4]. Offshore wind turbine systems are also on average larger than onshore systems to make use of the much better wind conditions. However, the initial installation cost and the O&M cost, due to the offshore installations requiring much more maintenance, are significantly more as opposed to land based systems.

1.2 Current Wind Turbine Drive-Train Technologies

The classical wind turbine drive train consists of a directly grid-connected high speed conventional induction generator (IG) with a squirrel-cage rotor and usually a three stage gearbox as shown in Fig. 1.4(a). Only a small percentage of mostly the older wind turbine installations still in use today make use of this topology. Due to the use of standard components this is one of the cheapest options available. These systems also require a *"soft-starter"* and power factor correction equipment which is usually a capacitor bank as shown in Fig. 1.4(a). Many of these systems employ the classical stall concept which passively limits the wind turbine power output if the wind speed increases above the rated wind speed. In later installations active stall is used where the pitch angle of the blades are actively adjusted to limit the wind turbine power output. Many small-scale wind turbine systems utilising a tail vane for passive yawing, employ passive furling techniques to limit the turbine power in high wind conditions by turning the turbine away from the oncoming wind direction. In [24] a comparison is done between active pitch control and passive furling techniques for small scale wind turbines. Disadvantages of the topology in Fig. 1.4(a) include reduced energy harvesting, higher audible noise levels and higher loading on the drive-train components due to the stiff grid connection and this topology operating at fixed speed. Another major disadvantage is the difficulty of this type of system to comply to grid code specifications. As explained in [25] and [26] to allow some margin of variable speed operation pole-changing induction machines, where the pole number of the machine can be changed to allow it to operate at two different operating speeds, are utilised as well. Also for early cage rotor IGs it was not uncommon to have dual speed systems utilising two induction machines as for example in [27], with some of these wind turbine systems still in use today although limited as mentioned in [26]. A variation of the classical IG concept is the so-called *"opti-slip"* or *"flexi-slip"* systems as shown in Fig. 1.4(b). In this case the cage rotor is replaced by a wound rotor and an external resistance is added to the rotor circuit to control the slip of the IG, which also allows some margin of variable speed operation. This, is especially helpful if the turbine experiences a wind gust. By increasing the rotor resistance the rated slip increases, which makes the grid connection less stiff and reduces the loading on the wind turbine components.

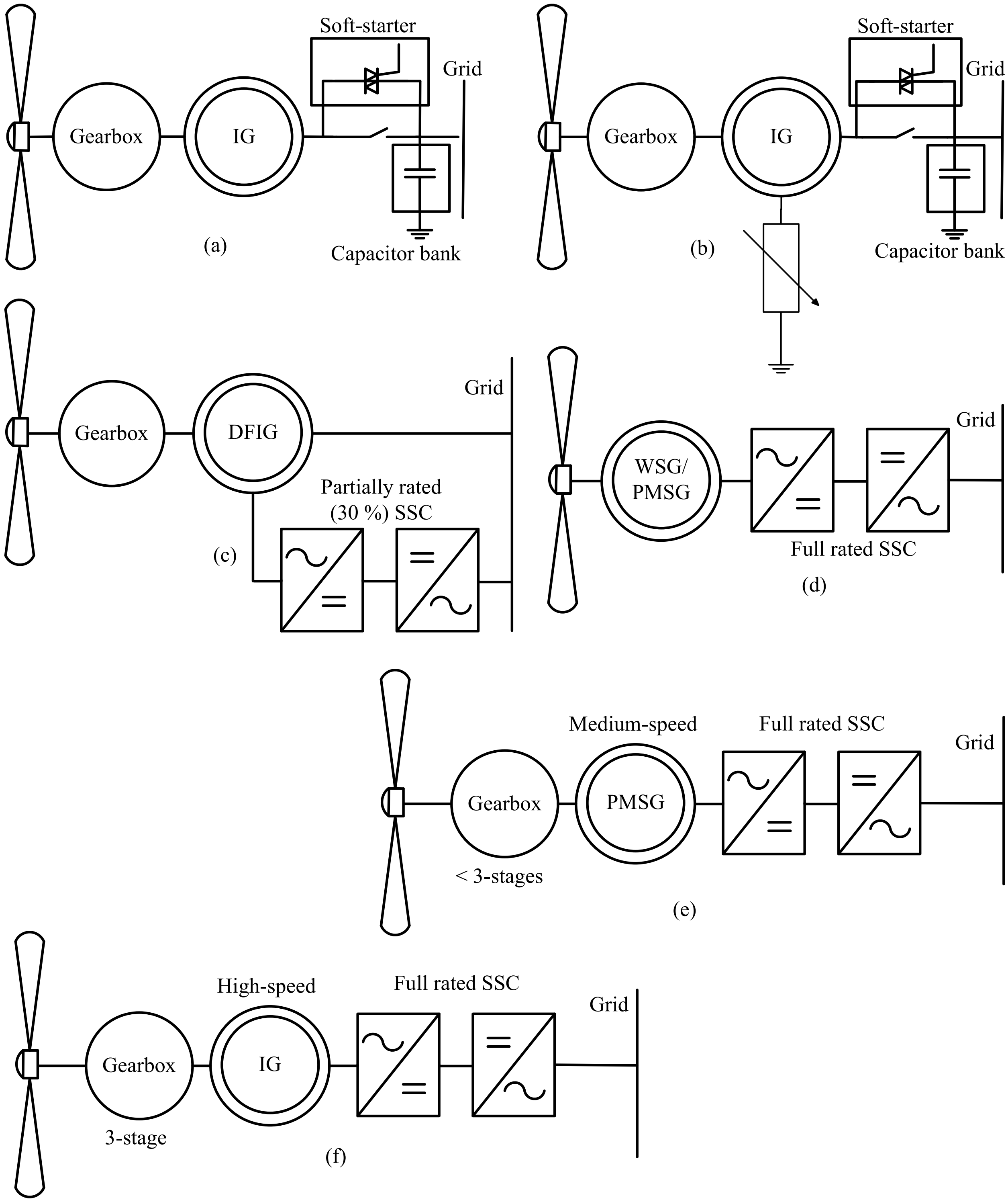

Figure 1.4: Different wind turbine drive-train layouts currently in use with (a) the conventional high speed induction generator (IG) and gearbox, (b) conventional induction generator with wound rotor and external resistance *(Opti-slip or Flexi-slip)* (c) the variable speed doubly-fed induction generator (DFIG) with gearbox and partially rated converter, (d) direct-drive wound synchronous generator (WSG) or permanent magnet synchronous generator (PMSG) and full rated power electronic converter, (e) medium speed PMSG having a gearbox with fewer stages and a full rated power electronic and (f) high speed IG operated with a 3-stage gearbox and full rated power electronic converter.

More recent installations based on the IG concept make use of the doubly-fed induction generator (DFIG) with also a three stage gearbox as shown in Fig. 1.4(c) which is at current the most installed type of wind generator. This IG also has a wound rotor instead of the squirrel cage rotor, with a partially rated converter (about 25-30 % of the rated power) connected to the rotor windings [25,26]. This is a variable speed wind generator with a speed range of more or less 60 % to 110 % of the rated speed as mentioned in [25]. Important disadvantages of the DFIG are the use of slip-rings and the grid compliance of the generator relating to the ability of the generator to stay connected to the grid during grid faults. However, as mentioned in [25] a number of studies have been conducted on the improvement of the low voltage ride through (LVRT) capabilities of the DFIG. Although mostly only experimental in nature it has also been proposed to use a brushless doubly-fed induction generator (BDFIG), which is being proposed for use as a medium speed wind generator as well. This machine has two sets of stator windings, with a short-circuited rotor having nested loops. The main advantages as opposed to a conventional DFIG is that the BDFIG requires no slip-rings and have better LVRT capabilities. A drawback, however, is the increase in generator size as opposed to the same rating DFIG.

A recent trend in wind turbine drive trains, is the use of direct drive wind generators with no gearbox. The motivation for utilising direct drive wind generators is to decrease the number of components in the drive train and to eliminate the maintenance issues associated with gearboxes, which should, thus, reduce the O&M costs of the wind turbine system. In this case a synchronous generator (SG) with a wound rotor or a permanent magnet synchronous generator (PMSG) is connected directly to the turbine, with the generator connected to the grid via a full rated power electronic converter as shown in Fig. 1.4(d). At current most utility scale installed direct drive systems make use of a wound rotor SG. Most small scale wind turbine systems make use of a directly turbine mounted PMSG, of which the output is either rectified for battery charging applications, or connected to the grid via a full rated power electronic converter known as *"grid-tie"* systems. By using a full rated converter the wind turbine can be operated over its full speed range, which increases the energy harvesting of the wind turbine system. The grid compliance characteristics of generators operated in conjunction with a power electronic converter is also far better than that of other wind turbine systems. Limiting factors of these systems, however, are the shear size and mass (especially of the wound rotor SG) and the high cost and volatility of the PM material price for direct drive PMSGs.

Thus, with the mass and cost of direct drive systems a significant consideration, medium speed SGs (mostly PMSGs) operated with a gearbox having fewer gearing stages, also known as *"multibrid"* systems, are also considered as shown in Fig. 1.4(e) and for example in [28] and [29]. The gearbox with fewer gearing stages will be more reliable and more efficient. In this case the generator is also connected to the grid via a full rated power electronic converter. Due to the low component cost some manufacturers also make use of a three stage gearbox and high speed squirrel-cage induction generator system as in Fig. 1.4(a), but with the generator connected to the grid via a full rated converter as shown in Fig. 1.4(f), to allow for variable speed operation and to improve the grid compliance of the system.

1.3 Cost of Wind Turbine Systems

For background only a broad and very basic overview is given of the cost distribution of typical wind turbine installations in this section as found in literature. The cost distribution of a typical offshore wind turbine installation is shown in Fig. 1.5. It is seen that the actual wind turbine component

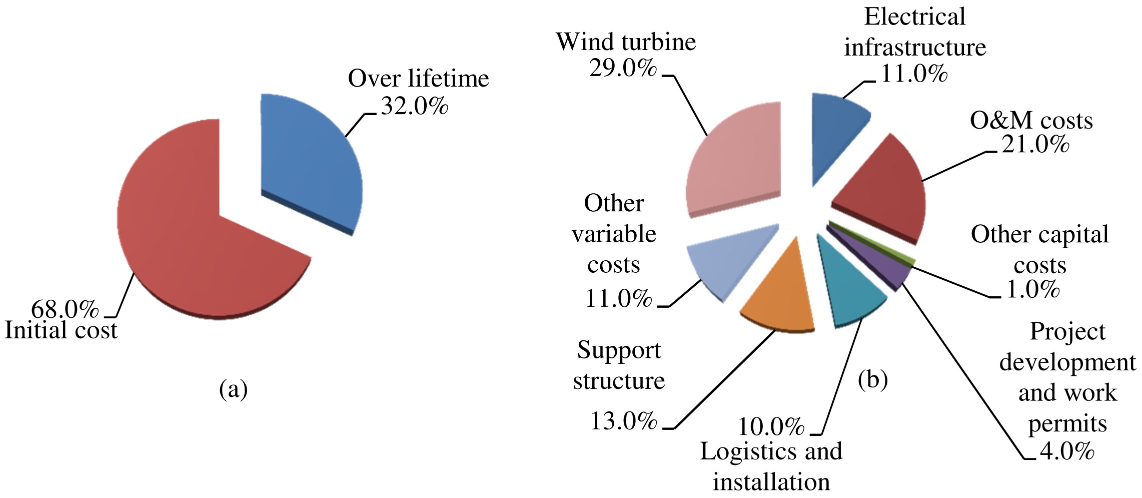

Figure 1.5: Total cost distribution for a typical offshore wind turbine installation with (a) a breakdown of the initial and the running costs and (b) breakdown of all the cost components over the lifetime of the wind turbine installation [4].

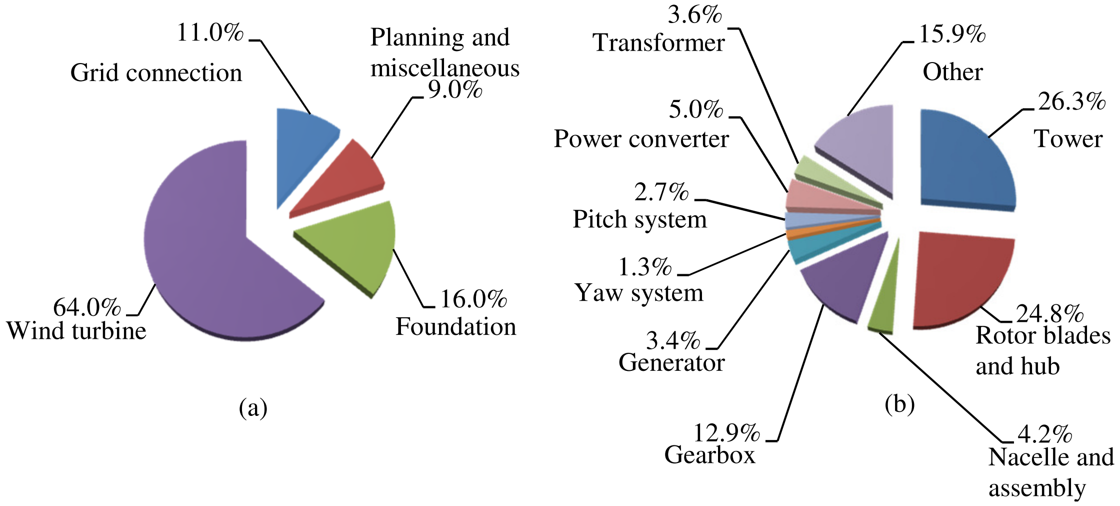

Figure 1.6: Initial capital cost distribution for (a) the overall wind turbine installation and (b) the different components of the wind turbine [5].

cost is less than a third of the total cost of the wind turbine system. Furthermore, the operational costs incurred over the lifetime of the wind turbine is shown to amount to almost a third of the total cost. Fig. 1.6 shows the initial capital cost breakdown for a typical land based wind turbine system. With the drive train components (gearbox, generator and power electronic converter) amounting to just over 20 % of the wind turbine component costs in Fig. 1.6(b), it amounts to less than 15 % of the total system cost by taking the distribution in Fig. 1.6(a) into account. If the drive train cost is considered in Fig. 1.5 with the total lifetime cost of the wind turbine system taken into account it is seen that the drive train only amounts to just over 6 % of the total system cost in this case. Fig. 1.7 shows the difference in the cost breakdown of the different installation aspects of offshore versus onshore wind turbine installations. Clearly the wind turbine component comprises far less

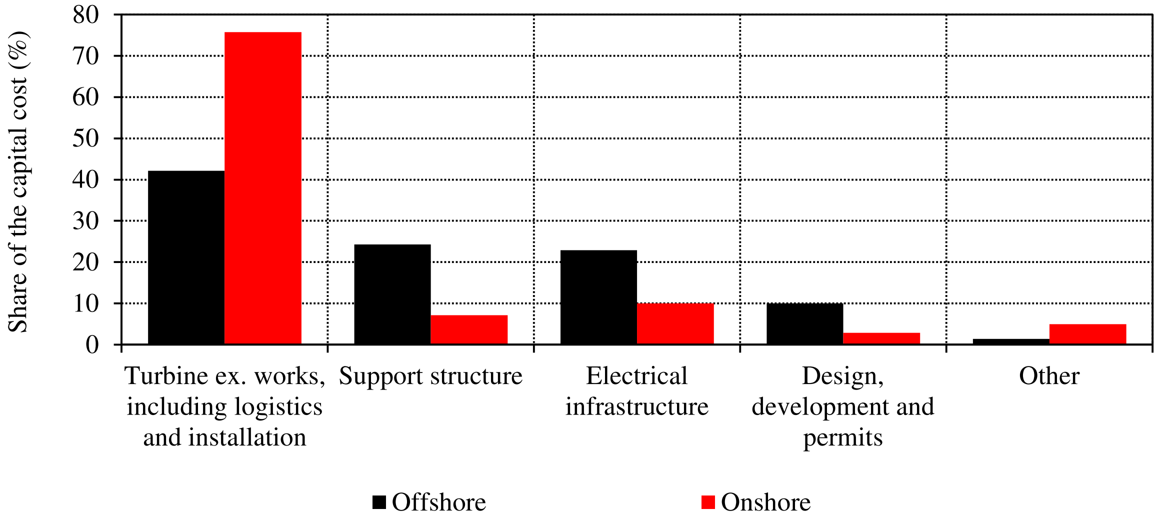

Figure 1.7: Comparison of the initial capital cost breakdown for both offshore and onshore wind projects [4].

of the total capital cost in percentage compared to onshore projects. As most available data are for DFIG type wind turbine systems, due to these systems being the most installed, Fig. 1.8 show the cost breakdown comparison of only the drive trains of four different wind turbine technologies [6]. The data shown are for a conventional DFIG with 3-stage (3G) gearbox, direct drive WSG and PMSG, and a medium speed PMSG with one stage gearbox. All of the generator systems shown in Fig. 1.8 are rated at 3 MW. The DFIG has a partially rated converter and full rated converters are used for the rest of the generator systems. The data obtained from [6] is modified to include a more recent reflection of the PM price. It is shown in Fig. 1.8 that due to the current high price of PM material, the direct drive PMSG is the most expensive drive train solution.

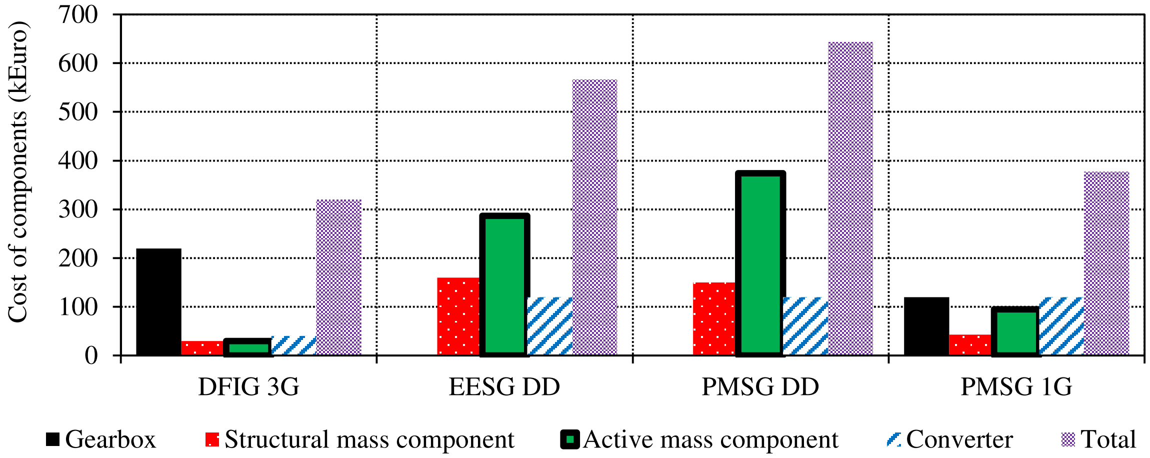

Figure 1.8: Comparison of the initial capital cost breakdown for the drive trains of different wind turbine technologies at a power rating of 3 MW [6].

1.4 Reliability of Wind Turbines

Fig. 1.9 shows a breakdown of the different operation and maintenance cost components for the Horns Rev offshore wind farm in Denmark as given in [7]. It is clear that corrective maintenance and serial failures dominate the O&M costs. Apart from other implementation issues, such as mass, initial capital cost, efficiency and grid compliance, O&M cost as seen in Figs. 1.5 and 1.9 are clearly a very important consideration, especially for isolated wind farms with limited access such as offshore installations. Offshore installations are much less accessible than land based systems, especially in adverse weather conditions which makes maintenance difficult as seen in Fig. 1.9 regarding the cost component of vessels and helicopters required to access these wind turbine installations. Some studies suggest that for offshore installations O&M costs can amount up to almost a quarter of the total cost of a wind farm and up to 30 % of the cost per unit of energy generated. In [4] it is mentioned that O&M costs for offshore wind farms are two to three times higher than for onshore installations.

As seen from the above mentioned it is, thus, important that adequate knowledge of the reliability of the different wind turbine system components are obtained. Several studies have been done on the reliability of wind farms, but it is difficult to get an accurate representation, with the information given varying from source to source, as only a few commercial wind farms are reaching the end of their lifetimes at current. As given in [30] that if a wind turbine needs to be designed for a 20 year lifetime it needs to operate for approximately

$$20 \text{ years} \times 365.25\frac{\text{days}}{\text{year}} \times 24\frac{\text{hours}}{\text{day}} \times \text{ capacity factor of } 0.4 = 70128 \text{ hours.} \tag{1.1}$$

The same capacity factor of 0.4 is used as in [30]. Most wind turbine sites might have lower capacity factors as mentioned in [31], with average capacity factors for land based systems given between 20 and 30 % and between 20 and 40 % for offshore installations and in some cases even as high as 50 %, as mentioned in [4]. From (1.1) it is seen that the wind turbine needs to be designed to operate for approximately 70000 hours. This is a significant number compared to for instance auto-mobiles which are typically designed for 5000 hours!

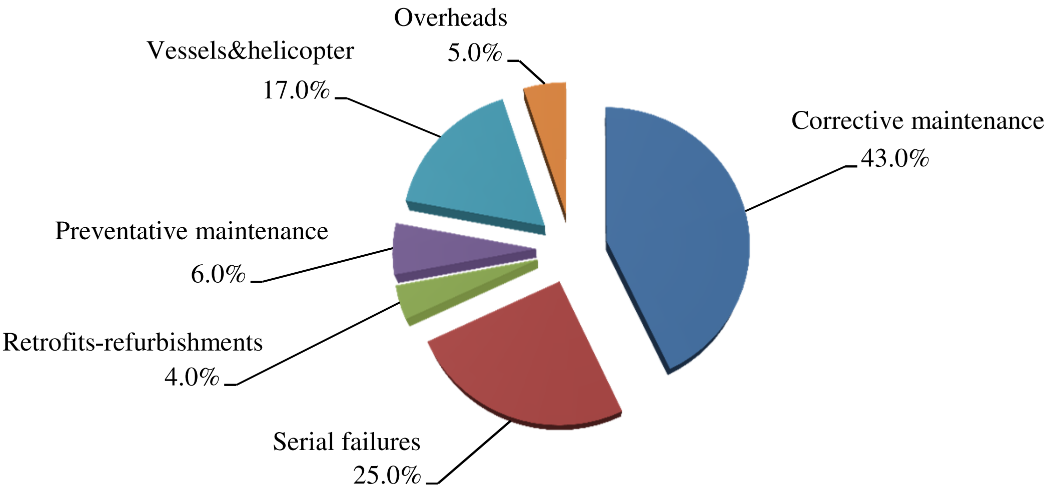

Figure 1.9: Estimation of the O&M cost breakdown at the Horns Rev offshore wind farm in Denmark [7].

As mentioned most small-scale wind turbine systems make use of a directly turbine connected PMSG and power electronic converter in the drive train [5, 8, 26, 32]. Due to these generators being much smaller than utility scale turbines with also a smaller tower and supporting structure the power electronic converter comprises a significant portion of the overall cost for small wind turbine systems. Also in the reliability analysis of these systems the power electronic converter is one of the components considered the most. Replacements of parts of the power electronic unit are also more expensive compared to the rest of the system as opposed to utility sized wind turbines. In [8] an in depth study is done regarding the reliability of the power electronic converter of a small wind turbine system. Fig. 1.10 shows the failure distribution of the different components in a small wind turbine system. The data obtained is the average of different European suppliers as given in [8]. The failure distribution is clearly dominated by the electrical system, which is mainly the power electronic converter for small scale wind turbine systems, and the blades and pitching systems. Fig. 1.11 shows the reliability of the power electronic converter unit of a small scale system over time as calculated in [8]. From Fig. 1.11 it is seen that for almost the last half of the turbine's lifetime, with the estimated lifetime as given in (1.1), the reliability of the power electronic unit will be below 50 %. Furthermore, due to the distributed nature of small scale wind turbines, with many of these systems installed in rural and isolated locations, as mentioned in [5] robustness and maintenance requirements are very important aspects of small wind turbines. To improve the economic viability of these systems it is, thus, essential that the O&M costs are significantly reduced.

The most recent study found in literature on the reliability of utility scale wind turbines, known as the EU FP7 Reliawind project, is reported in [33] and [9]. The results from this study is shown in Fig. 1.12. In [9] 350 onshore wind turbines operating for varying lengths of time were evaluated. Over the course of the study 35,000 downtime events were logged. In Fig. 1.12 the results from [9] are categorised in more general sub-categories for better presentation. The two sets of data shown are the % contribution to the total failure rate (% failures/turbine/year) for each different component and the contribution to the average downtime (% hours/year) per failure per component. In [9] the total downtime caused by a failure is regarded as the most critical for an availability measure of a wind energy facility. From Fig. 1.12 the component failing most frequently is the pitch system which also contributes to the largest downtime %. Same as for the failure rate of small wind turbines as

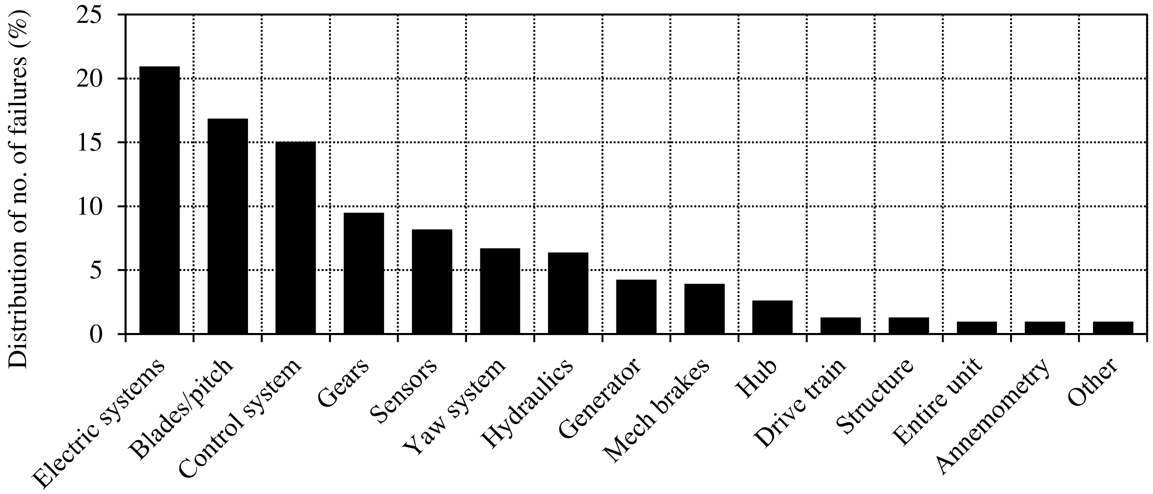

Figure 1.10: Distribution of failures for small scale wind turbines [8].

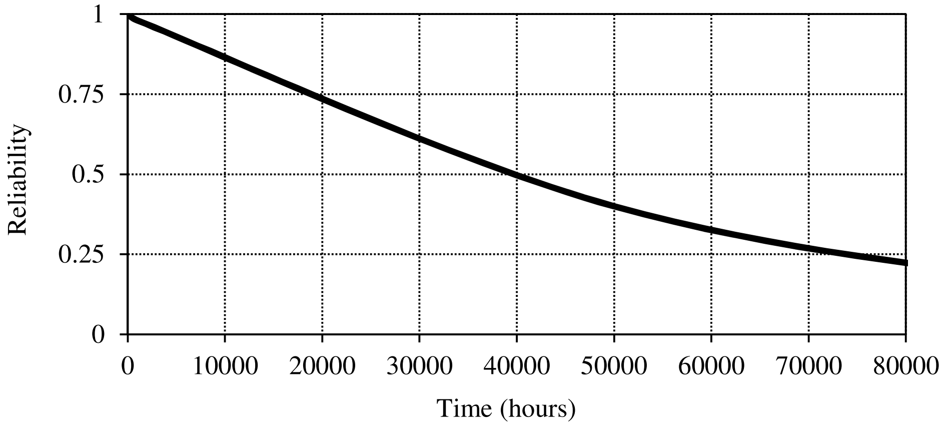

Figure 1.11: Reliability of the power electronic converter unit over time in a small-scale wind turbine system [8].

shown in Fig. 1.10, the power electronic converter contributes to a significant % of failure occurrence and downtime contribution in this case as well.

However, although the measure of downtime caused by each failure is taken as the criteria to evaluate the impact of a failure in [9], it should be noted that some failures are more expensive to replace than others. Observing Fig. 1.6 it is seen that the tower, foundation, blades and gearbox contributes to significant portions of the overall cost of the wind turbine system. Failures in these components will be much more expensive to replace than the replacement of certain of the components of the power electronic converter and pitching system. With the grid-connection and electrical

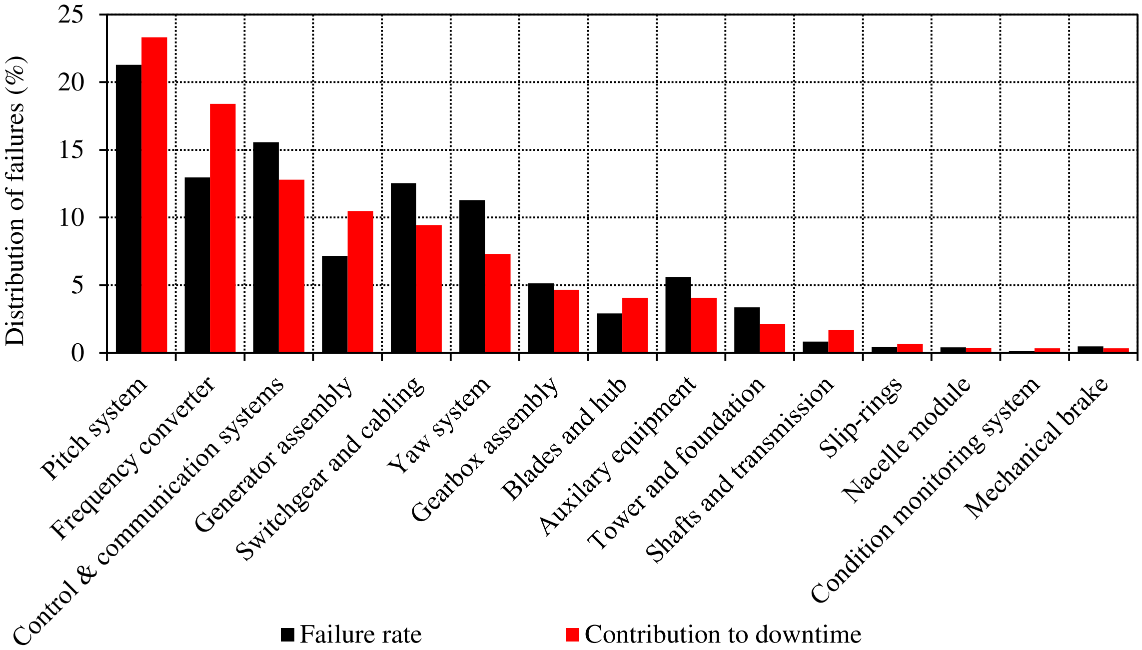

Figure 1.12: Distribution of failure rate and the contribution to downtime for 350 onshore wind turbines from the data given in [9].

infrastructure as shown in Figs. 1.5 and 1.6 also owing to a substantial portion of the overall cost, especially for offshore installations and with switchgear and cable failures also featuring significantly in Fig. 1.12 these failures could also potentially be a significant consideration in the reliability analysis. Another interesting observation from Fig. 1.12 is the low failure rate of the slip-rings, which is mentioned by many as a significant consideration regarding the reliability of wind turbines. An interesting analysis in future studies would be to compare the total life-cycle cost attributed to each type of failure.

In [9] it is not clearly stated what type of drive train technologies are considered. It is assumed that with most installed systems making use of the DFIG and partially rated converter as shown in Fig. 1.4(c) the data shown are mainly applicable to these type of systems. The failure distribution and O&M costs associated with medium speed and direct-drive systems, thus, requires definite further investigation. As mentioned in [34] it cannot always be assumed, as is generally the case, that direct-drive generators will be more reliable than geared systems. Furthermore, due to the power electronic converter of these systems having a power rating of more than three times that of the partially rated DFIG converter, which already features significantly in the reliability analysis, the failure rate of these large converters are a question. The low electrical frequencies at which direct-drive generators operate are also known to cause increased thermal cycling which could further decrease the reliability of the converter. There are some studies such as reported in [35–37] where methods to more accurately predict the failures of power electronic converters are being evaluated. In [35] it is mentioned that due to the increase in the power capacity of wind power systems the use of full scale power electronic converters are being questioned, due to reliability issues caused by thermal cycling.

1.5 Non-Conventional Wind Generator Concepts

To improve the performance, reduce the mass and increase the reliability of wind turbine generators several non conventional technologies are proposed in literature. Examples include new direct drive generator topologies such as transverse flux PM generators and other novel large diameter generator topologies. Magnetically geared PM generators are also being considered by many and superconducting direct drive generators are also receiving significant interest in recent times [25]. With the focus of this study being on the direct grid connection of a synchronous wind generator the topologies proposed in literature where a SG is connected directly to the grid are evaluated in this section. Although not extensively used in wind power applications, directly grid connected synchronous generators have been used successfully for decades for power generation with widespread acceptance by both the power generation industry and network operators. Direct grid SGs are also proposed in other renewable energy applications such as for example micro-hydro turbines as shown in [38].

1.5.1 External Damping of SG Wind Turbine Systems

Due to the oscillatory behaviour of SGs during load changes caused by the limited amount of damping for the direct-grid SG, these generators cannot be connected directly to the grid in a transient torque application with sudden load changes such as wind power generation. It is common practice in industry to make use of damper windings, but this does not seem to be sufficient for wind energy applications.

An example of a topology where external mechanical damping is proposed for a direct grid synchronous wind generator is the spring and damper system proposed to damp power angle oscillations

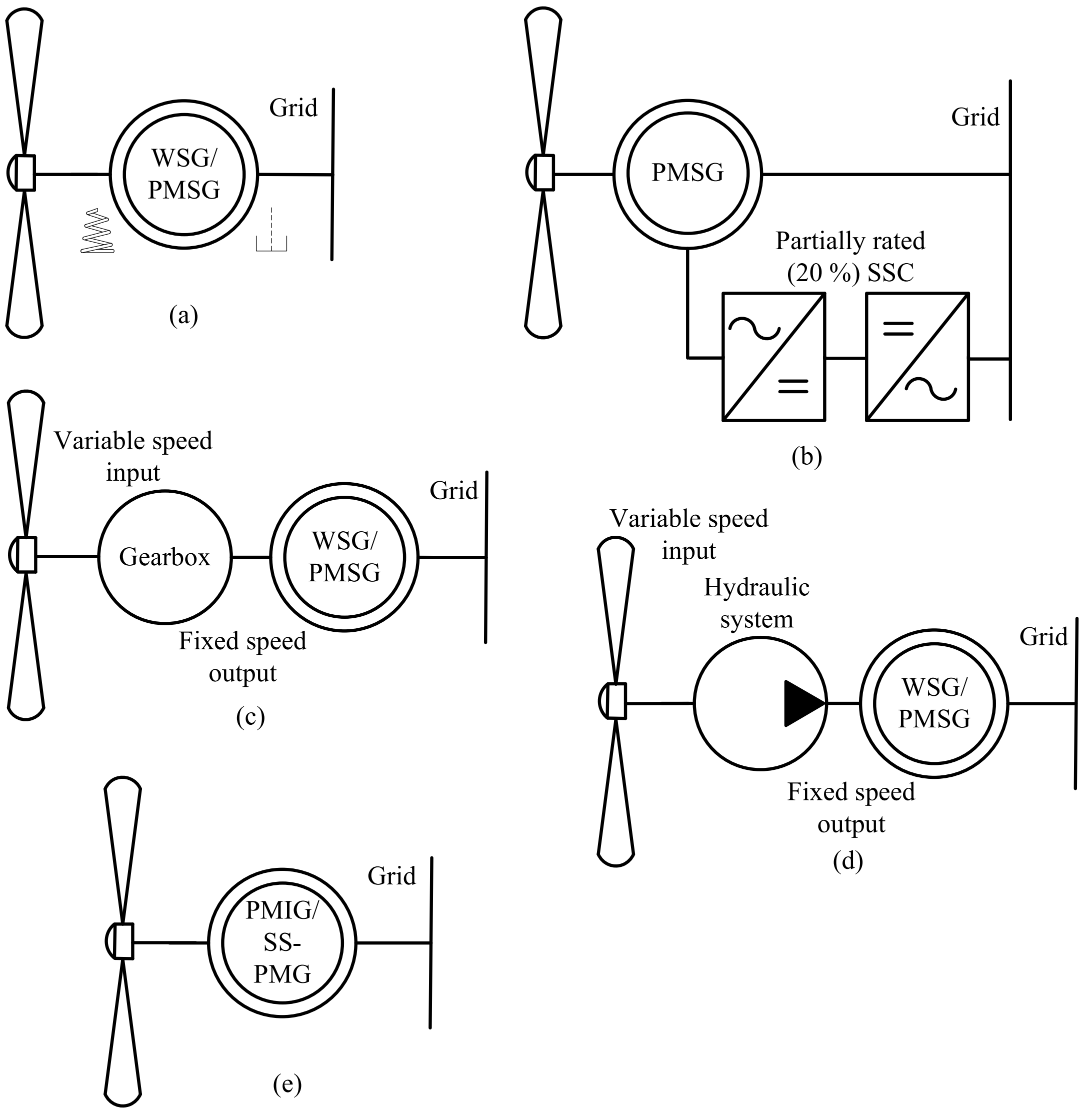

Figure 1.13: Different non conventional directly grid connected SG wind turbine drive-train layouts with (a) the spring and damper system in combination with a SG, (b) PMSG with partially rated star point converter, (c) gearbox with variable speed input and fixed speed output with SG, (d) hydraulic system and SG and (e) PMIG or SS-PMG systems.

by [39] as shown in Fig. 1.13(a). The stator is mounted on an additional bearing arrangement and is connected to the nacelle structure by means of the spring and damper configuration. Another direct-grid PMSG wind generator topology using external damping reported in literature is the concept proposed in [40] where a partially rated converter (about 20 % of the rated system power) is placed in the star point of the generator as shown in Fig. 1.13(b). Power fluctuations can then be actively damped by means of this converter. Although, the above mentioned technologies are proposed as feasible solutions, no evidence of practical verification could be obtained in the relevant literature studies. The practicality of these concepts are, thus, not clear from the information currently available.

1.5.2 Variable-Speed Input and Fixed-Speed Output Devices

Several studies are currently being conducted on devices where the variable speed input from the turbine is transformed to a fixed speed output at the generator side as shown in Fig. 1.13(c) and (d). The fixed speed output also enables the direct grid connection of a SG in this case. There are certain studies where hard gearing with physical gear changes are proposed such as in [41]. Many of these systems, however, employ continuously variable transmission (CVT) topologies as discussed in [42–45].

Other wind turbine systems with variable speed input fixed speed output transmission systems make use of an hydraulic power transfer stage in the drive train. Hydrodynamic systems such as the work reported in [46], combines the hydraulic stage with a gearbox. Depending on the gearing ratio either a high speed or medium speed synchronous generator can then be connected directly to the grid. Based on the study reported in [46], prototypes are being developed by DeWind, with successful prototype tests conducted as reported in [47]. From the modelling and transient response of this system as done in [46] and from the grid tests conducted in [47] several favourable grid supporting capabilities of the direct grid SG are mentioned, such as enhanced LVRT capabilities, the fact that the direct-grid SG can satisfy a much higher reactive power demand as opposed to other wind generator topologies, that it can act as a buffer regarding frequency variations during sudden load changes and also several favourable voltage regulation characteristics at the distribution level with the direct grid SG acting as a synchronous compensator.

Hydrostatic hydraulic power transfer systems making use of positive displacement pumps are also being evaluated by some. A Mitsubishi industry partner, Artemis Intelligent Power, is currently in the process of developing a prototype hydrostatic hydraulic power transfer system with an industry standard direct grid SG for wind energy devices as mentioned in [48]. This is based upon the work done in [49]. Other studies on hydraulic power transfer for wind power applications includes the work reported in [50–53]. A major concern regarding these systems is the efficiency, with total system efficiency values given of just over 80 % in the reviewed literature, whereas conventional system efficiencies are usually above 90 %. However, it is mentioned that these systems are significantly lighter than other wind turbine systems currently in use. It is evident that much more work is still required before conclusions can be made regarding the feasibility of hydraulic power transfer for wind turbines. It would be insightful to obtain an idea of the cost of energy produced by these systems over the lifetime of the wind turbine system, as well as the financial benefits associated with the mentioned benefits of having a directly grid-connected SG, as opposed to other wind turbine systems.

1.5.3 Permanent Magnet Induction Generators

The permanent magnet induction generator (PMIG) is another directly grid connected generator topology which can also be connected directly to the turbine as shown in Fig. 1.13(e). As shown in Fig. 1.14(a) the PMIG consists of a conventional 3-phase winding stator and short-circuited cage-rotor. A second freely rotating PM-rotor on a separate set of bearings induces a voltage in the stator winding at grid frequency as indicated in the equivalent circuit of the PMIG in Fig. 1.14(b). The PMIG was initially proposed to improve the power factor of conventional induction machines, by reducing the magnetizing current (I_m) as shown in Fig. 1.14(b).

The PMIG is based on the concept first introduced in 1926 by [54]. In the proposal of [54] electromagnets were used to provide the excitation for the machine. However, due to practical considerations the technology did not seem feasible at that stage. In later studies such as in [55]

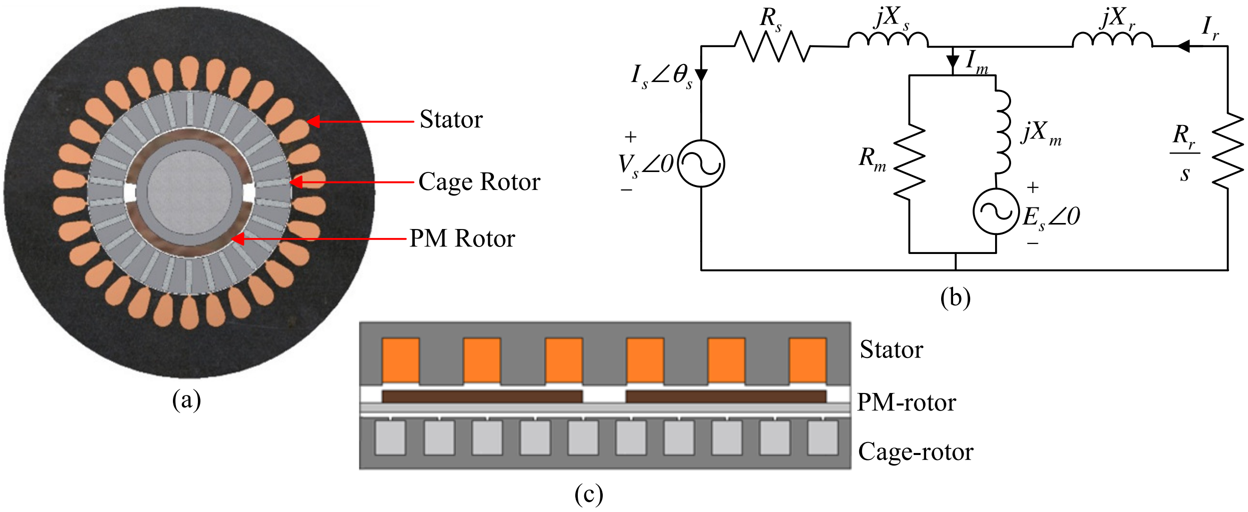

Figure 1.14: (a) Prototype example, (b) equivalent circuit and (c) section diagram of the permanent magnet induction generator.

in 1959 and [56] in 1967 the use of PMs are proposed, but due to the low energy densities of PMs back then the practicality of the concept could still not be adequately justified. The technology became more feasible when in 1992 the use of high energy density PM material was suggested for use in a PMIG proposed for a geared wind generator by [57]. Several PMIG research studies were conducted in Japan by [58] and [59] at the Toyota Technological Institute. Further research on this concept in Japan is reported in [60–65] at the Kanazawa Institute of Technology. The first local research on the PMIG concept is reported in [66] and further research on the PMIG concept is reported in [67] and [68]. Most of the above mentioned studies focus on the improvement of the power factor of conventional induction machines. From 1999 onwards more relevant literature surfaced in Germany as reported in [69–73]. In these studies the PMIG was proposed for the first time for use as a direct-drive-direct-grid PM wind generator. Other studies of the PMIG in a wind generator setup includes the work done in [74–76] where the reactive power characteristics of the PMIG are evaluated in more detail.

The discussion above is a summary of the most relevant literature on the conventional PMIG concept, with the contribution of each more thoroughly discussed in [77]. Although many of the studies in the literature reviewed proposes the PMIG for implementation as a direct-drive-direct-grid wind generator, only small scale prototype generators were ever manufactured and practically tested. In most cases an existing low pole number induction machine was modified to include the second freely rotating PM-rotor. Some of these systems were compared with conventional unmodified induction machines of the same power rating and size and relatively good results were obtained. However, no evidence could be obtained regarding the manufacturing and testing of a high pole number, low speed permanent magnet induction wind generator. The main reason for the lack of practical validation seems to be the apparent difficult construction of the PMIG, which is mentioned as a potential drawback by some.

The first variation of the PMIG concept is proposed in [78] at the Massachusetts Institute of Technology (MIT). In this study the PMIG slip-rotor is wound and a partially rated power electronic converter is connected to the rotor-winding in the same way as for a doubly-fed induction generator. Due to the conventional PMIG being a fixed speed generator, this topology allows the PMIG to operate as a variable speed wind energy converter allowing for higher energy yield. Further

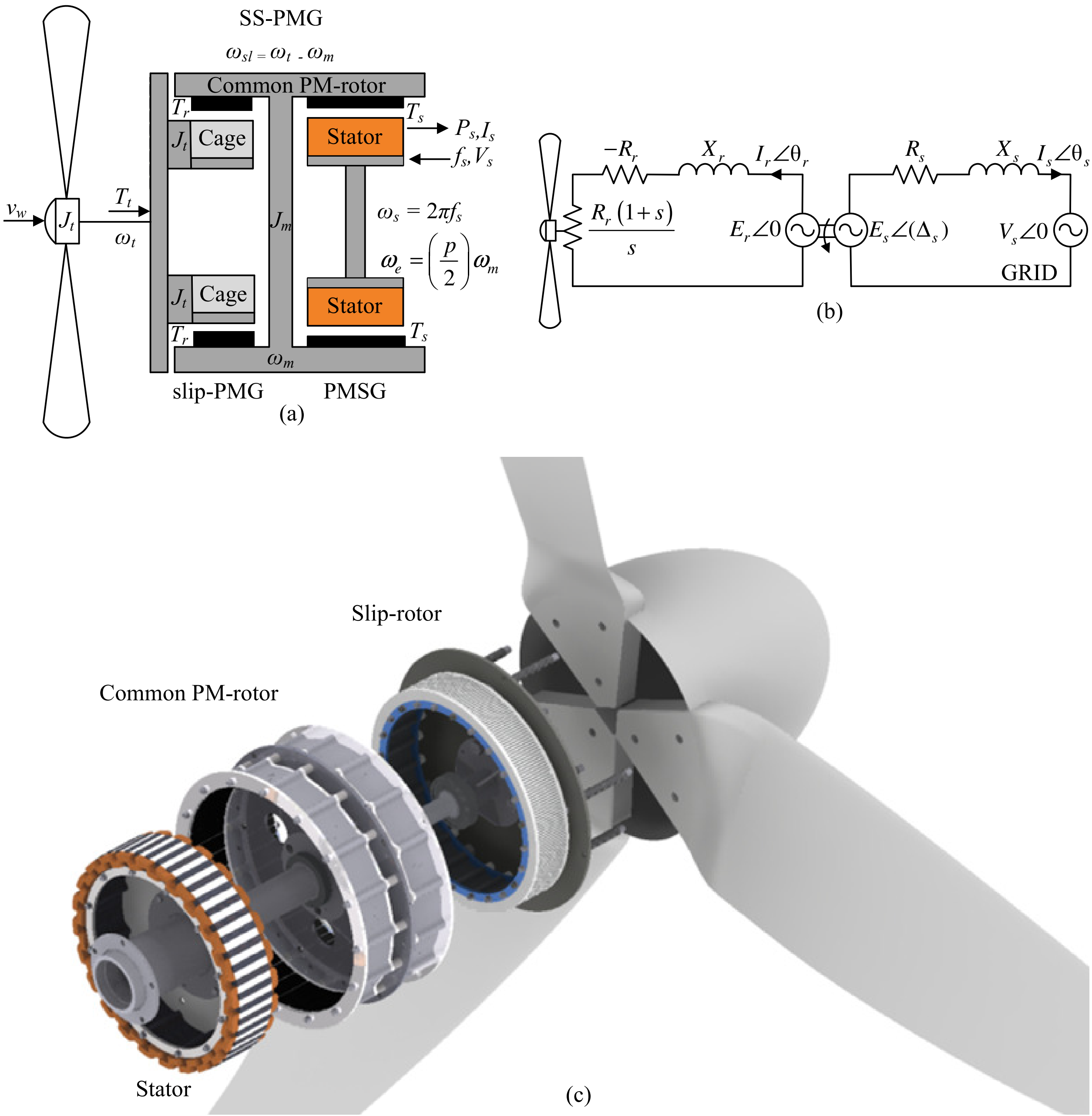

Figure 1.15: (a) Cross-section diagram, (b) equivalent circuit and (c) prototype example of the SS-PMG.

work conducted at MIT on this concept are reported in [79] and [80], which focussed more on the implementation of the prototype generator system.

1.6 New Concept SS-PMG

The directly grid-connected wind generator topology evaluated in this study is called a slip-synchronous permanent magnet generator (SS-PMG). This generator topology is based upon the PMIG as discussed in the previous section, with the main difference being that the short-circuited slip-rotor winding and grid connected stator winding are electromagnetically separated. The SS-PMG consists of two integrated generating units, a slip permanent magnet generator (slip-PMG) with the short-circuited rotor, similar to an induction machine cage-rotor mounted directly to the turbine, and a PMSG unit of which the stator terminals are connected directly to the grid. These two units are linked mechanically via a common free rotating PM-rotor with separate sets of magnets for each of the generating units. The slip-PMG and PMSG can be separated either radially or in an axial fashion. Figs. 1.15(a) and (b) respectively show a section diagram and example of the SS-PMG generating system, with the two generating units axially separated. The common PM-rotor rotates at synchronous speed in accordance with the grid frequency. The turbine connected slip-rotor rotates at a relative slip speed with regard to the PM-rotor. Separate voltages are induced in the stator winding, at synchronous speed, and in the slip-rotor winding, at slip-speed, as shown in the equivalent circuit for the SS-PMG in Fig. 1.15(c). A torque is generated between the slip-rotor and the PM-rotor (T_r), while a counter torque is generated between the stator and the PM-rotor (T_s). Power transfer, thus, takes place from the turbine to the slip-rotor and then via the PM-rotor to the stator and the grid.

Thus, far the SS-PMG has only been proposed, with a brief overview of the technology and its characteristics in [77]. Other studies include the development of a grid synchronisation controller for the SS-PMG in [81], evaluation of the LVRT characteristics of the SS-PMG in [82] and the development of a tap-changing transformer for reactive power control of the SS-PMG is discussed in [83]. Other studies focussing more on the mechanical design of the SS-PMG and the feasibility of implementing this concept at the utility scale level is currently ongoing.

1.6.1 SS-PMG versus PMIG

The modular construction of the SS-PMG system due to the electromagnetic separation of the two generating units alleviates many of the constructional issues previously associated with PMIGs. The main differences and advantages of the SS-PMG versus the PMIG can be summarised as given below:

- The amount of PM material used in the SS-PMG is the same as in the PMIG.
- The yoke-mass of the SS-PMG will be higher, but this increase will be little in high pole number machines relative to the total mass.
- The number of poles and size of the two machine units in a SS-PMG can differ, which is advantageous from a design point of view, also, for a slip-PMG with a higher pole number than the PMSG-unit the yoke mass of the slip-PMG will be substantially less than that of the PMSG. These design aspects are not possible in a conventional PMIG.
- For the SS-PMG, non-overlap windings can be used in both the PMSG and slip-PMG, which is an advantage in terms of reduced cogging and load torque ripple and ease of manufacturing. A low cogging torque and load torque ripple cannot be overemphasized for the SS-PMG as it affects the start-up of the SS-PMG and the stability of the freely rotating PM rotor.
- In a SS-PMG with the two machine units mounted in tandem as shown in Fig. 1.15(b), the air gap diameters of both the slip-PMG and PMSG units can be set to a maximum which improves the performance of the machine.

- Modularity and simplicity of the system is largely improved due to the two units operating independent of one another. Both designs can, thus, be done completely independent of one another, furthermore by removing the slip-PMG unit from the generator system, the resulting generator is similar to a conventional PMSG, which can be evaluated as a normal PM wind generator connected to the grid via a power electronic converter.

1.6.2 Main Advantages and Disadvantages of the SS-PMG

The main justification for utilising a SS-PMG wind turbine system is to increase the simplicity and robustness and to improve the reliability and, thus, reduce the operation and maintenance costs of wind turbine systems as well as the added benefits of having a directly grid connected synchronous wind generator. The main characteristics, as well as the advantages and disadvantages of the SS-PMG, as opposed to other wind generator systems can be summarised as given below:

- With no gearbox or full rated power electronic converter the SS-PMG comprises of an extremely simple drive train. The PMSG-unit is similar to PM generators commonly used in the wind industry, which are considered to be highly reliable. Furthermore, it is evident that the slip-PMG unit which runs at an extremely low slip-speed, with no risk of insulation breakdown, is even more reliable than the PMSG. With the gearbox and full rated power electronic converter, being some of the components mostly considered in the analysis of the reliability of a wind turbine, the SS-PMG has a major advantage in this regard.

- Thus, especially for sites with limited access, such as for instance offshore installations where maintenance is a significant issue, the SS-PMG could have and advantage above other types of wind turbine systems. With interest in HVDC transmission for offshore wind farms increasing, it is mentioned in [46] that the direct-grid SG combines well with the classical thyristor based line commutated converter (LCC). LCC based HVDC transmission which have been successfully used for several decades is still considered by some to be the most reliable and cost effective manner of DC-transmission as mentioned in [84]. Furthermore, as shown in Fig. 1.7 the cost of the wind turbine and, thus, the electrical generator contributes to a much smaller share of the overall cost compared to onshore installations. Thus, by increasing the cost of the electrical generator for offshore installations, it will not be as significant as for onshore wind turbine systems.

- An interesting comment mentioned in [26] is that designs for small-scale wind energy systems utilising fixed speed induction generators are emerging again in order to omit the need for a power electronic converter and increase the reliability. An example of a commercial wind turbine product of this type is given in [85]. The SS-PMG might also be very well suited for rural electrification with mini-grids. Due to the simplicity and robustness of the SS-PMG without a complex power electronic converter, this type of wind generator might be extremely favourable for these type of solutions.

- The SS-PMG has several favourable grid voltage supporting capabilities. As mentioned in [46] and [47], the directly grid-connected synchronous generator can provide the highest amount of reactive power compensation with respect to other wind generator topologies currently in use. The directly grid-connected SG topology of [47] is also implemented as a compensation device for grid voltage variations at the distribution level. For the direct-grid connection of a PMSG a special type of tap-changing transformer is proposed as discussed in [83]. It would also be possible to replace the PMSG with a conventional wound rotor SG, which is also used by many of the other direct-grid wind generator topologies. The use of wound rotor SGs for wind generators are considered feasible by some due to the current high price of PM material.

- With higher penetration of wind power, a major concern is the loss of grid-inertia, due to the decoupling of the rotor from the grid, with the use of power electronic converters as discussed in [86–91]. By reducing the grid-inertia, it becomes much more susceptible to sudden load variations, with a much lower inertial buffer to counter-act against frequency variations. It is, thus, anticipated that future grid-code requirements would require the wind farm operator to contribute to the grid inertia. Many of the directly grid connected synchronous wind generators discussed including the SS-PMG have a major advantage in this regard as the large inertia of the wind turbine rotor can provide a significant spinning reserve. Although it is proposed by some, to emulate turbine inertia by means of power electronic converter control, the direct-grid generators might still have an advantage as it can handle overload conditions better. For power systems in general a normalised inertia constant referred to as the H constant is normally used to obtain an indication of the inertial response of a generator. As given in [92], the H constant is defined as

  $$H = \frac{\text{the stored kinetic energy at synchronous speed}}{\text{the generator VA rating}} = \frac{\frac{1}{2}{\omega_m}^2}{S_{rated}} \tag{1.2}$$

  which normally falls within the range of 1 to 10 for synchronous generators. For the case study 15 kW system evaluated in this study H is calculated as 2.7. In [93] a generic scaling expression versus wind turbine power is derived to calculate the H factor, which is given as

  $$H = 1.87P_t^{0.0597}. \tag{1.3}$$

  For a typical 3 MW wind turbine (1.3) gives a H value of just over three.

- Due to the SS-PMG being a fixed speed wind turbine, it is true that for especially low wind speed sites the SS-PMG might not be a viable alternative. However, for good wind sites, such as for instance offshore installations, the difference in total energy capture with fixed speed versus that of variable speed turbines is not that significant, which makes the use of a SS-PMG system more viable. In [26] it is actually mentioned that no clear economic basis could be found for the move from fixed speed to variable speed systems as the actual gain in energy was minimal and can easily be offset by the higher cost and the loss of efficiency in the power electronic converter. In [94], [95] and Appendix C figures indicating the difference in energy harvesting for variable and fixed speed systems of between 10 % and 23 % are given. The reasons for utilising variable speed wind turbines, thus, seems to be more technical in nature as fixed speed systems do not seem to combine well with pitch controlled blades. Another reason mentioned is the improved grid compliance of systems with full rated converters. Furthermore, to improve the energy harvest of fixed speed systems it is important as mentioned in [95] that the correct design rotor speed is selected for the fixed speed system depending on the wind site. In [96] a blade design optimisation is also specifically done for a fixed speed wind turbine, to improve the energy yield of fixed speed wind turbines.

- Another concern of fixed speed wind turbine systems is the increase in noise levels, especially at lower wind speeds.

- The possibility also exists to operate the SS-PMG as a variable speed wind generator. Similar to the proposal in [78–80] the slip-rotor of the SS-PMG can be replaced by a wound rotor and connected to a partially rated converter as for a DFIG. Furthermore, new HVDC transmission options with voltage source converters (VSCs) for offshore wind farms are currently being investigated by some manufacturers as mentioned in [97] and [98]. To also allow for variable speed operation of the SS-PMG, it is proposed in [99] that several SS-PMGs are connected in a common AC-collector grid of which the voltage and frequency are made variable by a single VSC. The power generated can then be transmitted through a central DC-link as proposed in [97] and [98]. The feasibility of this concept, however, still requires further investigation and it should also be compared to the converter and DC transmission topologies evaluated in [100].

  If the PMSG is replaced by a wound-rotor SG, the practicality of pole changing schemes, as reported in [101] and [102], for different pump and turbine speeds in hydro pump storage applications can be investigated. As previously mentioned it was not uncommon for early IG based wind turbine systems to utilise two speed generator systems.

- As the SS-PMG consists of two direct-drive generators it is a concern that this electrical generator will be less efficient. However, conventional systems consist of either a gearbox or converter in conjunction with a generator or both and a generator. This means that the total efficiency is calculated as $\eta_t = \eta_{gear} \times \eta_s \times \eta_{conv}$, whereas for the SS-PMG it is calculated as $\eta_t = \eta_s \times \eta_r$. The efficiency of the PMSG-unit is indicated by η_s and that of the slip-PMG unit by η_r.

- Another possible disadvantage of the SS-PMG is that it needs to be operated at the electrical grid frequency. In order to decrease the steel and PM losses the rated electrical frequency of direct-drive wind generators connected to a power electronic converter is usually decreased, which especially improves the partial load efficiency. For small scale systems this will not be as much of a drawback. Due to the higher rotating speed of small-scale systems, and the use of higher pole numbers to decrease the yoke mass, the rated electrical frequency of the generator is usually higher. Furthermore, if the SS-PMG is combined with HVDC transmission as mentioned above, the rated frequency of the common collector grid can also be lowered. Also if the SS-PMG is used in conjunction with a geared system, as a high speed or medium speed generator, the frequency dependent losses will be not as much of a concern due to the lower steel volume in this case.

- A major concern regarding the SS-PMG system, is the increase in mass and cost, due to the addition of a second direct-drive PM generator. It is, thus, important that in the design of both the PMSG and slip-PMG units, the mass of the generator is reduced to an as low as possible value. In the cost calculation of the SS-PMG as opposed to a PMSG and power electronic converter topology, it should be taken into account that the cost of the power electronic converter needs to be omitted. Furthermore, it is expected that the operational cost of the SS-PMG should be less due to the reduced maintenance requirements.

- It is also a concern that by adding the second generator to the design the complexity of the electrical generator increases significantly. However, it should be noted that the slip-rotor of the second generator is similar to a conventional cage-rotor with a simple construction. Furthermore, due to the low slip-speed and almost zero electrical frequency, solid magnets, yokes and conductors can be used and very little wear will be experienced by the bearings. By axially separating the two machine units as shown in Fig. 1.15 easy assembly of the complete SS-PMG is possible, which is not significantly more complex than the assembly of conventional PMSGs.

1.7 Objectives of Study

From the above mentioned discussion there are clear advantages of implementing the SS-PMG as a wind generator system, which definitely motivates further study regarding this concept. There are, however, several disadvantages and several aspects which need to be addressed before the SS-PMG can be proposed as a viable alternative to other wind generator technologies. The main objectives of this study are summarised below.

1. One of the most important aspects to consider is the stability of the SS-PMG system connected directly to the grid, with regard to turbine and grid voltage transient conditions. If a stable grid connection is not possible, no utility will allow the connection of such a system. It should also be ensured that the SS-PMG comply with the relevant grid code specifications especially regarding LVRT and reactive power flow.

2. A significant issue identified in previous work is the correct estimation of the short circuit performance of the machine which is shown to be mostly influenced by the per phase inductance (L_s). An incorrect calculation of L_s can lead to a significant error in the calculation of the torque profiles of both the slip-PMG and the PMSG unit as well as the short-circuit current and power factor of the direct grid PMSG.

3. Another very important aspect is the extra mass, cost and complexity of adding a second PM generator to the design. The mass and cost of the slip-PMG-unit, thus, needs to be sufficiently minimised in the design optimisation, without significantly increasing the complexity of the generator system. More information is also required regarding the exact design requirements of the turbine connected slip-PMG unit.

4. Although the PMSG unit is similar to PMSGs currently in use for wind generators, there are different design requirements due to the direct grid connection. Special attention needs to be given to the specifications in the relevant grid code requirements in the design optimisation to ensure that the final generator design is grid compliant.

5. An essential objective of this study is to demonstrate the SS-PMG technology practically, both in the laboratory and in a field tested environment interfaced with an existing small-scale 15 kW prototype wind turbine system.

1.8 Thesis Structure

The stability analysis of the SS-PMG connected directly to the grid is addressed in Chapter 2. Several aspects which is important in the design of the slip-PMG and PMSG units are also identified in Chapter 2. The correct prediction of L_s and the effects of the end-winding inductance and variations in the PM characteristics on L_s are discussed in Chapter 3. With more accurate calculation methods for L_s obtained and with a clearer indication on the design specifications from Chapter 2, Chapters 4 and 5 discusses all the aspects regarding the design optimisation of the slip-PMG and PMSG units. Optimum designs are presented for several different slip-PMG and PMSG topologies.

The practical validation of the SS-PMG is given in Chapters 6 and 7, both in the laboratory and for the SS-PMG interfaced with an existing 15 kW prototype small-scale wind turbine system.

Chapter 2

Dynamic Modelling and Analysis

One of the most important aspects of the SS-PMG technology is the ability of this system to achieve a stable grid-connection. It is evident that no utility will allow the connection of such a system if this is not possible. The aim of the study in this chapter is to thoroughly characterise the dynamic behaviour of the SS-PMG system to transient turbine and grid disturbances, as well as to torque ripple disturbances within the machine itself. A transfer function model is developed in the dq-reference frame to evaluate the dynamic performance of the wind generator system. Another objective is to obtain an indication as to which parameters influences the stability of the SS-PMG the most in the design optimisation.

2.1 Dynamic Wind Generator Aspects

To evaluate the dynamic behaviour of the SS-PMG under transient torque conditions and transient grid voltage disturbances, information is required on the characteristics of these disturbances. Furthermore, knowledge is required of the relevant standards and grid codes as given in [10] in order to obtain an idea of what is expected of the SS-PMG system regarding its dynamic behaviour when connected to the grid. In the following section the three main types of disturbances in a wind generator setup are described.

2.1.1 Turbine Transients

As explained in literature there are torque disturbances in a wind generator system, which could cause amongst other things, serious voltage flickering. This is an important aspect in wind power generation and its effect should be kept as low as possible. Typical methods to asses flickering are specified according to international standards and guidelines as in the IEC 61400-21 standard, and in general the wind generator needs to comply with all the aspects within the IEC Technical Specification Series, TS 61400. The application of this standard is thoroughly discussed in [103]. Flickering is caused by several stochastic and periodic power fluctuations prevalent in wind generator systems as mentioned in [104] and [105]. These fluctuations are mainly low frequency in nature and correspond mostly to multiples of the rotational frequency of the turbine. The rotational frequency is defined as $f_t = (n_t/60)$ where n_t is the rotational speed of the turbine in r/min. The disturbance frequency components are defined in multiples of the rotational frequency as nf_t, where n gives the harmonic order of the disturbance. The most common turbine disturbances are caused by the influence of wind shear and tower shadowing at $n = 3$, and tower oscillations with $n = 1$.

Furthermore, rapid changes in wind speed, for example gusts and turbulence caused by the turbine itself, and the wake effect caused by different wind turbines upon one another can also be a cause of flickering. In [106] a more through explanation is given on how to model the occurrence of gusts. For a non site specific modelling of the wind conditions including the turbulence intensity, the parameters in the IEC 61400-1 standard making use of the Kaimal spectrum as explained in [107] can be used.

2.1.2 Generator Torque Ripple Transients

Another important factor which needs to be taken into account is the effects of cogging torque and load torque ripple on the system. In [108] a direct drive PM wind generator is evaluated where it is mentioned that the cogging torque should not be more than 1.5 - 2 % of the rated torque. It is even specified as low as 0.5 % in some cases. It is mentioned that at very low rotational speeds a clear resonance frequency area is prevalent. Although the resonance area is mostly below the operating speed range of the turbine, it could cause serious damage to the system if too severe as the rotor speed goes through resonance during start-up. Furthermore, under certain conditions there are frequency components which can excite the natural frequencies of the whole turbine and tower structure which could cause serious resonance in the physical structure and increase the fatigue loading of the system. Thus, as it is known that the torque ripple is problematic especially at low frequencies, the torque ripple of the slip-PMG unit, which operates only at slip frequency, should definitely be adequately investigated.

2.1.3 Grid Voltage Transients

As specified in all grid codes, the ability of the generator to stay connected during grid faults is of extreme importance. Typical LVRT specifications as given in [10] are shown in Fig. 2.1(a) for small scale wind turbines (0 - 100 kVA) and in Fig. 2.1(b) for larger wind turbine systems (larger than 100 kVA). The main issue of synchronous generators with a direct grid connection is the ability of the generators to stay in synchronism after major voltage drops [46]. Furthermore, it is stipulated in [10] that the generator needs to be able to handle frequency variations between 47 Hz and 52 Hz at a rate of change of 1.5 Hz/s. There are also several harmonic components present in the grid voltage, which could influence the dynamic behaviour of the SS-PMG.

2.2 Modelling of the SS-PMG

As mentioned in Chapter 1 due to the SS-PMG consisting of two electromagnetically separated generating units, it can also be modelled as two independent, decoupled machines. In the modelling, the slip-rotor is referred to the grid frequency and the slip-speed is taken as positive in generator mode. The modelling of the generator is done in the dq-reference frame fixed to the PM-rotor, for both the grid frequency and slip frequency generator components. Fig. 2.2 shows a section diagram of the SS-PMG and the relations of the different inertial, torque and speed components with regard to one another.

2.2.1 Modelling Equations

The dq-equivalent circuits of the slip-PMG and PMSG are shown in Fig. 2.3. Note that positive current is taken as flowing out of the machine. Hence, the dynamic dq-equations of the slip-PMG

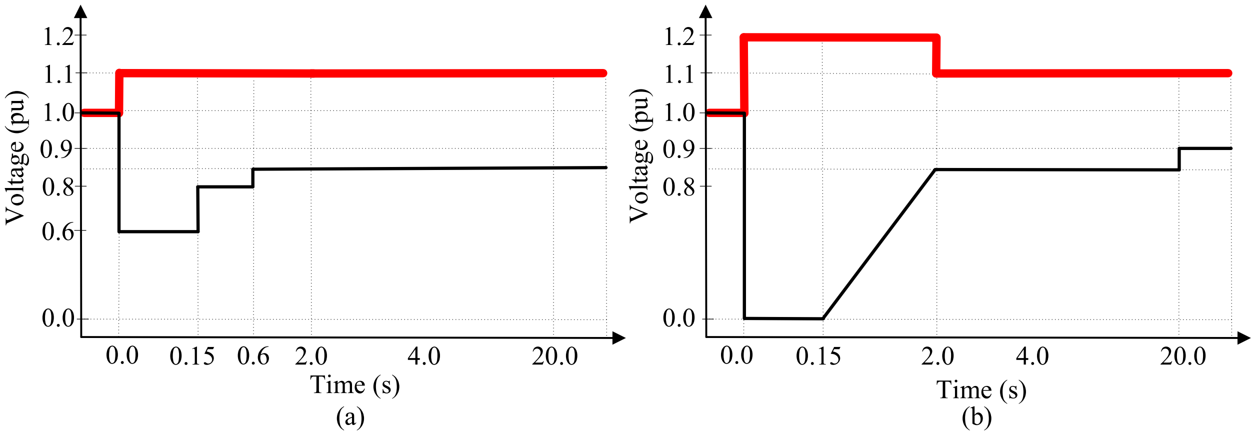

Figure 2.1: Low Voltage Ride Through (LVRT) specification for renewable energy power plants according to [10] for (a) a power rating of 0 kVA - 100 kVA and (b) for a power rating larger than 100 kVA.

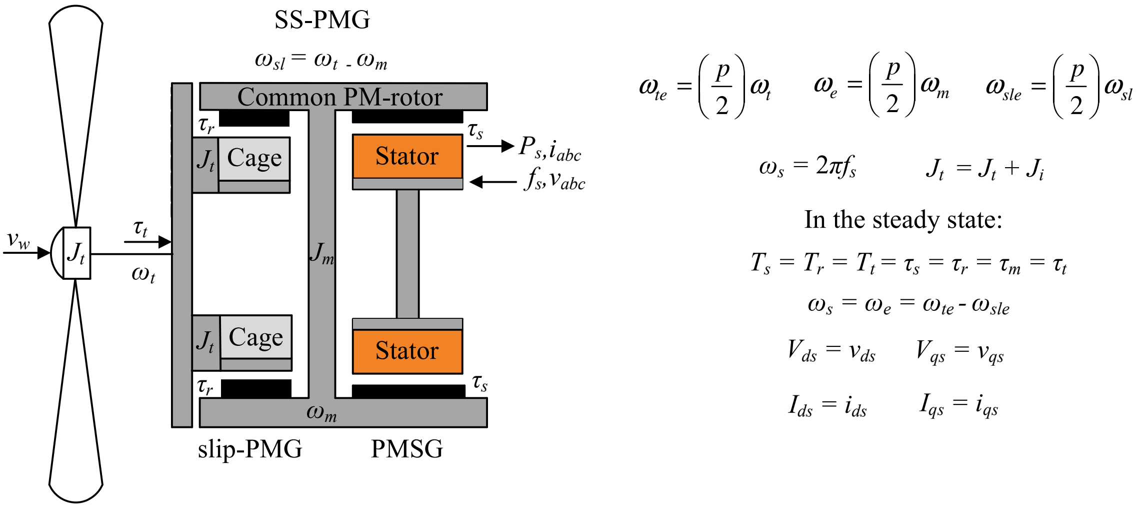

Figure 2.2: Section diagram of the SS-PMG indicating the relations between the different, inertial, speed and torque components.

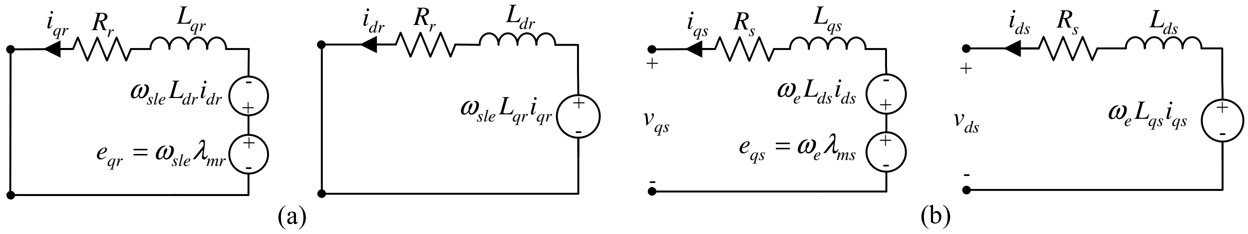

Figure 2.3: The dynamic *dq*-equivalent circuits of (a) the short-circuited slip-PMG and (b) grid-connected PMSG.

and PMSG fixed to the PM-rotor are given respectively by

$$\begin{aligned} 0 &= -R_r i_{qr} - L_{qr}\frac{di_{qr}}{dt} - \omega_{sle} L_{dr} i_{dr} + \omega_{sle}\lambda_{mr}, \\ 0 &= -R_r i_{dr} - L_{dr}\frac{di_{dr}}{dt} + \omega_{sle} L_{qr} i_{qr} \end{aligned} \tag{2.1}$$

and

$$\begin{aligned} v_{qs} &= -R_s i_{qs} - L_{qs}\frac{di_{qs}}{dt} - \omega_e L_{ds} i_{ds} + \omega_e \lambda_{ms}, \\ v_{ds} &= -R_s i_{ds} - L_{ds}\frac{di_{ds}}{dt} + \omega_e L_{qs} i_{qs} \end{aligned} \tag{2.2}$$

where ω_{sle} is the electrical slip speed equal to $\omega_{sle} = p/2(\omega_t - \omega_m)$, and where ω_t and ω_m are the turbine and PM-rotor angular velocities respectively, with $\omega_e = (p/2)\omega_m$. The subscript "r" refers to the slip-PMG-rotor, the subscript "s" indicates the PMSG-stator and the subscript "e" donates electrical speed. Hence, (L_{qr}, L_{dr}) and (L_{qs}, L_{ds}) are the dq-inductances of respectively the slip-PMG and the PMSG, and the flux linkages due to the PMs are respectively indicated by λ_{mr} and λ_{ms}. The dq-inductances of the slip-PMG and PMSG are determined in general by

$$L_q = \frac{\lambda_q}{-I_q} + L_e; \qquad L_d = \frac{\lambda_d - \lambda_m}{-I_d} + L_e. \tag{2.3}$$

For the inductance calculations it is important that the end-effects in the PMs and the end-winding inductance (L_e in (2.3)) are taken into account. L_e is calculated by means of the methods presented in Chapter 3. For accurate simulation the dq-inductances are obtained from 2D or 3D FE-analysis. Although these inductances are shown to vary during different load conditions caused by saturation and cross-coupling effects, they are taken as constant to simplify the dynamic modelling.

The torques generated by the slip-PMG and PMSG are given respectively by

$$\tau_r = \frac{3}{4}p[(L_{qr} - L_{dr})i_{dr}i_{qr} + \lambda_{mr}i_{qr}] \tag{2.4}$$

and

$$\tau_s = \frac{3}{4}p[(L_{qs} - L_{ds})i_{ds}i_{qs} + \lambda_{ms}i_{qs}]. \tag{2.5}$$

The dynamics of the turbine (plus slip-rotor) and PM-rotor are expressed by

$$\tau_t - \tau_r - b_r\omega_t = J_t\frac{d\omega_t}{dt} \tag{2.6}$$

and

$$\tau_m = \tau_r - \tau_s - b_s\omega_m = J_m\frac{d\omega_m}{dt}, \tag{2.7}$$

where τ_t is the torque generated by the turbine and τ_m the resultant torque acting on the PM-rotor, and where J_t and J_m are the inertias of the turbine (plus slip-rotor (J_i)) and PM-rotor as shown in Fig. 2.2(a). The friction coefficients are indicated by b_r and b_s for the slip-PMG and PMSG units respectively.

2.2.2 Modelling Implementation

From the mathematical equations in the previous section a complete transfer function simulation model of a single grid-connected SS-PMG wind energy system is obtained as shown in Fig. 2.4. The simulation model is implemented in Matlab Simulink. The input parameters of the system are the wind speed, v_w, and grid voltages v_{abc} at a certain frequency, f_s with F_s the nominal grid frequency given in [10], where V_{abc} are the peak voltage values for the three phases. The function generator (FG) in Fig. 2.4 gives the torque-speed curves of the turbine versus wind speed and rotational

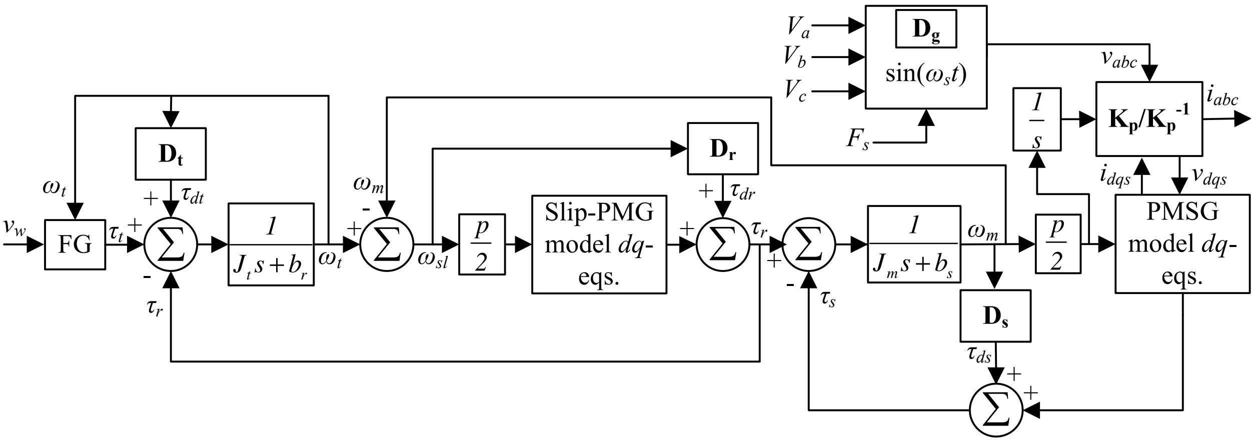

Figure 2.4: Top level transfer function diagram of the grid and turbine connected SS-PMG wind energy system.

speed. The voltages v_{abc} are transformed to v_{dqs} by means of the park transformation $\mathbf{K_p}$. In Fig. 2.4 the outputs are the grid currents, i_{abc}, calculated by means of the inverse park transform $\mathbf{K_p}^{-1}$. Figs. 2.5(a) and (b) shows the implementation of the dq-equivalent circuit blocks in Fig. 2.4 for the PMSG and for the slip-PMG.

The disturbances as discussed in Section 2.1, are injected into the system from three main sources: (i) the turbine disturbances, e.g. from tower shadowing, tower oscillations and turbine shear, indicated by the block function $\mathbf{D_t}$ in Fig. 2.4; (ii) the torque ripple disturbances caused by the interaction between the slip-rotor and stator with the common PM-rotor indicated by $\mathbf{D_r}$ and $\mathbf{D_s}$ respectively in Fig. 2.4; and (iii) grid voltage disturbances such as frequency variations, amplitude variations and harmonics indicated by $\mathbf{D_g}$. The turbine disturbance torque signal is indicated by τ_{dt}, and the torque ripple by τ_{dr} and τ_{ds} for the slip-PMG and PMSG respectively. Furthermore, these disturbance signals are dependent on ω_t, ω_{sl} and ω_m. Thus, to determine the disturbance signal to be injected into the system an amplitude and harmonic order n needs to be specified, which is coupled to a disturbance function. The amplitudes of the turbine, slip-PMG and PMSG torque disturbances are indicated by T_{dt}, T_{dr} and T_{ds} respectively. For the torque ripple disturbances the amplitude and the harmonic order of the torque ripple waveform are determined from FE-analysis. Fig. 2.6 shows the modelling of the disturbance functions as done for $\mathbf{D_t}$, $\mathbf{D_r}$ and $\mathbf{D_s}$ in Fig. 2.4. The input is the relevant angular speed which is multiplied with the harmonic order n of the disturbance. First ω_{dn} is integrated to obtain the position θ_{dn} of which the sinus-value is obtained multiplied by the harmonic disturbance amplitude, T_{dn}, of the specific signal. The result of Fig. 2.6 can, thus, be written as $\tau_d = \tau_{d1} + \tau_{d3} + ...\tau_{dN} = T_{d1}\text{sin}(\theta_{d1}) + T_{d3}\text{sin}(\theta_{d3}) + ...T_{dN}\text{sin}(\theta_{dN})$. For both the turbine disturbance and torque ripple disturbance characteristics the dominant disturbances are usually in multiples of 3.

Fig. 2.7 shows the grid voltage block with output v_{abc}. These voltages are dependant on a certain value of f_s and amplitude V_{abc}. From [10] certain specifications are given regarding the frequency, with the most important for the stability analysis being that the generator can handle frequency variations at a rate of change of 1.5 Hz/s indicated by the function $h_f(t)$ with the nominal frequency $F_s = 50$ Hz and the synchronous grid speed $\omega_s = 2\pi f_s$. The function $h_{LV}(t)$ indicates the required LVRT specification function as in Fig. 2.1 which modifies V_{abc} accordingly. The harmonics injected in the grid voltages are indicated by $v_{a2...n}$, $v_{b2...n}$ and $v_{c2...n}$. For each phase the harmonic voltages

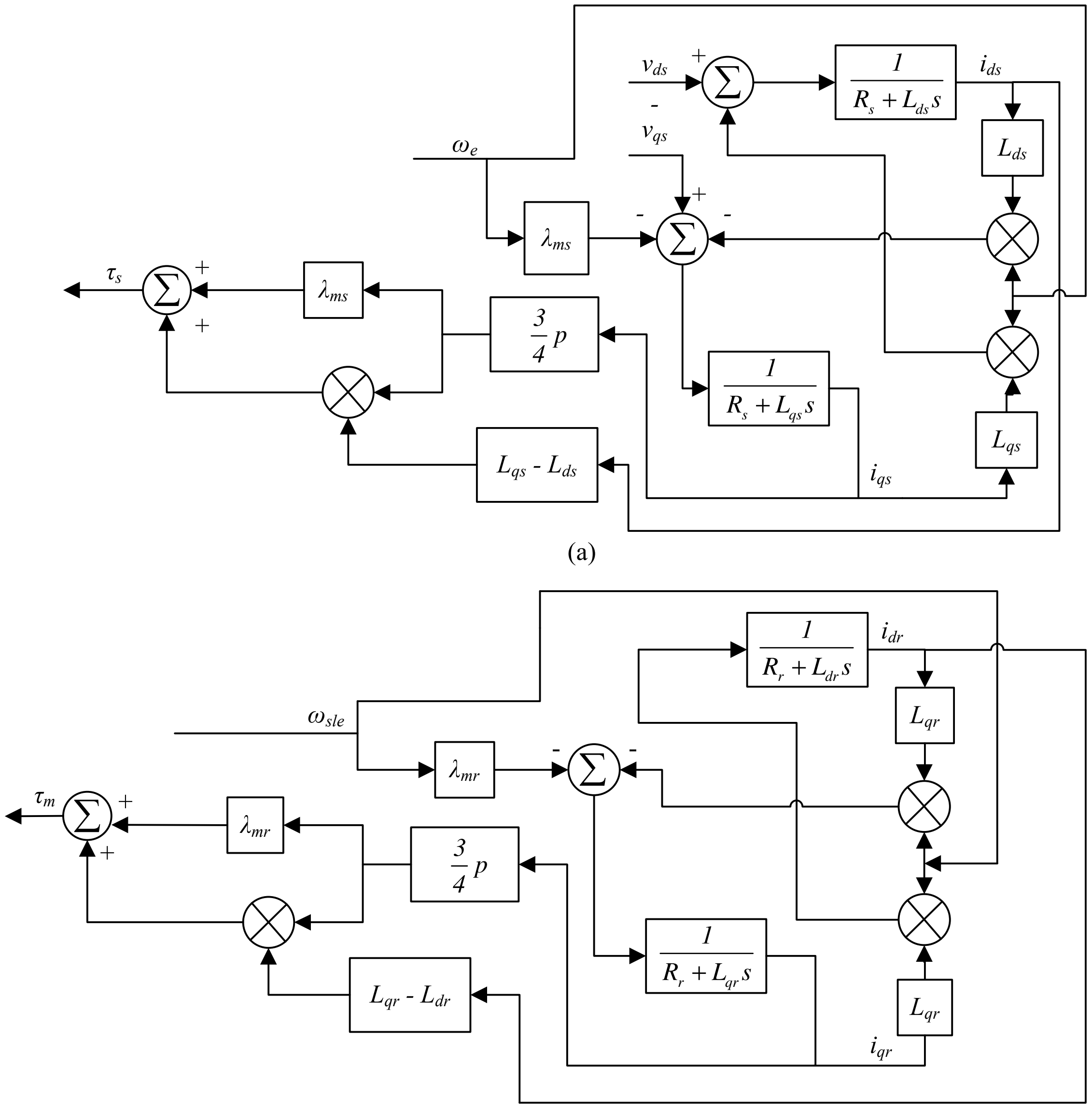

(a)

(b)

Figure 2.5: Transfer functions of the dq-equivalent circuit blocks of (a) the PMSG and (b) the slip-PMG unit.

are calculated in the same manner as in Fig. 2.6 for the torque disturbance inputs. Except in this case the torque amplitudes are replaced by the voltage amplitude corresponding to the relevant harmonic, usually given in percentage of the nominal grid voltage, and the speed input is ω_s.

2.3 Simulation Results

To gain a better understanding of the above mentioned theory presented in this chapter, simulation results of the modelling of a case study SS-PMG are shown in this section. These simulation results are again categorised as the results of turbine, torque ripple and grid voltage disturbances.

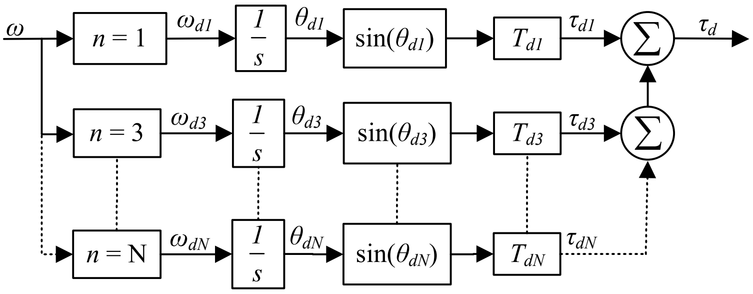

Figure 2.6: General modelling block diagram for each torque disturbance function namely $\mathbf{D_t}$, $\mathbf{D_r}$ and $\mathbf{D_s}$ of Fig. 2.4.

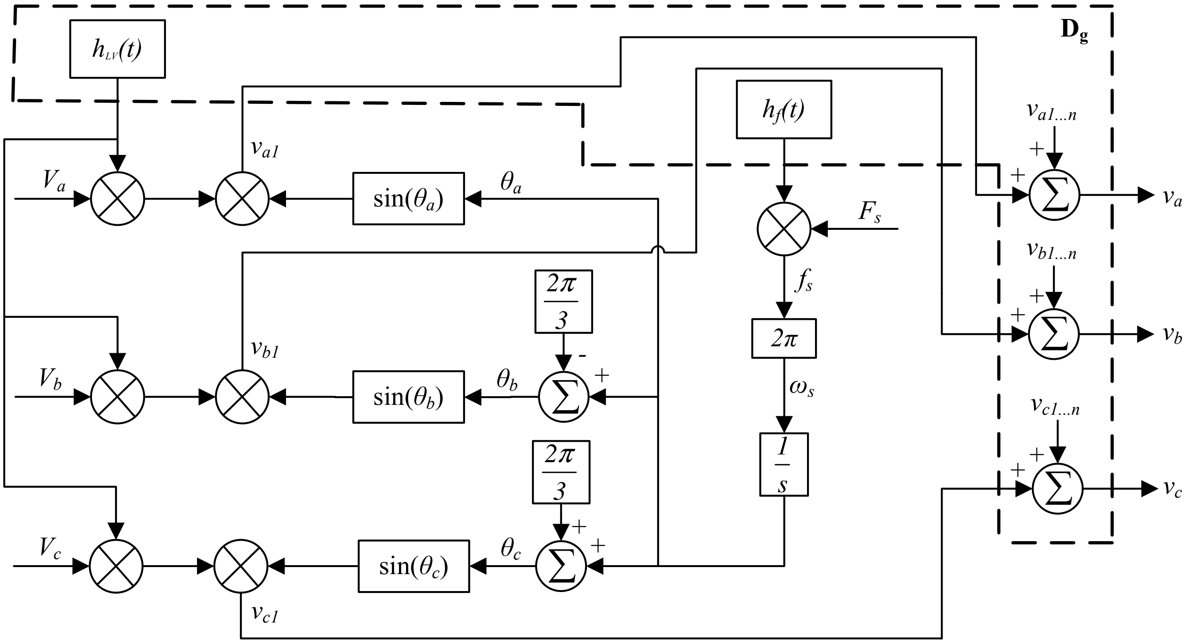

Figure 2.7: General modelling block of the grid voltage with the added disturbances of Fig. 2.4.

2.3.1 Case-study SS-PMG

The case study SS-PMG consists of a non overlap single layer (SL) winding PMSG-unit shown in Fig. 6.6(a) in Chapter 6, and a non overlap double layer (DL) winding slip-PMG with solid aluminium bar-coil windings shown in Fig. 6.3(c) in Chapter 6. The parameters of the case-study SS-PMG are given in Table 2.1. Some of the parameters as given in Table 2.1 are also varied in the dynamic simulation to gain a better understanding of the effect each of these parameters have on the stability of the system. The test-bench setup and the small scale 15 kW turbine system considered in this study are discussed in Chapter 6 and Appendix B in more detail. Two test bench systems, a smaller and larger system, are considered. The reasons for utilising two test benches are discussed in Chapter 7.

Table 2.1: Parameters of the wind turbine system dynamically evaluated.

Parameter	**Value**	**Parameter**	**Value**
$V_{s(rated)}$	230 V / 400 V	p	40
$I_{s(rated)}$	23 A	$I_r(rated)$	9.2 kA
F_s	50 Hz	$s_{(rated)}$	3 %
R_s	0.39 Ω	R_r	5.87 μΩ
L_{ds}	8.4 mH	L_{dr}	101.77 nH
L_{qs}	10.3 mH	L_{qr}	137.61 nH
L_{es}	2.9 mH	L_{er}	32.88 nH
λ_{ms}	1.04 Wb.t	λ_{mr}	3.62 mWb.t
J_m	8 kg.m^2	J_t	330 kg.m^2
$T_{t(rated)}$	1000 Nm	$n_{t(rated)}$	150 r/min

2.3.2 Transient Turbine Torque Conditions

The transient turbine torque conditions refer to the torque response of the SS-PMG due to changes in wind speed and due to turbine disturbances as discussed in Section 2.1.1. In Fig. 2.8(a) the transient response of the stator counter torque, τ_s, is shown for a turbine torque input step from 0 to rated torque at $\tau_t = 1000$ Nm. The corresponding power angle and PM-rotor speed response is shown in Fig. 2.9 and the stator grid current response is shown in Fig. 2.10. Such a severe torque step will seldom occur in a real application, but this gives an adequate indication as to the stability of the system regarding turbine torque changes. Even for this severe torque step a very stable over-damped response is observed for the case study SS-PMG. To obtain an indication of the effect of a gust on the system stability Fig. 2.8(b) shows the response of τ_s to a gust with a duration of 2 s. Gusts with durations of up to 20 s are considered in [106], but it is assumed that after 2 s the passive furling system for the small scale wind turbine considered would have responded.

The same torque step input is repeated in Fig. 2.8(a) for a change in the internal resistance of the slip-PMG, R_r, by reducing it by about 50 %, which can typically occur if the conductor material of the slip-PMG is changed from aluminium to copper. This will decrease the rated slip by

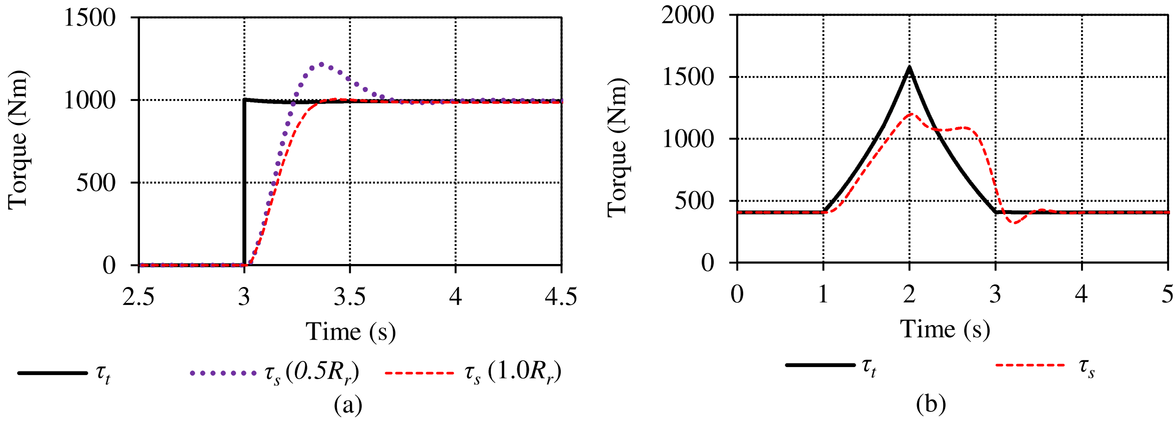

Figure 2.8: (a) Simulated torque response for a rated wind speed (11 m/s) step input for 0.5 × R_r and 1.0 × R_r. (b) Simulated torque response for a 2 s duration gust.

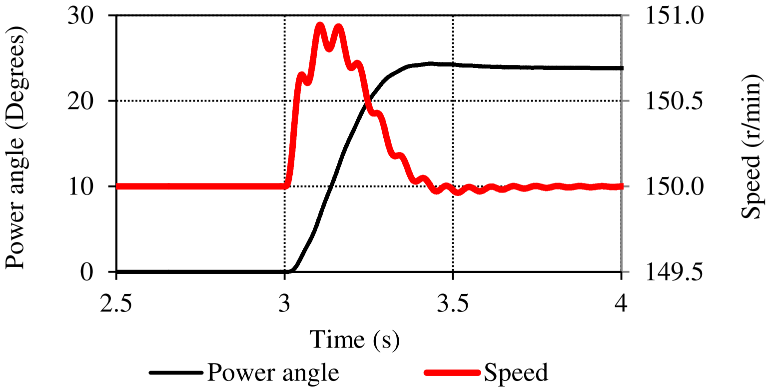

Figure 2.9: Stator power angle and PM-rotor speed response for a rated wind speed (11 m/s) input for $1.0 \times R_r$ for the SS-PMG.

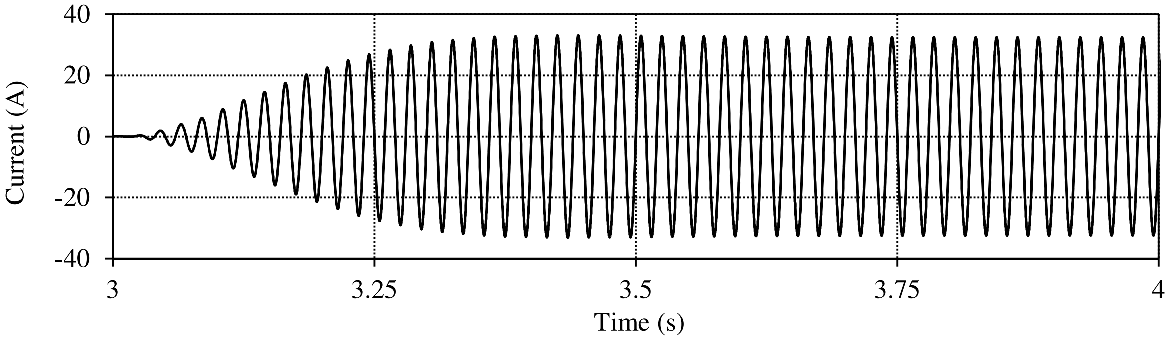

Figure 2.10: Simulated stator current response for a rated wind speed (11 m/s) step input for $1.0 \times R_r$ for the SS-PMG.

the same amount from 3 % to about 1.5 %. A clear overshoot is observed in Fig. 2.8(a), in this case for the slip-PMG. As explained in Chapter 4, the rated slip coincides with the rated efficiency of the machine, thus, a lower slip value leads to higher efficiency, but less stability. Also important in this case is the inductance value of the PMSG stator. It is found that if the stator inductance is decreased by more than 50 % of the given value for the non overlap SL winding machine, the system becomes unstable for this transient torque step input. This reduction in inductance can typically occur if a DL non overlap PMSG or conventional overlap winding PMSG is used for the grid connected stator. By changing the resistances and inductances and also the inertia of the common PM-rotor the electrical and mechanical time constants are influenced, which in turn dictates the damping ratio of the system.

In Fig. 2.11 the bandwidth of the system is shown with τ_t the input and τ_s the output. The frequency response is shown for three values of the turbine and slip-PMG inertia with $J_t = 330$ kg.m^2 corresponding to the turbine system with a swept diameter of 7.2 m, and $J_t = 205$ kg.m^2 corresponding to the larger laboratory test setup, which includes the inertia of the driving machine and gearbox. For the smaller test system used the inertia is calculated as $J_t = 31$ kg.m^2. A clear difference in frequency response is observed in Fig. 2.11 for the different values of J_t. For the larger laboratory test system a bandwidth of about 1 Hz is observed and for the actual turbine system a bandwidth of about 0.5 Hz is observed. For the smaller test system the bandwidth is about 6 Hz,

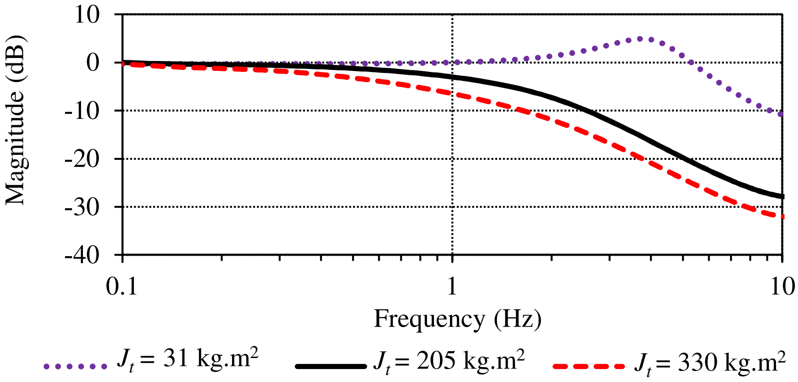

Figure 2.11: Frequency response of $\Delta\tau_s/\tau_{dt}$ for $J_t = 31$ kg.m^2 (small lab test setup), $J_t = 205$ kg.m^2 (large lab test setup) and $J_t = 330$ kg.m^2 (7.2 m turbine) of the SS-PMG system.

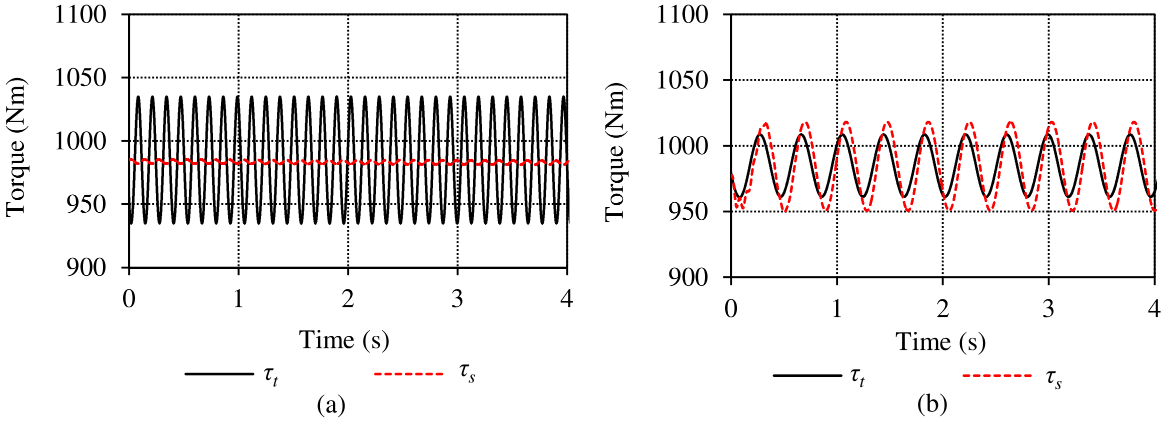

Figure 2.12: Simulated torque (τ_s) response of the SS-PMG system for (a) $J_t = 330$ kg.m^2 with a disturbance frequency of 7.5 Hz (typical tower shadow effect) and (b) $J_t = 31$ kg.m^2 with a disturbance frequency of 2.5 Hz (disturbance at mechanical frequency of test-bench).

with an observable resonance occurring in the region between about 2 and 5 Hz in this case.

Typical disturbances as discussed in Section 2.1.1 will generate turbine torque pulsation frequencies of nf_t with $n = 1$ and $n = 3$. It is clearly seen from Fig 2.11 that all the disturbances with a frequency of 2.5 Hz and higher are well above the wind turbine system's cut-off frequency, with $J_t = 330$ kg.m^2. This explains the zero torque-output response in Fig. 2.12(a) for a 7.5 Hz turbine-disturbance-torque input typically caused by the tower shadow effect. This is a significant result for the proposed fixed speed SS-PMG wind turbine system, as possible voltage flickering on the grid due to tower shadowing, wind shear, tower oscillation and yaw error will not occur. However, for the smaller test bench with $J_t = 31$ kg.m^2, at a rated speed of 150 r/min, $f_t = 2.5$ Hz, which is shown to be just inside the resonance area of Fig. 2.11. Thus, with a disturbance of $nf_t = 2.5$ Hz added to the mechanical torque input of the small test-bench it is clearly shown in Fig. 2.12(b) that this disturbance is passed on through the system with a slight amplification observed. For all practical purposes the mechanical input speed can be taken as constant with a maximum variation of only 3 % corresponding to the rated slip.

2.3.3 Generator Torque Disturbances

Internal generator disturbances refer to the torque ripple interaction between the slip-PMG plus the PMSG-stator and the common PM-rotor, and are modelled as indicated in Figs. 2.4 and 2.6. Due to the much lower inertia of the common PM-rotor, the bandwidth is much higher. This could be problematic, especially as the torque ripple frequency of the slip-PMG is very low due to the fact that the slip-PMG operates at slip frequency. In Section 6.4 in Chapter 6 the no-load cogging torque and the full load torque ripple are shown for the different slip-PMG topologies considered in this study. Clearly a large spectrum of torque ripple characteristics are prevalent, with clear differences between the different topologies observed. Differences are also observed between the no-load and load toque ripple, with the load torque ripple higher than the no-load cogging torque in most cases.

With the slip-frequency, f_{sl}, equal to sf_s the torque ripple frequency of the slip-PMG is calculated as $f_r = nf_{sl}$ where n is the harmonic order. For the slip-PMG the torque ripple frequency will, thus, vary with slip. The main harmonics identified are at $n = 6, 12, 18$ and 30 as shown in the frequency spectrum of Fig. 2.13 for the different slip-PMG topologies. It should be noted that in Fig. 2.13 the torque ripple frequency spectrum of the overlap winding and brushless-DC slip-PMGs are plotted on the vertical axis to the right, due to their much smaller torque ripple amplitudes compared to the non overlap winding slip-PMGs. The torque ripple frequency for the PMSG is fixed as the common PM-rotor rotates at a fixed speed. It is found that due to the very high frequency of this ripple component with $nf_s = 300$ Hz for $n = 6$ and $f_s = 50$ Hz, it has very little effect on the dynamic performance of the system.

Fig. 2.14(a) shows the bandwidth of the torque ripple disturbance input for $\Delta\tau_s/\Delta\tau_{dr}$, for the case-study SS-PMG, where $\Delta\tau_s$ is the ripple component in the PMSG torque response. A clear resonance area is observed as indicated in Fig. 2.14(a), with the peak resonance value occurring at about 15 Hz and with the cut-off frequency just above 20 Hz. For the case study slip-PMG the two main torque ripple components are identified at $n = 6$ and $n = 12$. Also shown in Fig. 2.14(a) is generator load (indicated by slip, with the rated slip at $s = 0.03$) versus torque ripple frequency for the two components $n = 6$ and $n = 12$. It is shown that the component at $n = 6$ does not go through resonance in the operational range of the slip-PMG, however, for the component at $n = 12$ it is shown that for a large part of the operational area $\Delta\tau_s/\Delta\tau_{dr}$ will be in resonance. In Fig. 2.14(b) the bandwidth of $\Delta\tau_s/\Delta\tau_{dr}$ is shown for different values of PM-rotor inertia. Again a clear resonance area is observed in all cases, with the frequency value at which the resonance area

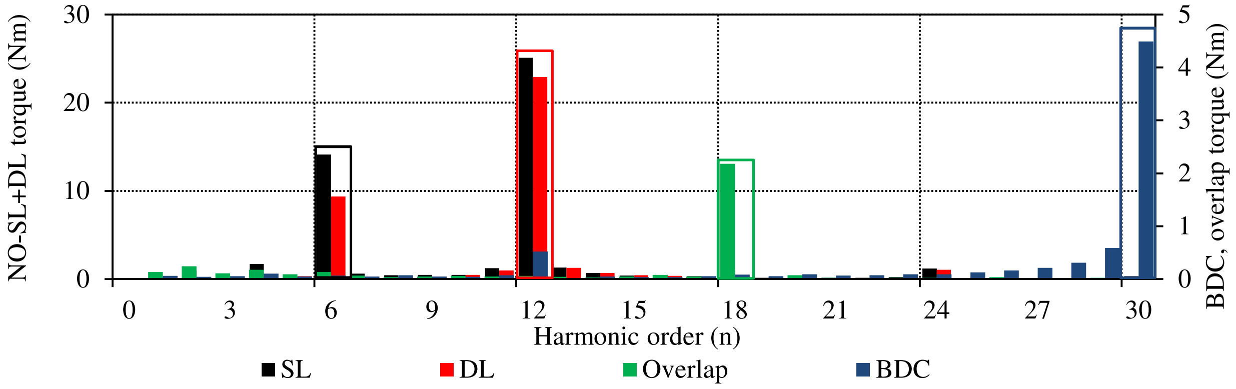

Figure 2.13: Frequency spectrum of the different slip-PMG prototypes (non overlap SL and DL, brushless-DC (BDC) and overlap winding slip-PMGs as explained in Section 6.2.1 in Chapter 6).

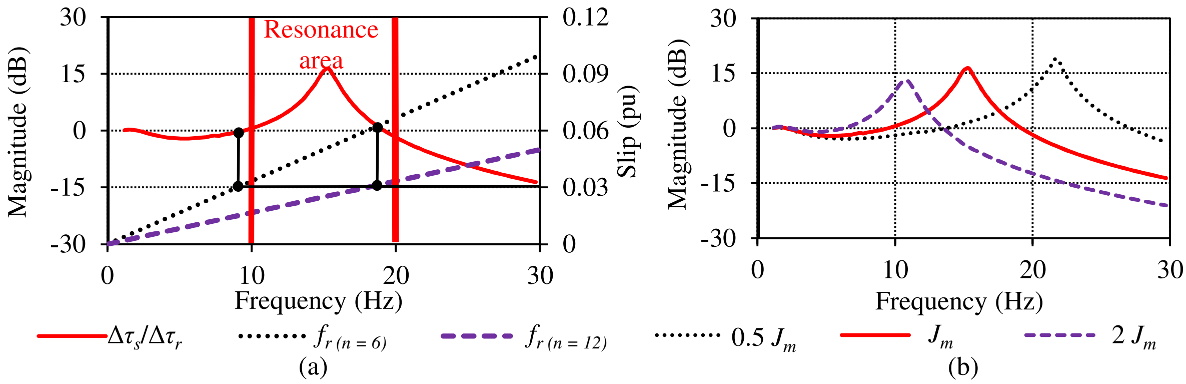

(a) (b)

Figure 2.14: Frequency response for a torque ripple disturbance input, in the stator torque response $\Delta\tau_s/\Delta\tau_{dr}$ of the directly grid-connected SS-PMG system for (a) the case-study slip-PMG with the resonance area indicated, as well as s versus f_r for $n = 6$ and $n = 12$, and (b) with a variation in the PM-rotor inertia.

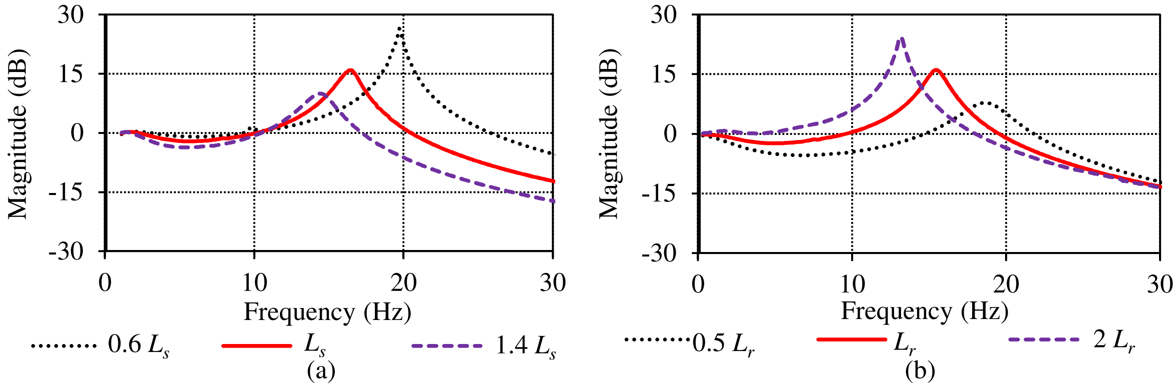

(a) (b)

Figure 2.15: Frequency response for a torque ripple disturbance input, in the stator torque response $\Delta\tau_s/\Delta\tau_{dr}$ of the directly grid-connected SS-PMG system for (a) a variation in the per phase PMSG inductance and (b) a variation in the slip-PMG slip-rotor inductance.

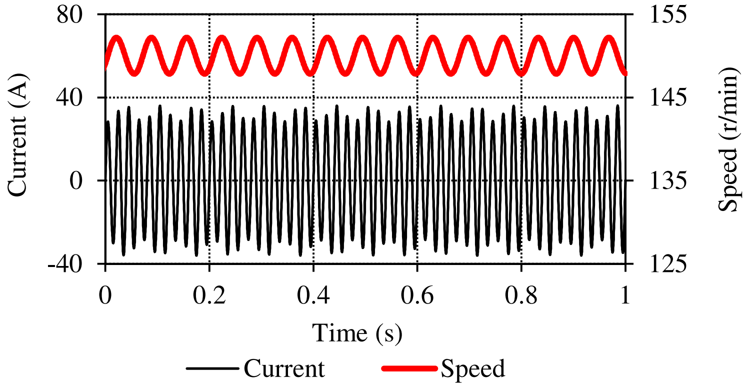

Figure 2.16: Grid current and PM-rotor speed versus time for a disturbance input at peak resonace frequency of $f_r = 15$ Hz.

occurs dependent on the size of J_m. Figs. 2.15(a) and (b) show the bandwidth for $\Delta\tau_s/\Delta\tau_{dr}$ for a variation in the per phase inductance of the PMSG and slip-PMG respectively, which is also shown to have a significant effect on the characteristics of the torque ripple disturbance input bandwidth.

For the case study slip-PMG if is found from the observed torque ripple characteristics that the low frequency torque ripple of the slip-PMG is passed through the system to the grid current over the whole load range of the SS-PMG at $\Delta\tau_s/\Delta\tau_{dr} = 1$. The rated slip of the system and the value of the harmonic order n for the torque ripple waveform will, thus, determine whether this resonance area falls within the operating region of the slip-PMG. Fig. 2.16 shows the effect on the PM rotor speed and grid current if the disturbance input frequency is at $f_r = 15$ Hz. Although it is not found to destabilise the system dynamically in any way, it could cause flickering effects on the grid if the unwanted disturbance frequency is in the range where flickering is a concern. It is, thus, essential that the torque ripple is minimised to an as low as possible value in the design optimisation of the slip-PMG.

2.3.4 Grid Voltage Disturbances

The disturbances from the grid relates to variations in the voltage and frequency as discussed in Section 2.1.3. Fig. 2.17 shows the harmonic content in the measured laboratory grid voltage where the SS-PMG is to be interfaced. A clear 5^{th} and a less dominant 7^{th} order harmonic component is observed. Although the 5^{th} order harmonic shown in Fig. 2.17 is less than 1.5 % the harmonic planning limit is specified as 6 % in [109] for $n = 5$. Fig. 2.18 shows the effect on the stator torque and the PM-rotor speed when a 6 % 5^{th} order harmonic component is added to the voltage waveform. This leads to a high frequency oscillation in τ_s, which is not transferred to the rest of the system, as can be seen in the PM-rotor speed of Fig. 2.18.

Fig. 2.19(a) show the response in grid, PM-rotor and turbine electrical speed (ω_s, ω_e and ω_{te} respectively, with $\omega_s = 2\pi f_s$) for a frequency variation between 50 Hz and 47 Hz at a rate of 1.5 Hz/s as specified in [10]. Clearly no oscillatory behaviour is observed. From the observed results in [110] and [111] it is seen that the frequency response of mini-grids typically created with a diesel gen-set is much different from conventional utility grids, with much more transient frequency behaviour. Fig. 2.19(b), thus, show the response of ω_s, ω_e and ω_{te} for a step input in f_s. Although some transients are observed, even for this sudden change in frequency the SS-PMG is shown to be dynamically stable.

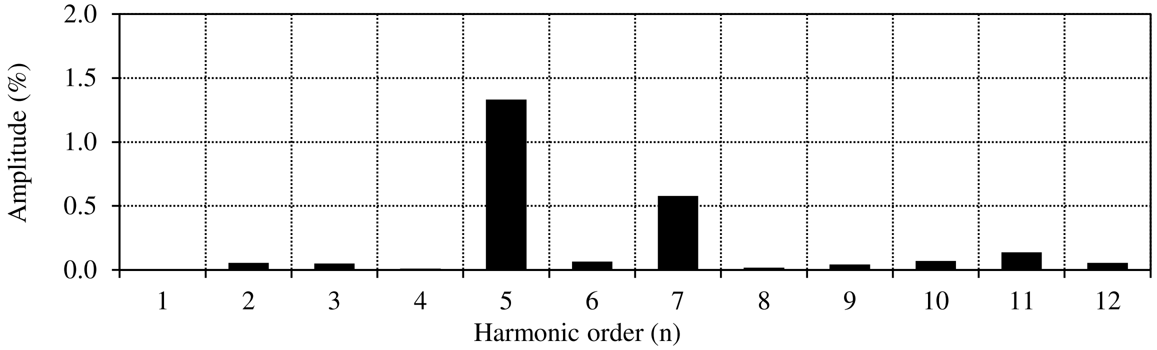

Figure 2.17: Harmonic content in the measured laboratory grid voltage as a percentage of the fundamental voltage component.

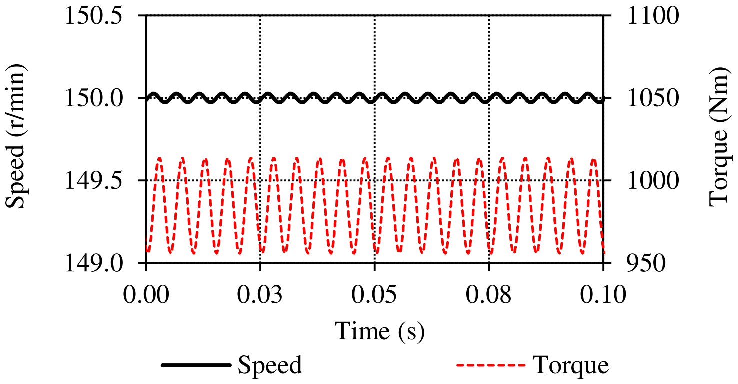

Figure 2.18: Simulated PM-rotor speed and stator counter torque response for a 6 % fifth order harmonic in the grid voltage waveform.

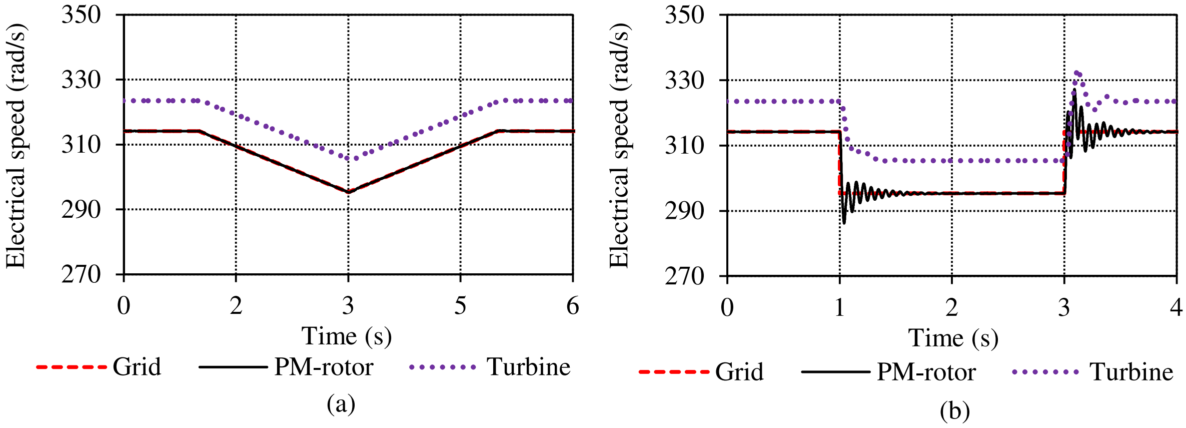

Figure 2.19: Response in turbine and PM-rotor electrical speed (ω_{te} and ω_e) for a variation in grid frequency at (a) a rate of change of 1.5 Hz/s as given in [10] and (b) for a unit step reduction in grid frequency, with the grid speed given as $\omega_s = 2\pi f_s$.

To model the LVRT and over-voltage response of the system the voltage specification given by Fig. 2.1 is used. The aim of this study is only to determine whether the SS-PMG is stable under transient grid voltage conditions and not the evaluation of techniques to limit the short-circuit current as done in [82]. Although the case-study SS-PMG is a small-scale wind turbine system which need only to comply to the voltage specifications given in Fig. 2.1(a), the dynamic response of the voltage specification given in Fig. 2.1(b) for larger wind turbine systems are also evaluated. In Fig. 2.20 the peak current response is shown for a three phase over-voltage in all three phases as specified in Fig. 2.1(b). Fig. 2.21 show the response of n_m (n_m is the PM-rotor speed in r/min) and Δ for the over-voltage condition. It is clear that the over-voltage condition of Fig. 2.1(b) does not lead to any instability in the dynamic response of the case-study SS-PMG.

For the low voltage conditions specified for large wind turbines in Fig. 2.1(b) it was found that the case study SS-PMG with a non overlap SL winding could not handle a three-phase fault and the system became unstable. It was found, however, to continuously operate dynamically stable for a single phase fault for the specification of Fig. 2.1(b). The reason for the unstable behaviour during a three-phase fault is because the value of the power angle, Δ_s, exceeds 180 degrees as the

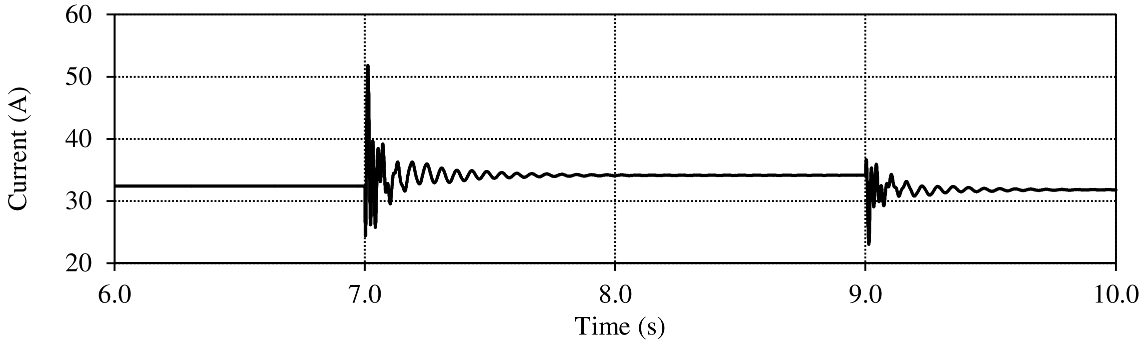

Figure 2.20: Simulated peak stator current response for a three phase over-voltage grid fault at rated power for the case-study SS-PMG for the specification in Fig. 2.1(b).

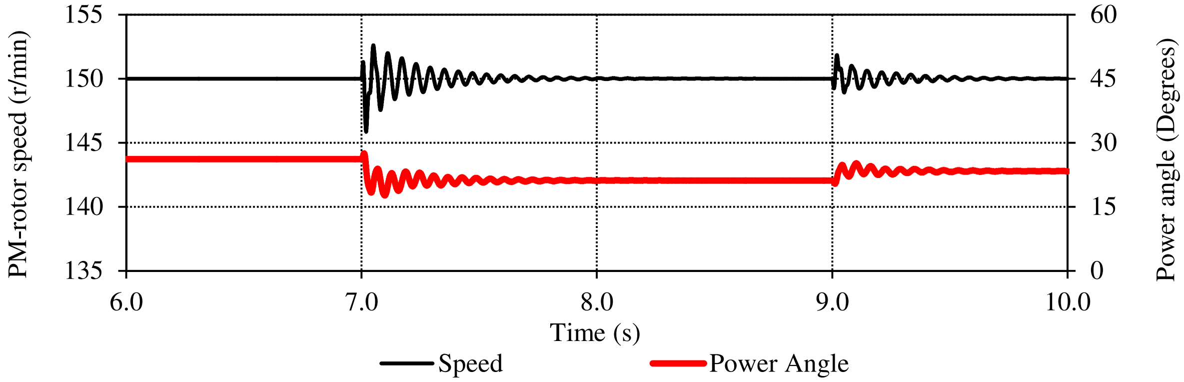

Figure 2.21: Simulated PM-rotor speed and power angle response for a three phase over-voltage grid fault at rated power for the case-study SS-PMG for the specification in Fig. 2.1(b).

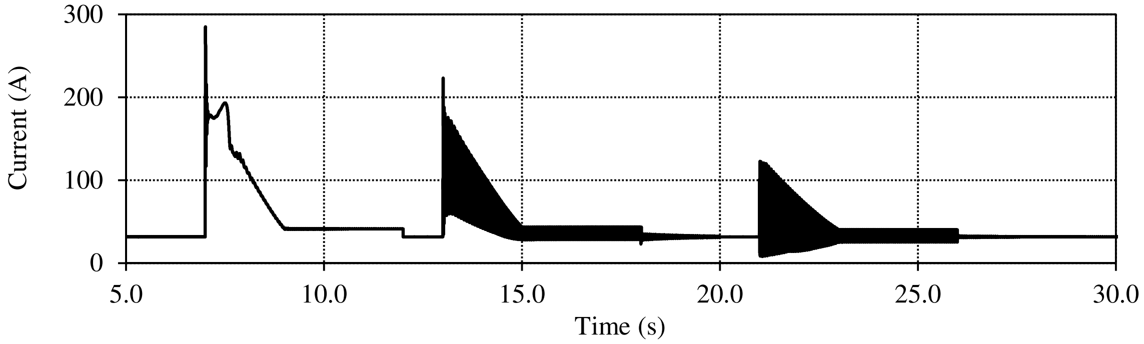

Figure 2.22: Simulated peak stator current response for a three phase, a two phase and a single phase grid fault, shown from left to right, at rated power for the SS-PMG with the inductance values reduced by 45 %.

peak torque the generator is capable of is not sufficient to keep it in synchronism and pole slipping occurs. Pole slipping is mentioned as undesirable in [46], however, if the generator is pulled back into synchronism, the system becomes stable again. In this case the dq-inductances of the PMSG-unit are reduced by a factor of $0.55 \times (L_{ds}, L_{qs})$. This is typically the case if the SL-non-overlap

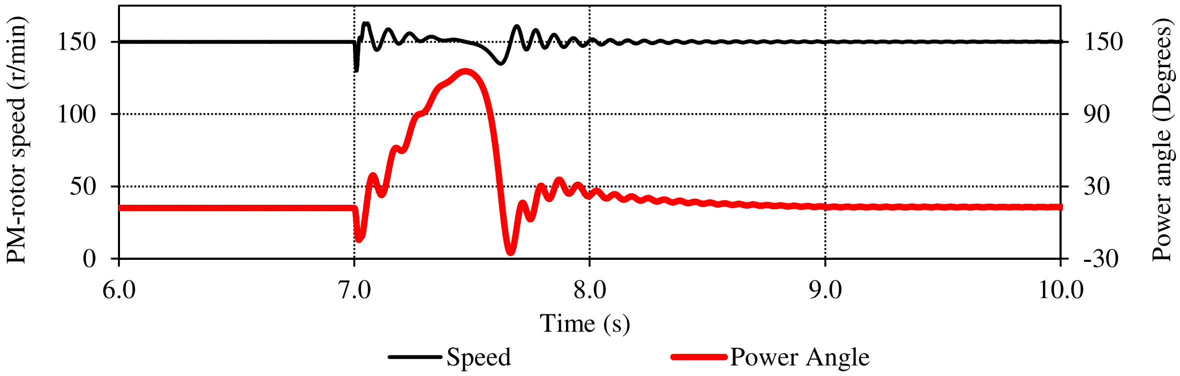

Figure 2.23: Simulated PM-rotor speed and power angle response for a three phase grid fault at rated power for the SS-PMG with the inductance values reduced by 45 %.

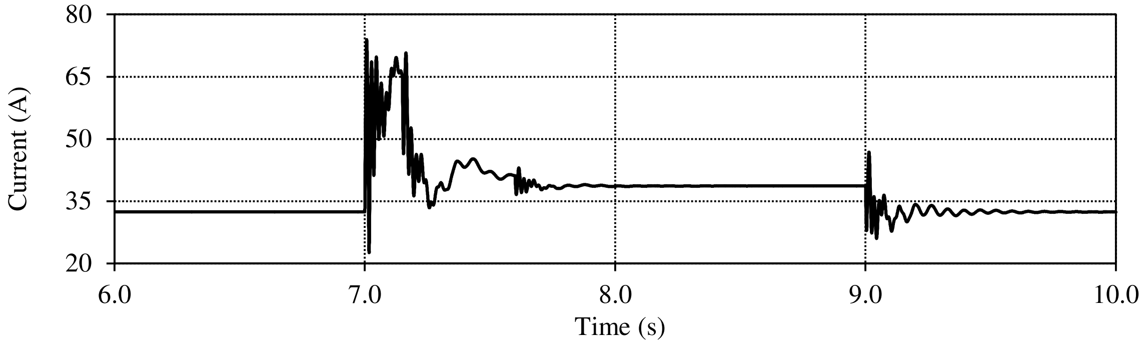

Figure 2.24: Simulated peak stator current response for a three phase grid fault at rated power for the case-study SS-PMG for the specification in Fig. 2.1(a) for small-scale wind turbines.

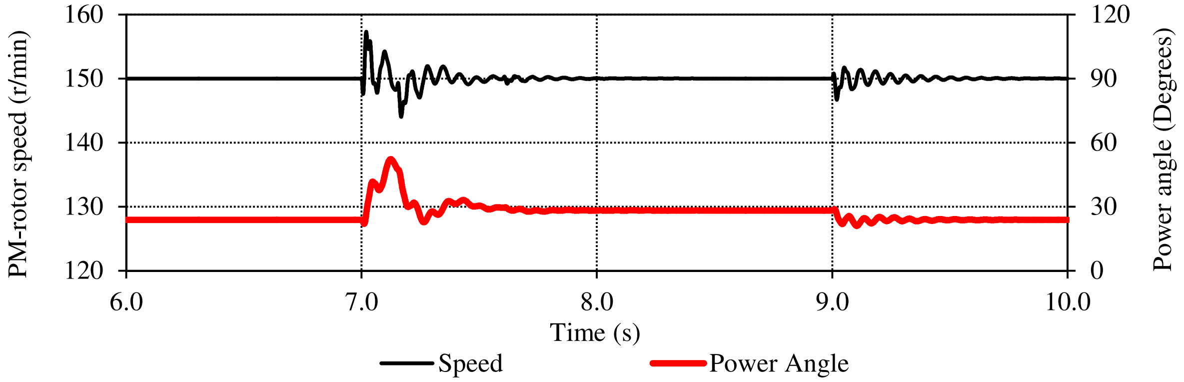

Figure 2.25: Simulated PM-rotor speed and power angle response for a three phase over-voltage grid fault at rated power for the case-study SS-PMG for the specification in Fig. 2.1(a) for small-scale wind turbines.

winding is replaced by a DL-non-overlap winding. This reduction in inductance, however, means that the peak fault current increases significantly. From left to right in Fig. 2.22 the peak current response is shown for three phase, two phase and single phase grid faults for the inductances of the

SL PMSG-unit modified. The three phase fault is clearly shown to be the most severe for the SS-PMG. Fig. 2.23 show the response of n_m and Δ_s for the three phase fault. Figs. 2.24 and 2.25 show the peak current response and the response of n_m and Δ_s respectively for a three phase low voltage fault as specified in Fig. 2.1(a). In this case the generator is shown to operate dynamically stable throughout the fault condition. The small-scale case-study SS-PMG is, thus, shown to comply to the grid code specifications of [10] regarding grid voltage fault conditions.

2.4 Summary

The transfer function model developed for the SS-PMG in this chapter is shown to give a good indication of the dynamic characteristics of the system. From the simulated response of the case study 15 kW SS-PMG system it is shown that the system remains stable even for large step inputs in turbine torque. Interesting findings are the effects of the per phase resistance of the slip-PMG and inductance of the PMSG on the stability of the SS-PMG. It is found that when replacing the aluminium winding of the slip-rotor with copper, and when the PMSG stator winding is changed and the per phase inductance is reduced, the damping ratio of the system is reduced. Furthermore, it is found that the SS-PMG wind generator system has a very low bandwidth (< 1 Hz). This causes the system to act as a filter against turbine pulsation torques caused by e.g. tower shadow, wind shear and tower oscillation, which prevent voltage flickering from occurring, which is a huge advantage. A problematic dynamic disturbance is the torque ripple of the slip-PMG. The high frequency torque ripple of the PMSG is shown to be filtered out and is not a factor. It is shown that the torque ripple of the low frequency slip-PMG is passed through to the grid current over the entire load range. It is, thus, essential that the torque ripple of the slip-PMG should be minimised to an as low as possible value in the design optimisation. Care should also be taken regarding the harmonic content of the slip-PMG torque ripple as some torque ripple frequency components might fall within the identified resonance area in the operational range of the SS-PMG. The torque ripple, however, is shown not to destabilise the dynamic operation of the SS-PMG in any way.

It is furthermore shown that although the SS-PMG is sensitive to grid voltage changes, it still complies with the relevant grid code specifications. Grid harmonic voltages are shown to cause harmonic currents of the same order to flow in the PMSG-unit, but do not influence the dynamic operation of the rest of the system. The response of the SS-PMG to grid faults is shown to largely depend on the inductance value of the PMSG unit. With higher inductance values leading to lower short-circuit currents, but with the generator more vulnerable to pole slipping and loss of synchronisation. Lower inductance values leads to higher short-circuit currents but better susceptibility to pole slipping due to a higher maximum torque value. Furthermore, during low voltage conditions the directly grid-connected PMSG supports the grid voltage by means of reactive current, which is much higher than the reactive current support provided by other wind generator topologies.

Chapter 3

Winding and PM End-Effects

As found in previous studies, the accurate prediction of the short-circuit performance of both the slip-PMG and PMSG is an aspect which requires much more attention. The short-circuit machine performance was found to be largely influenced by incorrect inductance calculations. As the performance of the slip-PMG is defined by its torque versus slip profile it is important that the short-circuit torque is accurately predicted. Also for PMSGs in general it is important to know the correct short-circuit torque characteristics, especially for systems utilising electromagnetic braking as explained in [112]. In previous studies such as [77], errors in the calculation of the maximum breakdown torque magnitudes of more than 30 % are mentioned.

Furthermore, the maximum short-circuit torque amplitude influences the mechanical design of the generator. If winding failures occur in PM machines as mentioned in [113] or grid faults in the case of all the directly grid-connected SG topologies discussed in Chapter 1 the short-circuit current can be extremely high. It is, thus, essential that the correct short-circuit current amplitude is known as this can influence the design of the PMs due to demagnetization concerns, and influence the sizing and specification of switchgear and transformers used for grid connection. Also for the directly grid-connected topologies an incorrect prediction of the per phase inductance can result in the power factor of the generator being significantly different to what was expected. Furthermore, apart from the applications considered in this thesis, is the effect of incorrect inductance prediction, on electrical machine control modelling, especially position sensor-less control methods as in [114]. Also in the design of LC-filters placed on the machine side for electrical machine drives or power electronic converter controlled wind generators as in [115] and [116], the internal machine parameters could potentially influence the filter design parameters.

With the maximum short-circuit torque and current values mostly influenced by the size of of the per phase inductance, L_s, it is, thus, of immense importance that L_s is calculated correctly as this parameter can have a significant impact on the final machine design. In this chapter mainly the influence of the end-effects in the windings and the PMs on L_s are investigated, and also the effects of an incorrect prediction of L_s on the short-circuit performance of the machine. It is common knowledge that in the case of electrical machines with large diameters and short axial lengths, thus, with low aspect ratios, the end-effects have a significant influence. However, in many cases due to the short end-winding coil length of non overlap winding machines the end-winding inductance is ignored, which is shown in this chapter not to be valid.

3.1 Existing End-Winding Inductance Calculation Theory

Although there are several methods available in literature regarding the calculation of the end-winding inductance, a thorough analysis is done in this study on the accuracy of these methods due to the importance of calculating L_s correctly in this case. Some of the most relevant methods and arguments found in literature for the calculation of the end-winding inductance are discussed below.

In most cases the end-winding is assumed to be fully encapsulated in air and the end-coil shape is assumed to be circular or semi-circular. Examples are the analytical approximation used in [117] and [118]. A typical analytical method, as proposed in [119] and [120], is to combine the two coil ends to form a circular or oval shaped coil in air, of which the inductance can be easily calculated from the formulas in [19]. However, in reality the shape of concentrated coil end-windings is not always circular and is in many cases much closer to the stack. From the findings in [119] and [121–123] it can be observed that the effects of the lamination stack on the end winding inductance cannot be ignored. In [119] an analytical parameterised expression is derived for the calculation of the end-winding inductance. The values from several different case study end-coil configurations were used to develop the parameterised equation. However, the expression given in [119] was not found to give any meaningful results for the applications in this study. In [122] and [123] the method of images, as will be further explained in this paper, is proposed for the calculation of the end-winding inductance. It is also stated in [121] that care should be taken with regard to the rest of the permeable machine structure, for instance the machine casing and turbine mounting plate in direct-drive wind generators.

The most accurate calculation method for the end-winding inductance is 3D finite element (FE) inductance calculations, as explained in [124] and [125]. In this calculation of the end-winding inductance, the per phase 2D-FE inductance is first calculated and subtracted from the per phase 3D-FE calculated inductance. However, 3D-FE modelling is difficult and 3D-FE simulations are time consuming, which does not make this method suitable for use in design optimisation iterations and for a quick evaluation of the end-winding inductance. In [126] a 2D-FE calculation method for the end-winding inductance is proposed. With this method some of the other permeable machine structure components can also be brought into account. Another FE method proposed in literature to calculate the end-winding inductance is the simplified 3D-FE method reported in [127]. In this case only the end-winding region is modelled in 3D-FE and a small part of the lamination stack. However, even for this much simpler 3D-FE model the simulation times will be significantly more than that of 2D-FE simulations. There is, thus, a lack in literature of simple and accurate calculation methods for the end-winding inductance and also little mention is made of the effect this parameter can have on the machine performance.

3.2 End-winding Inductance Calculation Methodology

In this study of the end-winding inductance two different analytical methods for the calculation of this parameter, of which one is a new proposal, and two FE calculation methods are compared with each other with regard to accuracy. The method proposed in [119] where a parameterised expression is obtained, is not considered in this study as the analytical approaches evaluated are deemed far easier to implement. Five different non-overlap winding PM machines are evaluated in order to obtain a valid comparison and a better indication of the accuracy of the calculation methods.

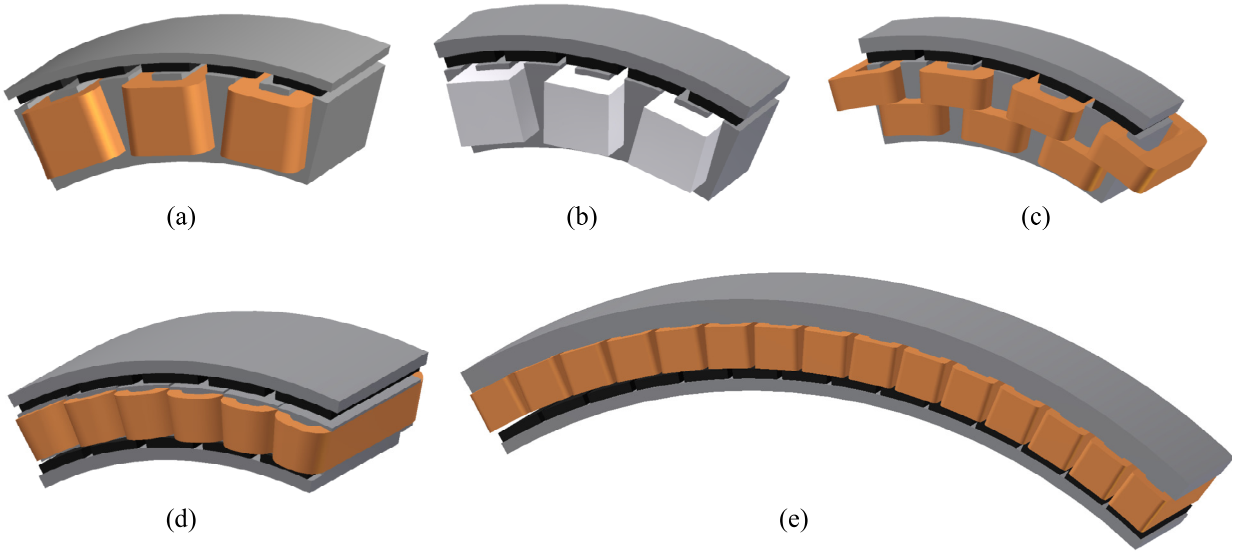

(a) (b) (c)

(d) (e)

Figure 3.1: Sections of the studied PM machines, with (a) Machine 1 [11], (b) Machine 2 [12], (c) Machine 3 [12], (d) Machine 4 [13] and (e) Machine 5 [14].

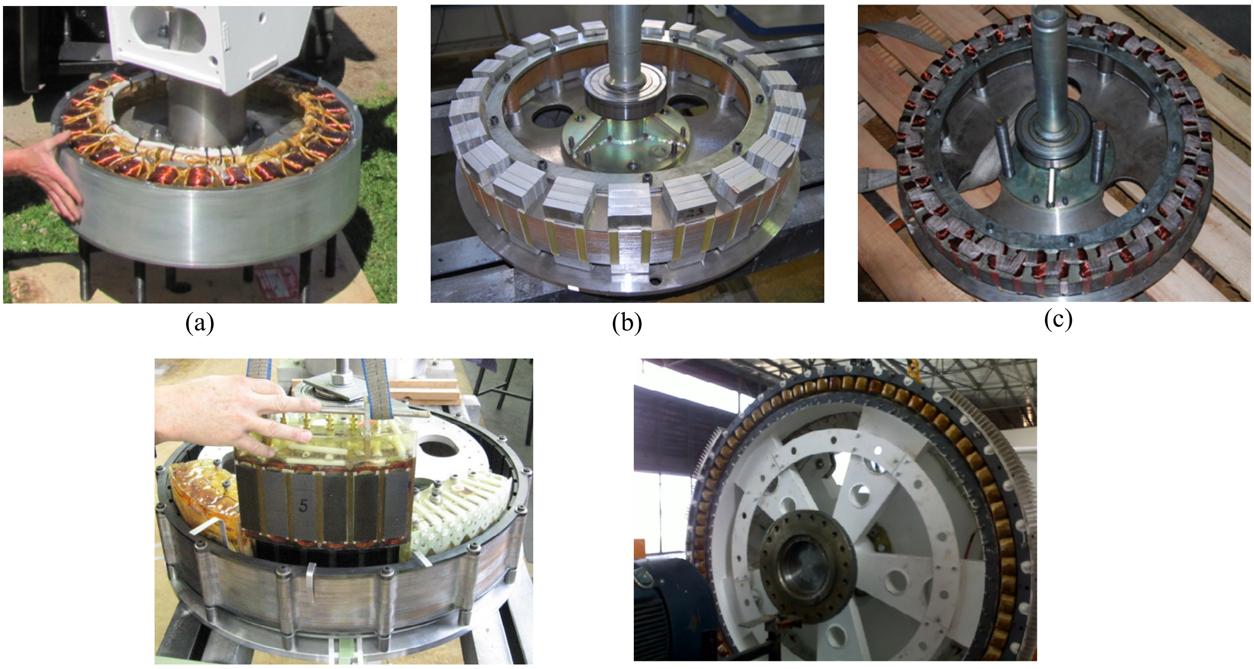

(a) (b) (c)

(d) (e)

Figure 3.2: (a) Machine 1 [11], (b) Machine 2 [12], (c) Machine 3 [12], (d) Machine 4 [13] and (e) Machine 5 [14].

3.2.1 Case-Study Machines

All of the non overlap winding PM machines studied in this investigation is for wind power generators, as for example in [11–14]. The motivation for the specific choice of machines is due to lab

Table 3.1: Dimensions and Description of Different PM Machine Structures.

Machine	**1**	**2**	**3**	**4**	**5**
$P_{s(rated)}$ (kW)	15	0.8	1.1	15	350
$T_{s(rated)}$ (Nm)	1000	850	1000	1000	67 kNm
$n_{s(rated)}$ (r/min)	150	9	10.5	150	50
$V_{s(rated)}$ (V)	230	14 mV	7.7	230	230
$I_{s(rated)}$ (A)	23	1400	30	23	511
r_c (mm)	285.0	277.1	277.4	293.5	1150
Aspect	0.160	0.102	0.102	0.170	0.107
w_t (mm)	22.63	26.97	18.81	21.50	43.77
w_c (mm)	18.00	12.00	17.50	8.500	24.90
h_c (mm)	48.90	47.28	25.90	27.00	73.38
h_g (mm)	2.00	2.00	2.00	2.00	4.00
h_m (mm)	6.00	8.00	8.00	6.32	19.25
NdFeB grade	N48H	N48H	N48H	N48H	N35H
Winding	SL	SL	DL	DL	DL
N_c	400	1	230	180	26
q	8	8	16	16	25
n_a	8	8	8	8	5

test results being available for them at the time. This ensures that the results obtained from this study are realistic. Table 3.1 gives some information on the five different PM machines evaluated. Fig. 3.1 shows the sections of the five PM machines under consideration with Fig. 3.2 showing the machines practically evaluated. Machines 1 to 4 are similar in size and power rating with different coil dimensions and winding configurations. For further characterisation of the different calculation methods Machine 5 which is a much larger direct-drive wind turbine generator, is also evaluated. All the machines make use of non-overlap modular windings. Machines 1 and 2 make use of a single layer (SL) winding configuration where every alternate tooth is wound and Machines 3 to 5 use double layer (DL) windings where each tooth is wound. Also Machine 2 makes use of a solid bar winding with only one turn. Some of the coil and machine parameters given in Table 3.1 and necessary for the calculations, are the average coil radius r_c, the coil width w_c, the average tooth width w_t and the height of the coil h_c. The aspect ratio, as commonly used in electrical machine sizing and given in Table 3.1, is the ratio of the axial stack length l to the air gap diameter D_{ag} of the machine. It is clear From Table 3.1 and Figs. 3.1 and 3.2 that several different non-overlap winding machine topologies are evaluated in this paper, which gives a good indication on the accuracy of the calculation methods considered in this study.

3.2.2 First Analytical Calculation Method

The first analytical equation presented in this paper makes use of the elementary method of combining the two end-coil sections to form a circular coil in air, as is used in [119]. To calculate the inductance, the formula for a circular air-cored coil with rectangular cross section given in [19] is used. Fig. 3.3 shows how the two end-winding sections on both sides of the stack are combined to form the circular coil. For this method it is assumed that the end-coil sides of all the machines in Table 3.1 are circular in shape. From the dimensions of the circular coil, the per phase end-winding inductance can be expressed from [19] as

$$L_{e(1)} = \frac{1.9739}{n_a^2}\left(\frac{2a^2}{b}\right) N_c^2 qK, \quad (\mu H) \tag{3.1}$$

with n_a the number of parallel circuits, N_c the number of turns per coil and q the number of coils per phase. The constant K is given by

$$K = k_1 - k_2, \tag{3.2}$$

with k_1 and k_2 given in Appendix A as functions of the dimensional variables a, b and c. These variables are given as $a = 0.5l_e$, with the average end-length given as $l_e = w_t + w_c$, $b = h_c$ and $c = w_c$.

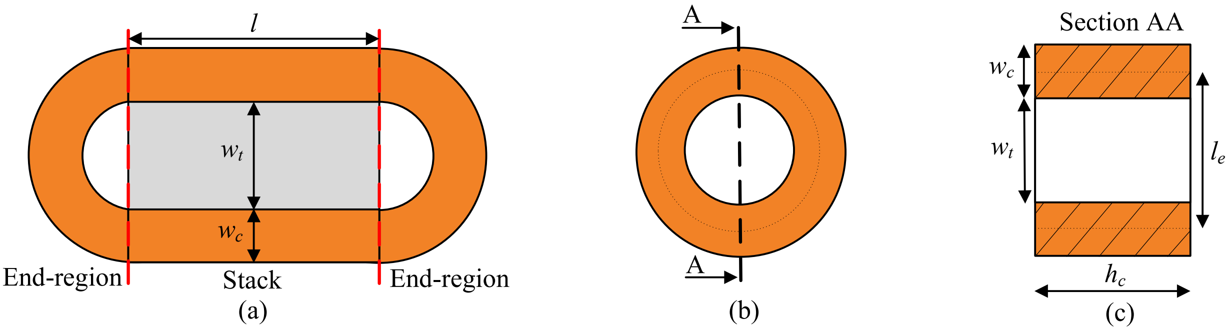

Figure 3.3: (a) Top view of coil, (b) combination of two end-coil sections into one circular coil and (c) cut through section of circular coil.

3.2.3 Second Analytical Calculation Method

In this approach the effect of the lamination stack on the end-winding inductance is taken into account by means of the theory in [122]. In this case the per length inductance is calculated of a large circular coil shown in Fig. 3.4(c) that has N_c turns and is placed against a laminated core as shown in the cut through section of Fig. 3.4(a). It is experimentally proved by [122] that the laminated core can be taken as a medium of infinite permeability in the calculation of the inductance of the coil at rated frequency; the idea that the induced eddy currents in the laminations due to the axial end-winding flux prevent the end-winding flux from penetrating the core is found to be untrue in [122]. According to the mirror-image principle the core plane of infinite permeability can be removed and replaced by the mirror-image of the circuit, i.e. by means of a second coil in air and placed as shown in Fig. 3.4(b). The circuits of Fig. 3.4(a) and (b), thus, generate the same amount of flux and have the same flux pattern.

If the two coils of Fig. 3.4(b) are considered as one coil with N_c turns and double the current to generate the same flux, then the inductance of the coil in Fig. 3.4(a) will be double the inductance of the coil in Fig. 3.4(b), i.e. $L_{(a)} = 2L_{(b)}$. The inductance $L_{(b)}$ of the coil in air of Fig. 3.4(b) can be calculated by using the formula as given by (3.1). To calculate the, per end-winding length inductance, of the large circular coil of Fig. 3.4(c) the formula of (3.1) must be multiplied by the factor $l_e/2\pi a$, where the term $2\pi a$, with $a = r_c$, gives the circumference of the large circular coil. Furthermore, to include the inductance of the other half of the end-winding the formula must be

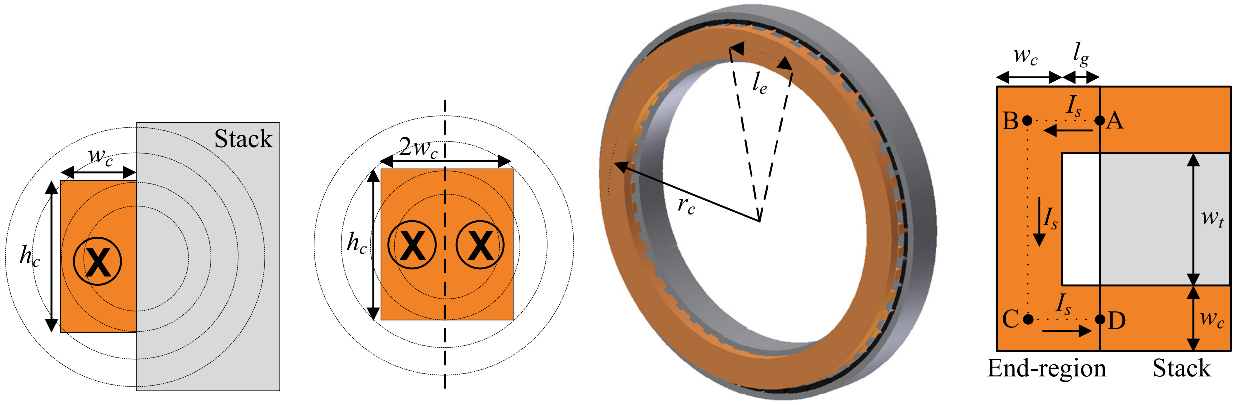

(a) (b) (c) (d)

Figure 3.4: (a) Cross section of coil ring with dimensions $h_c \times w_c$ on laminations and (b) cross section of coil ring with dimensions $h_c \times 2w_c$ in air. (c) Coil ring with radius r_c used for analytical calculation number two. (d) Actual end-winding path length.

further multiplied by a factor two. Hence, the per phase end-winding inductance in the second analytical method is calculated by

$$L_{e(2)} = 2 \times \frac{l_e}{2\pi a} \times 2 \times \left[\frac{1.9739}{n_a^2}\left(\frac{2a^2}{b}\right) N_c^2 qK\right] = \frac{1.257}{n_a^2} l_e \left(\frac{2a}{b}\right) N_c^2 qK. \quad (\mu H) \tag{3.3}$$

In the case of (3.3), $a = r_c$, $b = 2w_c$ and $c = h_c$.

At this point it is very important to specify the correct end-winding length as will be seen in Section 3.3.1. In (3.1) and Fig. 3.4(c) it is approximated as $l_e = w_t + w_c$. This corresponds to the end-winding section indicated by BC in Fig. 3.4(d). However, observing Fig. 3.4(d), if Sections AB and CD are taken into account, it is seen that the actual end-winding length is closer to $l_e = w_t + 2w_c + 2l_g$, with l_g the distance of the end-winding from the lamination stack. With the current direction of the end-winding sections AB and CD assumed perpendicular to the current flowing in Section BC, it would normally be assumed that these extra end-winding sections are not affected by the lamination stack. From FE observations it was, however, found that even for this end-winding section the lamination stack does have an effect. For this particular study it was found that for coils with $l_g < 2.5$ mm the effect of the stack on this section can make a substantial contribution to the overall end-winding result. For coils with $l_g > 2.5$ mm the observed effect of the lamination stack is not as critical for this particular end-winding section, and it is sufficient to assume that this extra section is solely influenced by air. Thus, a third analytical approach is devised with

$$L_{e(3)} = \begin{cases} L_{e(2)\ (l_e = w_t + 2w_c + 2l_g,\, b = 2w_c)} & \text{for } l_g < 2.5 \text{ mm}, \\ L_{e(1)\ (l_e = w_c + 2l_g,\, b = w_c)} + L_{e(2)\ (l_e = w_t + w_c,\, b = 2w_c)} & \text{for } l_g > 2.5 \text{ mm}, \end{cases} \tag{3.4}$$

and with $a = r_c$ and $c = h_c$.

3.2.4 FE-Calculation Methods

As no end-effects are taken into account by conventional 2D-FE analysis, a simple 2D-FE method as proposed in [126] is used to calculate the end-winding inductance. This simplified FE model is shown in Fig. 3.5 for Machine 1. A conductor with dimensions of $w_c \times h_c$ and model depth l_e is placed next to half of the rotor and stator stack as shown in Fig 3.5(a). This conductor is defined as a coil and excited with the rated machine current $I_s = I_{s(rated)}$. From the resulting, single static 2D-FE solution the end-winding flux linkage (λ_e) and inductance are determined with $L_e = \lambda_e / I_s$.

To shed more light on the accuracy of the analytical methods, use is made of 3D-FE-analysis to calculate the inductances, with Fig. 3.6 showing the 3D-FE field plot of Machine 1. To determine the end-winding inductance of the PM machine the 2D total per phase inductance is subtracted from the 3D total per phase inductance. Note that in this case 2D-FE analysis refers to conventional 2D-FE simulation and not to the simplified 2D-FE end-winding inductance calculation method as in Fig. 3.5. To eliminate the permanent magnet end-winding leakage flux linkage and to simplify the calculation, the permanent magnets are "switched off" in this analysis. This will obviously change the magnetic saturation levels of the core, but it will have little effect on the end-winding inductance as the reluctance of the end-winding flux-path is almost entirely dominated by air.

In both the conventional 2D and 3D-FE solutions balanced instantaneous three-phase currents are used to include the mutual flux linkage between the phase windings. The total phase inductance is determined simply from the total phase flux linkage divided by the instantaneous phase current, with $L_s = \lambda_s / I_s$. In this calculation, thus, one 2D static FE solution and one 3D static FE solution are required. This is the most accurate method to calculate the end-winding inductance as the correct shape of the end-coils as well as the permeable mediums around the end-coils, are taken into account. To investigate the effect of the mutual flux coupling between the phase end-windings, the above FE calculations are repeated but with only one phase excited.

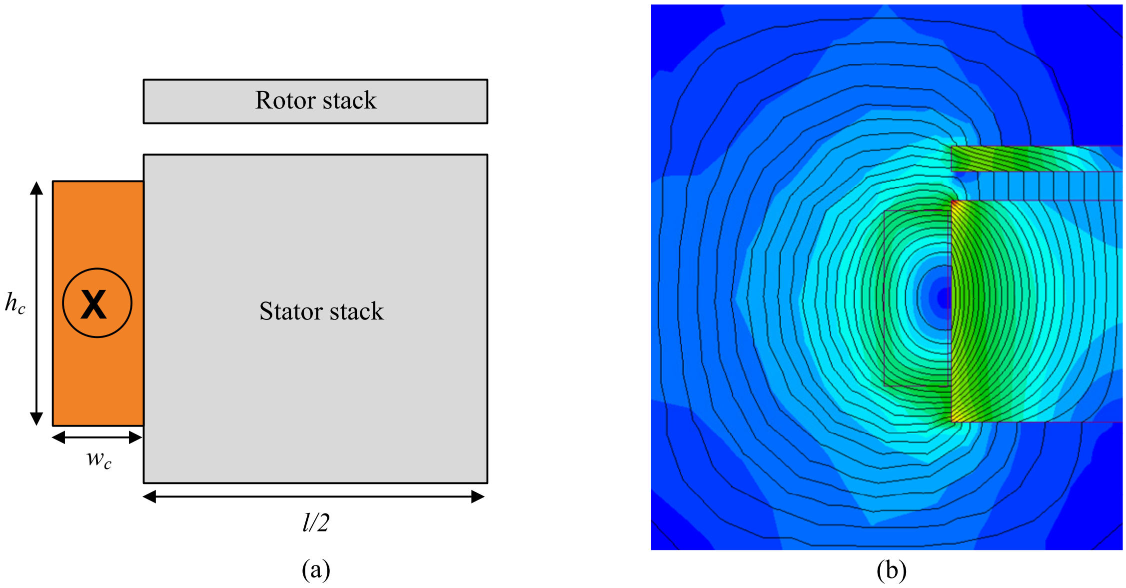

(a) (b)

Figure 3.5: (a) Model and (b) field plot of the 2D-FE end-winding inductance calculation method.

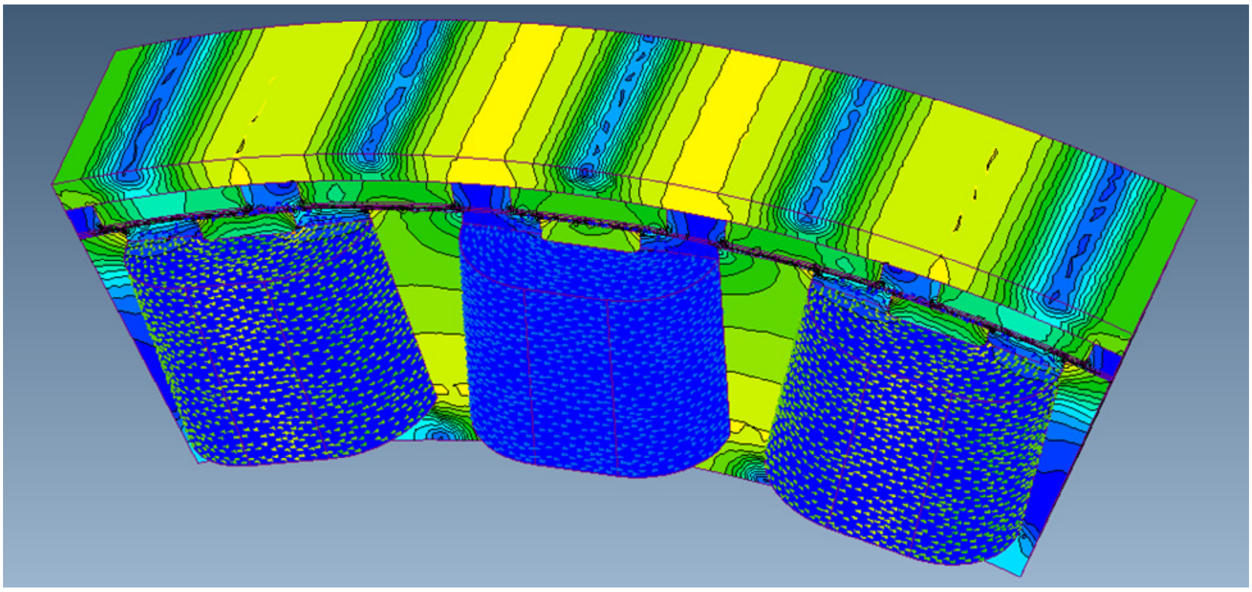

Figure 3.6: 3D-FE field plot of Machine 1.

3.3 End-Winding Inductance Calculation

The explanation of the calculated results in this section is divided into two sub-sections. In the first section the accuracy of the formulas from literature are evaluated against the results from FE-analysis. In the second section the calculation results for all the discussed analytical and FE methods applied to the different PM machine topologies are shown.

3.3.1 Verification of Formulas

In Table 3.2 the formula (3.1), obtained from [19] for the calculation of a circular coil in air is verified. This is done by calculating the inductance values of a 3D-FE model of the end-winding circular coil of Fig. 3.3(b) as shown in Fig. 3.7. An average accuracy of 7.18 % is obtained for the five PM machines, which validates the formula in [19]. The method of images as experimentally analysed in [122] is also verified again with FE analysis by calculating the inductances of the conductors defined in Fig. 3.4(a) and (b). Fig. 3.8(a) shows the 2D-FE field plot of the coil in air as shown in Fig. 3.4(b). In Fig. 3.8(b) half of the coil is placed next to a steel medium as in Fig. 3.4(a) to obtain a more realistic representation of the actual conditions. Fig. 3.8(b) shows half of the coil placed

Table 3.2: Verification of the calculation results in [19] with 3D-FE.

Machine	Analytical-1 [19]	3D-FE	% Error
1 (mH)	0.340	0.310	8.82
2 (nH)	2.994	2.823	6.06
3 (mH)	0.259	0.242	6.56
4 (mH)	0.135	0.125	7.41
5 (μH)	21.45	19.94	7.04

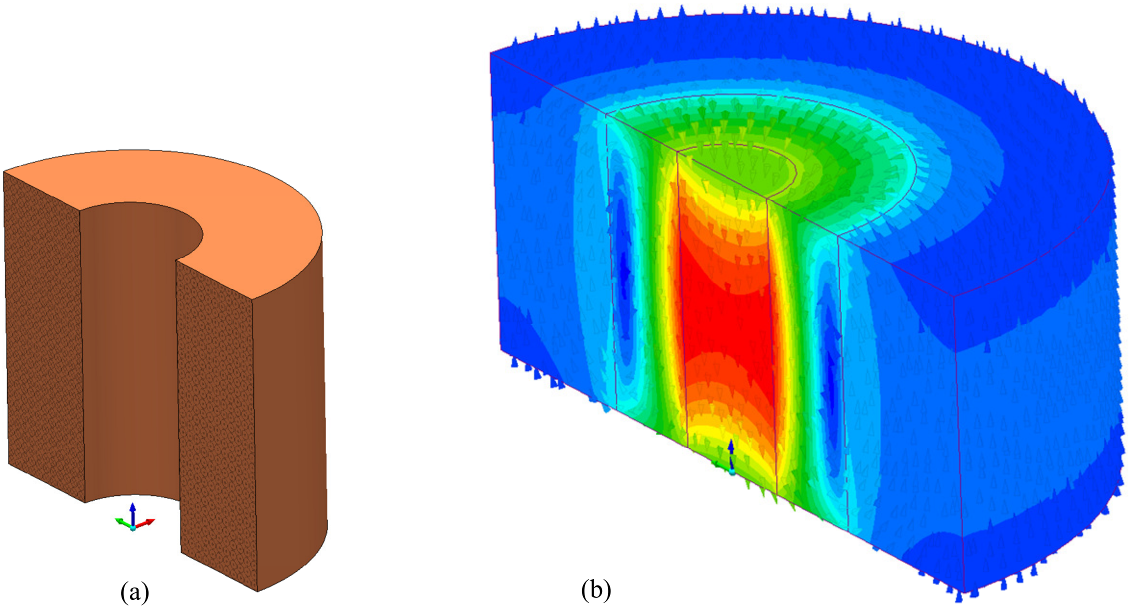

Figure 3.7: (a) 3D-FE model and (b) 3D-FE field plot of the circular coil of Fig. 3.3(b) with the dimensions of Machine 1 used.

Table 3.3: Verification of the method of mirror-images by means of FE.

Coil	Dimensions and turns	Current	Inductance, $L_{(a),(b)}$ (mH)
Fig. 3.4(a)	$h_c \times w_c$, N_c turns	I_s	1.996
Fig. 3.4(b)	$h_c \times 2w_c$, N_c turns	$2I_s$	0.994
		$L_{(a)}/L_{(b)}$	**2.008**

next to a medium of infinite permeability, which is created by applying a field normal boundary condition to the model. As shown in Table 3.3 it is found that $L_{(a)} = 2L_{(b)}$, which validates the method of images as used in this chapter.

3.3.2 Calculation Results

In Table 3.4 the calculated end-winding inductances of the five PM machines are given using the two analytical and two FE analysis methods. It is clear that the effect of the lamination core cannot be ignored, as the inductance values of the first analytical method are far lower than the values obtained from the other methods. The inductance values obtained from the 2D-FE method are also shown to be a bit on the low side. The importance of specifying the correct value for l_e is also clearly seen by comparing the results of $L_{e(2)}$ with $l_e = w_t + w_c$ for all cases and $L_{e(3)}$ with l_e as defined in (3.4). It is shown that $L_{e(3)}$ as in (3.4) gives the best inductance values compared to the values of the 3D-FE method given in Table 3.4 of the five PM machines, especially for the single layer windings. The total per phase inductance, L_s, calculated by means of 3D-FE is also shown in order to obtain an indication on the relative size of L_e with respect to L_s. It is clear that a large portion of L_s can be attributed to L_e, in some cases more than 20 %!

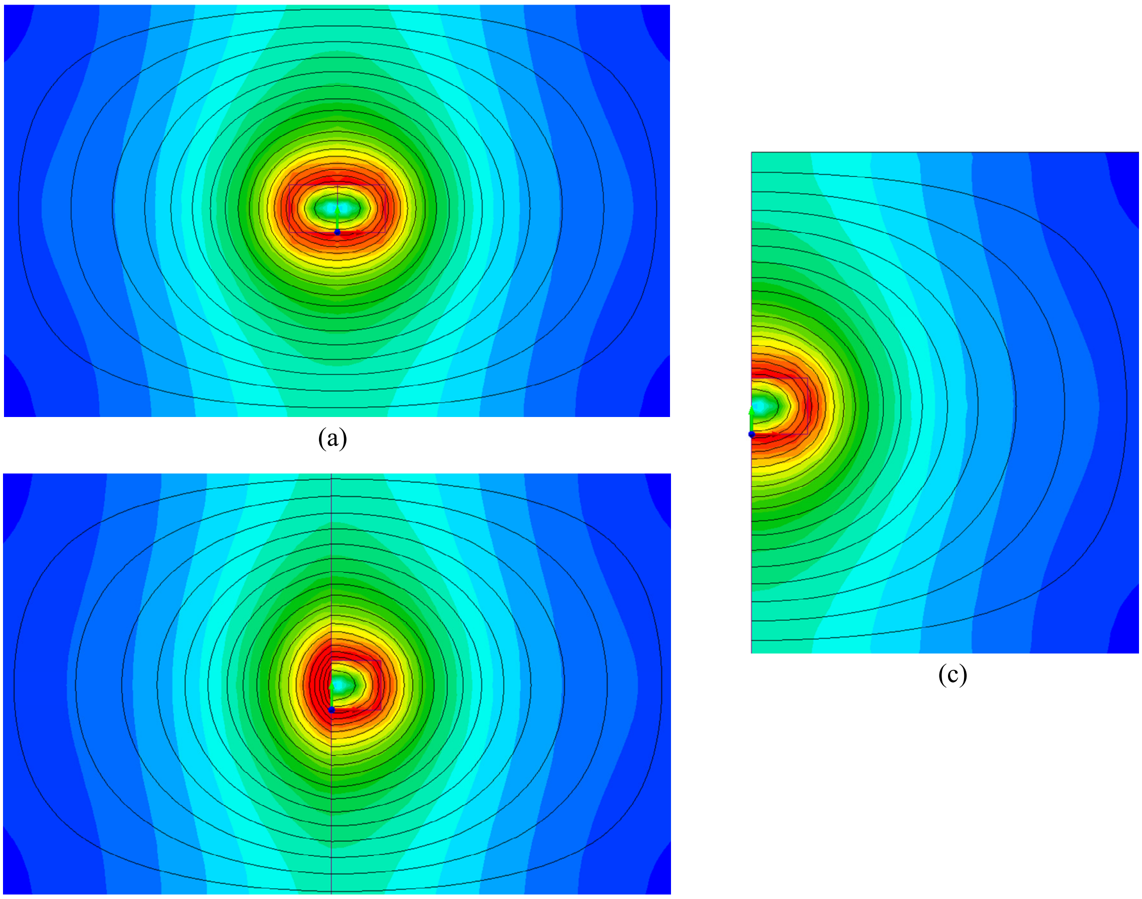

(a)

(c)

(b)

Figure 3.8: 2D-FE field plots of (a) the coil in Fig. 3.4(b), with (b) the left half of the model replaced by a steel stack, similar as for the coil in Fig. 3.4(a) and (c) a medium of infinite permeability created by adding a field normal boundary condition to the side of the coil model.

To shed some more light on the results of Table 3.4, Table 3.5 gives the percentage mutual phase cross-coupling (M_c) inductance component for the end-windings of the five machines. It is clearly seen that the double layer windings are much more affected by mutual phase cross-coupling, with a substantial percentage increase in L_e observed. These effects are also less for Machine 3 compared to Machine 4 and Machine 5, which also use a double layer winding. The reason is that the two

Table 3.4: End-winding inductance results calculated analytically and by FE-analysis.

Machine	$L_{e(1)}$	$L_{e(2)}$	$L_{e(3)}$	2D-FE	3D-FE	L_s
1 (mH)	0.340	1.814	2.800	1.414	2.904	15.67
2 (nH)	2.994	10.24	16.80	9.641	17.76	80.16
3 (mH)	0.259	1.199	1.613	0.962	1.773	7.950
4 (mH)	0.135	0.681	0.817	0.512	0.922	3.135
5 (μH)	21.45	108.6	135.2	100.5	155.5	1065

Table 3.5: Effects of mutual phase cross-coupling on L_e.

Machine	M_c	K_M	$L_{e(3)M_c\neq 0}$	%Error
1 (mH)	1.73%	1.02	2.856	1.68%
2 (nH)	1.65%	1.02	17.14	3.58%
3 (mH)	5.92%	1.11	1.790	0.95%
4 (mH)	16.8%	1.11	0.907	1.65%
5 (μH)	10.9%	1.11	150.1	3.60%

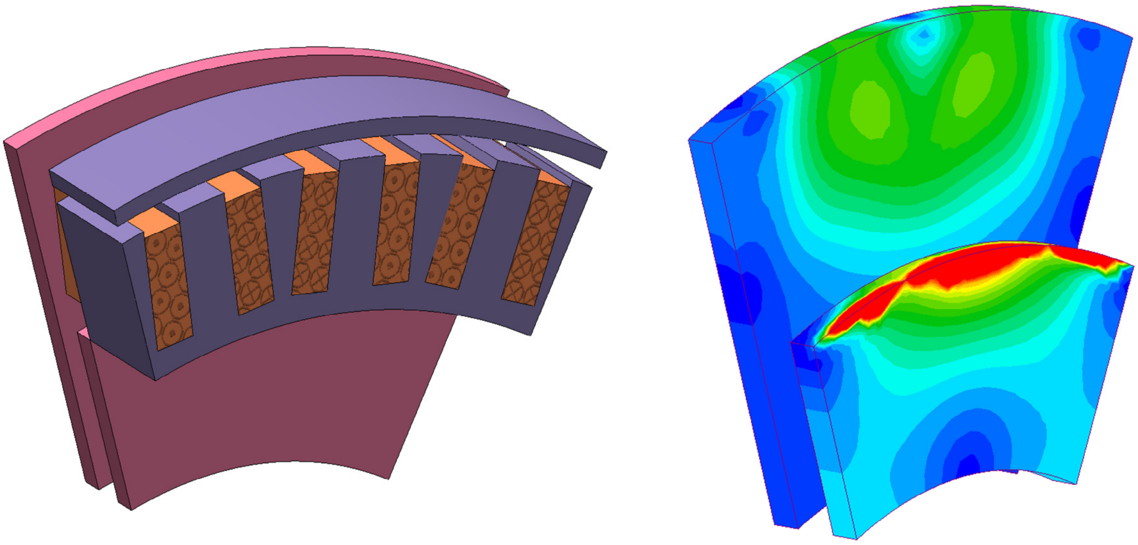

(a)

(b)

Figure 3.9: 3D-FE field plot of the turbine and stator mounting plates for Machine 1 (maximum flux density range in red = 0.2 T).

Table 3.6: Effect of permeable construction mediums on L_e.

Permeable medium	%Change in L_e
PM rotor yoke	4.43 %
Turbine mounting plate	9.27 %
Stator mounting	0.21 %

double layer coils of Machine 3 are stacked on top of one another instead of being adjacent as is the case for Machine 4 and Machine 5.

For a generalised approach to calculate the end-winding inductance more accurately a mutual phase cross-coupling factor K_M is calculated from the average values of M_c in Table 3.5. To take M_c into account (3.4) should be changed to $K_M \times L_{e(3)}$ with $K_M \approx 1.02$ for single layer windings, which is almost negligible, and $K_M \approx 1.1$ for double layer windings. The new values calculated for

L_e are shown in Table 3.5. A much better match is obtained between the values of the analytical expression of $K_M \times L_{e(3)}$ and the values from 3D-FE analysis for the five different non-overlap winding PM machines. An average error of only 2.3 % is observed.

In Table 3.6 the effect of other permeable mediums in close proximity to the end-windings, especially the turbine mounting plate which is typical for PM wind generators on L_e are also shown. Fig. 3.9 shows the flux density distribution in the turbine mounting plate and stator mounting caused by the flux from the end-winding. Thus, if it is deemed necessary due to the mechanical topology of the electrical machine, $L_{e(3)}$ can be multiplied by another generalised factor of $K_p \approx 1.1$, to take an approximated 10 % contribution for the permeable construction mediums into account.

3.4 PM End-Flux Fringing

As will be shown in Figs. 6.16(a) and 6.23(b) in Sections 6.6 and 6.7 in Chapter 6, even by taking the end-winding inductance into account there is still a significant difference between the measured and 2D FE-predicted short-circuit performance of the evaluated machines. It is found that by changing the magnetic saturation levels in the machine a much better match is obtained between FE and measurements. The changes in magnetic saturation levels can be attributed to variations in the characteristics of the PMs. Thus, a further investigation is launched into the influence of PM end-effects on the machine performance. Some mention is made in literature regarding this aspect. It is mentioned that especially for large diameter, axially short machines [128], machines with a small air gap [129] and at load values higher than rated [130] the PM end-effects cannot any longer be ignored. In [131] and [132] the output performance parameters are multiplied by a fringing factor and in [133] by a further magnetic saturation correction factor. These factors are calculated by observing the difference in 3D and 2D FE calculations for a specific range of PM machines. In [128] an analytical approach making use of fictitious PM arrays is used to calculate the 3D-PM field distribution.

3.4.1 Effects of Parameter Variations

To obtain an indication on the influence of the PM end-flux on the machine performance, 3D-FE analysis is again utilised. The goal is to obtain an expression or factor to implement in the 2D-FE modelling which matches 3D-FE and measured results. The prototype generator as shown in Figs. 3.1(a) and 3.2(a) with 3D-FE field plot as shown in Fig. 3.6 are used as a case study. Fig. 3.10(a) shows the flux density field plot of Machine 1 with the PMs isolated and where a flux tangential boundary condition is applied to the side of the machine in the FE-modelling (same as 2D-FE). In the field plot of Fig. 3.10(b) the boundary condition is removed and the simulation is run again. It should just be noted that for 3D-FE half of the machine section is modelled in the axial direction. At the end-sections of the PMs a disturbance can clearly be observed, with the PM end-flux fringing area (A_e) indicated in Fig. 3.10(b). In literature this disturbance area is used to calculate a constant PM flux fringing factor, K_f. The 2D calculated results can then be multiplied by this factor, e.g. for the PM flux linkage $\lambda'_{ms} = K_f \lambda_{ms}$ with λ'_{ms} the “corrected” PM flux linkage.

Furthermore, some of the machine parameters, which include the axial length l, magnet height h_m, magnet span σ_m and airgap height h_g, were varied with the effects shown in the 3D-FE flux density plots of Fig. 3.11. In each case the dimensions of Machine 1 are taken as reference base values. In Fig. 3.11(a) the axial stack length is varied, with $l = 100$ mm, the base value of Machine 1. A_e does not vary significantly for a variation in l, being only slightly different for the shorter stack lengths. An interesting observation is also the slight change in magnetic saturation for the shorter

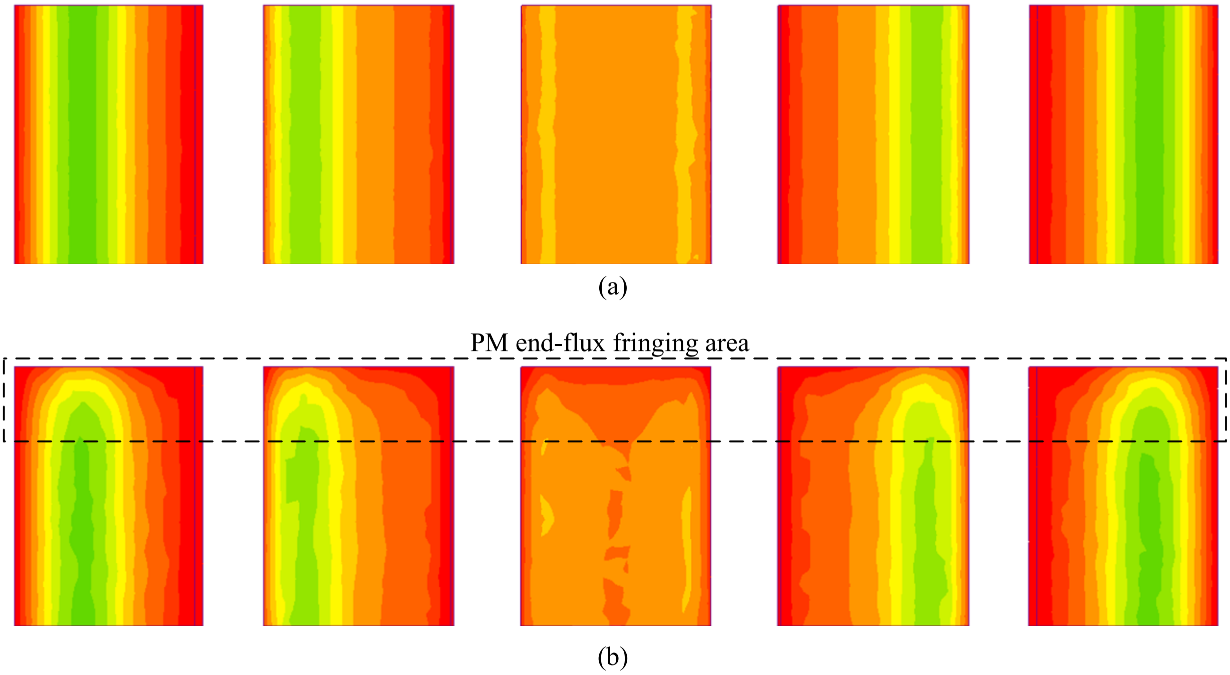

Figure 3.10: Flux density plots shown for the PMs of Machine 1 isolated, with (a) boundary conditions applied to the side of the machine (same as 2D-FE) and (b) with no boundary conditions applied to the side of the machine (3D-FE).

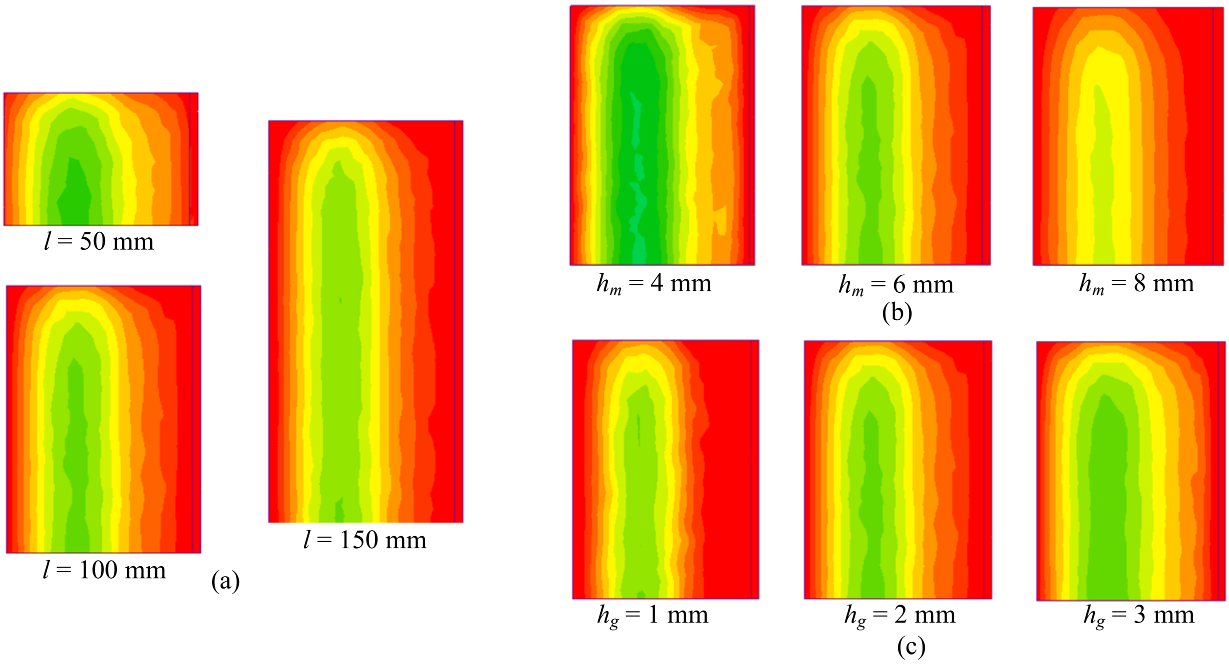

Figure 3.11: Investigation of the PM end-flux fringing area for a variation in (a) axial stack length l, (b) magnet height h_m and (c) airgap height h_g (flux density colour scale the same for all cases).

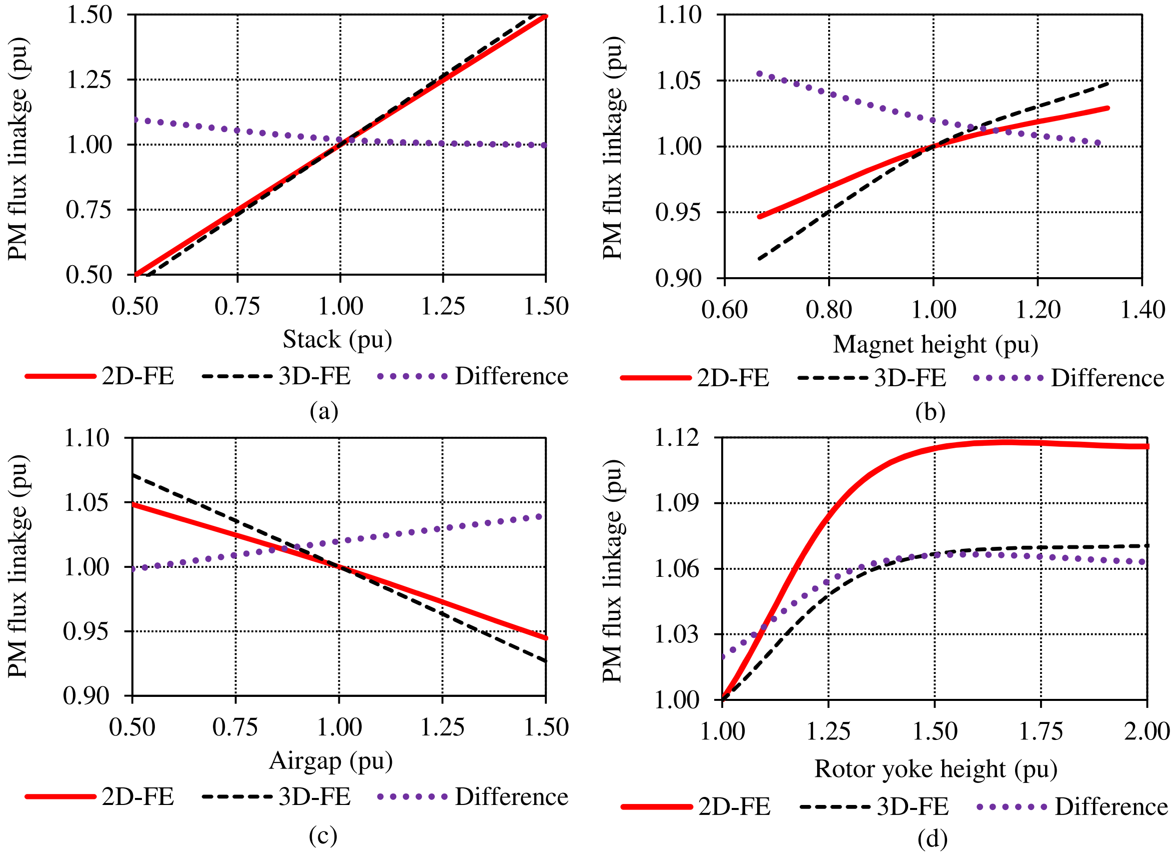

Figure 3.12: Investigation of PM end-flux fringing for (a) a variation in the axial stack length l, (b) a variation in the magnet height h_m, (c) a variation in the airgap height h_g and (d) a variation in the rotor yoke height h_{ry}.

stack. It is evident though that the per unit value of A_e as a function of the total PM area will be much less for the longer stack lengths. Fig. 3.11(b) shows the effect of a variation in h_m with $h_m = 6$ mm for Machine 1 on A_e. In this case a much more substantial change in A_e is observed, with A_e clearly increasing for higher values of h_m. The effect on A_e for a variation in h_g is shown in Fig. 3.11(c). Although the size of A_e does not change significantly the saturation levels in the machine changes considerably.

To gain further insight on how the magnetic saturation levels influences the machine design Fig. 3.12 show the per unit variation in λ_{ms} for a per unit variation in the dimensions of Machine 1 similar as in Fig. 3.11, for both 2D-FE and 3D-FE. The base values of λ_{ms} is the respective 2D and 3D FE calculation results at the original dimensions of Machine 1. Also shown in Fig 3.12 is the per unit difference between the 2D and 3D-FE calculated value of λ_{ms} which is defined as $\lambda_{ms(3D)}/\lambda_{ms(2D)}$. It is clear from Fig. 3.12 that the per unit change in λ_{ms} calculated by 2D-FE is not the same as the per unit change in λ_{ms} calculated by 3D-FE. Furthermore, an important aspect is that the difference in λ_{ms} calculated by 2D and 3D-FE respectively does not stay constant. Very interesting is that in some cases there is almost no difference between the 2D and 3D-FE calculations. It is, thus, clear that the effects of magnetic saturation play a significant role in the magnitude of the influence of the PM end-flux fringing effect. From the results of Figs. 3.11 and 3.12 it is evident that due to the non linear nature of the PM end-flux fringing, it would be extremely difficult to

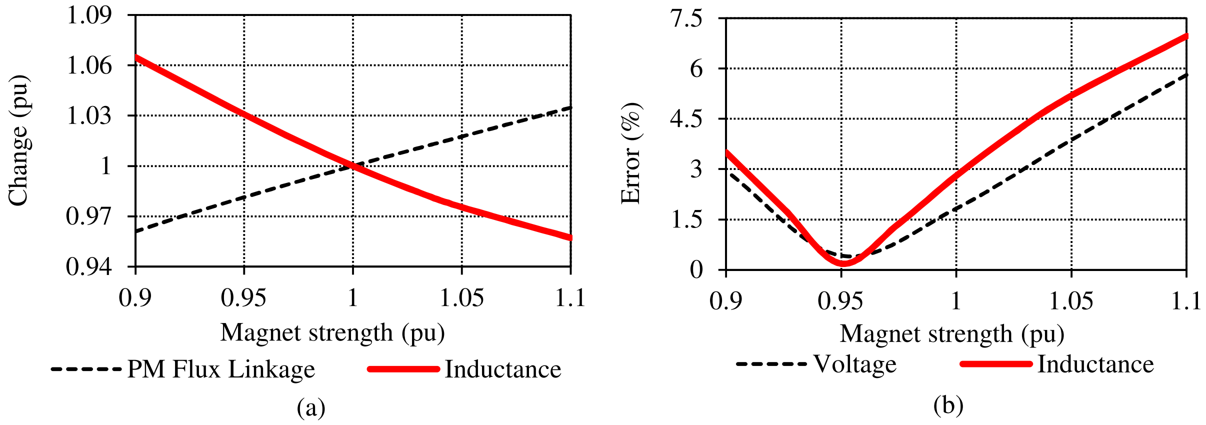

Figure 3.13: (a) Per unit reduction in FE-calculated per phase inductance (L_s) and PM flux linkage (λ_{ms}) versus per unit change in PM remanence flux density (B_r) for Machine 1. (b) Percentage error between the measured and FE calculated phase inductance (L_s) and voltage (V_s) versus per unit PM remanence flux density for Machine 1.

analytically calculate the magnitude of this phenomena due to magnetic saturation effects.

3.4.2 Including PM End-Flux Fringing in 2D-FE

From the above discussion it is found that it is very difficult to take the PM end-flux fringing into account in 2D-FE with the fringing factor method proposed in literature. Due to the large amount of flux fringing around the PM-ends the magnetic saturation levels changes. Thus, to reflect the magnetic saturation effects in the 2D-FE calculated results, rather than using K_f to reduce λ_{ms} or any other 2D-FE calculated results as suggested in literature, it is proposed in this study that the PM strength of the magnets used in the 2D-FE modelling is modified by a factor. This is done by modifying the PM BH-curve data used in FE by shifting the BH-curve line downwards, similar as with an increase in temperature as shown in Fig. 3.14. Usually in the analysis of the PM BH-curve the flux density at zero magnetic field intensity is referred to as the remanence flux density (B_r), hence in this case the PM strength is modified with $B_r' = K_f B_r$.

Fig. 3.13(a) shows the effect of this variation in PM strength on λ_{ms} and L_s with again $L_s = \lambda_s/I_s$, with I_s constant for Machine 1. One would expect that λ_{ms} would decrease at the same rate as the PM strength, but clearly λ_{ms} is only changing at less than half of this rate. L_s on the other hand increases at about double the rate of change of λ_{ms} for the same reduction in PM strength. It is, thus, clear that magnetic saturation plays a significant role in the calculation of λ_{ms} and L_s. The proposal in literature to modify the performance parameters calculated by 2D-FE by means of a "*correction*" factor is, thus, clearly not valid. In order to obtain an indication on whether the approach to rather modify the PM strength is valid, an experimental analysis is included within the PM end-flux fringing investigation. In Fig. 3.13(b) the error between the 2D-FE calculated and measured open circuit voltage and also the 2D-FE calculated, with $L_{e(3)M_c \neq 0}$, and measured inductance are shown as a function of magnet strength for Machine 1. The open circuit voltage is measured at the rated speed of 150 r/min. L_s is calculated by means of the classical open circuit and short circuit tests for synchronous machines as described in [134] and Section 6.7 in Chapter 6.

3.5 PM Demagnetization and Temperature Effects

Demagnetization and PM temperature (T_m) effects which also causes changes in the PM characteristics are investigated as well. An in depth study on demagnetization of PMs in electrical machines is conducted in [135]. Demagnetization is typically caused by high short circuit currents, high temperature and the PM geometry, especially the PM height, h_m. If irreversible demagnetization occurs, which will result in a further reduction in PM strength, it is evident that the short-circuit performance of the machine will be influenced even more.

3.5.1 PM Demagnetisation Theory

Fig. 3.14 shows the normal BH-curves in the second quadrant for the used N48H NdFeB PM material at different PM temperatures, with the data shown obtained from [15]. For interest sake the intrinsic BH-curves for $T_m = 20$ °C and $T_m = 80$ °C are also shown. These curves are not normally used as the behaviour of the PM in a magnetic circuit is described by the normal curves. It is clear that the characteristics of the PMs are significantly influenced by temperature. As T_m increases the BH-curve shifts downwards indicating a reduction in PM strength. It is also seen that the behaviour of the BH-curves tends to become more non-linear in the second quadrant with an increase in T_m. The region where non-linearity occurs is usually referred to as the *"knee-point"*. Although T_m is kept constant in the analysis, this aspect should definitely be considered for PM machines with a high operating temperature or a high PM loss component. For the used N48H PM material at 20 °C, $B_r = 1.39$ T and the coercivity is given as $H_c = 1054$ kA/m. Fig. 3.15(a) show the per unit variation in B_r for a variation in T_m, with the base value the magnitude of B_r at 20 °C for the used N48H PM material.

The load line shown in Fig. 3.14 is used to obtain the working point(W_{p1} or W_{p2}) of the PM indicated by H_m and B_m. A more thorough explanation on magnetic circuit analysis can be found in typical electrical machine design textbooks such as [136]. As explained in [135] the load line

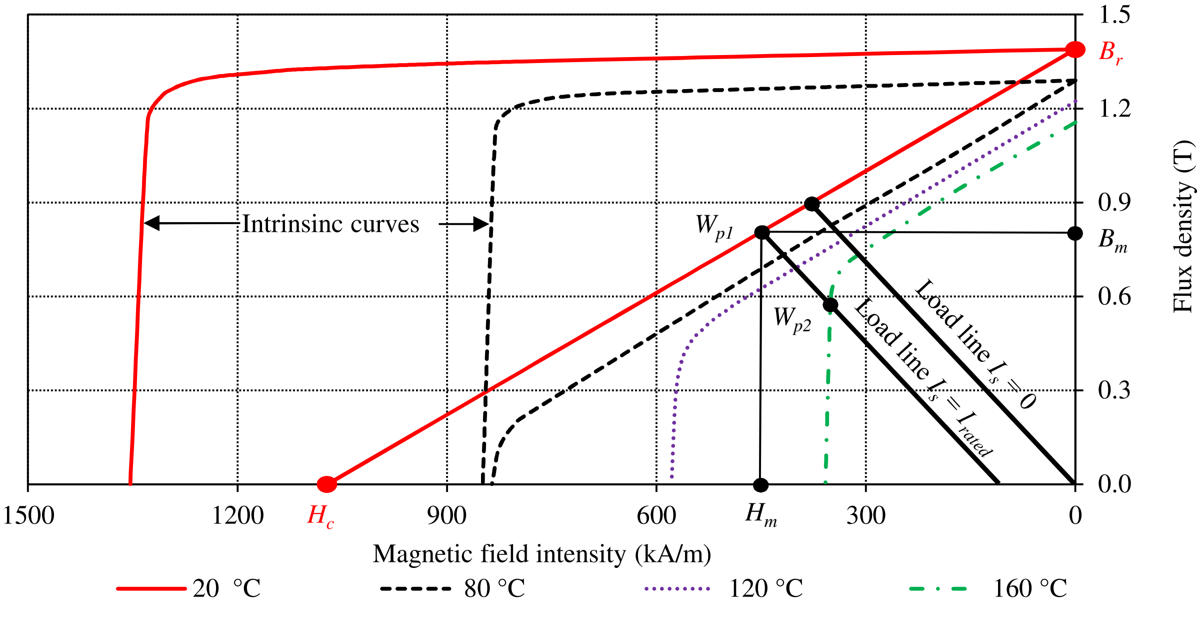

Figure 3.14: BH-curves in the 2^{nd} quadrant for NdFeB N48H PM material for different PM temperatures [15].

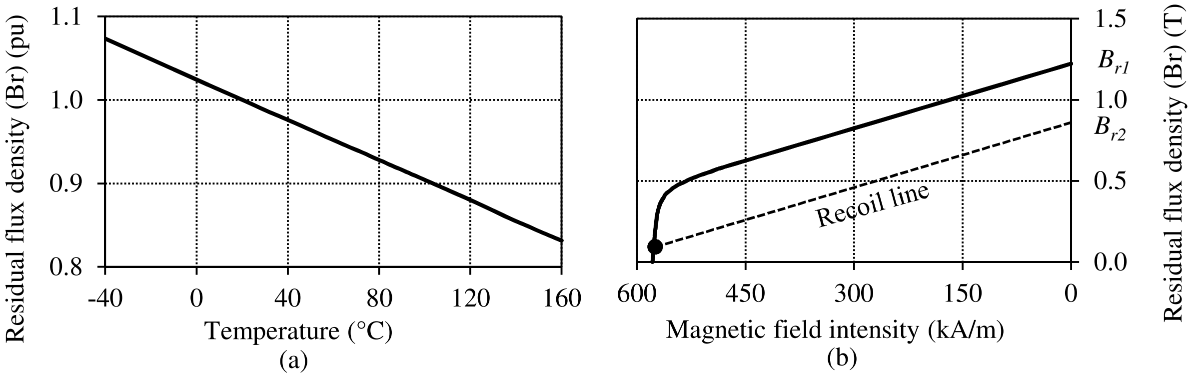

Figure 3.15: (a) Per unit change in the remanence of N48H PM material versus PM temperature and (b) normal BH-curve and recoil line at $T_m = 120$ °C.

shifts slightly to the left of the B-axis when there is current flowing in the windings and it no longer goes through the origin as indicated in Fig. 3.14. Partial irreversible demagnetization occurs when the operating point shifts below the *"knee-point"* as indicated by W_{p2}. Shown in Fig. 3.15(b) is the normal BH-curve at $T_m = 120$ ° with the PM operating point below the *"knee-point"*. After the machine operating conditions return to normal B_r of the now partially demagnetised PM changes to $B_r = B_{r2}$ instead of $B_r = B_{r1}$, with B_{r1} the original remanence of the PM. B_{r2} is calculated by the recoil line as indicated in Fig. 3.15(b), which will be linear if the demagnetisation is below 10 % and only slightly non-linear for higher values of demagnetisation as mentioned in [135]. Depending on how far the operating point is below the *"knee-point"* will, thus, determine the magnitude of demagnetization with total demagnetization occurring when B_{r2} approaches zero.

3.5.2 Demagnetisation Case-Study

To obtain an indication on demagnetisation for the type of PM machines considered in this thesis, Machine 1 is again used as a case-study. Fig. 3.16 show the demagnetization prediction by means of FE analysis of Machine 1, where Fig. 3.16(a) and (b) show the result of ignoring the end-effects. It is found that if the end-effects are ignored demagnetization effects start to occur at $T_m = 60$ °C, with slight demagnetisation effects observed as shown in Fig. 3.16(b), as opposed to $T_m = 80$ °C with the end-effects taken into account as shown in Fig. 3.16(a). For $T_m = 100$ °C it is clear that by increasing h_m the demagnetization effects are less severe as shown in Fig. 3.16(c) opposed to lower values of h_m as shown in Fig. 3.16(d). For $h_m = 4$ mm demagnetization effects already starts to occur at $T_m = 40$ °C. It is mentioned in [77] that a maximum value of T_m is measured at about 40 °C after prolonged operation of Machine 1. However, tests were also conducted where the PMs were made solid instead of being segmented with values of T_m up to 100 °C measured in this case. This value of T_m would clearly be a concern regarding demagnetisation of the PMs.

3.6 Variations in Lamination Steel

Inconsistencies in the electrical steel used as mentioned in for example [137] and [138], can further influence the magnetic saturation levels and flux path reluctances and, thus, λ_{ms} and L_s. Furthermore, as mentioned in [138] the frequency at which the BH-curve is calculated can also influence the machine performance calculations. Fig. 3.17 shows the BH-curves for M19-26Ga lamination steel

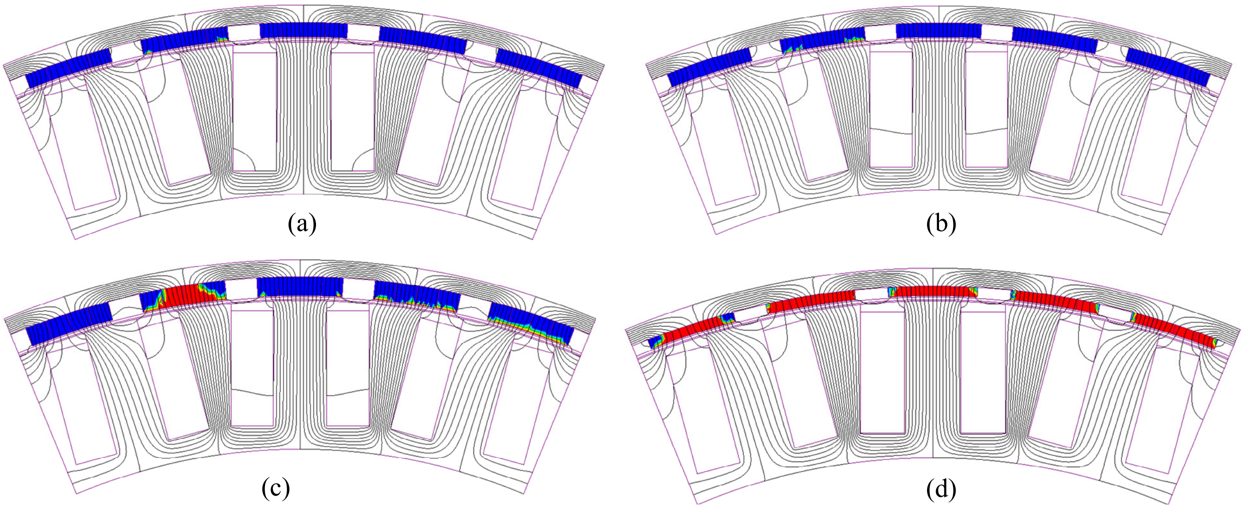

Figure 3.16: Demagnetization prediction of Machine 1 by means of FE analysis, where areas in red indicate the occurrence of demagnetisation in the PMs, with (a) $T_m = 80$ °C, $L_e = L_{e(3)M_c \neq 0}$, $K_f = 0.95$ and $h_m = 6$ mm, (b) $T_m = 60$ °C, $L_e = 0$, $K_f = 1$ and $h_m = 6$ mm, (c) $T_m = 100$ °C, $L_e = L_{e(3)M_c \neq 0}$, $K_f = 0.95$ and $h_m = 8$ mm and (d) $T_m = 100$ °C, $L_e = L_{e(3)M_c \neq 0}$, $K_f = 0.95$ and $h_m = 4$ mm.

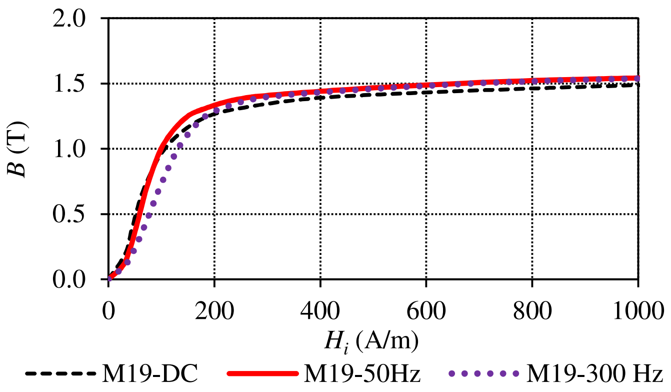

Figure 3.17: Different BH-curves for M19-26Ga lamination steel at 0 Hz, 50 Hz and 300 Hz [16].

measured at different frequencies, with clear differences observed in the BH-curve depending on the frequency. Fig. 3.18 show the effect of using different lamination steels on λ_{ms} and L_s with clear differences observed depending on the type of lamination steel. Thus, it is evident that by not using the correct BH-curve in the FE-modelling, further inaccuracies in the calculation of the short-circuit performance of the machine is possible. All the BH-curve data were obtained from [16], which provides data for most of the commonly used lamination steels. Furthermore, as is mentioned in [137] it cannot always be assumed that the BH-curve provided is correct as variations in the properties of different batches of the same type of electrical steel frequently occur.

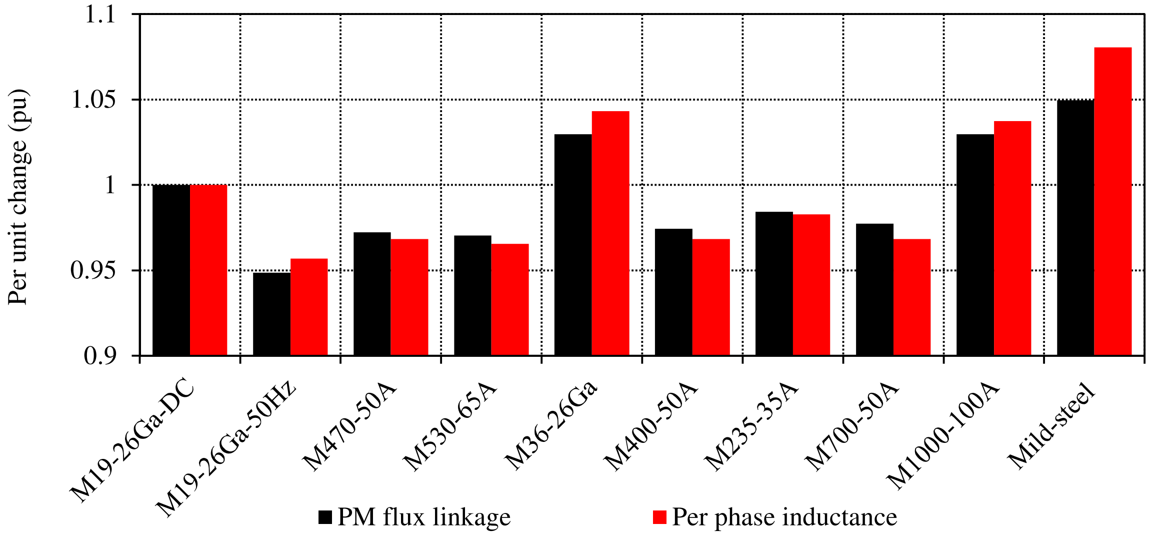

Figure 3.18: Per unit change shown for λ_{ms} and L_s for different lamination steels, with M19-26Ga using the DC-BH curve, taken as the base value.

3.7 Summary

It is clearly shown in this chapter that the end-effects of non overlap winding PM machines cannot be ignored in the analysis, especially in the above rated region. This is especially true for PM machines with low aspect ratios typical for direct-drive PM wind generators. For the SS-PMG technology evaluated in this thesis adequate knowledge of the short-circuit machine performance is especially important. In Sections 6.6 and 6.7.2 in Chapter 6 the effect of ignoring the end-winding inductance and PM end-flux fringing is clearly shown.

It is furthermore shown that commonly-used methods that ignore the effect of the laminated core in the calculation of the end-winding inductance are not valid. In this thesis a new analytical approach with $L_e = L_{e(3)}$ and $M_c \neq 0$, to calculate the end-winding inductance of non overlap winding PM machines, is presented. This calculation formula is shown to give consistently good results compared to 3D-FE analysis for a series of non overlap winding PM wind generators.

Furthermore, it is also found that the fringing flux occurring at the PM end-sections has a substantial effect on the short-circuit characteristics of the machine. It is shown that it is not valid to multiply the output performance parameters of the machine simply by a constant fringing factor as proposed in literature. A method is proposed in this study where the PM fringing flux effect is taken into account in 2D-FE analysis by reducing the PM strength by a certain factor. By means of 3D-FE it was found that for the investigated machines a PM strength reduction of about 5 % is sufficient to take the fringing effect into account. The effects of demagnetization and PM temperature on the characteristics of the PMs are also clearly indicated. Furthermore, care should also be taken with regard to the use of the correct BH-curve for the used lamination steel in the FE modelling of the machine.

Chapter 4

Slip-PMG Design

The focus of the work presented in this chapter is on the design and analysis of the slip-PMG unit as shown in Fig. 4.1. The main function of the slip-PMG unit is to transfer torque from the turbine to the PMSG unit in a dynamically stable way, which is possible due to the damping provided by the slip of this generating unit. Operation of this unit is very similar to conventional eddy-current couplings which have been in use for a long time. Due to eddy-current couplings being applied in several industrial applications, the work presented in this chapter is also applicable to the application of eddy-current couplings in general. The slip-PMG can, thus, also be referred to as a slip permanent magnet coupling (slip-PMC). In this chapter several different slip-PMG technologies are evaluated and a number of interesting novel concepts are introduced.

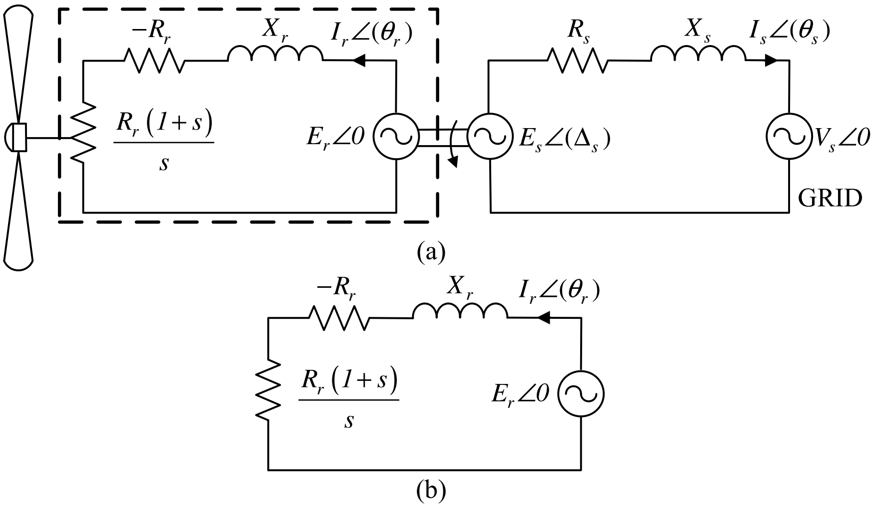

(a)

(b)

Figure 4.1: Equivalent circuit diagram of (a) the complete SS-PMG system and (b) only the slip-PMG as investigated in this chapter.

4.1 Background on Eddy-Current Couplings

Eddy-current couplings are employed in many industrial applications for power transmission [17, 139–144]. Some of the advantages of eddy current couplings due to there being no mechanical or

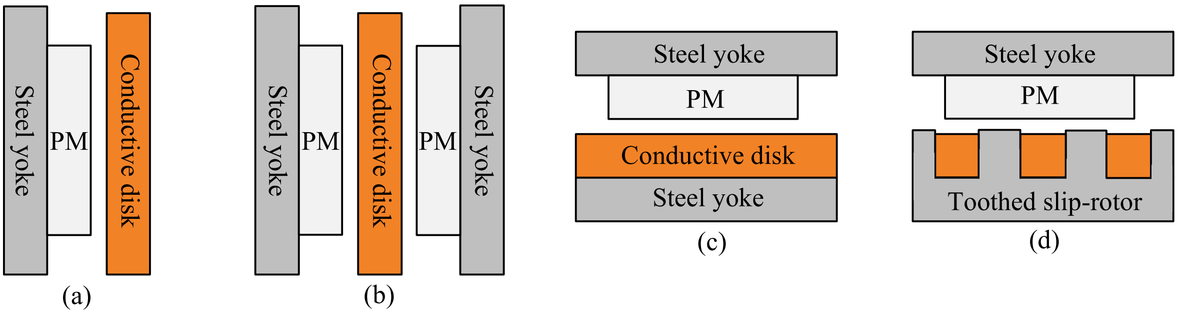

Figure 4.2: Different eddy-current coupling configurations with (a) a single sided configuration with only field member and conductive structure, (b) a double sided topology and (c) a single sided topology with a yoke provided for the conductive structure and (d) a toothed slip-PMC.

frictional contact are faster response times, increased damping of torque transients, better susceptibility to misalignment, much more isolation between loads during over-torque conditions, reduced wear, reduced maintenance and increased reliability and lifetime of components. The eddy-current coupling consists of a field member, comprising of either electromagnets as was commonly used in the past, or permanent magnets (PMs) which are more frequently used in newer applications, and a conductive disk or ring in which eddy-currents are induced. These couplings operate on the principle of slip where more eddy-currents are induced with an increase in speed which means that more power is dissipated in the conductive part of the coupling.

Typical eddy-current coupling topologies as found in literature are shown in Fig. 4.2(a) - (c). The simplest topology as shown in Fig. 4.2(a) consists of a field member and conductive disk or ring. In Fig. 4.2(b) a double rotor topology is employed and in Fig. 4.2(c) a back yoke is added to the conductive structure in order to improve the flux linking through the conducting part of the coupling. Both radial and axial flux eddy-current couplings are used, with axial flux topologies utilised in many cases, because of the ability to adjust the airgap which allows some margin of torque control. This, however, increases the mechanical complexity of the device. It is possible to obtain torque control by adjusting the field strength if electromagnets are used, but these type of couplings are not as popular any more due to their high mass and large size. In [143] it is mentioned for PM topologies that if the conducting structure is wound it is possible to add an external resistance to the winding and also achieve some margin of torque control, similar to the *"flexi-slip"* or *"opti-slip"* IG topologies of Fig. 1.4(b) in Chapter 1. Again, however, the added complexity of the windings and external resistance circuit is a question.

In general the application of eddy-current couplings are limited by their cost and mass. It is, thus, clear that significant scope exist to reduce the mass and cost of these systems. Utilising a topology as shown in Fig. 4.2(d) with a toothed layout similar to conventional electrical machines is mentioned in [143] but not investigated further. The working principle of such a coupling, referred to in this study as a slip-PMG or slip-PMC, is basically the same as that of a short-circuited PM machine and can, thus, be modelled as such. It is true that by using this type of layout the complexity of the device might increase, but due to the effective airgap being reduced it is evident that substantial potential exist to reduce the PM content, which in turn can lead to a significant reduction in material cost. It would, thus, be an insightful exercise, as done in this chapter, to investigate the feasibility of replacing the conventional eddy-current couplings with the topology in Fig. 4.2(d).

Furthermore, for the SS-PMG a major concern is the extra mass, cost and complexity of adding a second generator to the design as mentioned in Chapter 1. It is, thus, important that the slip-PMG topology selected to be interfaced with the SS-PMG has a low mass and PM content with a simple mechanical construction. Several different toothed slip-PMGs are evaluated and optimally designed by means of FE methods to the specifications of the prototype 15 kW SS-PMG wind turbine system in Appendix B. Although the final design requirements will be different, the design methodology can also be applied to the design of slip-PMC devices for overall use in industry. With a clear design criteria lacking for the slip-PMG, this aspect is addressed in this chapter by determining the most important performance constraints and to achieve the optimum design by evaluating several different slip-PMG concepts on the basis of active mass, PM content and manufacturability.

4.2 Different slip-PMG Technologies Considered

Due to the slip-PMG only transferring torque significant freedom exists in the design, which means that several different topologies can be considered. Fig. 4.3(a) and (b) show a non overlap winding single layer (SL) topology and double layer (DL) topology respectively. Non overlap windings are known to have a lower torque ripple than other machine topologies, which is important for the design of the slip-PMG as mentioned in Chapter 2. The SL winding is considered due to its simple construction. The DL winding is known to perform better than the SL winding, but the DL slip-PMG is more difficult to manufacture if solid windings are used. However, for the DL winding a slight modification is made as proposed in this study. Instead of connecting the two adjacent non overlap coils in series, each coil is short-circuited individually, which means that solid bar windings can now be used without difficulty for the DL winding as well. The same high winding factor (k_w), 10/12 pole slot combination as in Chapter 5 for the PMSG unit is considered for the slip-PMG.

To improve the torque performance of the slip-PMG a conventional 3-phase overlap cage winding as shown in Fig. 4.3(c) is investigated as well for this application. Overlap windings are known to have a large torque ripple though. An interesting observation was made with the evaluation of overlap cage winding slip-PMGs, that if the number of slots per pole are increased the torque ripple decreases accordingly. Also observed was that the current induced in each bar mimics the working of a brushless-DC machine as is shown and explained later on in this chapter. An example of such a machine structure is shown in Fig. 4.3(d).

The slot size of the brushless-DC slip-PMG as shown in the structure of Fig. 4.3(d) becomes extremely small due to the large amount of slots. The smaller the slot size becomes, the more difficult it becomes to manufacture the machine, due to the problem of adequately fixing the bars to the end-rings. The bar-end-ring connection is of utmost importance and if the contact resistance becomes too large the torque performance and efficiency of the machine are significantly reduced. For this reason the brushless-DC concept is also proposed as an axial flux machine as shown in Fig. 4.3(e). For an axial flux slip-PMG the cage can easily be manufactured as one solid piece. The solid cage can then be fixed to a solid steel disk, which acts as the slip-rotor yoke. In this case there is no contact resistance in the electrical circuit. The manufacturing of the brushless-DC slip-PMG also becomes more realistic in this case and it is possible for the specific wind generator application to utilise a large part of the construction mass as part of the active mass. However, single-rotor axial flux PM machines are known to have exceptionally large attraction forces, in this case between the PM-rotor and the slip-rotor [145].

In [17] an eddy-current coupling similar to the topologies in literature are proposed for use in the SS-PMG setup. Although the modelling of this machine is not dealt with in this particular study the results from [17] are included for comparison purposes. For the SS-PMG and in many other aplications of slip-PMCs it is important that torque is transferred smoothly. In this regard the conventional toothless eddy-current coupling should have an advantage due to it having zero torque ripple. Conventional type eddy-current couplings are also easier to manufacture than the toothed proposals as proposed in this study. However, although air cored direct drive PM wind generators have been proposed before as for example in [146–148], a known issue is the large amount of PM material required by these machine types. A prototype eddy-current coupling structure is shown in Fig. 4.3(e). For further reduction in material costs, the viability of using aluminium instead of copper as conductor material is also considered in this study.

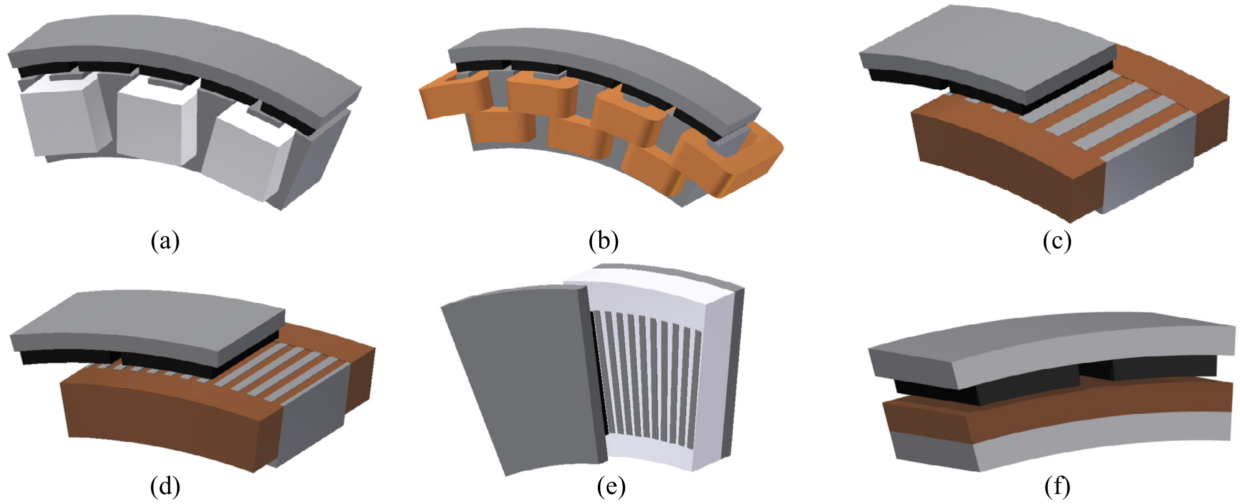

Figure 4.3: (a) SL, (b) DL non overlap, (c) 3-phase overlap, (d) radial-flux brushless-DC, (e) axial-flux brushless-DC slip-PMG configurations and (f) a conventional eddy-current coupling [17].

4.3 Slip-PMG Modelling

Two types of modelling are done for the slip-PMGs, which is combined with FE-analysis. The induced rotor bar currents of some of the slip-PMGs (DL and SL non overlap) are sinusoidal and these machines can be modelled in the dq-reference frame. However, for the brushless-DC slip-PMGs the current waveforms induced in the bars are trapezoidal or quasi-square-wave in nature as shown in Fig. 4.4(a). A flat topped DC magnitude is observed which corresponds to the magnet pitch (σ_m). Due to this flat current profile, the bar current is considered as a DC quantity during conduction which simplifies the modelling significantly.

4.3.1 DQ-Equivalent Circuit Modelling

From Fig. 4.5(a) the steady state dq-equations of the short circuited slip-PMG unit, with positive current taken as flowing out and I_{dr} and I_{qr} the steady-state dq-currents, are given by

$$0 = -R_r I_{qr} - \omega_{sle} L_{dr} I_{dr} + \omega_{sle} \lambda_{mr} \tag{4.1}$$

and

$$0 = -R_r I_{dr} + \omega_{sle} L_{qr} I_{qr} \tag{4.2}$$

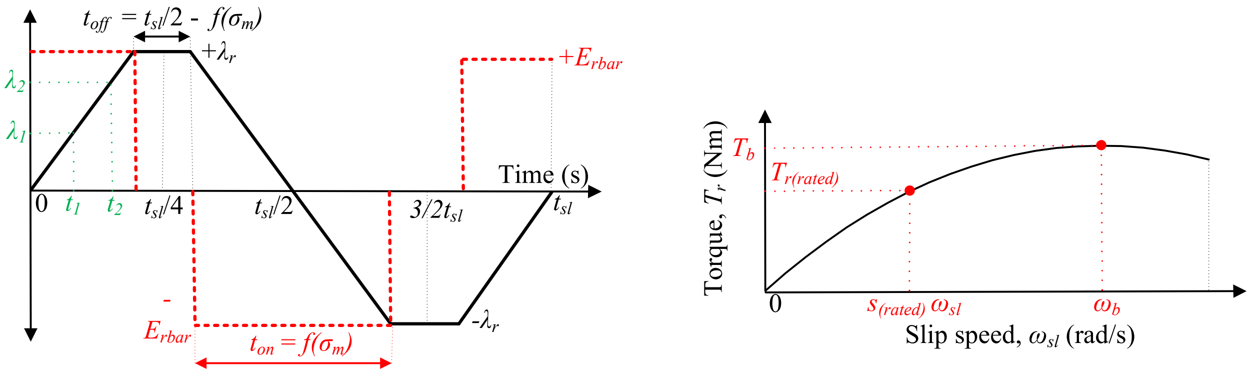

(a) (b)

Figure 4.4: (a) Typical flux linkage and voltage waveform for the brushless-DC slip-PMC and (b) typical torque versus slip curve of the slip-PMC.

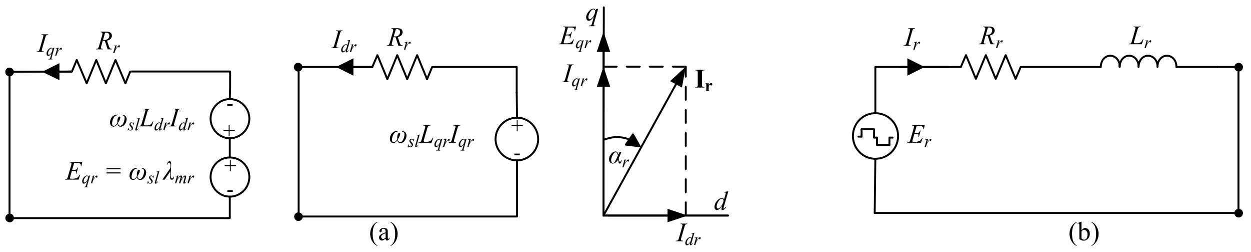

(a) (b)

Figure 4.5: (a) dq-equivalent modelling and vector diagram and (b) brushless-DC modelling used to calculate the bar currents of the slip-PMC.

respectively where ω_{sle} is the same as in Chapter 2 the electrical slip speed equal to $\omega_{sle} = \omega_{te} - \omega_s$, with ω_{te} the electrical turbine speed and $\omega_s = 2\pi f_s$, the electrical grid speed. The dq-inductances in (4.1), (4.2) and Fig. 4.5(a), with λ_{dr}, λ_{qr} and λ_{mr} indicating the dq and PM flux linkages respectively, are again as in Chapter 2 defined as

$$L_{qr} = \frac{\lambda_{qr}}{-I_{qr}} + L_{er}; \qquad L_{dr} = \frac{\lambda_{dr} - \lambda_{mr}}{-I_{dr}} + L_{er}. \tag{4.3}$$

The per phase end-winding inductance L_{er} of the slip-PMG is calculated by means of the methods in Chapter 3. The general relations of current and copper losses are given by (4.4) - (4.6) as

$$\begin{bmatrix} I_{qr} \\ I_{dr} \end{bmatrix} = \sqrt{2} I_r \begin{bmatrix} \cos\alpha_r \\ \sin\alpha_r \end{bmatrix}, \tag{4.4}$$

$$I_{qr}^2 + I_{dr}^2 = 2I_r^2, \tag{4.5}$$

and

$$I_r^2 = \frac{P_{cur}}{3R_r}, \tag{4.6}$$

with P_{cur} the copper loss, R_r the per phase bar resistance, I_r the RMS current in this case and α_r the current angle. The developed torque of the slip-PMG is expressed as

$$T_r = \frac{3}{4} p[(L_{qr} - L_{dr}) I_{dr} I_{qr} + \lambda_{mr} I_{qr}]. \tag{4.7}$$

The efficiency is given by

$$\eta_r = \frac{P_r}{P_t} = \frac{T_r(\omega_t - \omega_{sl})}{T_r\omega_t} = \frac{T_r\omega_m}{T_r\omega_t} = 1 - s \tag{4.8}$$

where P_t and P_r respectively indicates the mechanical turbine input and the output power of the slip-PMG.

Another very important parameter in the design of the slip-PMG is the breakdown torque (T_b). Fig. 4.4(b) shows a typical slip-PMG torque versus slip curve, which clearly shows the operational and breakdown torque regions. However, calculating this parameter accurately is difficult. To get an indication of the magnitude of T_b, ω_{sle} needs to be calculated where the derivative of (4.7) with respect to ω_{sle} is equal to zero. The first step is to rewrite (4.1) and (4.2) in order to have I_{dr} and I_{qr} in terms of ω_{sle}. This is also necessary for the FE-modelling method as discussed later on. This gives the following for I_{dr} and I_{qr} respectively as

$$I_{dr} = \frac{\omega_{sle}^2\lambda_{mr}L_{qr}}{R_r^2 + \omega_{sle}^2 L_{dr}L_{qr}} \tag{4.9}$$

and

$$I_{qr} = \frac{\omega_{sle}\lambda_{mr}R_r}{R_r^2 + \omega_{sle}^2 L_{dr}L_{qr}}. \tag{4.10}$$

By substituting (4.9) and (4.10) in (4.7) the following expression for T_r in terms of ω_{sle} is obtained as

$$T_r = \frac{3}{4}p\lambda_{mr}^2 R_r\left[\frac{\omega_{sle}^3(L_{qr} - L_{dr})L_{qr}}{\left(R_r^2 + \omega_{sle}^2 L_{dr}L_{qr}\right)^2} + \frac{\omega_{sle}}{\left(R_r^2 + \omega_{sle}^2 L_{dr}L_{qr}\right)}\right]. \tag{4.11}$$

However, finding the derivative of (4.11) is a complex mathematical exercise. Observing (4.7) and knowing that $L_{dr} \approx L_{qr}$ for the surface mounted PM machines considered, it can be concluded that the maximum torque is dominated by the term $\lambda_{mr}I_{qr}$. It would be much easier to find ω_{sle} where I_{qr} is at a maximum. With I_{qr} as given in (4.10)

$$0 = \frac{dI_{qr}}{d\omega_{sle}} = R_r^2 - \omega_{sle}^2 L_{dr}L_{qr} \tag{4.12}$$

and finally

$$\omega_b \approx \frac{R_r}{\sqrt{L_{dr}L_{qr}}}. \tag{4.13}$$

The value for the breakdown slip speed, ω_b, calculated in (4.13) can now be used in (4.11) to calculate T_b. It is also shown in the results of Section 6.5 in Chapter 6 that for the machines considered the torque curve has a very flat profile in the region of the breakdown torque. The calculated value of ω_b in (4.13) should, thus, be sufficient as slight variations in ω_{sle} will not influence the torque result significantly in the region of the breakdown torque.

4.3.2 Brushless-DC Modelling

If the voltage waveform is known to be square-wave in nature and the flux linkage waveform triangular and if the peak flux linkage λ_r is known (in this study it is calculated by means of FE analysis) and knowing that the peak value occurs within one quarter period of the flux linkage waveform as shown in Fig. 4.4(a) with $\Delta t = \frac{1}{4}t_{sl}$, E_r can be calculated as

$$E_r = \frac{2}{\pi}\lambda_r \omega_{sle} = K_r \omega_{sle}, \text{ with } \omega_{sle} = 2\pi f_{sl}, \tag{4.14}$$

with the armature reaction ignored and f_{sl} the electrical slip frequency and K_r the machine constant. However, for the brushless-DC machine, the voltage waveform is quasi-square wave in nature as shown in Fig. 4.4(a) which means the triangular shaped flux linkage waveform will have a flat topped quantity as is also shown in Fig. 4.4(a), which is a function of σ_m. Thus, a more accurate calculation of E_r would rather be to calculate the gradient of the flux linkage waveform ($\lambda_r(t)$) in the linear region of $\lambda_r(t)$ as

$$E_r = \frac{d\lambda_r(t)}{dt} = \frac{\Delta\lambda_r}{\Delta t}. \tag{4.15}$$

From the equivalent circuit for the brushless-DC slip-PMG as shown in Fig. 4.5(b), the induced bar current (I_{brDC}) of the machine can be calculated as

$$I_{brDC} = \frac{E_r}{R_{br}} \tag{4.16}$$

with the bar resistance, R_{br}, calculated analytically from the given slot and end-ring dimensions. With I_{brDC} known the developed torque of the brushless-DC slip-PMG can be calculated for low slip values as

$$T_r = mK_r I_{brDC} \quad \text{with} \quad m = S \times \sigma_m. \tag{4.17}$$

The variable m in (4.17) indicates the effective number of bars active at any given time instance and is given as a function of σ_m and the total number of slots (S) of the slip-rotor. For the brushless-DC machine modelling, the parameters are calculated per bar, which is the reason for using the subscript *"br"*.

Due to the current waveform of the brushless-DC slip-PMG becoming more sinusoidal in nature for higher slip values, T_b is approximated with a per phase equivalent approach. Thus, for higher slip values, with only the fundamental of the current and voltage waveforms considered the torque is given by

$$T_r = \frac{\frac{S}{p} I_r^2 R_r}{\frac{2}{p}\omega_{sle}} = \frac{2SI_r^2 R_r}{\omega_{sle}}. \tag{4.18}$$

As the machine consists of S amount of slots and p sections, the term S/p indicates the number of phases. With all sections in parallel the peak per phase voltage is the same as the voltage per bar given by (4.14). The RMS phase current can, thus, be written as

$$I_r = \frac{E_r = \frac{K_r\omega_{sle}}{\sqrt{2}}}{\sqrt{R_r^2 + (\omega_{sle}L_r)^2}} \times p = \frac{pK_r\omega_{sle}}{\sqrt{2\left(R_r^2 + (\omega_{sle}L_r)^2\right)}}. \tag{4.19}$$

By substituting (4.19) in (4.18), the machine torque is given as

$$T_r = p^2 K_r^2 R_r S \frac{\omega_{sle}}{R_r^2 + (L_r\omega_{sle})^2}. \tag{4.20}$$

To obtain the maximum torque, same as above, ω_{sle} needs to be calculated where the derivative of (4.20) is equal to zero. Thus, with

$$0 = \frac{dT_r}{d\omega_{sle}} = R_r^2 - L_r^2\omega_{sle}^2 \tag{4.21}$$

ω_b, is given as

$$\omega_b \approx \frac{R_r}{L_r}. \tag{4.22}$$

By substituting (4.22) in (4.20) T_b can finally be approximated as

$$T_b \approx \frac{K_r^2 p^2 S}{2L_r}. \tag{4.23}$$

With $K_r \propto \lambda_r$ it can be seen from (4.23) that $T_b \propto \lambda_r^2/L_r$, which clearly shows the importance of calculating the correct values for λ_r and L_r, as explained in Chapter 3, in the calculation of T_b.

4.4 FE Simulation Procedure

Due to the large amount of optimisations required for this study, it is beneficial that the solving time be reduced. Instead of using transient FE analysis that takes time, a number of non-linear static FE solutions are used in combination with the equations given above to obtain the operating state of the slip-PMG and the performance of the machine at this operating point. The performance is calculated at a specified slip point in all cases. For both the machine types analysed, i.e. with respectively dq and brushless-DC analysis, a minimum of three static FE solutions are required to simulate the performance of the machine at the specific slip operating point. Fig 5.3 shows the FE models and field plots of three of the different slip-PMG configurations, as discussed in Section 4.2.

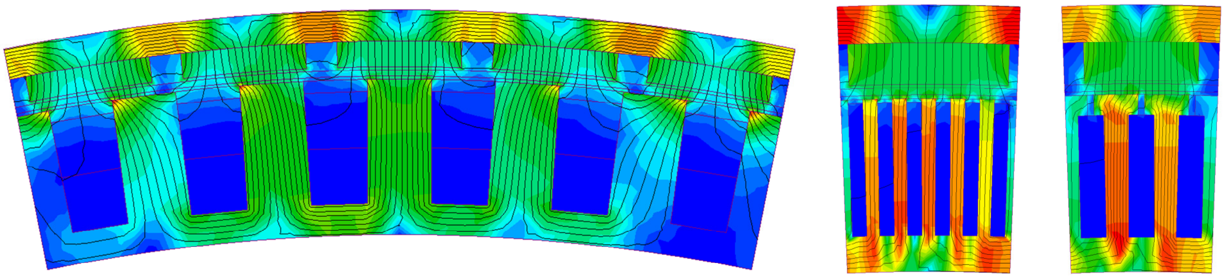

(a) (b) (c)

Figure 4.6: FE-models and field plots with (a) a DL non overlap, (b) brushless-DC and (c) overlap slip-PMG winding configuration.

4.4.1 FE Combined with *dq*-Modelling

For the slip-PMGs analysed by means of dq-equivalent circuit analysis the abc-flux linkages λ_{abc} are obtained at each static FE iteration. These flux linkages are transformed to the dq-reference frame and are then used to solve the equations in Section 4.3.1 to obtain the performance of the machine at the specified value of s.

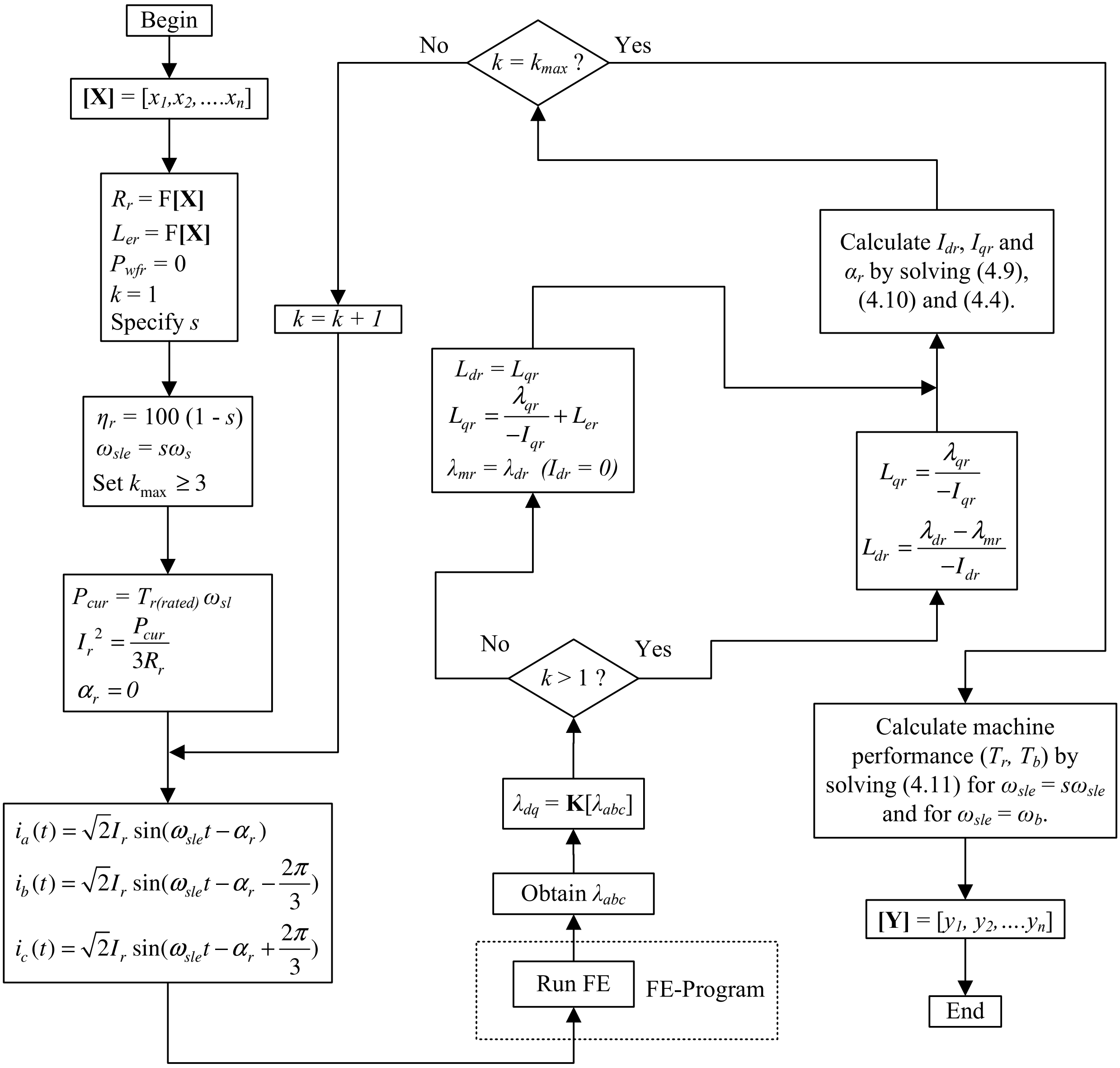

Figure 4.7: FE-modelling method described for the slip-PMG making use of dq-equivalent circuit modelling.

To calculate and evaluate the performance of the machine the following steps are used as is also described in Fig. 4.7:

1. A slip operating point is defined depending on the required efficiency, with $\eta_r = 100 \times (1 - s)$.
2. I_r is calculated from (4.6) with $P_{cur} = T_{r(rated)}\omega_{sl}$, where $T_{r(rated)} = 1000$ Nm for this particular case and with R_r calculated analytically according to the given slot dimensions.

3. With the current known α_r is set to zero and the three phase currents can then be written as

$$\begin{aligned} i_a(t) &= \sqrt{2}I_r sin(\omega_{sle}t - \alpha_r); \\ i_b(t) &= \sqrt{2}I_r sin(\omega_{sle}t - \alpha_r - \frac{2\pi}{3}); \\ i_c(t) &= \sqrt{2}I_r sin(\omega_{sle}t - \alpha_r + \frac{2\pi}{3}); \end{aligned} \tag{4.24}$$

   after which a first FE-iteration is run with the above current values as input.

4. λ_{dq} can be calculated from this first FE iteration, i.e. by transforming the FE-calculated phase flux linkages (λ_{abc}) to dq-parameters using Park's transformation. In this way the effect of the q-axis current, I_{qr}, on λ_{mr} is taken into account with $\alpha_r = 0$ and $I_{dr} = 0$, $\lambda_{mr} = \lambda_{dr}$.

5. Also at this first iteration it is assumed that $L_{dr} = L_{qr}$ with L_{qr} calculated as in (4.3) with $I_{qr} = \sqrt{2}I_r$ in this case. The end-winding inductance L_{er} can be calculated analytically as mentioned.

6. With the dq-inductances and λ_{mr} known I_{dr} and I_{qr} can now be calculated from (4.9) and (4.10) and α_r from (4.4).

7. With a new value for α_r known another static FE iteration is run with I_r and α_r again substituted in (4.24).

8. New values for L_{dr} and L_{qr} according to (4.3) are now calculated from the dq flux linkages with $L_{dr} \neq L_{qr}$ and λ_{mr} as calculated in the first iteration. A new more accurate value for α_r can be calculated as in point 6 above.

9. This new, more accurate value of α_r is then used in a third static FE iteration at which point the performance of the machine is evaluated by solving 4.11 for $\omega_{sle} = s\omega_s$, to obtain the operating point average torque and T_b with $\omega_{sle} = \omega_b$, with ω_b as calculated in 4.13.

10. For better accuracy more static FE iterations can be run, but a minimum of three static FE solutions are required.

4.4.2 FE Combined with Brushless-DC Modelling

The FE-modelling procedure of the brushless-DC slip-PMGs is less complicated than the dq-equivalent circuit modelling as shown in Fig. 4.8. From Fig. 4.8 the FE-modelling procedure to calculate and evaluate the performance of the brushless-DC slip-PMGs are discussed as below:

1. As for the dq-equivalent circuit modelling explained above a slip operating point is defined depending on the required efficiency, with $\eta_r = 100 \times (1 - s)$.

2. A first FE-iteration is run with the rotor angle set to $\theta_m = 0$ and with $I_{brDC} = 0$ and λ_1 is obtained as in Fig. 4.4(a).

3. A second FE-iteration is run with $\theta_m = \theta_p/4$ and $I_{brDC} = 0$ with θ_p the pole pitch angle and λ_2 is calculated as in Fig. 4.4(a).

4. E_{br} can now be calculated from (4.15) with $\Delta\lambda = \lambda_2 - \lambda_1$ and $\Delta t = (\theta_{m2} - \theta_{m1})/\omega_{slm}$, K_r from (4.14), I_{brDC} from 4.16 and T_r from 4.17, with R_{br} again from the given bar dimensions.

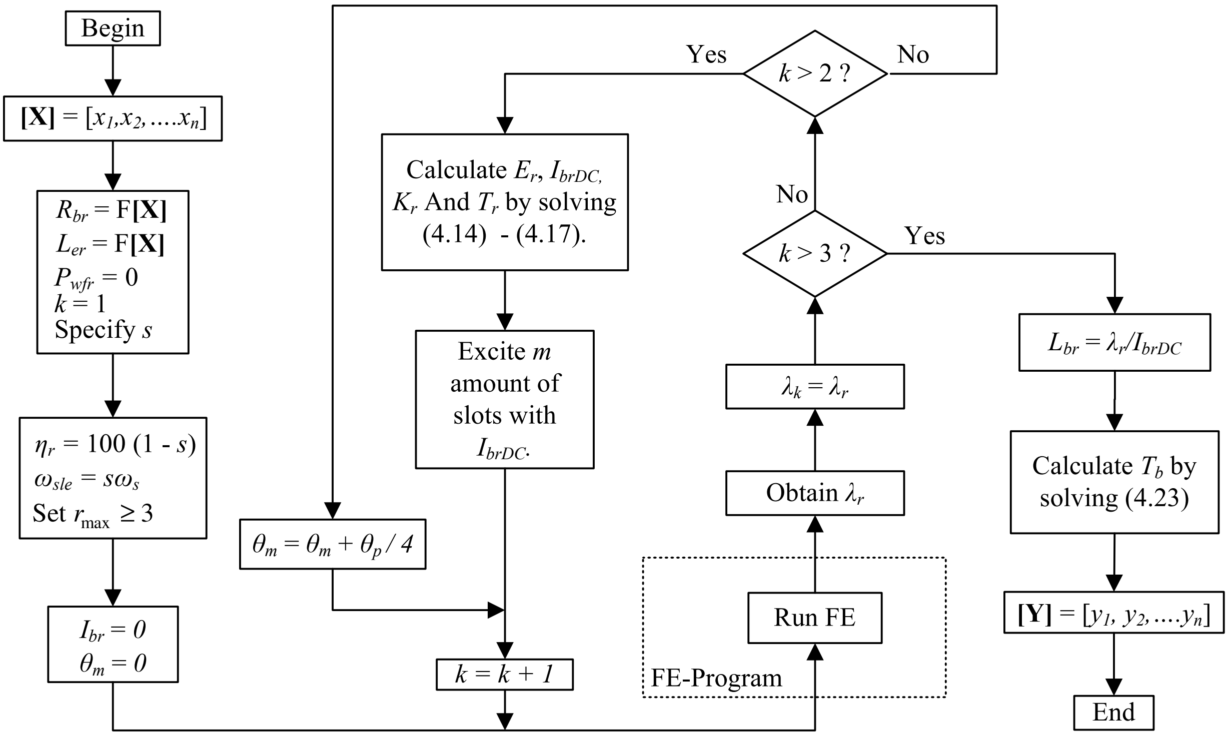

Figure 4.8: FE-modelling method described for the slip-PMG making use of brushless-DC modelling.

5. To calculate L_{br}, m amount of slots are excited with the rated bar current and a third FE-iteration is run. From the resulting value of λ_r obtained the bar inductance can be calculated as

$$L_{br} = \frac{\lambda_r}{I_{brDC}} + L_{er} \tag{4.25}$$

with L_{er} again calculated by means of the methods in Chapter 3 and referred to a per bar quantity in this case.

6. With L_{br} known T_b can be calculated from (4.23).

4.5 Design Optimisation

The design optimisation is done by means of the *Visual Doc* optimisation suite [149]. From the different optimisation algorithms available in *Visual Doc*, the gradient based, modified method of feasible direction (MMFD) is selected. This method is shown to consistently give the best results in the shortest amount of time for this particular study.

4.5.1 Optimisation Constraints and Methodology

All of the machine structures discussed in Section 4.2 are optimised subject to certain design constraints from the specific 15 kW SS-PMG wind turbine system in Appendix B for minimum active and PM mass. The physical design constraints are given in Table 4.1. The rated torque, $T_{r(rated)}$, corresponds to the torque value on the turbine curve at the rated power and speed as given in Table 4.1. For stable operation and to adequately brake the generator in high wind speeds it is

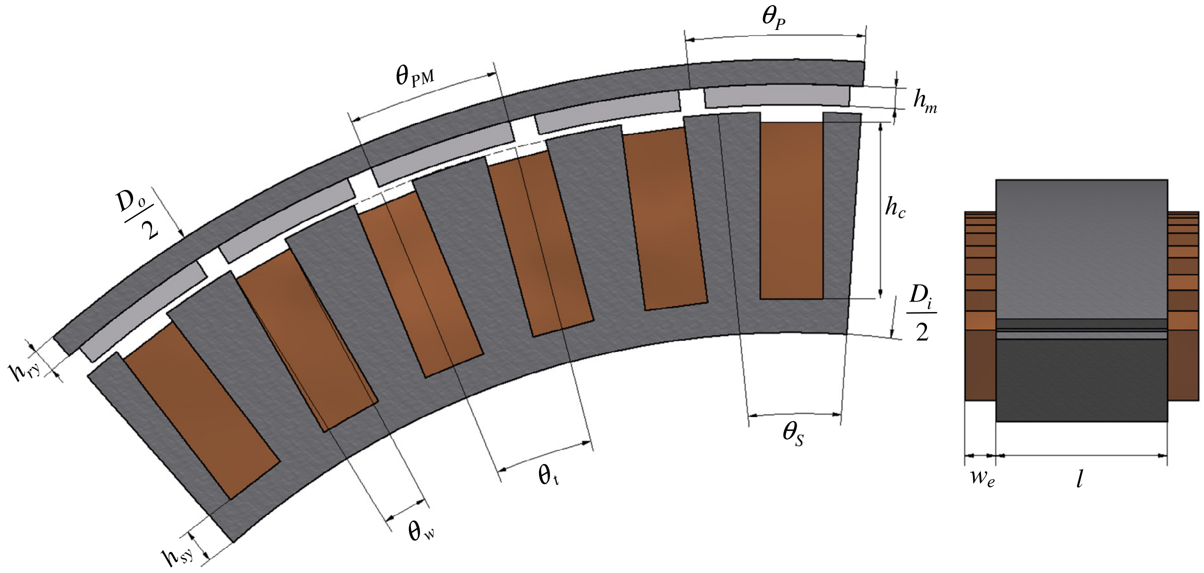

Figure 4.9: Optimisation parameters of the slip-PMG unit.

found from previous practical experience that the maximum breakdown torque should be defined as $T_b \geq 2$ pu. With efficiency deemed important in this case, for each of the optimised slip-PMGs the rated slip is specified as $s = 0.03$ pu which corresponds to an efficiency from (4.8) of 97 %. With the efficiency of the PMSG unit given in Chapter 5 as 94 %, the total system efficiency is just over 91 %, which compares well with other wind turbine drive train topologies currently in use. In order to allow for stable operation of the directly grid-connected SS-PMG, as discussed in Chapter 2 a no-load cogging torque of $\Delta\tau_{NL} < 2.5$ % is specified and a load torque ripple of $\Delta\tau_L < 4$ %. Also important to consider is the demagnetization of the PMs, due to the fact that the slip-PMG is basically a short circuited PM generator as discussed in Chapter 3. In many cases for the design of eddy-current couplings in general it is important to also consider the temperature of the machine which means the current density should be kept within certain limits. In this case due to the use of only air cooling it is limited at $J_r \leq 4$ A/mm^2. Furthermore, as there is no specification regarding f_{sl} in this case, and due to the value of f_{sl} being so low under normal operating conditions, the number of poles are selected as $p = 80$ to reduce the yoke heights, and to further decrease the mass of the slip-PMG.

Fig. 4.9 gives the optimisation parameters used in **[X]** with **Y** = **F[X]** where

$$\mathbf{X} = \begin{bmatrix} x_1 \\ x_2 \\ x_3 \\ x_4 \\ x_5 \\ x_6 \\ x_7 \\ x_8 \\ x_9 \end{bmatrix} = \begin{bmatrix} l \\ h_c \\ h_m \\ h_{ry} \\ h_{sy} \\ w_e \\ \sigma_w \\ \sigma_m \\ \sigma_t \end{bmatrix} ; \quad \mathbf{Y} = \begin{bmatrix} y_1 \\ y_2 \\ y_3 \\ y_4 \\ y_5 \\ y_6 \end{bmatrix} = \begin{bmatrix} M_{Tot} \\ M_{PM} \\ T_{ave} \\ T_b \\ \Delta\tau_{NL} \\ \Delta\tau_L \end{bmatrix} . \tag{4.26}$$

In (4.26) h_{ry} and h_{sy} indicate the PM-rotor and slip-rotor yoke heights respectively and w_e the end-ring width. With the magnet pitch to pole pitch ratio σ_m, slot pitch to average slot pitch ratio

Table 4.1: Design constraints of the slip-PMG.

Parameter	Value
Rated torque, $T_{r(rated)}$, Nm	1000
Rated slip, $s_{(rated)}$, pu	0.03
Breakdown torque, T_b, pu	≥ 2.0
No load torque ripple, $\Delta\tau_{NL}$, %	≤ 2.5
Full load torque ripple, $\Delta\tau_L$, %	≤ 4.0
Current density, J_r, A/mm^2	≤ 4.0
Number of poles, p	80
Maximum outer diameter, D_o, mm	655

σ_t and slot width to average slot pitch ratio σ_w defined as

$$\sigma_m = \frac{\theta_{PM}}{\theta_p}; \qquad \sigma_t = \frac{\theta_t}{\theta_S}; \qquad \sigma_w = \frac{\theta_w}{\theta_S} \tag{4.27}$$

where

$$\theta_S = \frac{2\pi}{S} \quad \text{and} \quad \theta_p = \frac{2\pi}{p} \tag{4.28}$$

where θ_{PM} is the magnet pitch, θ_t the slot pitch and θ_w the slot width pitch, with θ_S the average slot pitch.

4.5.2 Optimisation Results

Table 4.2 gives the optimisation results for the non overlap SL and DL slip-PMGs and Table 4.3 for the overlap cage winding and radial and axial flux brushless-DC slip-PMGs. In order to compare these results with that of conventional eddy-current couplings the optimisation results obtained in [17] for the same design specifications as in this study are also given in Table 4.2. The two dimensions given are the axial stack length (l) and the inside diameter (D_i) of the machine. The mass quantities shown are the PM mass (M_{PM}), conductor mass (M_C), steel mass (M_{Fe}) and the total active mass (M_{Tot}). The different slip-PMG configurations are also evaluated regarding complexity and ease of manufacturing. Fig. 4.10 shows a visual comparison of the results given in Tables 4.2 and 4.3.

For the results shown in Table 4.3 the optimisation is done subject to a constraint on the maximum allowable value of M_{PM} at about 3.5 kg. For the non overlap winding machines the value of M_{PM} shown is for the minimum achievable value of PM mass while the design still complies with the limits set in Section 4.5.1. The relationship between M_{Tot} and M_{PM} are shown in Fig. 4.11. In Fig. 4.11 the upper allowed limit for the PM mass is gradually reduced until the design no longer complies with the limits set in Section 4.5.1. For all the design cases except for the conventional eddy-current coupling the machines are optimised for both copper and aluminium used as conductor. In [17] aluminium was not considered as a conductor as the amount of PM material required for the specific application becomes too high.

From Tables 4.2 and 4.3 it is clear that the brushless-DC slip-PMG configurations yields a much lower active mass and lower PM content due to the much better torque performance of these winding types. This is especially true for the axial flux machine where for this particular application certain parts of the construction mass and active mass can be combined as mentioned. It is also clearly

Table 4.2: Optimisation results and comparison of the conventional eddy-current coupling (ECC) and SL and DL non overlap slip-PMGs.

	ECC [17]	**Non overlap-SL**		**Non overlap-DL**	
	Cu	Al	Cu	Al	Cu
T_b, pu	8.00	2.00	2.02	2.01	2.11
$\Delta\tau_{NL}$, %	0.00	2.54	1.43	1.65	1.94
$\Delta\tau_L$, %	0.00	3.12	3.91	1.18	1.82
l, mm	123.8	131.8	124.7	107.1	90.50
D_i, mm	564.5	579.0	593.0	562.0	578.0
M_{PM}, kg	**24.0**	**5.57**	**5.08**	**5.62**	**4.48**
M_{cond}, kg	14.0	12.2	21.5	12.5	23.2
M_{Fe}, kg	27.3	43.0	34.5	38.3	33.1
M_{Tot}, kg	**65.3**	**60.7**	**61.1**	**56.3**	**60.8**

Eddy-current coupling (ECC): Very simple construction. Zero torque ripple. Better susceptibility to misalignment. High mass and very high PM content.

SL non overlap: Simple construction. Easy use of aluminium. No contact resistance. High mass and PM content. Long stack length might be a problem.

DL non overlap: Easy construction. Easy use of aluminium. No contact resistance. High mass and PM content, but lower than SL.

seen that the slip-PMG topologies evaluated in this study use a considerable less amount of PM material as opposed to conventional eddy-current couplings. Depending on the topology used the active mass can also be reduced substantially.

Furthermore, surprisingly it is seen that by using aluminium instead of copper as conductor material the performance regarding active mass and PM content is not that much different. The aluminium machines also have a much lower value for M_C and it should be noted that aluminium is significantly cheaper than copper. It is true that the aluminium machines have a higher value for M_{Fe}, but steel is even cheaper than aluminium. Thus, for the same PM mass the aluminium machines are much cheaper per mass unit than the copper machines. An advantage of the copper machines, however, is that a slightly lower PM mass can be specified as shown in Fig. 4.11. The copper machines yield a lower minimum PM mass due to the fact that the aluminium machines have a larger steel volume which increases the per phase inductance which in turn influences the value of the maximum torque. This phenomenon is illustrated in Fig. 4.12, where it is shown how T_b is decreased with a decrease in D_i, which in turn increases h_c. However, if h_c is decreased to obtain the required magnitude of T_b, l needs to be increased to again obtain the required performance of the machine at the rated operating point. This explains the longer stack length of especially the SL non overlap winding slip-PMG.

Furthermore, also important to consider in the design optimisation is the end-ring width, with w_e not dependent on w_c as is the case for wound electrical machines. Fig. 4.13(a) and (b) show the variation in torque performance and conductor mass respectively for a per unit variation in w_e with the base value w_c for both the copper and aluminium overlap winding slip-PMGs. It is clearly shown that although copper is volumetrically a better conductor aluminium is a better conductor per mass unit, which clearly motivates the use of aluminium for high volume electrical machine applications such as the direct-drive wind generator application in this case.

Table 4.3: Optimisation results of the 3-phase overlap and brushless-DC slip-PMGs.

	Overlap 3-phase		**Brushless-DC radial flux**		**Brushless-DC axial flux**	
	Al	Cu	Al	Cu	Al	Cu
T_b, pu	2.02	2.02	2.03	2.40	2.10	2.39
$\Delta\tau_{NL}$, %	5.56	3.76	1.64	1.97	1.33	0.93
$\Delta\tau_L$, %	**10.78**	**9.94**	0.44	0.71	2.28	2.61
l, mm	82.0	66.5	62.5	55.0	55.5	44.6
D_i, mm	565.0	577.0	570.0	580.6	490.0	533.2
$\boldsymbol{M_{PM}}$, **kg**	**3.53**	**3.43**	**3.53**	**3.51**	**3.62**	**3.49**
M_{cond}, kg	8.99	17.05	7.22	12.38	10.16	16.34
M_{Fe}, kg	28.18	20.14	22.25	15.98	14.97	6.97
$\boldsymbol{M_{Tot}}$, **kg**	**40.70**	**40.62**	**33.0**	**31.87**	**28.76**	**26.80**

Overlap 3-phase Moderate to difficult construction. Depending on machine size aluminium casting is possible. Contact resistance is a problem if not casted. Medium to low mass and low PM content. High torque ripple.

Brushless-DC-radial Very difficult construction. Aluminium use might be difficult. Contact resistance is a problem. Low mass and PM content. Low torque ripple.

Brushless-DC-axial Moderate to easy construction. Easy use of aluminium. No contact resistance. Low torque ripple. Very low mass and PM content. Large attraction forces.

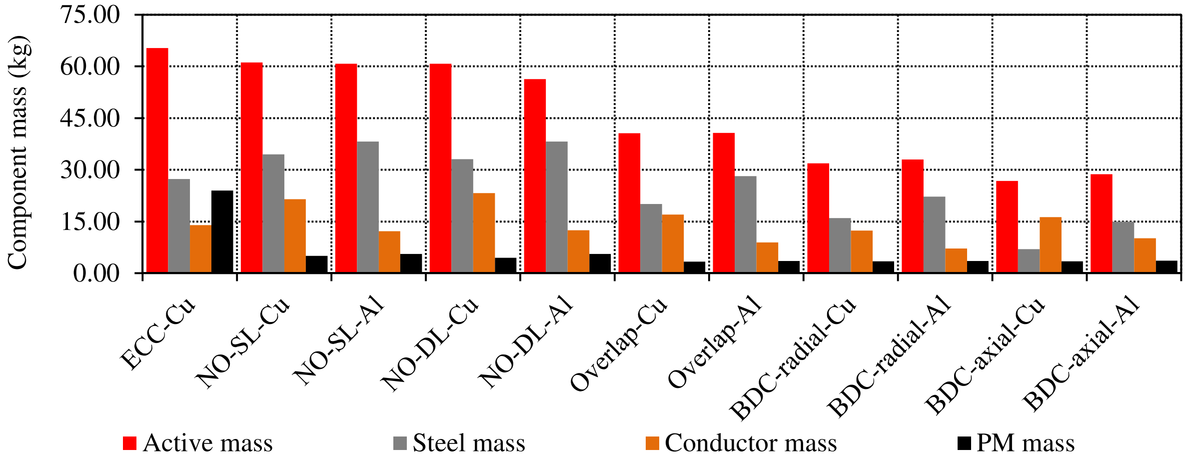

Figure 4.10: Comparison of the different active mass components for the different slip-PMG configurations.

Fig. 4.14(a) show the variation in per unit load torque ripple and average torque for a variation in σ_m for the overlap winding slip-PMG and Fig. 4.14(b) for the non overlap DL slip-PMG. It is clear that the non overlap winding slip-PMG have a far lower torque ripple than the overlap winding slip-PMG. Fig. 4.15(a) show the effect of increasing the number of slots per pole on the torque ripple of the brushless-DC slip-PMG. Clearly a significant reduction in torque ripple is observed. However,

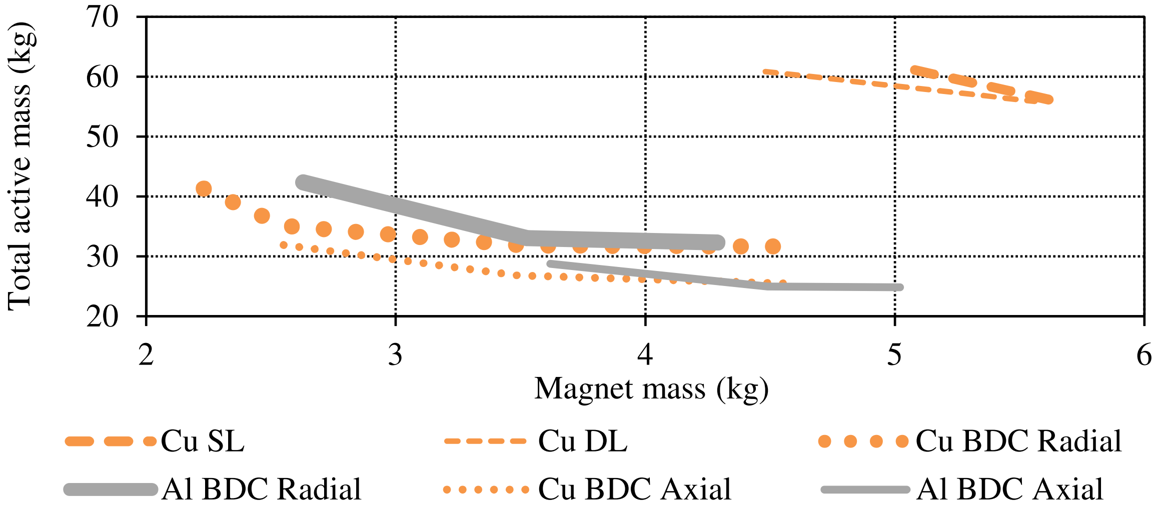

Figure 4.11: Active mass versus PM mass for the non overlap SL and DL and the brushless-DC (BDC) radial flux and axial flux slip-PMGs.

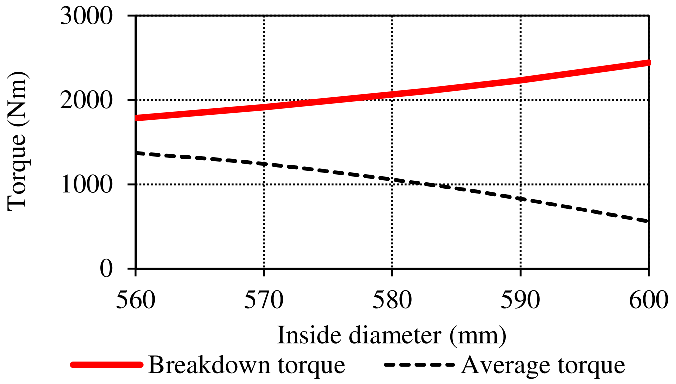

Figure 4.12: Average and breakdown torque versus inside diameter for the optimum SL-slip-PMG with an aluminium winding.

it is clearly shown in Fig. 4.15(b) that the slot width becomes incredibly small which increases the manufacturing complexity of the machine.

As mentioned, in this study the slip-PMG forms part of a small-scale wind turbine system as discussed in Appendix B. For the 15 kW SS-PMG wind turbine system the total tower top mass without the slip-PMG is about 500 kg. A construction mass of about 40 kg needs to be added for all the slip-PMG topologies as only the active mass is shown. The total system mass can be estimated as $M_{Top} = 540 + M_{Tot}$ kg where M_{Tot} is the optimised active mass for each topology shown in Tables 4.2 and 4.3. Thus, depending on the topology used the p.u. increase in total system mass by adding the slip-PMG to the system varies between 1.12 pu and 1.2 pu.

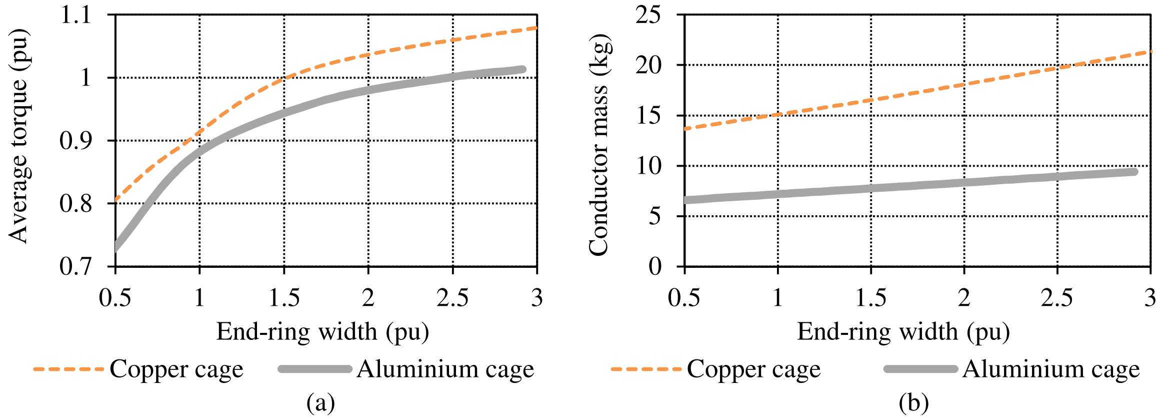

Figure 4.13: Variation in (a) per unit average torque and (b) conductor mass versus end-ring width for the optimum copper and aluminium overlap cage winding slip-PMGs.

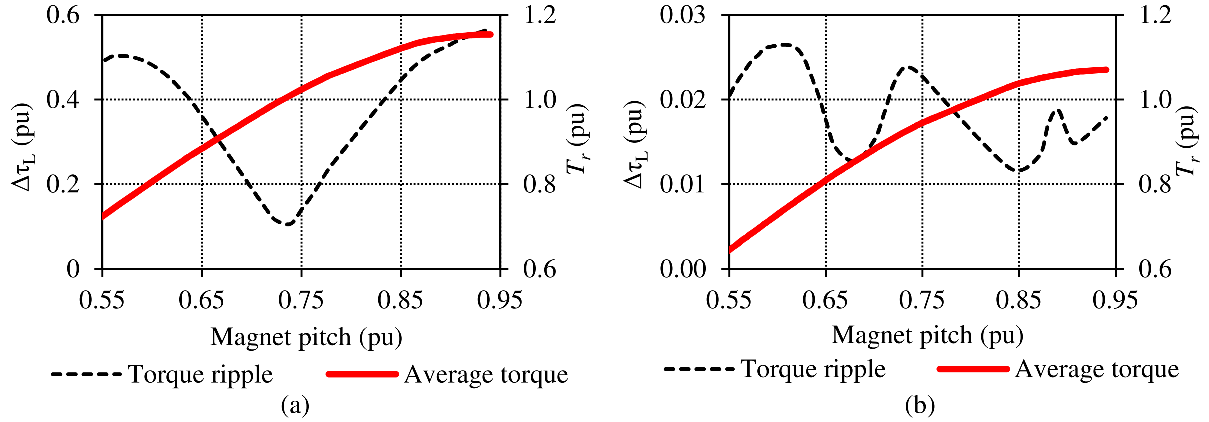

Figure 4.14: Per unit load torque ripple and average torque versus magnet pitch to pole pitch ratio for (a) overlap and (b) non overlap DL winding slip-PMGs.

4.6 Prototype machine Evaluation

Fig. 4.16(a) and (b) show the FE calculated flux linkage and induced bar voltage respectively for the brushless-DC slip-PMG at rated slip. Fig. 4.17(a) show the sinusoidally induced current per bar coil of the SL slip-PMG and the quasi-square current waveform of the brushless-DC slip-PMG calculated by means of FE. Fig. 4.17(b) show the bar current of the brushless-DC slip-PMG at the point where the maximum torque occurs with $s = s_b$. It is clearly seen that the current waveform of the brushless-DC slip-PMG becomes more sinusoidal with an increase in load.

Taking mass, PM content and manufacturability into account the overlap winding slip-PMG seems to be the best candidate for further prototype development. To limit the problem of contact resistance, which is especially a problem for aluminium connections it is proposed that the cage winding is cast. However, as seen in Table 4.3 the overlap winding slip-PMG have a large torque ripple, which is problematic due to minimum torque ripple being especially important for this specific application. Several methods are proposed in literature to minimise the no load cogging torque and load torque ripple. These techniques include skewing the magnets and stator slots, varying the

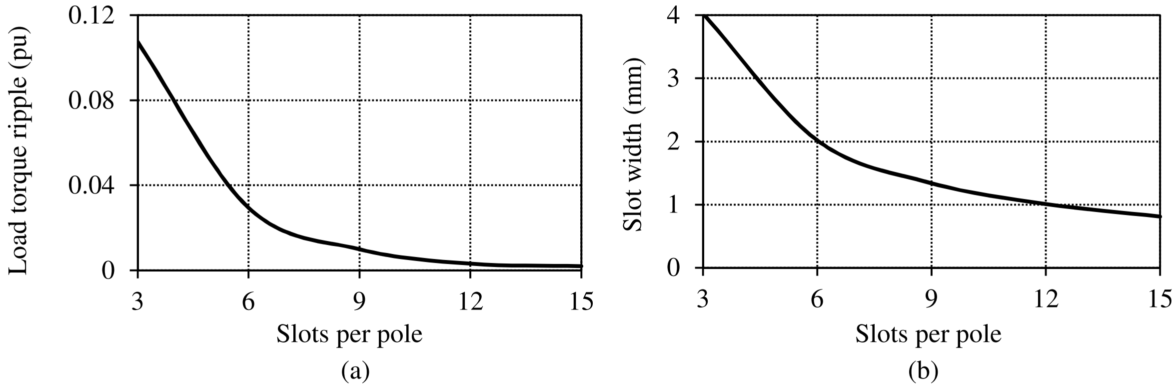

(a) (b)

Figure 4.15: (a) Per unit load torque ripple and (b) slot width (w_c) versus number of slots per pole for a brushless-DC type slip-PMG.

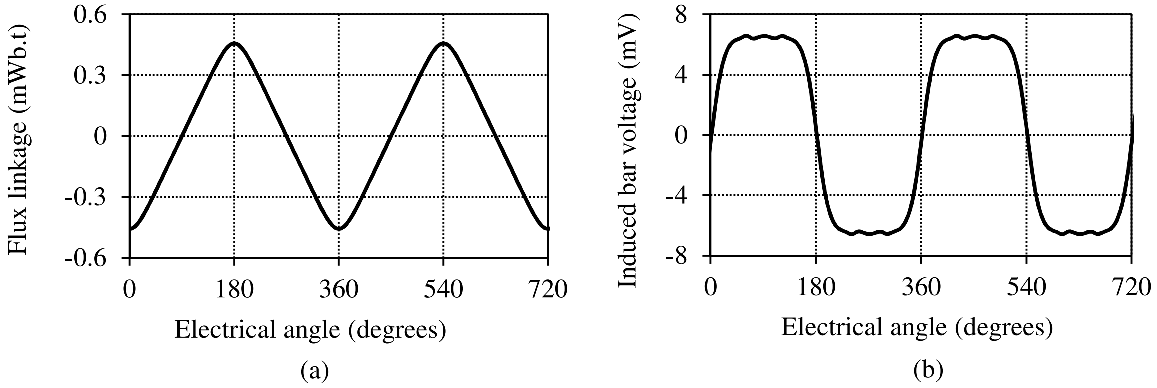

(a) (b)

Figure 4.16: (a) FE calculated flux linkage and (b) induced bar voltage of the brushless-DC slip-PMG versus electrical angle.

magnet positions, closing the slip-rotor slots, and introducing auxiliary slots and teeth [150–158]. As seen in [11], where an in depth study is done on the effects caused by parameter variations on the torque ripple magnitude, and as is also mentioned in [153] and [158] manufacturing and assembling tolerances can significantly influence the torque ripple of the machine with even slight variations causing a significant increase in the torque ripple magnitude. Also many of the techniques proposed, increase the constructional complexity, of the electrical machine.

Due to skewing being a concept which have been extensively employed in PM electrical machine design, this concept is further investigated for the overlap winding slip-PMG. In order to limit the increase in machine complexity, a special skewed PM concept is proposed. The magnet is made flat and not curved to ease manufacturing. Furthermore, the form of the magnet is such that it is skewed but still remains a solid a magnet as shown in Fig. 4.18(a). This is possible, because of the small value of θ_p in this case. Also in this case the lamination stack is modified to accommodate this skewed PM, without any significant reduction in performance. Fig. 4.19(a) show the reduction in torque ripple versus magnet skew segments. From Fig. 4.19(a) it is seen that it is sufficient to only use 3 skewing segments.

However, as mentioned in Chapter 2 also important to consider is the fundamental torque ripple frequency. For the unskewed case the fundamental component is identified at $n = 6$, and for two

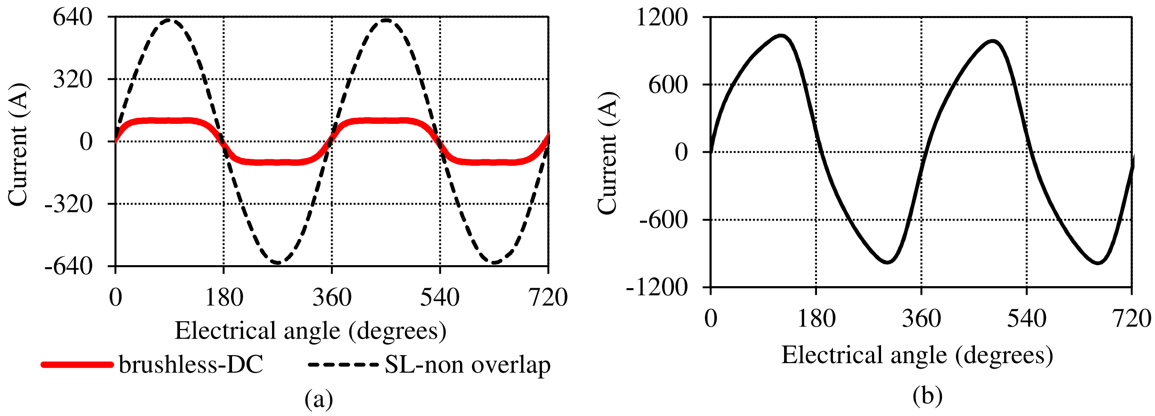

Figure 4.17: (a) FE calculated rated bar current of the SL-non overlap and brushless-DC slip-PMGs and (b) bar current of brushless-DC slip-PMG at $s = s_b$ versus electrical angle.

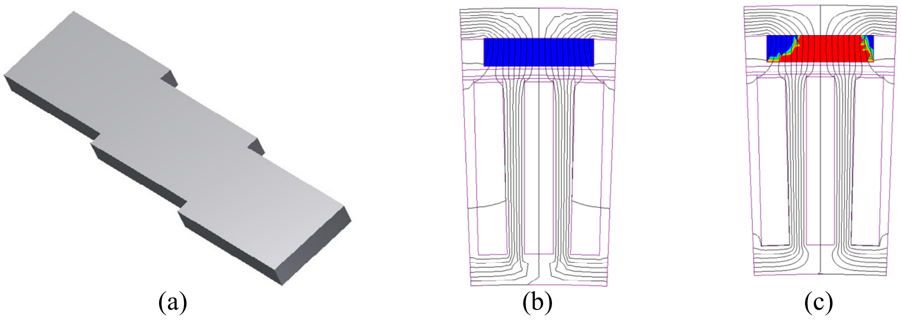

Figure 4.18: (a) Skewed PM proposal; and FE predicted demagnetization states of the overlap winding slip-PMG at (b) a magnet temperature of 100 °C and (c) at 160 °C.

skewing segments $n = 12$, and for three $n = 18$, as can be seen for the waveforms of the machine with different skewing segments in Fig. 4.19(b). Thus, due to p being double the value specified for the case study slip-PMGs in Chapter 2, for $n > 3$ the torque ripple disturbance will go through resonance. From the results in Chapter 2 the attenuation is calculated at $A_t = 6.6$ in the resonance area. Factoring this into the calculation of $\Delta\tau_L$ the resulting value is still far lower than that for the unskewed case and still below the limits set in Section 4.5.1. The torque quality of the prototype slip-PMG, thus, still seems to be sufficient for the current application. Furthermore, as stated in [10] the generator needs to comply with the power quality specifications given, from 0.2 pu generator load. Thus, for the case with $n = 18$ and $p = 80$ the torque ripple disturbance will go through resonance at around 0.2 pu load. If more than three skewing segments are utilised the resonance area will be shifted even further below the operating range of the slip-PMG.

With demagnetization more of a concern for lower values of h_m, as shown in Chapter 3, such as is the case for the overlap winding slip-PMG with $h_m = 4.5$ mm as opposed to $h_m = 6$ mm for the brushless-DC slip-PMG and $h_m = 8$ mm for the non-overlap winding slip-PMGs. In Fig. 4.18(b) the regions of demagnetisation is calculated for T_m set as 100 °C and 160 °C. It is observed that with the maximum short-circuit current flowing in the bars only after about 100 °C serious demagnetization effects starts occurring as indicated by the red area in Fig. 4.18(c) predicted by FE-analysis.

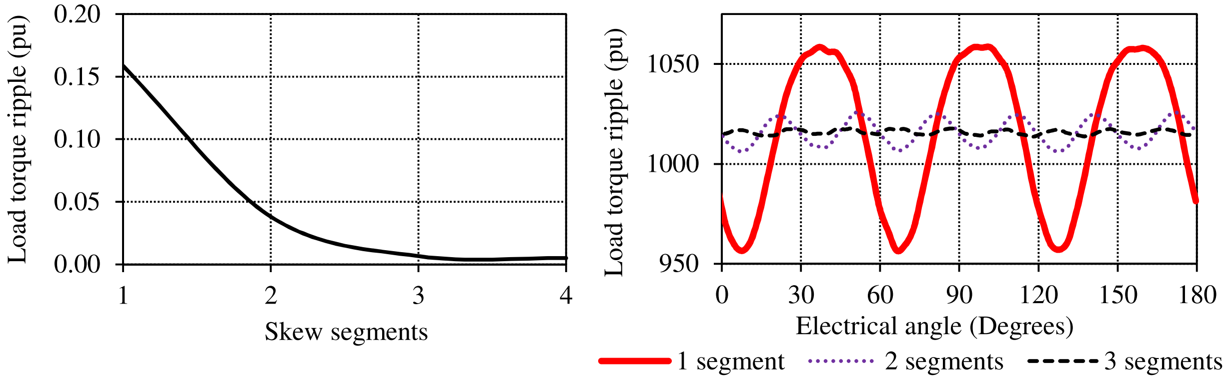

(a) (b)

Figure 4.19: Load torque ripple versus (a) PM skew increments and (b) versus electrical angle for the three skewing cases, for the optimum aluminium overlap winding slip-PMG.

4.7 Summary

In this chapter it is shown that the active mass (especially the PM mass) and, thus, the material cost of a slip-PMG can be reduced substantially compared to conventional eddy current couplings. For the SS-PMG wind turbine application considered the total increase in system mass is estimated at about 12 to 20 % if a slip-PMG is used to transfer the turbine torque as opposed to a same size direct-drive PM generator.

Several new slip-PMG topologies are introduced and evaluated in this study. For the novel brushless-DC winding slip-PMG an even further reduction in active and PM mass compared to the non overlap winding configurations are possible. Manufacturing, especially regarding the fixing of the bars to the end-rings, poses a significant challenge for the brushless-DC slip-PMG though. Other brushless-DC concepts such as the axial-flux configurations are evaluated to reduce the complexity of fixing the bars to the end-rings. The active mass of the axial flux machine is considerably lower due to the fact that some of the construction and active mass components of the machine can be integrated. However, the large attraction forces associated with this machine is a problem. The conventional 3-phase overlap winding also shows promising results for active mass reduction, with the torque ripple problem overcome by utilising a simple flat skewed PM topology.

Furthermore, surprisingly it is shown that aluminium can be used instead of copper without increasing the mass of the slip-PMG or by decreasing the machine performance. The use of aluminium has the potential to further reduce the cost of the coupling. Construction wise the conventional eddy-current couplings should be easier to manufacture. Alignment and airgap integrity is also less of an issue in this case, with the torque quality of these topologies much better than that of the other slip-PMGs. It is shown, however, that with careful design and parameter selections the torque ripple amplitude and frequency of the other topologies can be designed to comply to the specifications given.

Chapter 5

PMSG Design

In this chapter the focus shifts to the optimum design of the directly grid-connected PMSG unit of the SS-PMG as shown in Fig. 5.1. Due to the direct grid connection there are clear differences in the design requirements of this machine and those of conventional PM wind generators connected to the grid via a converter. Adequate knowledge is, thus, required on the definition of these design requirements which should be obtained from the relevant grid code specifications. Thus, in this chapter different PM generator topologies are evaluated with regard to ease of manufacturing, active mass, PM content and suitability for direct grid connection.

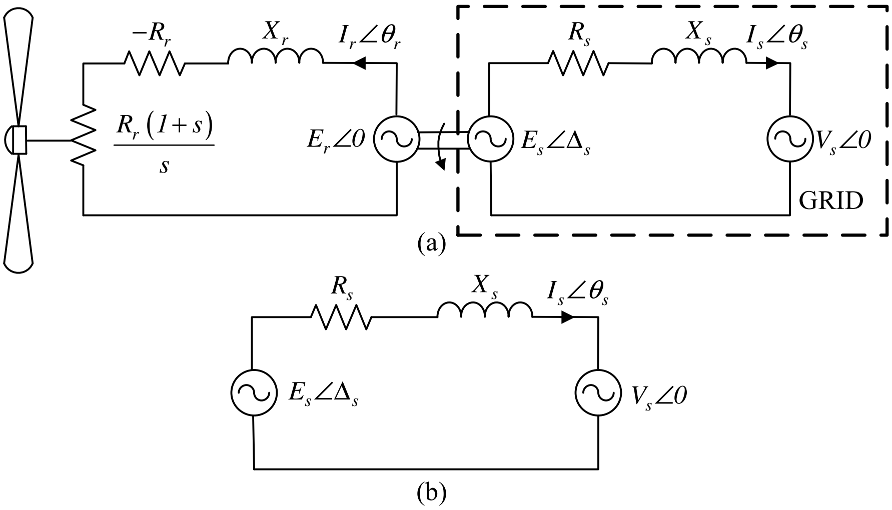

Figure 5.1: Equivalent circuit diagram of (a) the complete SS-PMG system and (b) only the PMSG as used in this chapter.

5.1 Design Specifications

The design aspects of the directly grid connected SS-PMG are assessed in two parts in this section. First the relevant grid code specifications are summarised and secondly the requirements for the specific turbine system and direct-drive wind generators in general are discussed. Furthermore, the whole aim of the SS-PMG is to have an as simple and robust as possible wind generator system. This design methodology is, thus, applied throughout the whole generator design process.

5.1.1 Direct Grid Specifications

For this study the local applicable grid-codes and regulations for wind turbine facilities are used as a basis to obtain the design specifications of the generator as stipulated in [10], [159] and [160]. As mentioned, the grid synchronisation of the SS-PMG is covered in [81], reactive power compensation techniques for utility scale systems is discussed in [83] and LVRT capabilities in [82] and Chapter 2. The systems as mentioned above are responsible for the implementation of the grid code requirements. However, it is still necessary that the generator design complies with many of the aspects listed below:

- From 0.2 pu generator load the power factor (PF) should not be less than 0.95 leading or lagging for systems $<$ 1 MVA, 0.975 leading or lagging for systems $>$ 1 MVA and $<$ 20 MVA and 0.95 leading or lagging for systems $>$ 20 MVA.
- For systems $>$ 1 MVA, reactive power and voltage control are required at the point of common coupling (PCC) as specified by the utility and as in [10]. This is not a requirement for systems $<$ 1 MVA.
- Reactive power and voltage should be controlled with a tolerance of 0.5 % of the rated power.
- The system needs to be able to operate in a voltage range of ±10 % around the nominal voltage for wind energy facilities $>$ 100 kVA, and between +10 % and -15 % for systems $<$ 100 kVA at the PCC continuously.
- The system should stay connected to the grid during low voltage and over voltage conditions as stipulated by the regimes shown in [10] and also evaluated in Chapter 2.
- In some cases active power control is needed, especially during grid frequency variations, to reduce the power delivered to the grid.
- Frequency variations between 47 Hz and 52 Hz at a rate of change of 1.5 Hz/s needs to be accommodated by the wind generator system.
- The quality of the power delivered should comply to the limits set in [159]. Individual levels are provided for the different harmonic orders and a total harmonic distortion (THD) level of 8 % is given. In [160] a THD of 5 % is mentioned for small scale systems. The generator needs to comply to the limits set from 0.2 pu load.

5.1.2 Design Issues in General

Several works on the design and comparison of direct-drive PM generators with regard to other drive-train topologies are available in literature as for example in [6, 20, 146, 161–164] and also for small scale PM generator systems as in [165] and [166]. The issues identified in the design and implementation of direct-drive PM wind generators are the high cost, with these generator types currently the most expensive drive-train solution in use, the high cost and also volatility of PM prices, the high active mass and also the structural mass at higher power levels as well as the large size which makes assembly, installation and transport difficult. It is, thus, essential that the mass and PM content of these generators be made as low as possible in the design optimisation. Other aspects include ease of manufacturing and segmentation, especially for larger generators. Furthermore, important in the design of PM generators is the load torque ripple and especially the no-load cogging torque as explained in [11].

For the 15 kW case study system under consideration, which is also shown in Appendix B, Table 5.1 gives some of the constraints associated with this design. From the turbine curves for the 15 kW wind generator system to be implemented, a rated torque value of $T_s = 1000$ Nm, at a rated turbine speed of $n_s = 150$ r/min, and rated wind speed of $v_w = 11$ m/s is selected. In order for the generator to operate at 50 Hz at 150 r/min a pole number of $p = 40$ needs to be selected. From the dimensions of the evaluated turbine, the maximum outer diameter of the generator is fixed at $D_o = 655$ mm. Normally for utility scale systems making use of mechanical and aerodynamic braking the maximum torque seldom exceeds a value $T_b \geq 1.5$ pu. However, for the 15 kW fixed-pitch passive furling generator system under consideration, electromagnetic braking is employed and in this case the maximum torque is specified as $T_b \geq 2.0$ pu [112].

From previous studies such as the design in [11], a no-load cogging torque value of $\Delta\tau_{NL} \leq 2.5\%$ and a load torque ripple of $\Delta\tau_L \leq 4\%$ are specified as in Chapter 4. In some cases a cogging torque value as low as $\Delta\tau_{NL} \leq 0.5\%$ is mentioned, but for this study the given value is deemed sufficient in order to obtain a fair comparison between the different generator systems evaluated. With the efficiency of the slip-PMG unit given as $\eta_r = 97\%$ in Chapter 4 and to have an overall system efficiency of $\eta_t = \eta_s\eta_r \geq 91\%$, the efficiency of the PMSG should be no less than $\eta_s \geq 94\%$. It is also essential that the partial load efficiency be adequately evaluated as this is the region in which the wind generator will be operated most of the time. Furthermore, the short-circuit current level needs to be limited during low voltage conditions to limit damage to switch gear and transformers and also to protect the PMs from demagnetisation. Same as for the slip-PMG design in Chapter 4 the stator current density is specified as $J_s \leq 4.0$ A/mm^2.

Table 5.1: Design constraints of the 15 kW case study SS-PMG system.

Parameter	**Value**
Rated torque, $T_{s(rated)}$, Nm	1000
Maximum breakdown torque T_b, pu	≥ 2.0
No-load cogging torque, $\Delta\tau_{NL}$, %	≤ 2.5
Full-load torque ripple, $\Delta\tau_L$, %	≤ 4.0
Required rated efficiency, η_s, %	≥ 94
Maximum outer diameter, D_o, mm	655
Rated rotor speed n_s, r/min	150
Grid phase or line voltage V_s, V	230/400
Grid frequency F_s, Hz	50
Number of poles p	40
Stator current density, J_s, A/mm^2	≤ 4.0

5.2 Generator Topologies Considered

For this study both non-overlap single layer (SL) and double layer (DL) windings as shown in Fig. 5.2(a) and (b) respectively, are evaluated. Furthermore, in this study a new type of toroidal winding is also considered as shown in Fig. 5.2(c). Next to each machine structure the slot layout with regard to the different phases are shown. For comparison the phase layout of a SL and DL conventional three phase overlap winding, making use of three slots per pole are also shown in Fig. 5.2(d). The toroidally wound machine makes use of six slots per pole.

Non-overlap windings are being considered in many machine design applications [167]. These machines have the advantages of easier manufacturing and segmentation as well as low cogging torque as opposed to conventional overlap winding machine types. The number of coils for the same pole number is also much lower and pre-formed modular coils can easily be used by slightly adjusting the slot-layout. This is even easier if a SL non-overlap winding, where each alternating tooth is wound, is utilised and the amount of coils are also halved as opposed to the DL winding. Furthermore, it is also known that the SL winding have a higher per unit inductance as opposed to the DL winding which could be beneficial in the direct grid connection of the generator to limit the magnitude of short-circuit currents. However, a drawback of the SL non-overlap winding as shown in previous studies is the large sub-MMF harmonic [11]. It is also known that the voltage quality of the SL winding is poorer than that of the DL winding. As for the design of the slip-PMG unit, the DL winding is also found to have a better performance than that of the SL non overlap winding machine regarding active mass and PM content. As opposed to the double layer winding configuration shown in Fig. 5.2(b) the coils can be placed adjacent to one another instead of stacked on top of one another. This will make segmentation of the non overlap DL winding easier. Fig. 5.3(b) shows a FE field plot of the DL non-overlap winding PM machine.

With $p = 40$, there are three options of single-layer pole-slot combinations with high winding factors (k_w) that can be selected for the PM wind generator as also discussed in [11]. These are the 40/36, 40/42, or 40/48 combinations [168]. The 40/42 combination with only one winding section ($W_s = 1$) [169] is immediately discarded due to the unbalanced magnetic field in the air gap under load. The 40/36 combination is also a question in this regard with a very low number of winding sections namely $W_s = 2$. The 40/36 option has a lower number of coils compared to the 40/48 combination, but the ratio of the open-slot opening to the magnet pitch is larger, which

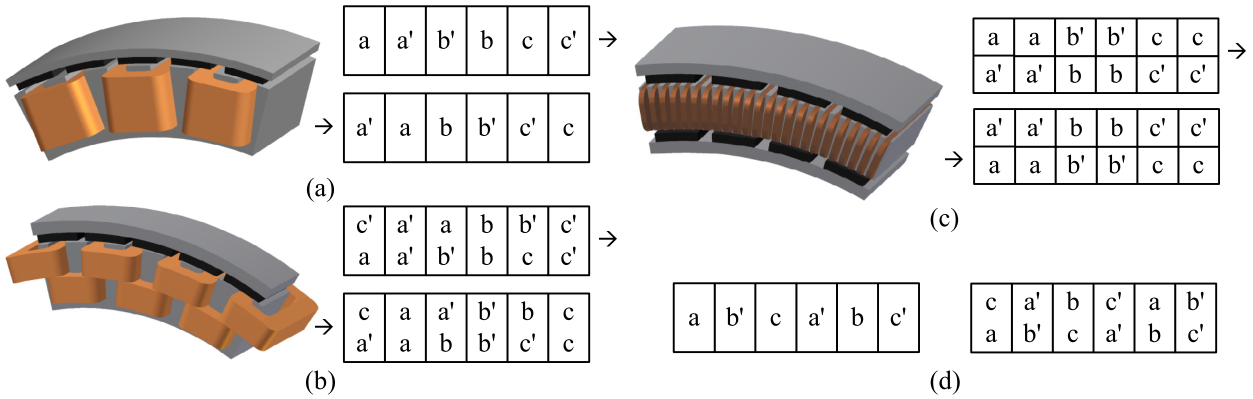

Figure 5.2: (a) Non-overlap SL and (b) DL, (c) double-rotor toroidal 6 slot/pole PMSG winding structures and phase layouts and (d) conventional three phase overlap winding SL and DL phase layouts.

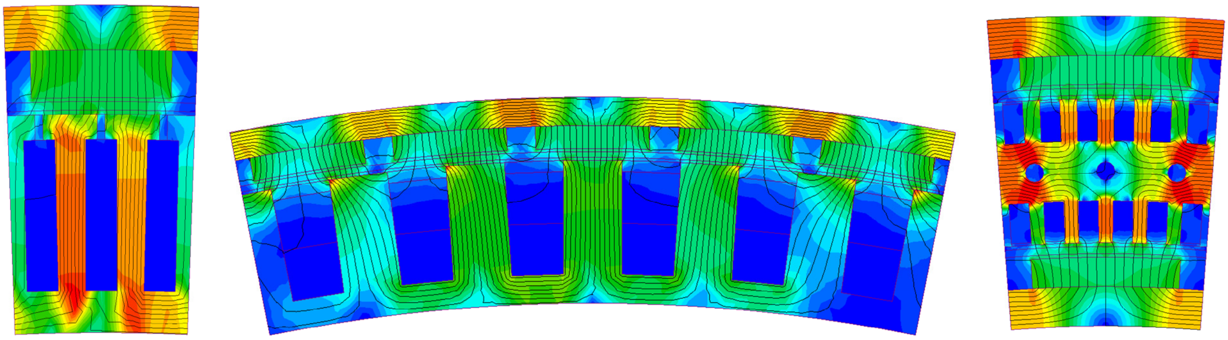

(a) (b) (c)

Figure 5.3: FE field plots for the (a) conventional three phase overlap, (b) non-overlap DL and (c) double-rotor toroidal 6 slot/pole winding PMSGs (Negative boundary conditions are used in the FE analysis for all configurations).

is a disadvantage, and the winding factor is also lower. Another option to look at is the 42/36 combination, with the rated turbine speed then slightly lower. The slot opening to magnet pitch ratio of the 42/36 combination, however, is even worse than the 40/36 combination. Hence, the 40/48 combination is selected with $W_s = 8$. In the FE modelling, negative boundary conditions can be used [169], and only five poles and six slots have to be meshed. Although k_w is slightly lower if the same pole slot combination is selected for the DL non overlap winding [168], in order to simplify the FE-modelling implementation the 40/48 combination is also utilised for the DL winding.

Overlap winding machines on the other hand are known to have a much better torque performance and should, thus, require less active and PM material for the same torque specifications. These machines, however, have the problem of a very large torque ripple and a high number of coils. Another drawback, especially for applications with low aspect ratios such as direct-drive wind generators is the long end-windings. Although non overlap winding machines are easier to manufacture, the conventional three phase overlap winding is manufactured by means of commercial winding processes which have been in use for a long time. A known problem for especially larger wind generators, though, is the segmentation of the stator winding. Furthermore, there are also questions regarding the effects of the known very low per unit impedance of these machines for the direct grid connection of this specific application. In Fig. 5.3(b) a FE simulated field plot of a conventional overlap winding PM machine with three slots per pole is shown.

Dual rotor PM machine topologies have also been proposed for wind generators as for example in [13] and [146]. However, in the case of overlap winding machines, the large end-windings could make it difficult to assemble the machine, which means that the eventual configuration might not be at the optimum machine dimensions. Many dual rotor PM machine topologies also have the disadvantage of a larger effective airgap. In this case it might be better to go for the toroidal type of topology such as in [170], [171] and much more recently in [172] as proposed for wind generators. Normally toroidally wound coils are wound around a steel cylinder with the stator being toothless. This allows for easier manufacturing but the drawback is a large airgap that requires more PM material. In this study a slotted stator configuration is used with slots on both the inner and outer diameters of the stator, with a common stator yoke, as shown in Fig. 5.2(c) and Fig. 5.3(c) which shows the FE field plot of the toroidal winding machine. The machine is assembled in such a way that two opposing magnet polarities are facing one another. The flux from the bottom magnet, thus links the bottom conductor and the flux from the top magnet links the top conductor. Currently it is difficult to comment on the manufacturability of the double rotor toroidal winding as this type of winding has not been extensively used before, especially for large diameter wind turbines. Especially for lower pole number machines the use of this type of configuration is questionable due to the large common yoke that would be required. However, segmentation for this type of winding should not be a problem due to none of the coils overlapping.

Furthermore, due to the successful use of aluminium as a conductor material in the prototype machines of Chapter 4 a further study is conducted in this chapter on the feasibility of using aluminium windings in direct-drive wind generators.

5.3 Design Methodology

As in Chapter 4 it is also not possible to know the operating state of the directly grid connected PMSG as the current angle cannot be controlled as is the case for a PMSG connected to the grid via a solid-state converter. A similar modelling procedure is, thus, employed in conjunction with the design equations presented in this section. This modelling procedure is also applicable in general to all of the directly grid-connected PMSG topologies discussed in Chapter 1.

5.3.1 Design Equations

Similar as in Chapter 4 the directly grid-connected PMSG is modelled in the dq-reference frame fixed to the PM-rotor. From the dq-equivalent circuits in Fig. 5.4 the steady-state dq-equivalent equations are given as

$$V_{qs} = -R_s I_{qs} - \omega_s L_{ds} I_{ds} + \omega_s \lambda_{ms} \tag{5.1}$$

and

$$V_{ds} = -R_s I_{ds} + \omega_s L_{qs} I_{qs}. \tag{5.2}$$

V_{ds} and V_{qs} and I_{ds} and I_{qs} indicate the d and q-axis voltages and currents respectively. R_s is the per phase resistance and $\omega_s = 2\pi f_s$ indicates the synchronous electrical angular speed. The dq-inductances L_{ds} and L_{qs} are again given as

$$L_{qs} = \frac{\lambda_{qs}}{-I_{qs}} + L_{es}; \qquad L_{ds} = \frac{\lambda_{ds} - \lambda_{ms}}{-I_{ds}} + L_{es} \tag{5.3}$$

with L_{es} the end-winding inductance component. The general relations of voltage and current are given from Fig. 5.4 by

$$\begin{bmatrix} V_{qs} \\ V_{ds} \end{bmatrix} = \sqrt{2} V_s \begin{bmatrix} \cos \Delta_s \\ \sin \Delta_s \end{bmatrix}, \tag{5.4}$$

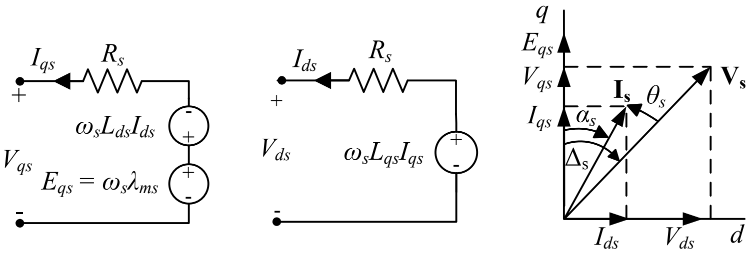

Figure 5.4: DQ-equivalent circuits and vector diagram for the modelling of the direct-grid PMSG.

$$\begin{bmatrix} I_{qs} \\ I_{ds} \end{bmatrix} = \sqrt{2} I_s \begin{bmatrix} \cos\alpha_s \\ \sin\alpha_s \end{bmatrix}, \tag{5.5}$$

$$V_{qs}^2 + V_{ds}^2 = 2V_s^2 \tag{5.6}$$

and

$$I_{qs}^2 + I_{ds}^2 = 2I_s^2. \tag{5.7}$$

The per phase grid voltage is fixed at $V_s = V_{rms} = 230$ V for this particular study, with I_s the RMS stator current fed into the grid which can be calculated as

$$I_s^2 = \frac{P_{cus}}{3R_s}, \tag{5.8}$$

with P_{cus} in (5.8) the copper loss of the stator winding which is given as an input parameter. For the modelling procedure as discussed below the steady-state dq equations must be manipulated to solve the unknowns of the PMSG unit. However, there are a large amount of variables, which complicates the calculations. To simplify the calculations, instead of solving for all the unknowns a slight modification is made for the solving of the PMSG steady-state dq equations, by solving V_{ds} and V_{qs} separately. This will be explained in the next section.

The equations used to solve for the PMSG are obtained by first manipulating (5.2) with the result given in (5.9) as

$$I_{qs} = \frac{V_{ds} + I_{ds}R_s}{\omega_s(L_{qs} + L_{es})}. \tag{5.9}$$

By substituting (5.9) in (5.1) the result is the term in (5.10) given as

$$I_{ds} = \frac{\omega_s(L_{qs} + L_{es})(\omega_s\lambda_{ms} - V_{qs}) - V_{ds}R_s}{R_s^2 + \omega_s^2 L_{ds}L_{qs}L_{es}^2}. \tag{5.10}$$

If V_{ds} and V_{qs} are known I_{ds} can be calculated from (5.10) and I_{qs} from (5.9) and α_s can then be calculated from (5.5).

The developed torque is given by

$$T_s = \frac{3}{4}p[(L_{qs} - L_{ds})I_{ds}I_{qs} + \lambda_{ms}I_{qs}]. \tag{5.11}$$

The peak torque calculation of the PMSG can be done exactly the same as for the slip-PMG in Chapter 4 except in this case the effective resistance is equal to $(R_s + R_b)$ where R_b is the braking resistance which dictates at which speed the peak torque occurs as explained in [112] with

$$\omega_b \approx \frac{(R_s + R_b)}{\sqrt{L_{ds}L_{qs}}}. \tag{5.12}$$

This value of ω_b can now be used in (4.11) in Chapter 4 to calculate T_b.

The efficiency of the generator is given by

$$\eta_s = \frac{T_s\omega_m - P_{Loss}}{T_s\omega_m}. \tag{5.13}$$

with the total generator losses defined as $P_{Loss} = P_{cus} + P_{cue} + P_{ecs} + P_{ecm} + P_{wfs}$. Depending on the type of winding used P_{cue} indicates the eddy current loss component in the conductors. P_{ecs} indicates the core losses in the stator steel. The core losses in the rotor yoke as well as the PM eddy losses for the PM-rotor is included in P_{ecm}. These values are calculated by means of FE-analysis in this study. The wind and friction losses are given by P_{wfs} which is a fixed value for the fixed speed SS-PMG system and is estimated by means of the wind and friction loss calculations given in [18] for rotating machinery in general. Finally the working power and reactive power supplying to or consuming from the grid is given as

$$\begin{bmatrix} P_s \\ Q_s \end{bmatrix} = 3V_sI_s \begin{bmatrix} \cos\theta_s \\ \sin\theta_s^* \end{bmatrix}. \tag{5.14}$$

5.3.2 Modelling Procedure

As in Chapter 4 the equations above are used in a static FE modelling procedure coupled with an optimisation algorithm. To calculate and evaluate the performance of the machine the following steps are used as is also described in Fig. 5.5:

1. I_s is calculated from (5.8), at the rated given copper losses. For the first iteration $\alpha_s = 0$ and with I_s known the three phase currents, which is the FE input, can be written as

$$\begin{aligned} i_a(t) &= \sqrt{2}I_s sin(\omega_s t - \alpha_s); \\ i_b(t) &= \sqrt{2}I_s sin(\omega_s t - \alpha_s - \frac{2\pi}{3}); \\ i_c(t) &= \sqrt{2}I_s sin(\omega_s t - \alpha_s + \frac{2\pi}{3}). \end{aligned} \tag{5.15}$$

2. From this first iteration λ_{dq} is calculated by transforming λ_{abc} obtained from FE to the dq-reference frame using Park's transformation. In this way the effect of the q-axis current can be taken into account, with $\alpha_s = 0$ and $I_{ds} = 0$, $\lambda_{ms} = \lambda_{ds}$.

3. Furthermore, for this first iteration it is assumed that $L_{ds} = L_{qs}$ with L_{qs} calculated as in (5.3) with $I_{qs} = \sqrt{2}I_s$ in this case and with L_{es} calculated as mentioned.

4. To solve (5.10) for I_{ds}, the values of V_{ds} and V_{qs} are required. With $I_{ds} = 0$ and $I_{qs} = \sqrt{2}I_s$ for the first iteration, (5.1) and (5.2) can be solved for V_{qs} and V_{ds}. From the vector diagram in Fig. 5.4(b)

$$\Delta_s = \tan^{-1}\frac{V_{ds}}{V_{qs}} \tag{5.16}$$

   which gives an approximate value for Δ_s. Now with Δ_s known, V_{qs} and V_{ds} are again calculated, except in this case by solving (5.6) with V_s the grid voltage. I_{ds}, I_{qs} and α_s can now be calculated from (5.10), (5.9) and (5.5) respectively.

5. Because I_{ds} and I_{qs} were not calculated in terms of I_s, a new value for I_s is calculated from (5.7) and also for P_{cus} from (5.8). With updated values for I_s and α_s another static FE iteration is run with the new values substituted in (5.15).

6. New values for L_{ds} and L_{qs} according to (5.3) are calculated from the dq flux linkages with $L_{ds} \neq L_{qs}$ and λ_{ms} as calculated in the first iteration. New more accurate values for I_s and α_s are obtained by again solving (5.7), (5.10), (5.9) and (5.5).

7. This new, more accurate values of I_s and α_s is then used in a third static FE iteration at which point the performance of the machine is evaluated by solving (5.11) - (5.14).

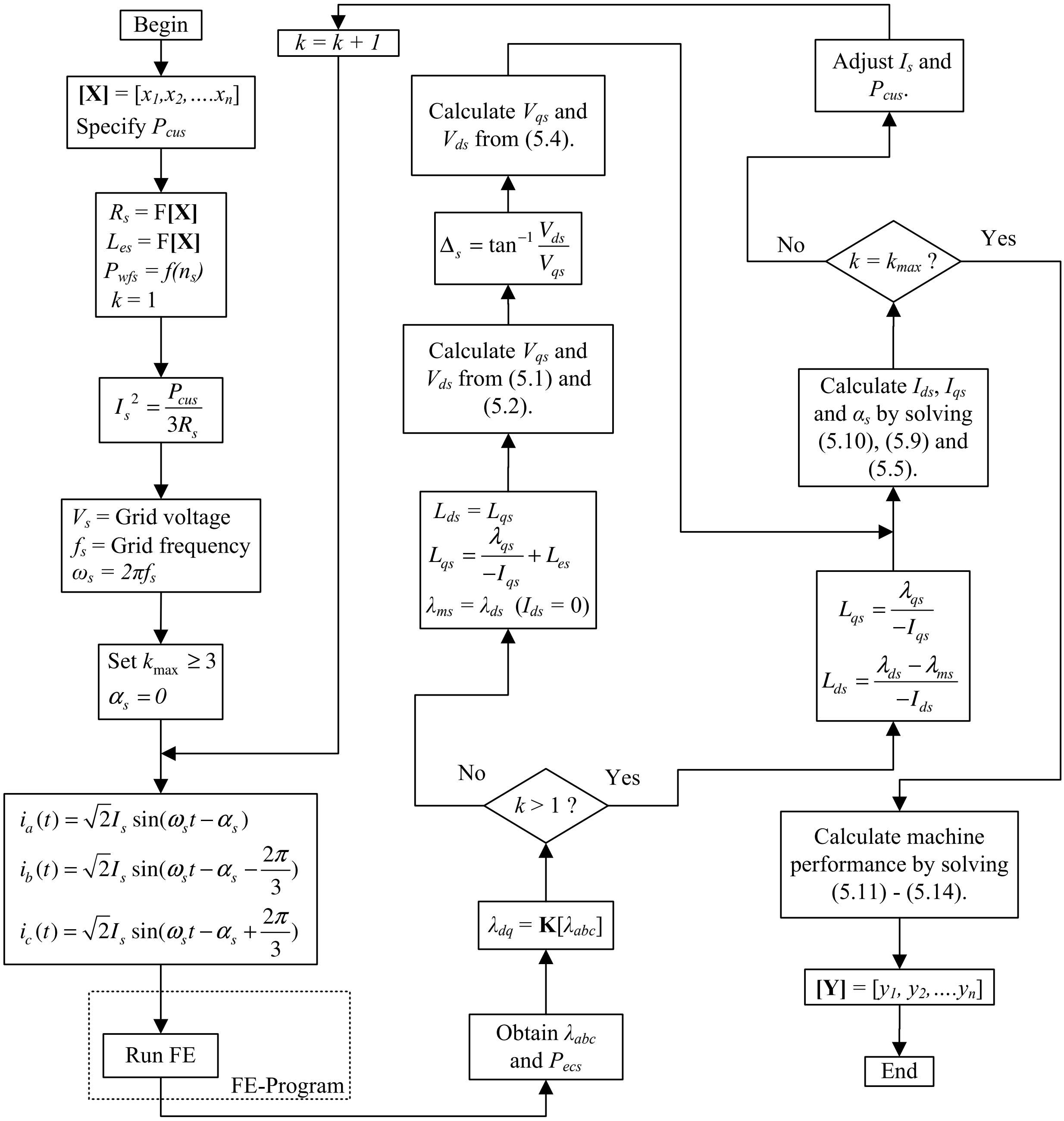

Figure 5.5: FE simulation method used to calculate the SS-PMG performance.

8. For better accuracy more static FE iterations can be run, but a minimum of three static FE solutions are required.

9. In this simulation procedure the slip-PMG and the PMSG are analysed separately. For the performance evaluation of the whole SS-PMG system, the performance of both units are evaluated against T_s. With P_{wfr} and P_{ecr} zero, $T_s = T_r = T_t$. T_s is, thus, the mechanical torque input of both machine units.

10. For each load case P_{cus} is the input parameter varied to obtain the machine performance at different loads.

5.3.3 Design Optimisation

For the design optimisation of the PMSG the *Visual Doc* optimisation suite is also used as in Chapter 4 [149]. The design objective in this case is again to minimise $y_1 = M_{Tot}$ and $y_2 = M_{PM}$ in (5.17), while the rest of the parameters in $\mathbf{[Y]}$ comply with the limits set in Section 5.1. Fig. 5.6 shows how the static FE modelling procedure discussed in Fig. 5.5 is coupled with the optimisation program. As is also shown in Fig. 5.6 after optimisation each optimum design is verified by means of transient FE, and slight adjustments are made to $\mathbf{[X]}$ so that all the performance output parameters in $\mathbf{[Y]}$ comply with the limits set in Section 5.1. The reason for transient verification is to accurately calculate the torque ripple as well as the eddy current losses, which cannot be accurately calculated by means of static FE-analysis. Upon completion of the FE-design iterations, a final check is done to determine if the generator design complies with the mentioned grid requirements. This is done with the help of the dynamic modelling methods as discussed in Chapter 2. If the dynamic grid performance of the generator is not sufficient, the optimum FE-design needs to be altered. The parameters which influence the grid behaviour the most are typically the size of the synchronous

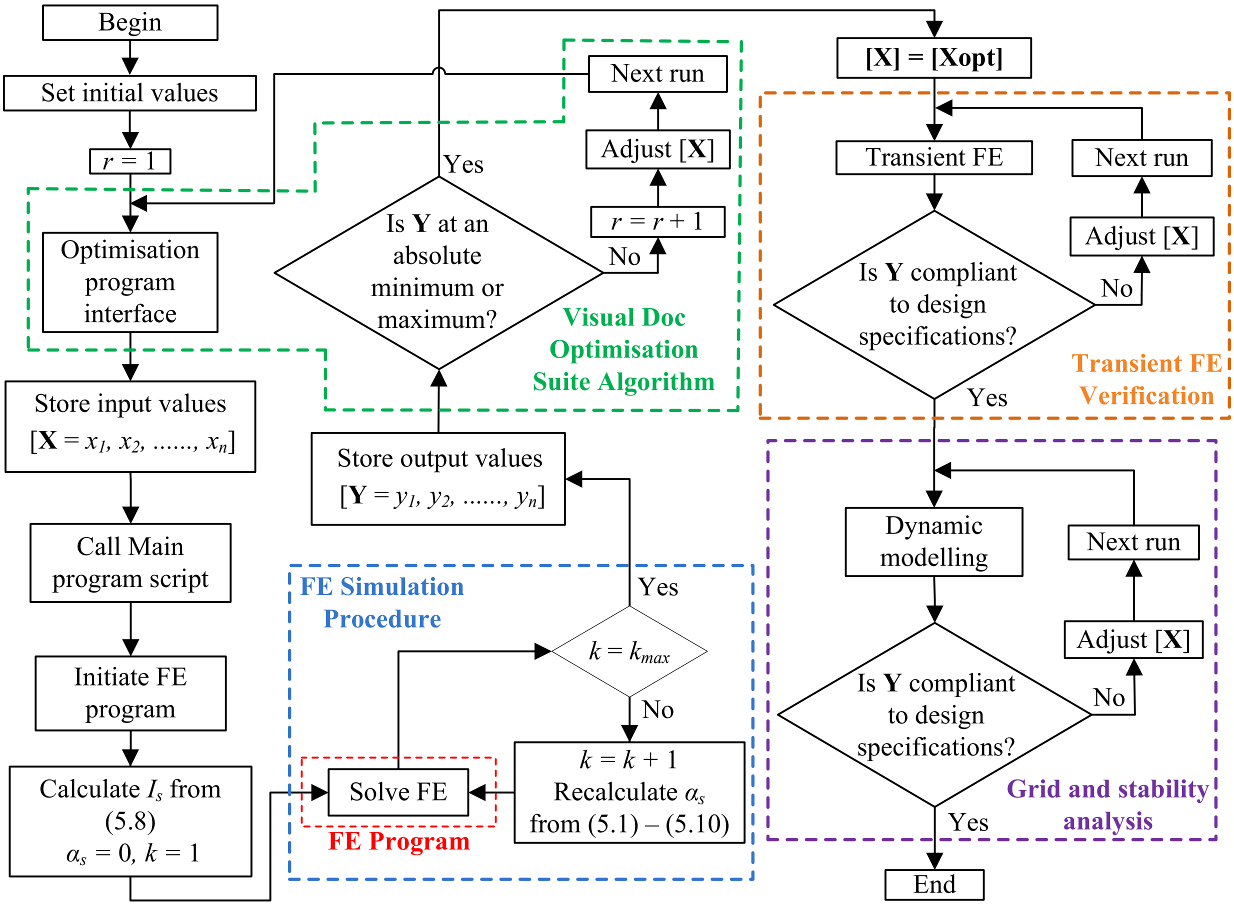

Figure 5.6: Optimisation program coupled with the simulation procedure and FE simulation program.

reactance ($X_s = \omega_s L_s$), and λ_{ms}.

The machine design parameters to be optimised for the PMSG, as is also shown in Fig. 4.9 in Chapter 4 for **[X]**, as well as the output parameters in **[Y]** are given in (5.17) as

$$\mathbf{X} = \begin{bmatrix} x_1 \\ x_2 \\ x_3 \\ x_4 \\ x_5 \\ x_6 \\ x_7 \\ x_8 \end{bmatrix} = \begin{bmatrix} l \\ h_c \\ h_m \\ h_{ry} \\ h_{sy} \\ \sigma_w \\ \sigma_m \\ \sigma_t \end{bmatrix} ; \quad \mathbf{Y} = \begin{bmatrix} y_1 \\ y_2 \\ y_3 \\ y_4 \\ y_5 \\ y_6 \\ y_7 \\ y_8 \end{bmatrix} = \begin{bmatrix} M_{Tot} \\ M_{PM} \\ T_{ave} \\ T_b \\ \Delta\tau_{NL} \\ \Delta\tau_L \\ \eta_s \\ \mathrm{PF} \end{bmatrix} . \tag{5.17}$$

5.4 Optimisation Results

Table 5.2 gives the optimisation results for the four PM machine topologies evaluated. An indication of the size of the machines can be found with l the active length and D_i the inside diameter. The maximum outside diameter of all the machines are also fixed at 655 mm from the constraints of the used turbine. The optimum PM mass (M_{PM}) for each machine topology is also found as discussed in Chapter 4 and with the help of Fig. 5.7.

From Table 5.2 it is seen that the two non overlap winding machines and the conventional three phase overlap winding topology have more or less the same active mass, but with the optimum PM mass of the DL non overlap winding at a slightly lower value. The double rotor toroidal winding on the other hand has a significantly lower active mass and lower optimum PM mass than the rest of the generator topologies. The minimum value of M_{PM} for the conventional overlap winding and that of the double rotor toroidal winding are both lower than that of the rest of the machine structures. This is due to the much better torque performance of these machines, with the maximum breakdown torque of the overlap winding more than 3 pu, and more than 4 pu for the double rotor toroidal winding. The reason for the much better performance regarding active mass of the toroidal winding machine compared to the conventional overlap winding machine is due to the much shorter end-windings of this winding configuration. In order to reduce the effect of the end-windings the active length is also much longer of the conventional overlap winding machine.

Due to the non overlap winding machines having a much higher per unit impedance it is much more difficult for these machines to achieve the required maximum torque of $T_b > 2.0$ pu. This is why the tendency of these machines during the design optimisation is to increase the stator inner diameter by decreasing h_c in order to decrease the steel flux path to reduce the inductance of the machine. To achieve the required efficiency the active length then needs to be increased. This is also very clearly illustrated in Fig. 4.12 in Chapter 4.

Regarding the direct grid connection of these different types of machines there are also other aspects which need to be addressed such as discussed previously in Chapter 2. This relates to the power factor of the machine, harmonic content of the current waveform and the low voltage ride through capabilities. The power factor and reactive power consumption of all the topologies depend very much on the terminal voltage. It is evident that the overlap and toroidal winding machines operate at almost unity power factor. Due to the lower value of the per unit impedance, X_s, this generator is more sensitive to grid voltage variations and also has a higher short-circuit current. For even small variations in the terminal voltage large unwanted reactive power flow can occur. Furthermore, both of these winding type machines, especially the conventional overlap

Table 5.2: Optimisation results of the non overlap SL and DL, conventional three phase overlap and double rotor toroidally wound PMSGs.

	SL-non-overlap	**DL-non-overlap**	**3ϕ-overlap**	**Toroidal**
T_{rated}, Nm	1000	1000	1000	1000
T_b, pu	2.22	2.16	3.11	4.40
$\Delta\tau_{NL}$, %	1.90	2.34	13.37	2.35
$\Delta\tau_L$, %	4.55	3.42	31.52	4.93
P_{ecs}, W	135.36	141.39	182.37	164.56
P_{ecr}, W	81.23	110.8	35.73	9.99
P_{cus}, W	604.18	588.48	683.78	711.71
η_s, W	94.57	94.44	94.01	94.00
D_o, mm	655	655	655	655
l, mm	129.0	125.0	114.5	80.00
D_i, mm	540.1	528.0	523.2	512.0
V_s, V	230.0	230.0	230.0	230.0
I_s, A	21.93	22.64	23.70	23.80
Δ, °	12.50	12.30	10.40	6.80
$\boldsymbol{X_s}$, pu	**0.247**	**0.208**	**0.082**	**0.068**
PF	0.964	0.974	0.996	0.997
$\boldsymbol{M_{PM}}$, kg	**7.62**	**7.00**	**7.82**	**6.49**
M_{Cu}, kg	16.69	20.16	25.22	21.04
M_{Fe}, kg	66.37	62.44	60.77	45.22
$\boldsymbol{M_{Tot}}$, kg	**90.68**	**89.61**	**93.91**	**71.43**

SL non overlap: High active mass and PM content. Very easy manufacturing. Moderate to easy reduction of torque ripple. Low to moderate grid current harmonic content. Medium to high short circuit current. Moderate response to grid voltage variations.

DL non overlap: High active mass and moderate PM content. Easy manufacturing. Easy reduction of torque ripple. Low grid current harmonic content. Medium to high short circuit current. Moderate response to grid voltage variations.

3-ϕ overlap: High active mass and PM content. Moderate to difficult manufacturing. Very high torque ripple. High grid current harmonic content. Extremely high short circuit current. Large unwanted reactive power flow if grid voltage varies from design value.

Double rotor toroidal: Low active mass and PM content. Moderate to difficult manufacturing. Moderate to easy reduction of torque ripple. High grid current harmonic content. Extremely high short circuit current. Large unwanted reactive power flow if grid voltage varies from design value.

winding machine, have a much higher harmonic content in the waveform of the current. Both these machines will, thus, need to be operated in conjunction with an additional series line reactance (SLR), which is not uncommon in power systems. The much better performance of the double-rotor toroidal winding needs to be weighed up against issues such as ease of manufacturing and the

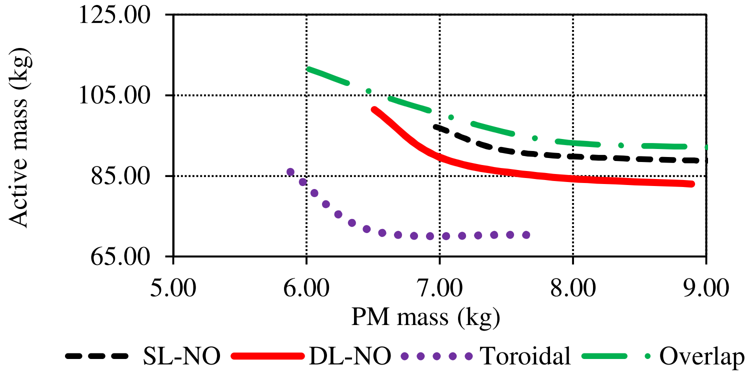

Figure 5.7: PM mass versus active mass for the four PMSG machine topologies evaluated.

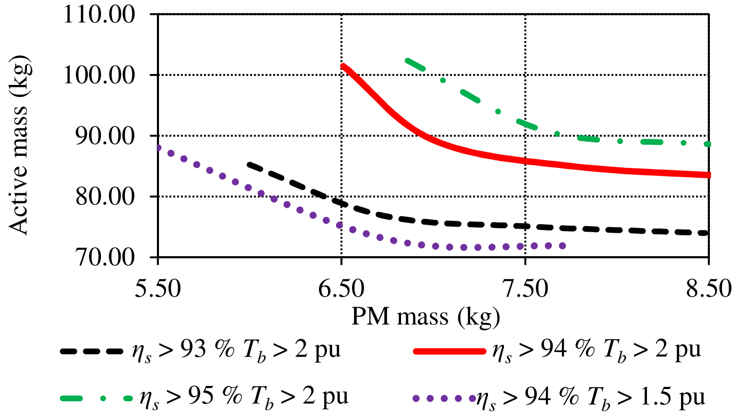

Figure 5.8: PM mass versus active mass for four different design cases of the DL-non overlap winding PMSG.

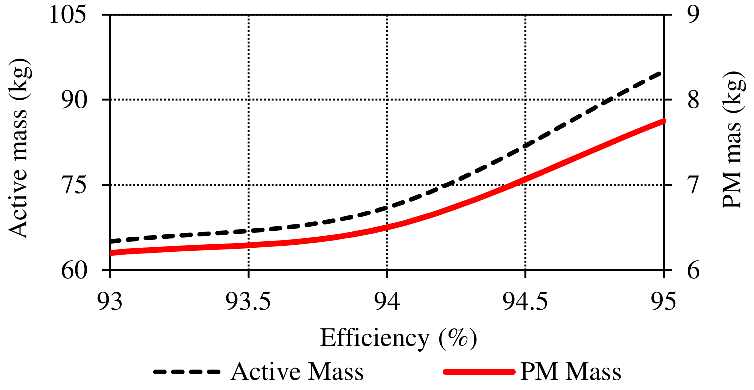

Figure 5.9: PM - and active mass versus efficiency of the toroidally-wound double-rotor PMSG.

suitability of this generator for direct grid connection.

The results shown in Fig. 5.8 for different efficiencies and maximum torque specifications of the DL non overlap winding machine are very interesting. When increasing the minimum efficiency from 94 % to 95 %, no major increase in mass is observed. However, when decreasing the maximum torque requirement from $T_b > 2.0$ pu to $T_b > 1.5$ pu, a significant reduction in mass is seen. This also explains the slightly higher efficiencies of the non overlap winding machines in Table 5.2 as the maximum torque requirement for the non overlap winding machines is a much more difficult parameter to comply with than the specified minimum efficiency. The relationship between active mass and PM content versus efficiency are shown for the double-rotor toroidally wound machine in Fig. 5.9. Only a marginal increase in active mass and PM content is observed when changing the minimum efficiency specification from $\eta_s > 93$ % to $\eta_s > 94$ %. However, for $\eta_s > 95$ % a significant increase in active mass and PM content is observed.

5.5 Further Analysis of Toroidal Winding

From Table 5.2 it is seen that the toroidal winding PMSG is definitely a machine to consider due to its better performance regarding mass and PM content. Although the difference is not so much at the lower power level for wind turbine applications, it is anticipated that the toroidal winding, will especially for higher power levels be more of a consideration due to the large amount of torque the machine have to develop from a limited diameter.

Table 5.3 show optimisation results for the DL non overlap (DL-NO) and toroidal winding PMSGs at three different power levels, 3 kW, 15 kW and 3 MW. The comparison at the 15 kW power level is the same as in Section 5.4. At the 3 kW power level it is seen that the toroidal winding PMSG have a much poorer performance regarding active mass and PM content with regard to the DL non overlap winding PMSG. At the utility scale power level of 3 MW it is seen that the toroidal winding performs much better especially regarding PM content. It is, thus, clearly seen that the performance of the toroidal winding increases with an increase in the number of poles. At low pole numbers the common stator yoke is much larger in comparison with the rest of the machine structure in order to prevent the yoke from saturating and magnetic coupling occurring between the top and bottom PM-rotors. With an increase in yoke height the end-winding length of the toroidal

Table 5.3: Comparison of optimisation results of the non overlap DL and toroidal winding PMSGs and conventional three phase overlap winding PMSG as in [20].

Winding	**DL-NO**	**Toroidal**	**DL-NO**	**Toroidal**	**DL-NO**	**Toroidal**	**3ϕ** [20]
$P_{s(rated)}$, kW	3	3	15	15	3000	3000	3000
$T_{s(rated)}$, kNm	0.1	0.1	1.0	1.0	1900	1900	1900
$n_{s(rated)}$, r/min	300	300	150	150	15	15	15
Poles	20	20	40	40	160	160	160
D_o, m	0.510	0.510	0.655	0.655	5.00	5.00	5.00
l, m	0.037	0.047	0.125	0.08	1.3	0.637	1.2
D_i, mm	0.416	0.357	0.528	0.512	4.770	4.811	4.600
η_s, kg	92.16	92.74	94.44	94.00	95.38	95.24	95.00
M_{PM}, kg	**1.21**	**3.51**	**7.00**	**6.49**	**1895**	**1298**	**1700**
M_{Cu}, kg	6.09	8.94	20.16	21.04	3018	2983	4300
M_{Fe}, kg	13.39	22.48	62.44	45.22	8973	7888	18100
M_{Tot}, kg	**20.69**	**34.94**	**89.61**	**71.43**	**13885**	**12170**	**24100**

winding increases accordingly, which means that the advantage of the toroidal winding, because of the shorter end-winding length decreases.

One of the advantages of the Toroidal winding machine is that a higher fill factor can be achieved due to the way it is wound with square conductors or sheet windings. However, eddy-currents in the conductors (P_{cue}) could increase the losses of the machine and decrease the efficiency. Normally if foil type windings are used it will be wound with the conductors placed as in Fig. 5.10(a). For the toroidal winding the conductors will be placed as in Fig. 5.10(b). Fig. 5.11 show the magnitude of P_{cue} in the conductors of the toroidal winding PMSG versus segmentation configuration. Clearly the way the conductors are placed makes a significant difference in P_{cue}. It is seen that by placing the conductors as in Fig. 5.10(a) almost no difference can be seen in P_{cue}. However, by placing the conductors as in Fig. 5.10(b), which is the case for the toroidal winding, a significant reduction in P_{cue} is possible. The toroidal winding PMSG, thus, have a significant advantage in this regard.

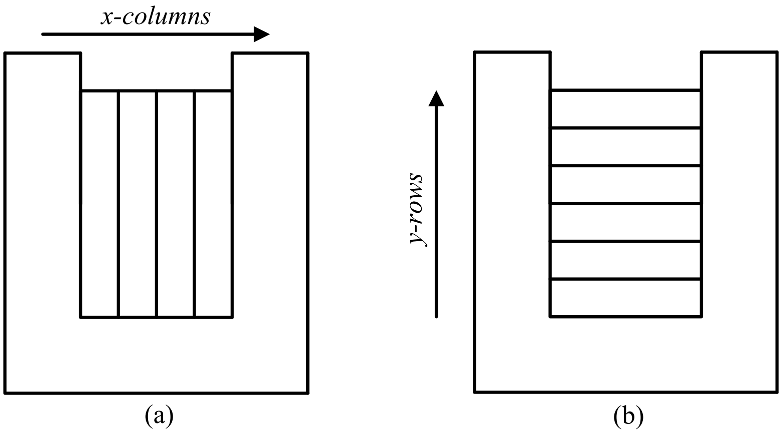

Figure 5.10: Segmentation of conductors in (a) x direction and (b) y direction.

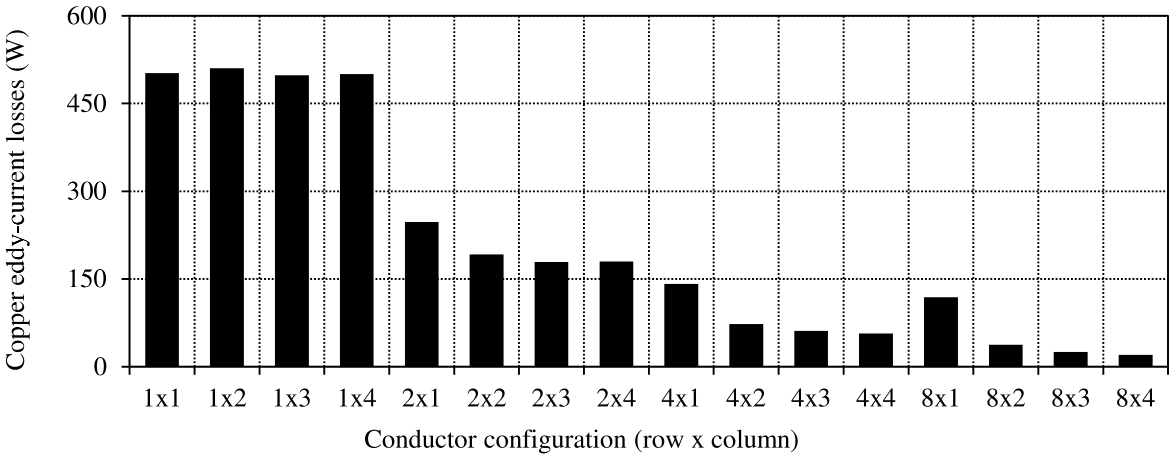

Figure 5.11: Eddy-current losses in the conductors of the toroidal winding PMSG at rated frequency.

5.6 Fill Factor and Aluminium Windings

As mentioned the possibility of using aluminium instead of copper as winding material is also investigated in this study. Due to aluminium being a better and cheaper conductor than copper per kg it is being considered in many electrical applications. Most overhead transmission lines make use of aluminium conductors as volume is not so much of a constraint in this case [173]. Aluminium is also being considered in many transformer applications, where it is mentioned in [174] that in some cases it is more economical to use aluminium than copper as conductor material. A historical concern regarding the use of aluminium is the reliability of connections made due to oxidation and the expansion coefficient of aluminium being very much different to that of other materials used in making connections. However, using proper modern installation techniques this aspect is no longer an issue as explained in [175]. New alloys also greatly increase the tensile strength of aluminium wire, which was also considered a potential drawback. It is, however, important to take care in the selection of the correct alloy due to the resistivity of aluminium being very sensitive to the addition of impurities.

Aluminium cage windings are being used extensively in commercial induction machines due to the low cost and the ease of making aluminium castings. However, aluminium wire is rarely used in the manufacturing of the stator windings of electrical machines. At current only for machines with a low duty cycle and lower efficiency class, such as for instance motors for electric gates and garage

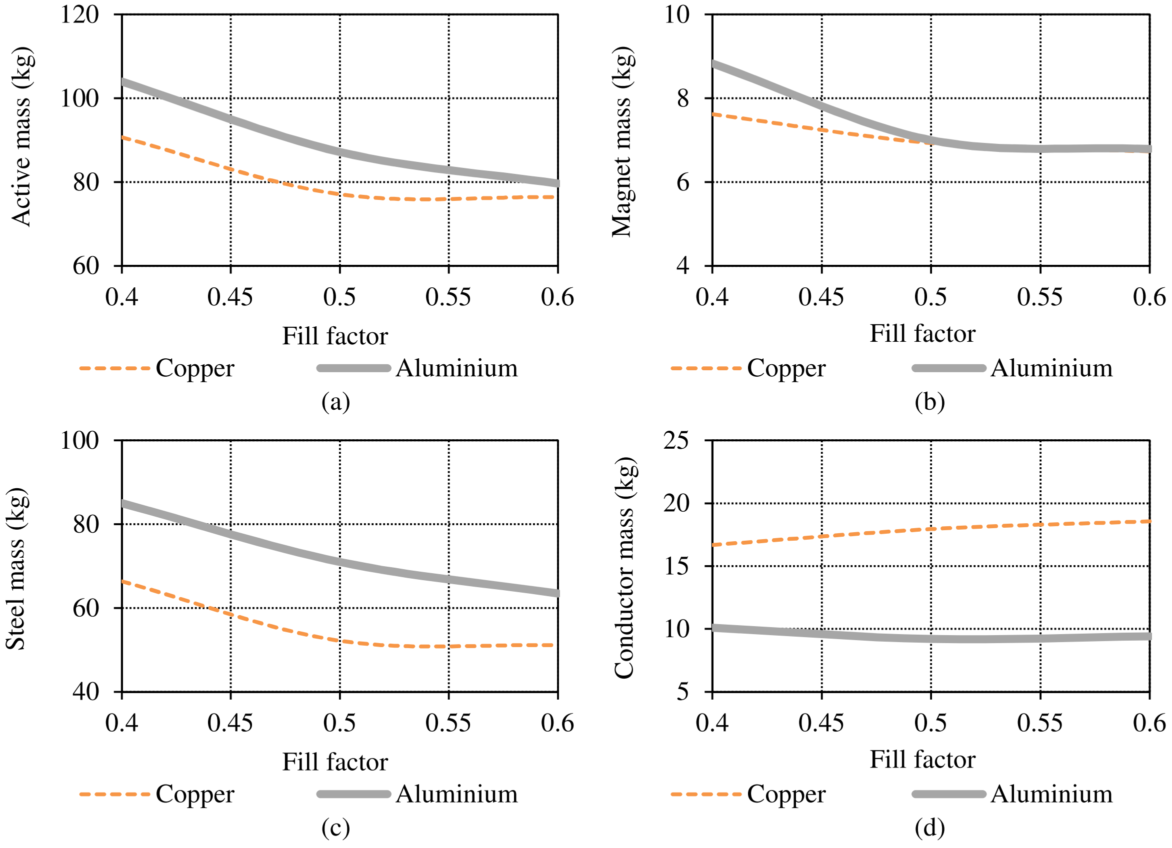

Figure 5.12: Variation in (a) total active mass, (b) PM mass, (c) steel mass and (d) conductor mass versus fill factor for optimum non overlap SL copper and aluminium winding PMSGs.

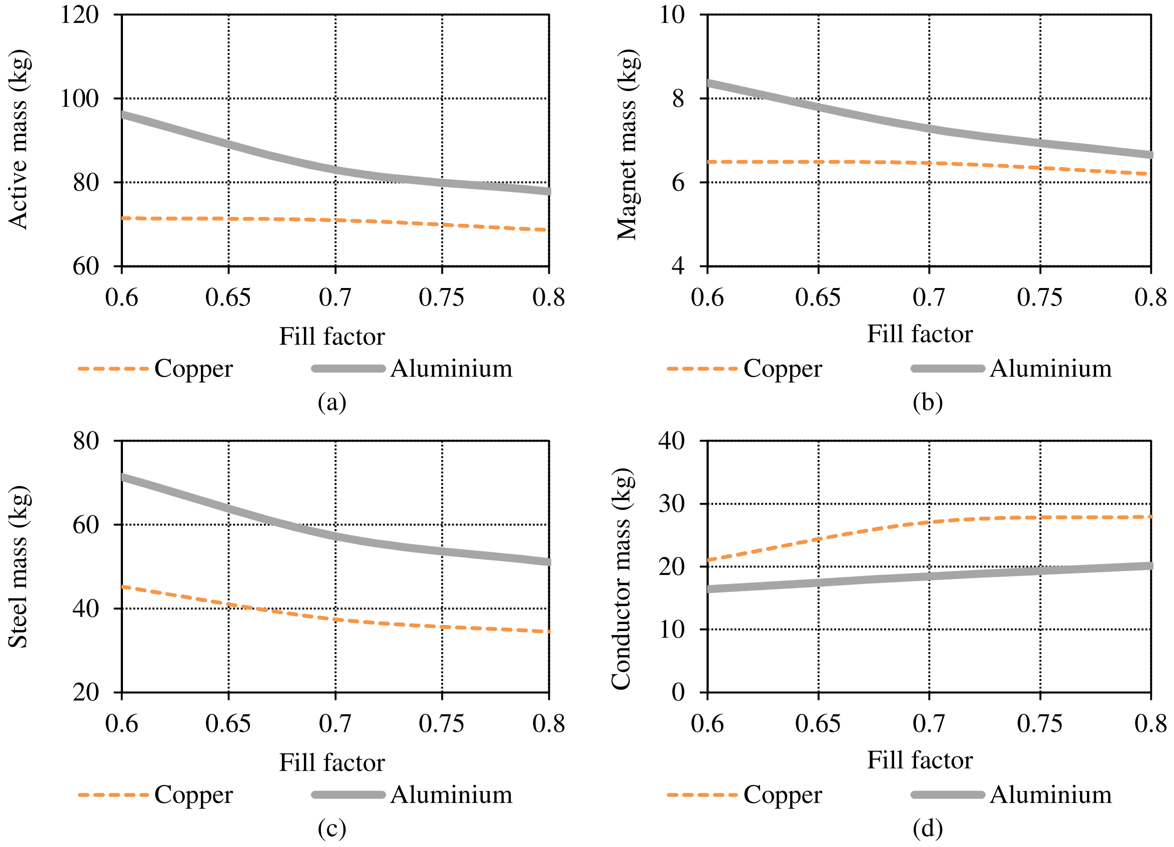

(a) (b) (c) (d)

Figure 5.13: Variation in (a) total active mass, (b) PM mass, (c) steel mass and (d) conductor mass versus fill factor for optimum Toroidal copper and aluminium winding PMSGs.

doors, it seems feasible to use aluminium as winding material. If the same efficiency specification is given for the aluminium winding machine as for the same rating copper winding machine the volume of the aluminium winding machine would need to be significantly larger to accommodate for the lower conductivity of aluminium. This is reported in [176], where a comparison is done between a copper and aluminium stator winding small induction motor. However, for large diameter wind turbines the use of aluminium as a conductor material could be more feasible as the increase in stator volume might not have such a significant effect on the overall machine size and mass. The only reference regarding the use of aluminium windings for wind turbine applications is found in [177].

Fig. 5.12(a) and (b) respectively show the variation in active mass and PM mass versus fill factor for the non overlap SL winding PMSG for both copper and aluminium used as conductor material. The importance of selecting the correct fill factor is clearly seen, which should be at least above 0.5 if a copper winding is used as seen in Fig. 5.12. The fill factor of the practical machines currently in use is just over 0.4, which is clearly shown to be unacceptable. If square wire is used, it should be possible to increase the fill factor to 0.6 which is shown to be achievable for the manufactured non overlap DL PMSG in [14]. Furthermore, it is shown in Fig. 5.12 that if the fillfactor can be increased to 0.6 the active mass of the aluminium and copper winding machines are almost the same. At a fill factor of 0.5 and higher the PM content of both the aluminium and copper windings are exactly the same.

Fig. 5.13 show the same variation as above, but for the toroidal winding PMSG. In this case it

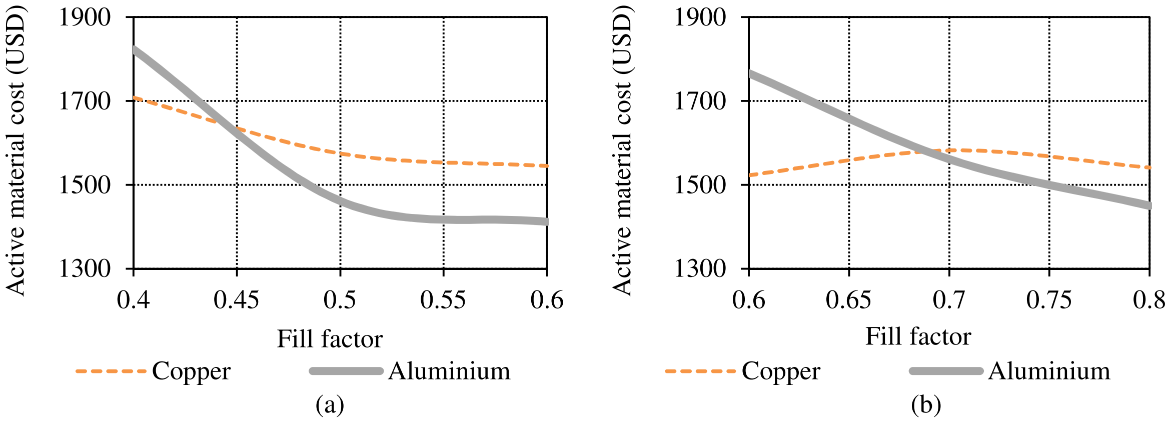

Figure 5.14: Variation in total active material cost for (a) non overlap SL and (b) toroidal, copper and aluminium winding PMSGs.

is seen that a higher fill factor is required to have the same performance for the aluminium winding machine as for the copper winding machine. Initial practical experiments suggest that it would be possible to obtain a fill factor of 0.7 for the toroidal winding PMSG due to the way it is wound. Fig. 5.14(a) and (b) show the cost distribution of the active material for the non overlap SL and Toroidal winding PMSGs for both copper and aluminium used as a conductor material. The price of the PM material per kg is taken as \$180 as given in [178] and the rest of the materials more or less the price as locally procured. The cost of aluminium wire is about two thirds of copper wire while the wholesale price of aluminium is about one third that of copper. For the non overlap SL PMSG it is seen that a 10 % reduction in material cost is possible by using aluminium as a conductor instead of copper depending on the cost of PM material. For a lower cost of PM material the percentage cost decrease for aluminium winding machines will be even higher.

5.7 Summary

From the results of this chapter it is clear that a different design approach is needed for the directly grid connected PMSG as opposed to conventional PM generator configurations connected to the grid via a power electronic converter. The generator design needs to comply with all the requirements stipulated in the relevant grid codes. A design approach is devised where the generator is optimised with a static FE modelling method coupled with an optimisation algorithm. After verifying the static FE-design with transient FE-analysis, a dynamic modelling procedure is carried out to determine whether the design is suitable for direct grid connection.

In this case the proposed toroidally wound double rotor PMSG is shown to give the best performance regarding active mass and PM content. This is especially true for high pole number applications with a deterioration in performance observed for lower pole number applications. Due to the much shorter end-windings of this generator it performs much better than the conventional three phase overlap winding PM generator. The manufacturing of this generator is, however, still a question as it is an unknown concept in direct-drive wind generator design. Furthermore, the induced voltage waveform of this generator can lead to the injection of harmonic currents into the grid. Also the relatively low synchronous reactance leads to high short circuit currents, and unwanted dynamic effects if grid voltage changes occur. The non-overlap SL winding machine is the easiest to manufacture, but has the highest active mass, and the current waveform also has a higher harmonic content than that of the DL non overlap winding. It is shown, however, that if the fill factor of the non overlap winding machines can be improved these machines become more competitive regarding active mass and PM content. Very interesting, it is also shown that for higher fill factors the use of aluminium as winding material becomes cost effective for these generator types.

For the investigated 15 kW power level the DL non-overlap winding machine is the most favourable topology regarding mass, power quality, direct grid connection and manufacturability. Thus, for small and maybe medium size direct drive wind generators the non overlap winding configurations might be the best choice due to the simplicity of these winding types. However, it is important to note that for higher power levels, the difference in mass and PM content between the non overlap winding machines and the overlap winding and toroidally wound machines might increase. Due to the low speeds and limits imposed upon the diameters of large electrical wind generators the ratio of torque to diameter does not increase linearly with an increase in power.

Chapter 6

General Machine Measurements

This chapter includes the practical evaluation of most of the slip-PMG and PMSG topologies presented in Chapters 4 and 5 with regard to general electrical machine tests in the laboratory, with the SS-PMG not connected to the grid. These types of tests include, the frequency dependent loss evaluation, torque quality evaluation, torque versus speed characteristics and the open circuit and short circuit tests as conducted for electrical machines in general. The directly grid connected measurements will be discussed in Chapter 7.

6.1 Testing Setup

Fig. 6.1 show a top level schematic of the laboratory test setup. An induction motor, which is controlled by means of a variable speed drive (VSD), and connected to the generator via a gearbox is used as a prime mover. In this case the generator is not synchronised to the grid and it is tested with the terminals connected as open-circuit, short-circuit or over a resistance load as indicated in

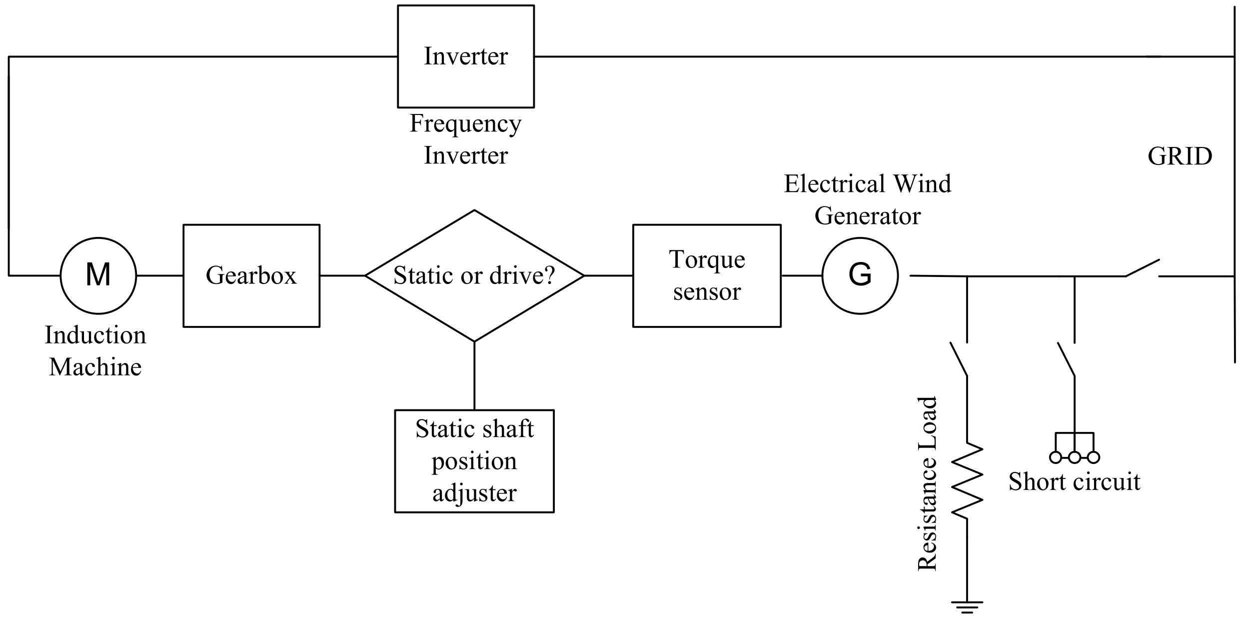

Figure 6.1: Electrical wind generator laboratory measuring setup diagram.

Fig. 6.1. Furthermore, in order to measure the no load cogging torque the gearbox and induction motor can also be removed from the system and the shaft position can be adjusted by means of a static torque adjusting mechanism as also shown in Fig. 6.1.

6.2 Prototype Machine Topologies

This section discusses the different slip-PMG and PMSG topologies practically evaluated, as well as some background on the construction methods employed in the manufacturing of these electrical machines. Fig. 6.2(a) show the PMSG unit mounted on the test bench with the common PM rotor part of the slip-PMG mounted to its front and Fig. 6.2(b) show how the slip-rotor of the slip-PMG is being mounted to the rest of the generator system.

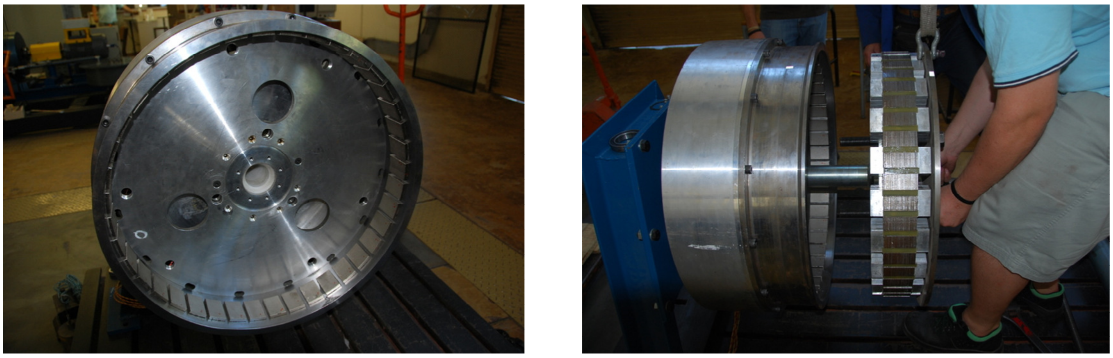
(a) (b)

Figure 6.2: SS-PMG being assembled on the test bench with (a) SL PMSG with PM-rotor side of slip-PMG mounted to its front and (b) slip-rotor being shifted into position.

6.2.1 Slip-PMG Prototypes

Fig. 6.3 show the different slip-PMG topologies which are considered in this chapter. It should be noted that the machines shown in Fig. 6.3 are not all optimally designed as in Chapter 4. However, the practically evaluated prototype slip-PMGs should give sufficient insight into the the operational characteristics of the various technologies and are also adequate to verify the FE predicted results.

The SL machine shown in Fig. 6.3(a) with solid bar-coils is a very simple unoptimised structure which fits within the dimensions of the DL machine in Fig. 6.3(b) and (c). As a first iteration for the DL slip-PMG as shown in Fig. 6.3(b) use is made of a wounded slip-rotor due to the difficulty of connecting the two adjacent solid bar-coils in series. However, as shown it is possible to short-circuit each coil individually which means that solid-bar coils can be used for the DL non overlap slip-PMG as shown in Fig. 6.3(c) similar to the SL non overlap winding slip-PMG of Fig. 6.3(a).

Fig. 6.3(d) show the overlap winding slip-PMG which is similar to squirrel cage induction machine rotors commonly used in industry with an aluminium cast cage winding. As discussed in Chapter 4 a simple, solid, flat skewed PM topology is proposed to reduce the torque ripple of the overlap winding slip-PMG as shown in Fig. 6.4(a). Due to the difficulty of fixing the very thin bars of the brushless-DC slip-PMG in Fig. 6.3(e) to the end-rings and the problem of contact resistance, a different approach is followed for the manufacturing of this machine. In this case each bar is an individually short-circuited coil with the current return path underneath the stack as shown in

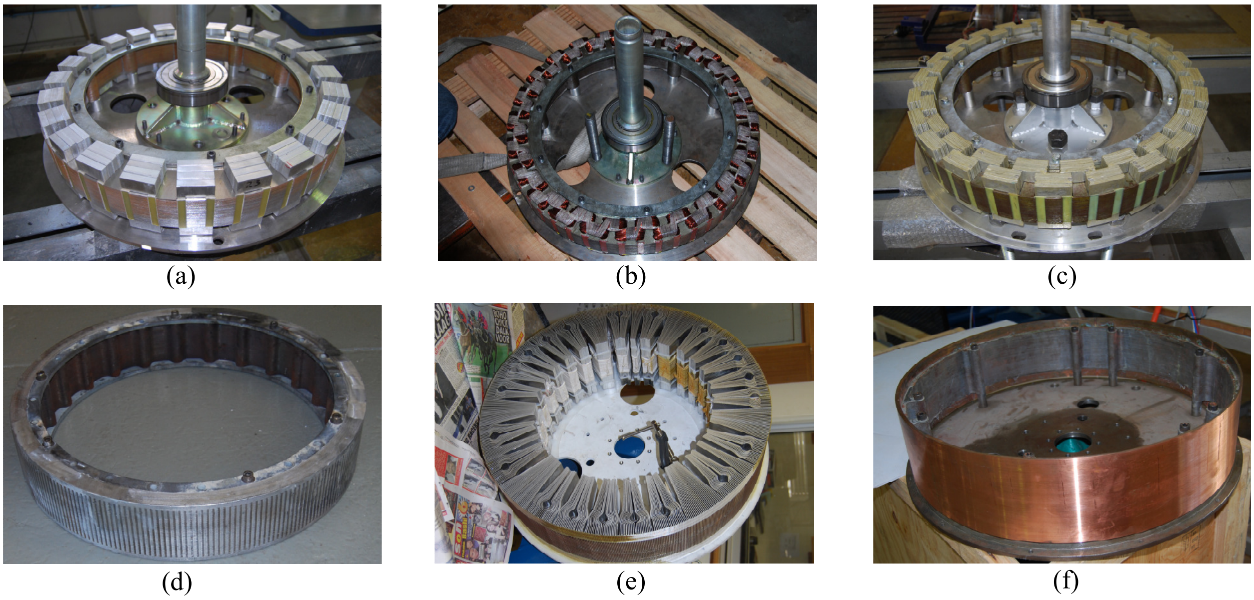
(a) (b) (c)
(d) (e) (f)

Figure 6.3: (a) SL non overlap, (b) wound DL non overlap, (c) solid bar winding DL non overlap (d) cast overlap cage winding, (e) brushless-DC and (f) conventional type eddy-current coupling [17] prototype slip-PMG slip-rotors.

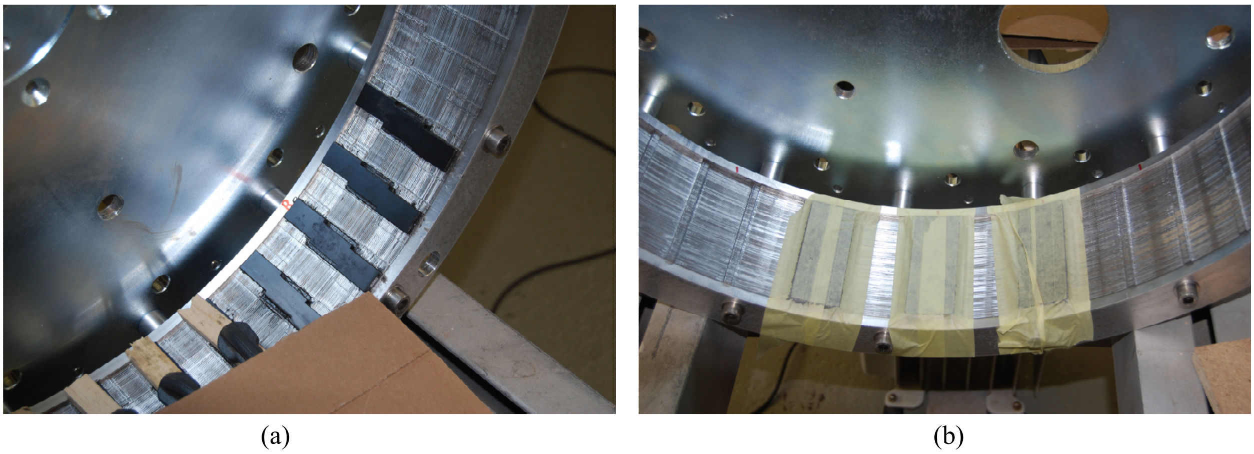
(a) (b)

Figure 6.4: Magnets being fixed for (a) the slip-PMG unit and (b) the PMSG unit side of the common PM-rotor.

Fig. 6.5. These solid bar coils are cut from very thin sheets of aluminium. The coils are shifted into position through a central opening in the lamination stack which is filled up after all the other coils are in position as shown in Fig. 6.5. Although this is not an optimum solution due to the very long current return path and, thus, high resistance, this prototype is sufficient to validate the concept of a brushless-DC slip-PMG. Fig. 6.3(f) show a conventional eddy-current coupling as evaluated in [17]. This machine structure corresponds to the eddy-current coupling topology shown in Fig. 4.2(c) and Fig. 4.3(f) in Chapter 4. A copper ring is pressed over a laminated steel yoke, with the machine designed to fit within the dimensions of the PM-rotor of the brushless-DC slip-PMG of Fig. 6.3(e).

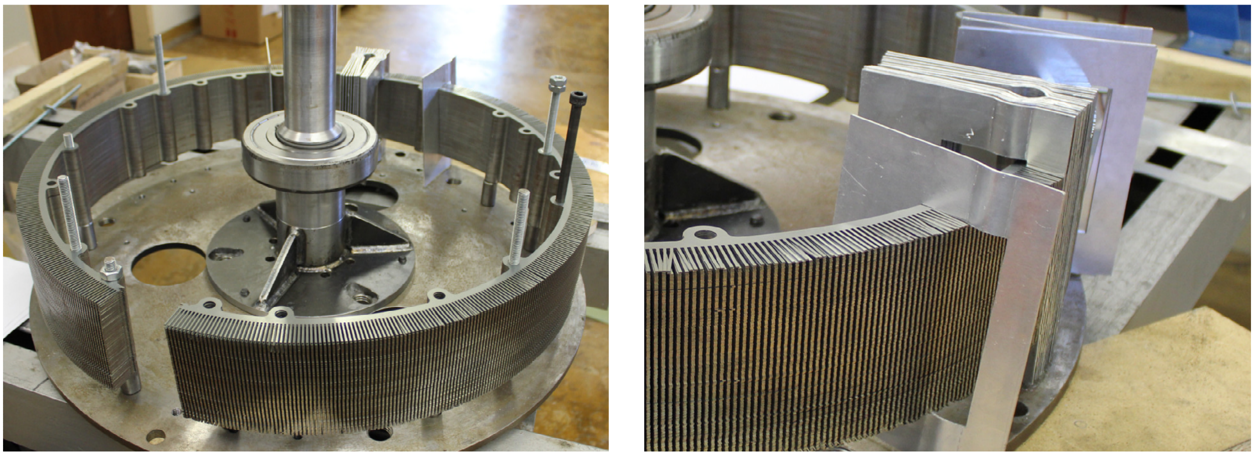

Figure 6.5: Manufacturing of the brushless-DC slip-PMG with (a) indicating the central opening and (b) indicating how the aluminium solid bar-coils are fixed into position.

6.2.2 PMSG Prototypes

For the PMSG three PM machine topologies are evaluated. The non overlap SL and DL winding PMSG stator topologies are shown in Fig. 6.6(a) and (b) respectively. Both PMSG topologies make use of preformed modular windings which are extremely easy to manufacture. The PMs of all the

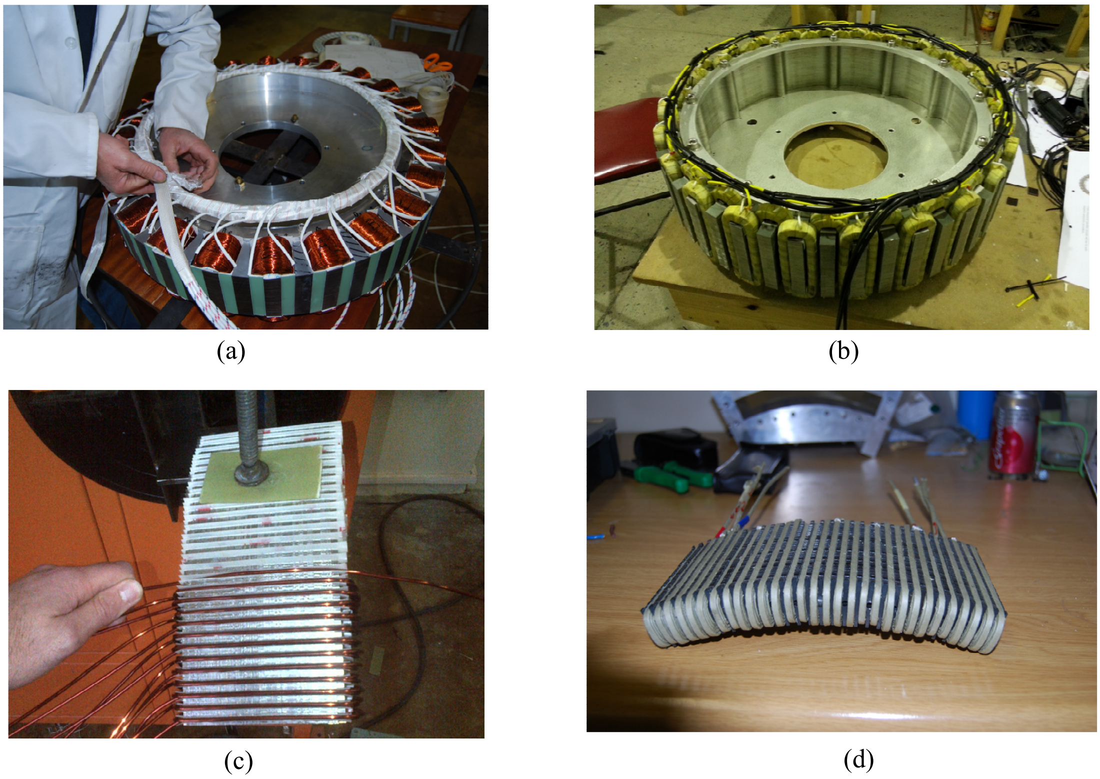

(a)

(b)

(c)

(d)

Figure 6.6: (a) SL non overlap, (b) wound DL non overlap and (c) and (d) toroidal winding PMSG wind generator topologies.

PMSGs are segmented into four segments to reduce the PM eddy current losses. The four separate segments are assembled and glued together before magnetisation to ease manufacturing. Fig. 6.4(b) show the magnets being fixed to the PMSG side of the common PM-rotor.

For the double rotor toroidal winding PMSG a segmented approach is followed for the construction as shown in Fig. 6.6(c). In this case the structure of the double rotor non overlap winding prototype presented in [13] and also evaluated in Chapter 3 is modified to include the toroidal winding stator in place of the used non overlap DL stator winding. The stator of this machine is divided in eight sections. Each section is assembled and mould in an epoxy casting which is fixed to a stator mounting plate. The stator of the toroidal winding is, thus, also divided into eight sections of which the laminates are held together with non-magnetic stainless steel clamps and bolts going through the middle of the common yoke. As shown in Fig. 6.6(d) square conductors can easily be used for the toroidal winding, which improves the fill factor.

6.3 No-Load Loss Measurements

Due to the PMSG being a fixed speed, fixed frequency generator in this case, it is important that the frequency dependent loss components (P_{ecs}, P_{ecm}, P_{wfs}, P_{cue}) be considered in the analysis. These losses are not considered in the practical analysis of the slip-PMG due to this generator only operating at slip frequency. Furthermore, due to wind turbines mostly being operated in the partially rated region the contribution of these loss components to the overall losses become even more significant.

Fig. 6.7(a) and (b) shows the FE-predicted and measured no-load loss versus rotor speed for the non overlap SL and DL winding PMSGs respectively. The no load losses versus rotor speed of the toroidal winding PMSG is shown in Fig. 6.7(c). The DL PMSG is shown to have the highest loss component by far, with the toroidal winding prototype yielding the lowest loss component. The main difference between the SL and DL prototype PMSGs is that the DL PMSG use much more PM material in order to obtain the required value of T_b. Furthermore, it is clearly seen, especially for the DL-PMSG, that there is a large difference between measured and FE-predicted results. Fig. 6.7 show the mechanical loss component, P_{wfs}, versus rotor speed calculated by means of the methods in [18]. It is, thus, clear that the no-load losses calculated by means of transient FE of the used FE package does not yield accurate results. This aspect definitely requires further investigation due to its importance regarding the specific application.

6.4 Torque quality

Only the measured no-load cogging torque for the different prototypes are shown as it is not possible to measure the load torque ripple due to the several dynamic effects caused by the driving system on the test bench. However, even measuring the no load cogging torque accurately as predicted is difficult. Due to the sensitivity of the cogging torque to dimensioned parameter changes, as more thoroughly explained in [11], even slight deviations from the specified parameters can change the cogging torque significantly. It is, thus, important that manufacturing and assembly tolerances, especially regarding the air gap and the PMs, should be kept to a minimum.

In this study to obtain a more accurate measurement of the cogging torque, a static torque measuring technique, similar to the method proposed in [179] as shown in Figs. 6.8 and 6.9 is used. This method also eliminates all transient effects within the machine itself, which means that only the cogging torque is measured. To measure the cogging torque the rotor angle is varied in discrete

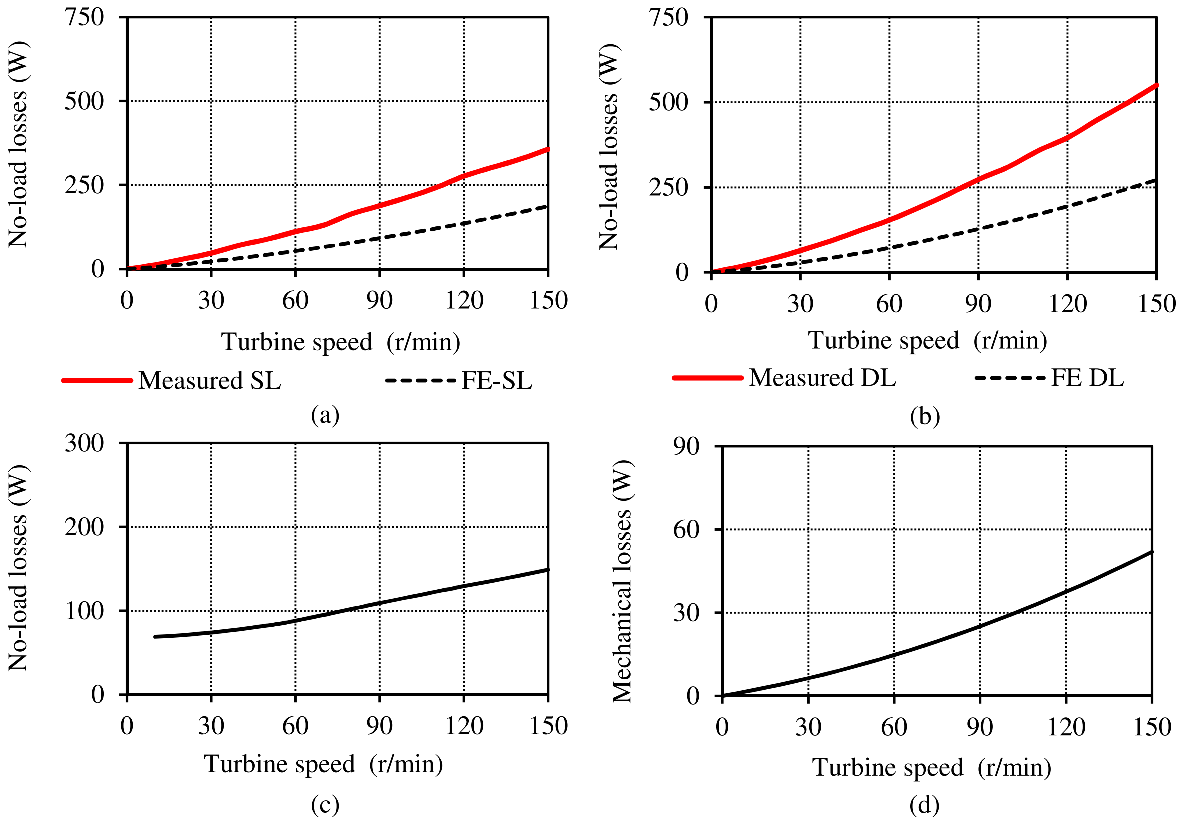

Figure 6.7: FE predicted and measured no-load loss versus rotor speed for (a) the non overlap SL, (b) DL and (c) toroidal winding PMSGs and (d) wind and friction losses from [18].

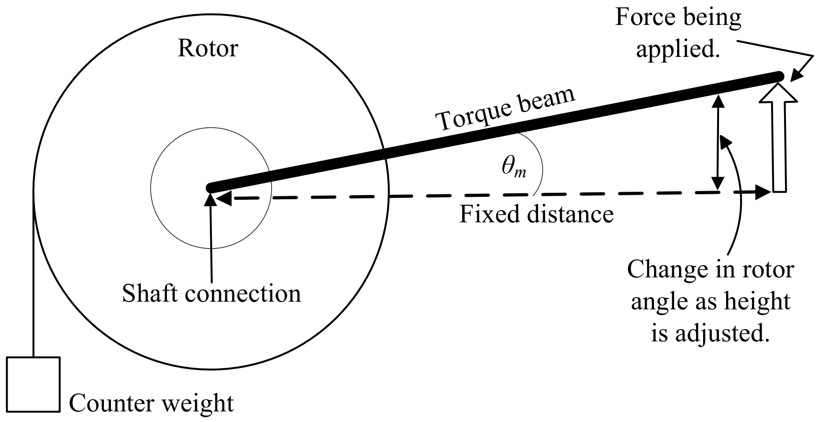

Figure 6.8: Static torque measurement setup schematic.

static steps and the static torque reading is taken at each discrete step. As shown in Figs. 6.8 and 6.9 the rotor angle is varied by applying a vertical force to the torque beam, which is connected to the machine shaft. The rotor angle can be calculated knowing that the distance from the shaft centre to the torque beam adjuster is fixed. The height to which the torque beam is set at the adjuster side corresponds to a specific rotor angle. By adjusting the torque beam in 1 mm height steps it is

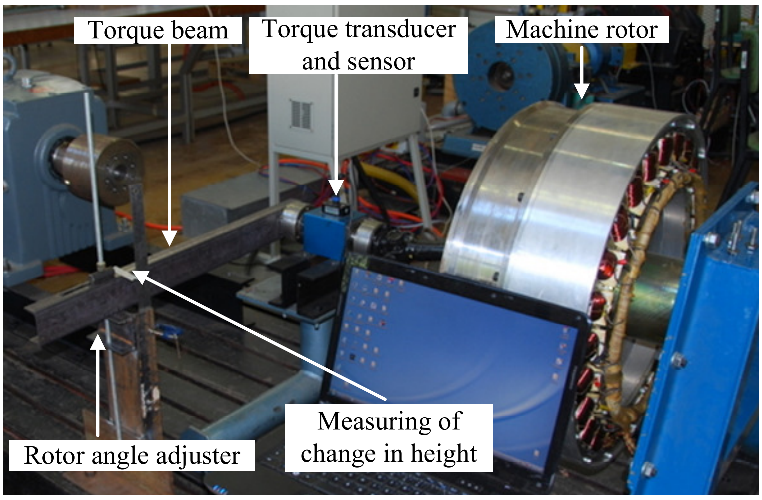

Figure 6.9: Static torque measurement setup with the drive train disconnected and the rotor angle adjuster connected to the shaft connecting the torque sensor.

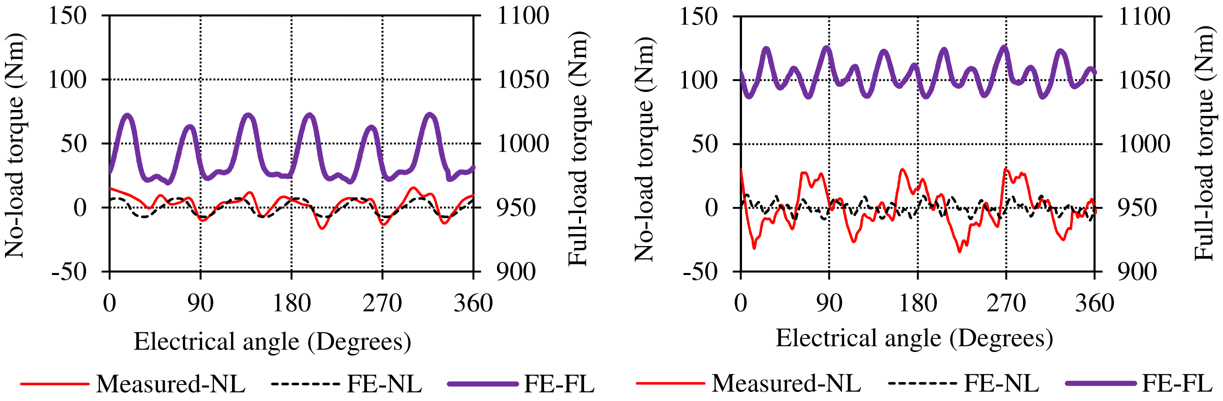

(a) (b)

Figure 6.10: FE-predicted no-load (NL) and full-load (FL) torque ripple and measured no-load torque ripple versus electrical angle for (a) the SL-PMSG and (b) DL-PMSG.

possible to obtain an angular measurement resolution of almost 0.1 degrees. To ease the taking of measurements it is advised that a counter weight is added to the machine rotor. The torque offset, which can be subtracted afterwards, allows for the measurement of only positive torque values.

Fig. 6.10(a) and (b) show the no-load cogging torque measurement of the SL and DL non overlap winding PMSGs together with the FE-predicted no-load cogging torque and rated load torque ripple. Fig. 6.11(a) and (b) show the no-load and rated load torque waveforms of the non overlap SL and DL slip-PMGs respectively and Fig. 6.12(a) and (b) for the brushless-DC and overlap cage-winding slip-PMGs. In most cases the measured no load cogging torque is shown to coincide well with the FE predicted values. The cogging torque of the DL-PMSG, however, does not match well which is caused by variations in the uniformity of the airgap due to manufacturing imperfections. Furthermore, the brushless-DC slip-PMG is clearly shown to have a much lower torque ripple than the other topologies. The cogging torque measurement of the overlap winding is also different from the FE-prediction due to manufacturing imperfections regarding the uniformity of the airgap.

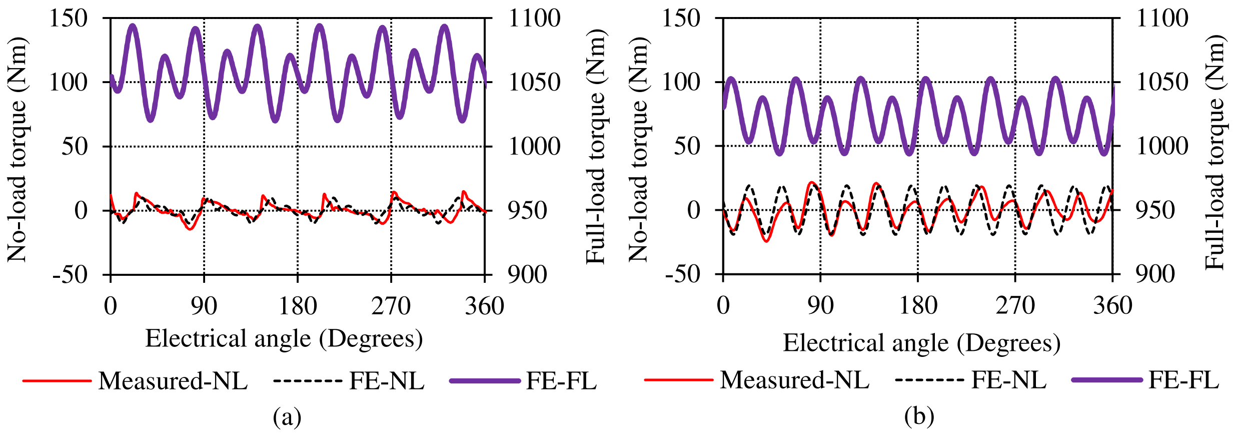

Figure 6.11: FE-predicted no-load (NL) and full-load (FL) torque ripple and measured no-load torque ripple versus electrical angle for (a) the SL slip-PMG and (b) DL slip-PMG.

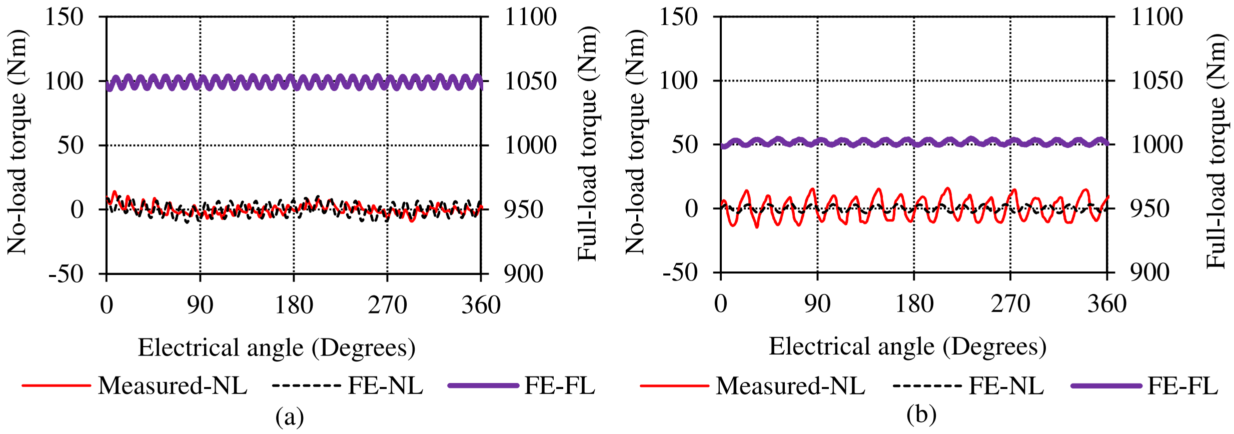

Figure 6.12: FE-predicted no-load (NL) and full-load (FL) torque ripple and measured no-load torque ripple versus electrical angle for (a) the brushless-DC and (b) overlap cage winding slip-PMGs.

However, it is still measured at about 3 % which is close to the limits set in Chapter 4.

Furthermore, it is observed that there are clear differences between the no-load cogging torque waveforms and the load torque ripple waveforms of the different slip-PMGs. There are also clear differences in the frequency content of the different torque ripple waveforms. In Chapter 2 the frequency spectrum of the load torque ripple waveforms of the SL and DL non overlap winding slip-PMGs as well as that of the brusless-DC and overlap winding slip-PMGs are shown. Both the SL and DL non overlap winding slip-PMGs have a strong harmonic component at $n = 6$ and $n = 12$. For the skewed overlap winding topology the dominant harmonic is at $n = 18$ and for the brushless-DC slip-PMG $n = 30$.

6.5 Slip-PMG Measurements

Fig. 6.13(a) shows the torque versus slip profiles of the non overlap SL and DL winding slip-PMGs (Fig. 6.3(a) and (b) respectively) and the eddy-current coupling from [17] and Fig. 6.3(f). It is seen that the non overlap DL winding machine have a higher breakdown torque value than the

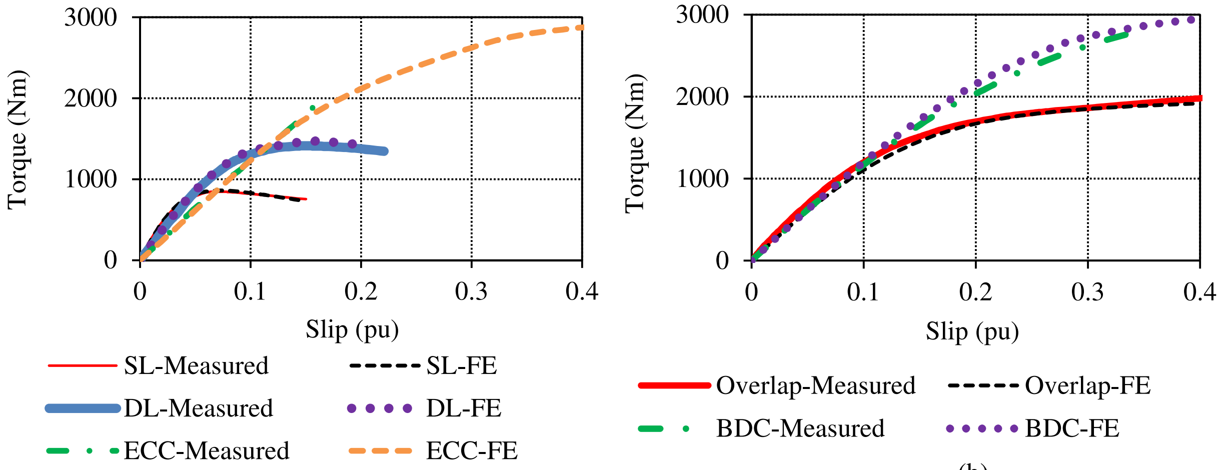

(a) (b)

Figure 6.13: Measured and FE calculated torque versus slip of the prototype (a) conventional eddy-current coupling (ECC) and non overlap single layer (SL) and double layer (DL) and (b) the overlap and brushless-DC (BDC) slip-PMGs.

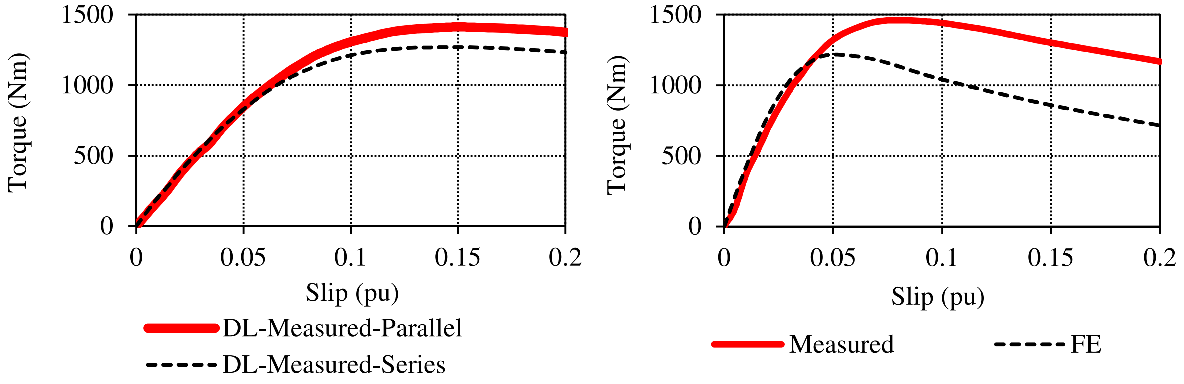

(a) (b)

Figure 6.14: Measured and FE calculated torque versus slip with (a) comparing the DL slip-PMG with the two adjacent coils in series and short-circuited individually (Fig. 6.3(b)) and (b) the new prototype DL winding with solid aluminium sheet windings as shown in Fig. 6.3(c).

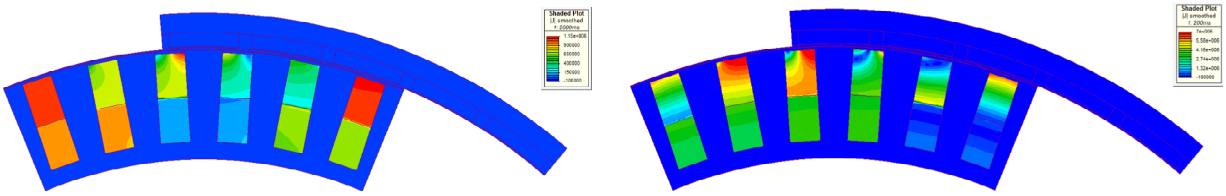

(a) (b)

Figure 6.15: Current density distribution of the DL slip-PMG of Fig. 6.3(c) at (a) $s = 0.01$ and (b) $s = 0.1$.

SL winding slip-PMG in this case. Although it is shown in Chapter 5 that both the optimum designed SL and DL slip-PMGs have more or less the same value of T_b, it is known that if the two machines have the same dimensions (as is the case for the machine structures shown in Fig. 6.3(a) and (b)) the per unit impedance of the DL winding will be less, which explains the higher maximum torque value. Furthermore, the value of T_b for the eddy-current coupling is more than double that of the non overlap winding slip-PMGs due to the very small per unit impedance of this machine.

Although the efficiency of the prototype brushless-DC slip-PMG (Fig. 6.3(f)) shown in Fig. 6.13(b) is low due to the high rated slip value caused by the long current return path, it is also shown to have a very high maximum torque value. For the overlap cage-winding slip-PMG it should be noted that the active mass and PM content of the prototype machine corresponds closely with the optimum design for the aluminium overlap winding slip-PMG in Table 4.3 in Chapter 4. However, although the value of T_b of the overlap winding slip-PMG is measured as calculated it has a higher rated slip value and lower efficiency. Due to the incorrect aluminium alloy used in the casting of the slip-rotor cage, R_r is significantly increased, which increases the rated slip and decreases η_r, which clearly shows the importance of using the correct aluminium conductor material.

Fig. 6.14(a) show the effect on the measured torque performance of the DL winding slip-PMG if the series connections of the two adjacent DL coils are removed and each coil is short circuited individually. Not only does the manufacturing complexity of the DL slip-PMG decrease, but a slight increase in torque performance is also observed in Fig. 6.14(a). The result of this modification is that the wound rotor of Fig. 6.3(b) can be replaced by the solid bar-coil winding of Fig. 6.3(c). As shown in Fig. 6.14(b) the measured rated slip now occurs at a value of 0.03, which yields an efficiency of 97 %.

However, in this case it is shown that the maximum torque is predicted incorrectly by FE even though all the end effects as explained in Chapter 3 are taken into account. The measured value of T_b is about 17 % higher than that calculated by FE. However, as shown in Fig. 6.3(c) the solid bar coils consist of several stacked aluminium sheets. The reason for not using solid conductors is due to the thinner sheets being much cheaper to laser cut than the thicker ones, even though the part count increases. Furthermore, due to the low slip frequency it was initially assumed that the skin effect will not play a role in the performance of the machine. However, as shown in Fig. 6.15(a) for $s = 0.01$, and (b) for $s = 0.1$, the current density distribution in the bars clearly become less uniform for higher slip values. This phenomenon seems to give the best explanation for the difference between FE and measured results in Fig. 6.14(b). For the non overlap SL slip-PMG of Fig. 6.3(a), of which the bar windings comprise of four segments, the segmented configuration yield a value for T_b of 16 % less than a solid bar-coil configuration. There are also several other effects such as the shape of the bars as well as deep bar effects, which should definitely be investigated further.

6.6 Electromagnetic Braking

For simplicity the prototype wind turbine system make use of an electromagnetic brake instead of mechanical or aerodynamic braking to bring the generator to a standstill. It is, thus, also important to know the correct short-circuit torque profiles of the PMSG unit to ensure that the generator can develop sufficient torque to brake the turbine and also to select the correct braking resistance value.

Fig. 6.16(a) show the wind turbine curves at $v_w = 12$ m/s and at $v_w = 12.5$ m/s with the generator torque profiles of the SL-PMSG also shown. The effects are shown for ignoring both the end-winding inductance and the end effects in the PMs. It is clearly seen that if the end-effects are ignored it could have large implications as to what wind speed the generator is capable of braking the turbine at. It is also seen that the maximum turbine torque is in the region of about 120 r/min for the shown turbine torque curves. Fig. 6.16(b) show how the braking curves of the

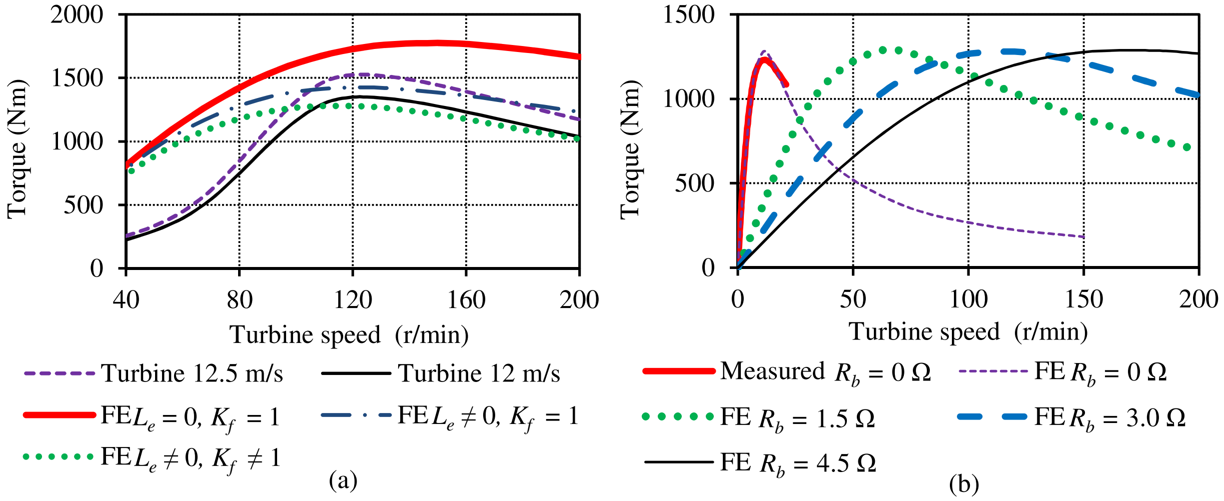

(a) (b)

Figure 6.16: (a) Turbine torque profiles and electromagnetic braking torque of the SL-PMSG with the end-effects ignored and taken into account versus turbine speed and (b) torque versus speed for the SL-PMSG for different values of the braking resistance.

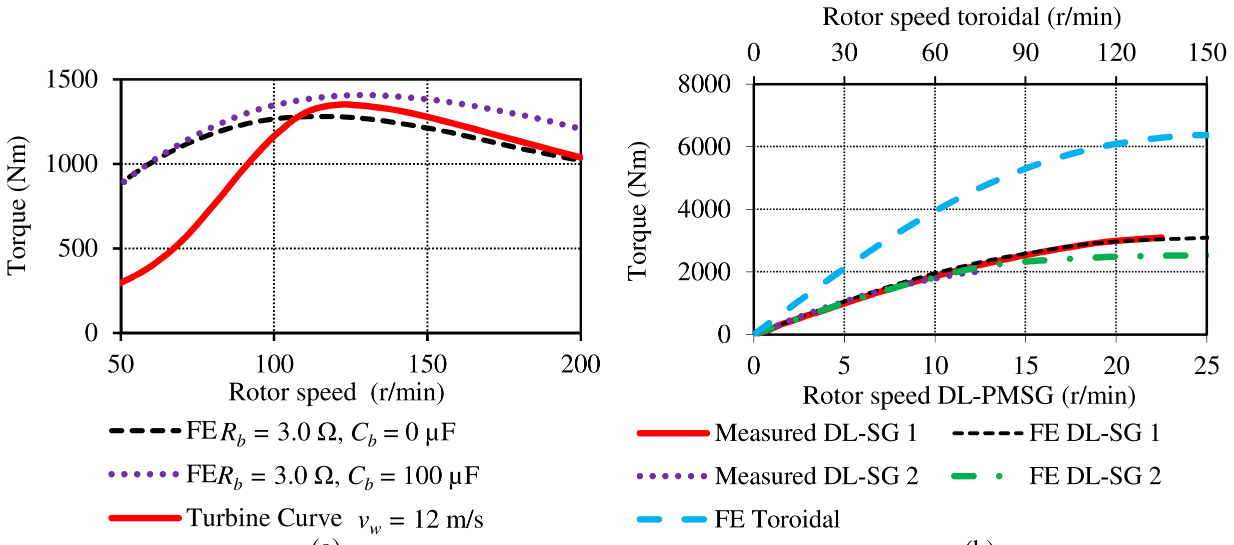

(a) (b)

Figure 6.17: (a) Torque versus speed for the SL-PMSG with only a resistive brake and with a braking capacitance bank added shown with a 12 m/s turbine torque curve. (b) Measured and FE predicted short-circuit torque versus speed curves for DL-SG 1 (Fig. 3.2(d) in Chapter 3), DL-SG 2 (Fig. 6.6(b)) and the toroidal winding PMSG (Fig. 6.6(c)) with all end-effects taken into account.

generator are shaped with different values of R_b in order to indicate the importance of selecting the correct value of R_b. It is seen that by changing the resistance value the peak is not affected but only the rotor speed at which the maximum braking torque occurs. To at least allow the case study SL-PMSG to brake safely up to a wind speed of 12 m/s Fig. 6.17(a) shows how the braking torque can be slightly increased by adding an external capacitance in conjunction with the braking resistors. The capacitance mitigates the effects of the higher inductance of the prototype SL-PMSG to some extent. Although the case study SL-PMSG do not comply with the limits set in Chapter 5, it is shown that the case study DL-PMSG as shown in Fig. 3.2(d) in Chapter 3 (DL-SG 1), the case study DL-PMSG from Fig. 6.6(b) (DL-SG 2) and also the toroidal winding PMSG shown in Fig. 6.6(c) all yield maximum torque values above 2000 Nm which is the minimum requirement specified. Furthermore, with the toroidal winding PMSG designed to fit within the dimensions of DL-SG 1, it is shown that this generator develops double the amount of torque for the same mass and PM content.

6.7 General Synchronous Machine Tests

General synchronous machine tests relates to the classical open circuit and short circuit tests, as explained in [134], which is being conducted on the different PMSG prototypes considered in this study. In this section the open circuit voltage waveforms of the different machines are first observed at rated speed. This is followed by the measurement of the open circuit voltage magnitude and short circuit current at different rotor speeds in order to calculate the per phase inductance. Fig. 6.18(a) show the per phase equivalent circuit for the machine during the open circuit test, Fig. 6.18(b) for the short circuit test and Fig. 6.18(c) with a resistance added across the generator terminals.

6.7.1 Voltage Waveforms

Fig. 6.19(a) and (b) respectively show the open circuit phase and line voltage waveforms at rated speed of $n_s = 150$ r/min for the SL-PMSG. It is evident that in both the phase and line voltages a clear harmonic content is visible, which in turn will have an effect on the harmonic content of the current fed into the grid. Fig. 6.20(a) and (b) respectively show the open circuit line voltages of the prototype DL-PMSG and toroidal winding PMSG. It is clear that the DL-PMSG has the best voltage quality with the lowest harmonic content observed in the open circuit voltage waveform. Fig. 6.21(a) show the induced voltage per coil and Fig. 6.21(b) show the per phase induced voltage of the toroidal winding PMSG. The waveform of Fig. 6.21(a) is very similar to the brushless-DC waveforms of the slip-PMGs in Chapter 4. Furthermore, observing Figs. 6.20(b) and Fig. 6.21(b) it is seen that phase and line voltage waveforms are clearly different regarding harmonic content due to the elimination of the third order harmonic resulting from the three phase connection.

6.7.2 Open Circuit and Short Circuit Tests

Fig. 6.22(a) and (b) shows the FE predicted and measured open circuit RMS phase voltages versus rotor speed for the SL-PMSG and DL-PMSG respectively. Fig. 6.23(a) show the open circuit phase

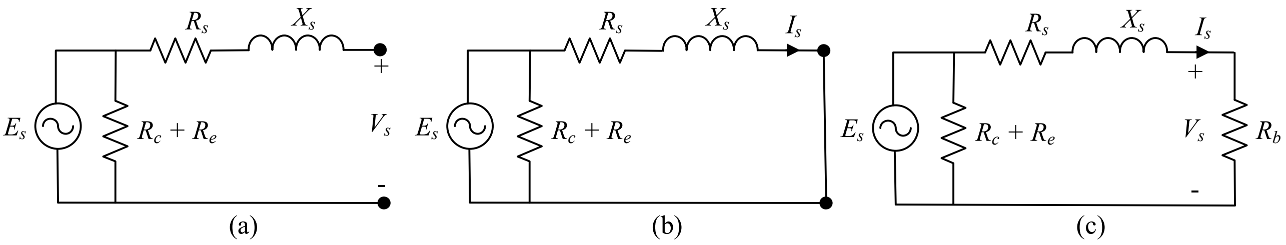

Figure 6.18: Circuit diagrams for (a) open circuit test, (b) short circuit test and (c) circuit with a resistance added across the generator terminals.

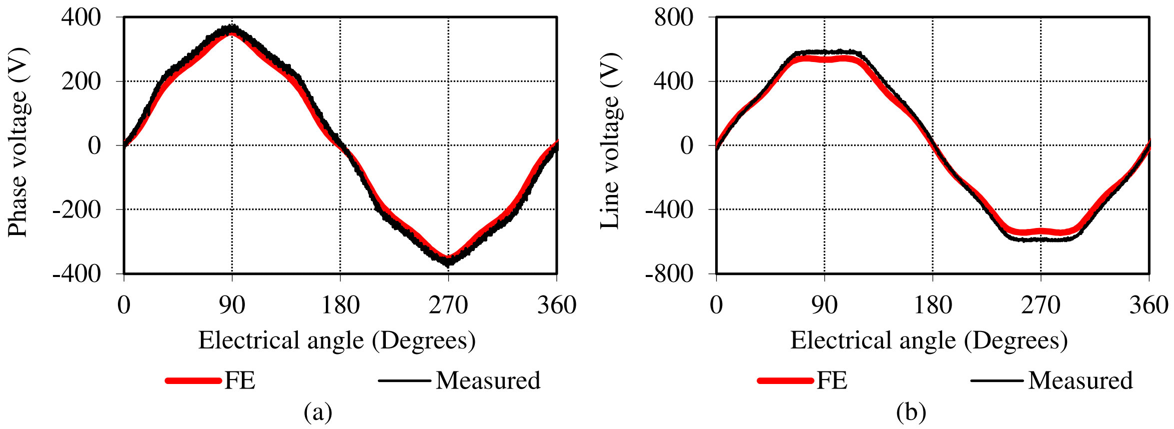

(a) (b)

Figure 6.19: FE-predicted and measured open circuit (a) phase and (b) line to line voltage waveforms versus electrical angle at rated rotor speed for the SL-PMSG.

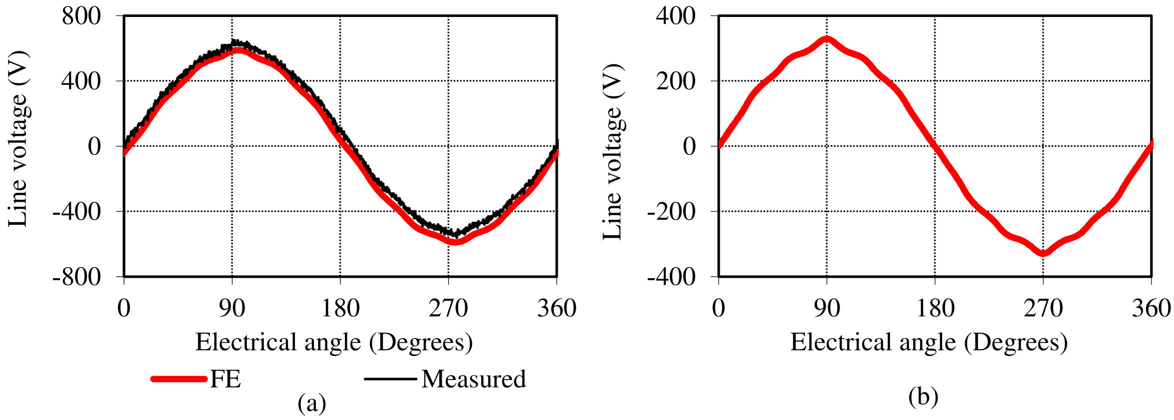

(a) (b)

Figure 6.20: FE-predicted and measured open circuit line voltage waveforms versus electrical angle at rated rotor speed for (a) the DL-PMSG and (b) toroidal winding PMSG.

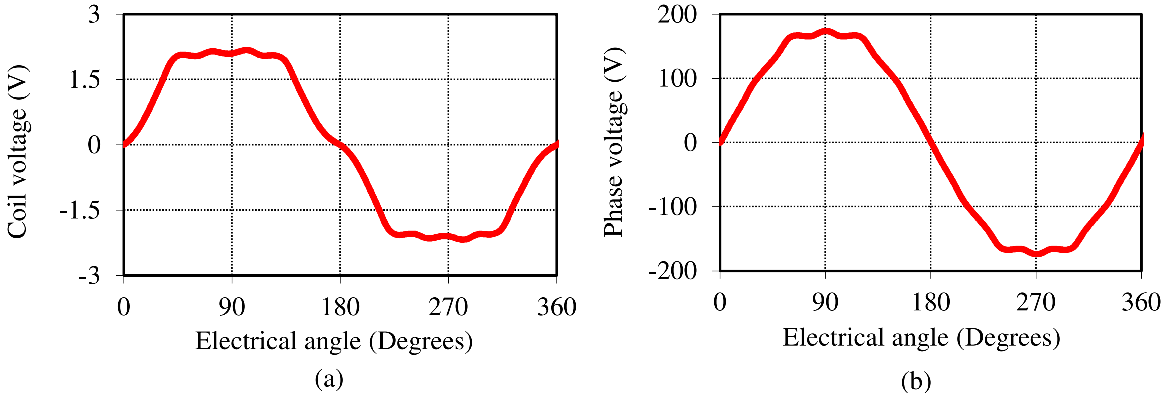

(a) (b)

Figure 6.21: FE-predicted open circuit (a) per coil and (b) per phase voltage waveforms versus electrical angle at rated rotor speed for the toroidal winding PMSG.

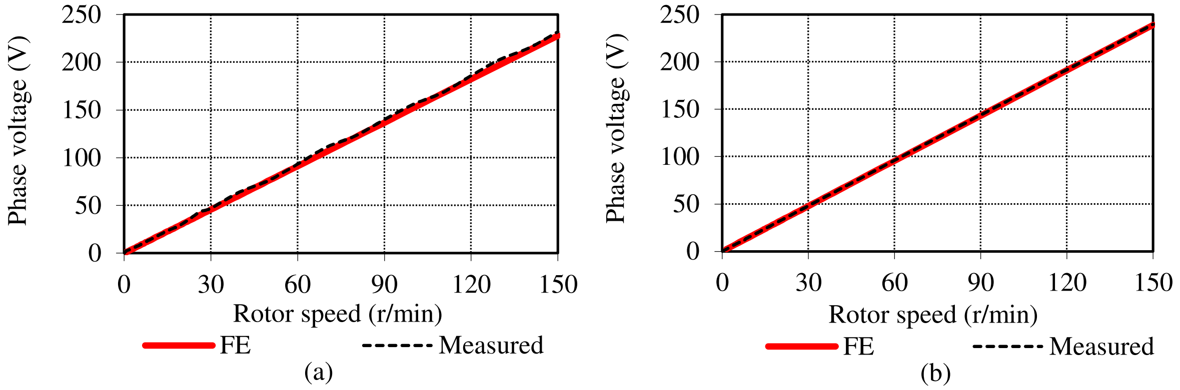

Figure 6.22: FE-predicted and measured open circuit phase voltage versus rotor speed for (a) the SL-PMSG and (b) the DL-PMSG.

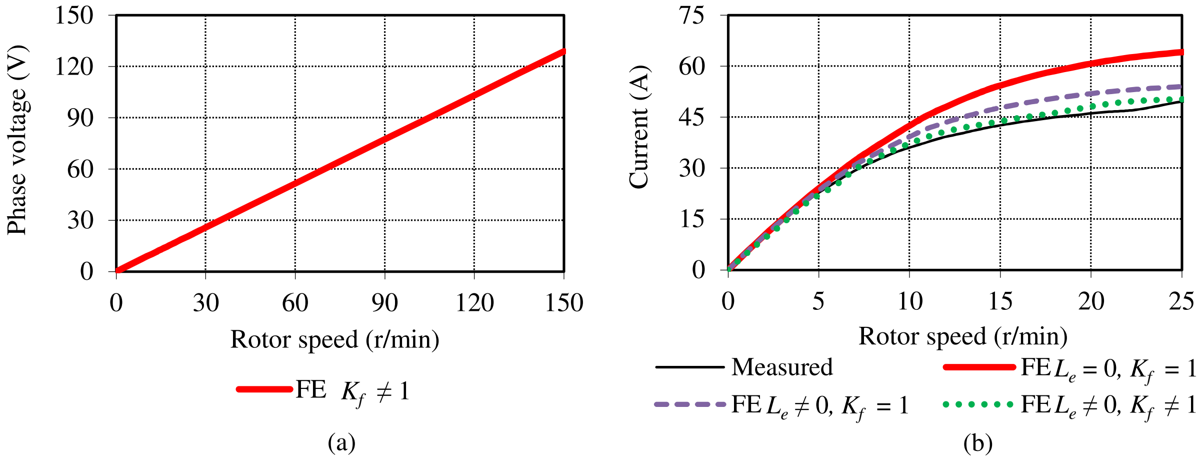

Figure 6.23: (a) Open circuit phase voltage versus rotor speed of the toroidal winding PMSG. (b) Measured and FE predicted short-circuit current (I_{rated} = 23 A) versus rotor speed of the SL-PMSG with the end-effects ignored and taken into account.

voltage versus rotor speed for the toroidal winding PMSG. The PM end-effects are taken into account in all cases by means of 2D-FE as explained in Chapter 3 by reducing the PM strength by 5 %. As seen in Fig. 6.22(b) the rated voltage value at 150 r/min for the DL-PMSG is slightly higher than the design value of 230 V. The reason for the higher per phase voltage of the DL-PMSG is due to inaccuracies in the manufacturing of the DL-PMSG, with the result being that the air gap of this machine is slightly smaller than the original design value. The FE results shown are for the air gap deviation taken into account.

As explained in Chapter 3 it is very important to take the end-effects into account in both the PMs and the end-windings, when predicting the short circuit performance of PM machines. This aspect is clearly shown in Fig. 6.23(b) where the short circuit current is calculated in FE for the SL-PMSG with all the end-effects ignored; with the end-winding inductance taken into account, but with the PM end-effects ignored; and finally with both the end-winding and PM end-effects taken into account with the methods proposed in Chapter 3. It is clear that significant differences between FE-predicted and measured short circuit performance can occur if the end-effects are ignored, especially

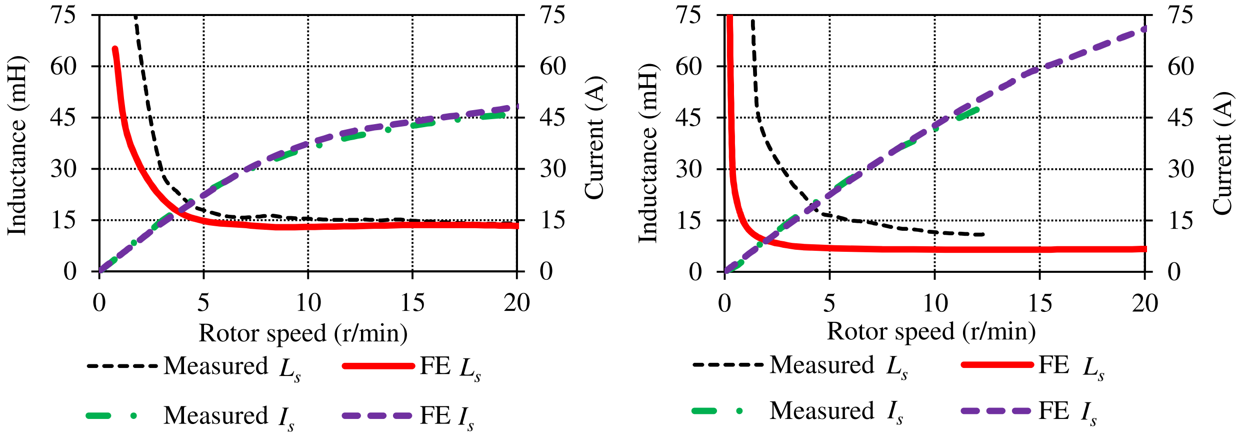

(a) (b)

Figure 6.24: Measured and FE predicted short-circuit current ($I_{rated} = 23$ A) and per phase inductance versus rotor speed of (a) SL-PMSG and (b) DL-PMSG.

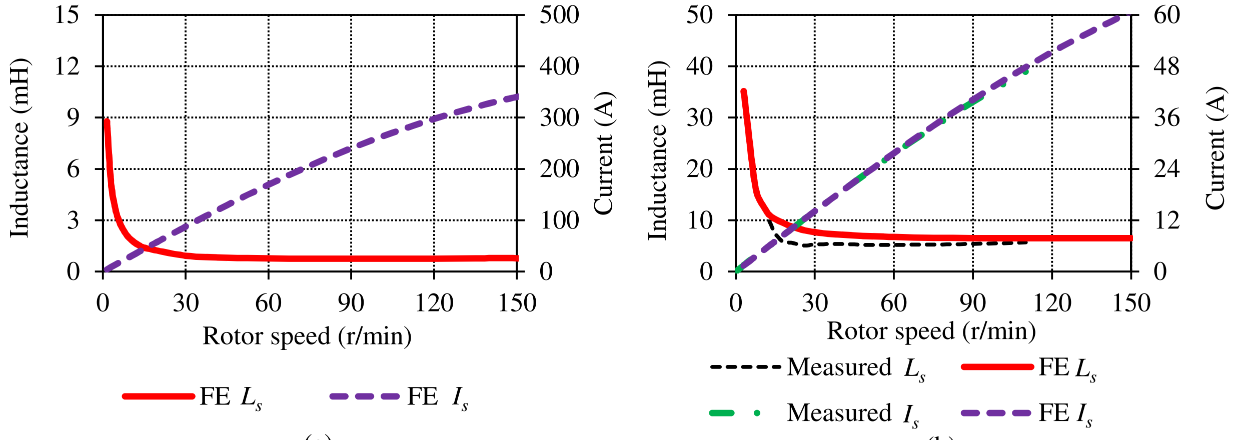

(a) (b)

Figure 6.25: (a) FE calculated short circuit current and per phase inductance of the toroidal winding PMSG. (b) Measured and FE predicted current ($I_{rated} = 23$ A) and per phase inductance versus rotor speed of the DL-PMSG with a resistance of 3 Ω added.

in the above rated region.

Fig. 6.24(a) and (b) show the measured and FE predicted short circuit current and per phase inductance of the DL-PMSG and SL-PMSG calculated by means of the open circuit voltage and short circuit current. Due to limitations of the test bench used, with a maximum allowable torque of 2000 Nm, the full short circuit current profile of the DL-PMSG could not be measured. Fig. 6.25(a) show the short circuit current and per phase inductance of the toroidal winding PMSG. Due to dynamic effects caused by the drive and the much more significant effect of the cogging torque at low speeds, it was found to be very difficult to measure the short-circuit current and open circuit voltage at these low speeds. Thus, a resistance is added across the terminals of the machine as shown in Fig. 6.18(c) (in this case the braking resistance with $R_b = 3$ Ω) to increase the speed at which the rated current of the machine occurs. Fig. 6.25(b) show the short circuit current and the per phase inductance for the case where the resistance is added. It is seen that a much better match is obtained between the measured and FE-calculated per phase inductance.

The same tendency, for both the FE calculated and measured per phase inductance, of all the PMSG topologies to have a considerably higher value of L_s at lower current values are observed. With $L_s = V_s/I_s$, as $I_s \to 0$, $L_s \to \infty$, which seems to explain this observed tendency.

6.8 Toroidal Winding PMSG Performance

As the toroidal winding PMSG is manufactured by modifying an existing PMSG topology it is mechanically not capable of being operated in conjunction with a slip-PMG unit. Thus, only the performance of the non overlap SL and DL winding PMSGs are evaluated for the machines connected directly to the grid. Unfortunately the toroidal winding PMSG is still being manufactured, which is the reason why only the FE-calculated results for this machine is shown.

Machine tests are conducted for the toroidal winding PMSG by connecting the machine to a resistance load as shown in Fig. 6.18(c). This resistance value is made variable with the rotor speed being fixed at $n_s = 150$ r/min to imitate the performance of the machine as if directly grid connected. This should provide sufficient representation of the machine performance due to the rated power factor of the toroidal winding PMSG being basically unity as shown in Chapter 5. Fig. 6.26(a) and (b) respectively show the electrical output power and efficiency of the toroidal winding PMSG versus load torque.

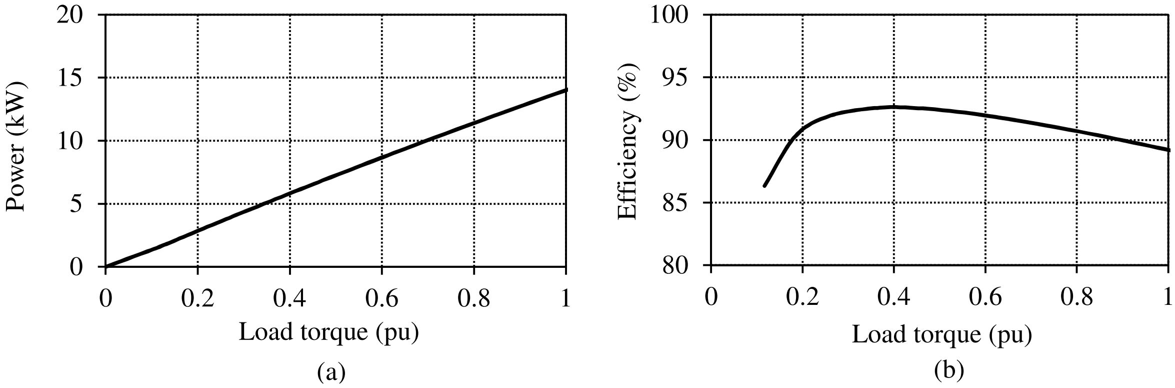

Figure 6.26: (a) Electrical output power and (b) efficiency of the toroidal winding PMSG versus load torque.

6.9 Summary

In this chapter several different slip-PMG and PMSG topologies are practically evaluated. A significant issue identified is the inability of the used FE program to accurately estimate the no load losses of the PMSG. This aspect is of extreme importance for the direct grid, fixed frequency SS-PMG, due the partial load efficiency of the generator being significantly influenced. Regarding the torque quality of the different machine topologies a good match is obtained between the FE-predicted and static measured no load cogging torque in most cases, except for the cases where there were significant air gap variations due to manufacturing tolerances.

Although it would normally be assumed that the skin effect can be negligible due to the low electrical frequency of the slip-PMG it is shown that this is not valid for the calculation of the maximum torque and care should, thus, be taken in the selection of the solid conductor dimensions. Further, aspects such as the deep bar effect and the shape of the conductors definitely needs to be investigated further in future studies. For the short circuit performance of both the PMSG and slip-PMG units, the importance of taking the end-effects into account is clearly seen, as significant deviations between the measured and FE predicted results can occur if ignored. Furthermore, in the calculation of the per phase inductance with the open circuit and short circuit tests it is seen to be very difficult to measure the inductance at low load values due to the dynamic effects on the test bench at low speeds. A proposal is, thus, made in this chapter to conduct the short-circuit test with a resistance added across the generator terminals in order to increase the rotor speed at which the per phase inductance is calculated. A much better measurement is shown to be obtained of the per phase inductance in this case.

Chapter 7

Directly Grid-Connected SS-PMG Measurements

In this chapter two prototype SS-PMGs are practically evaluated, connected directly to the grid. SS-PMG 1 consists of the non overlap SL-PMSG of Fig. 6.6(a) and the non overlap DL-slip-PMG of Fig. 6.3(c), in Chapter 6. SS-PMG 2 consists of the non overlap DL-PMSG of Fig. 6.6(b) and the overlap cage winding slip-PMG of Fig. 6.3(d), in Chapter 6. Practical tests are conducted in the laboratory and both SS-PMG systems are also installed in the field (field test site wind data given in Appendix C) where it is interfaced with a 15 kW wind turbine system as in Appendix B.

7.1 Laboratory Test Setup

Figs. 7.1 and 7.2 show SS-PMG 1 and SS-PMG 2 respectively on the laboratory test bench. Fig. 7.3 show the top level schematic of Fig. 6.1 in Chapter 6, modified to include the grid connection of the SS-PMG to the laboratory grid. As shown in Fig. 7.3 the electrical engineering building is fed by two 1 MVA transformers (T_1 and T_2). In order to provide isolation between the variable speed drive and the grid connection of the SS-PMG, the two transformer grid is utilised as a buffer, by connecting the VSD to the output of the one transformer (T_1) and the SS-PMG to the other (T_2). The isolation is necessary due to the rectifier part of the VSD distorting the voltage waveform at the

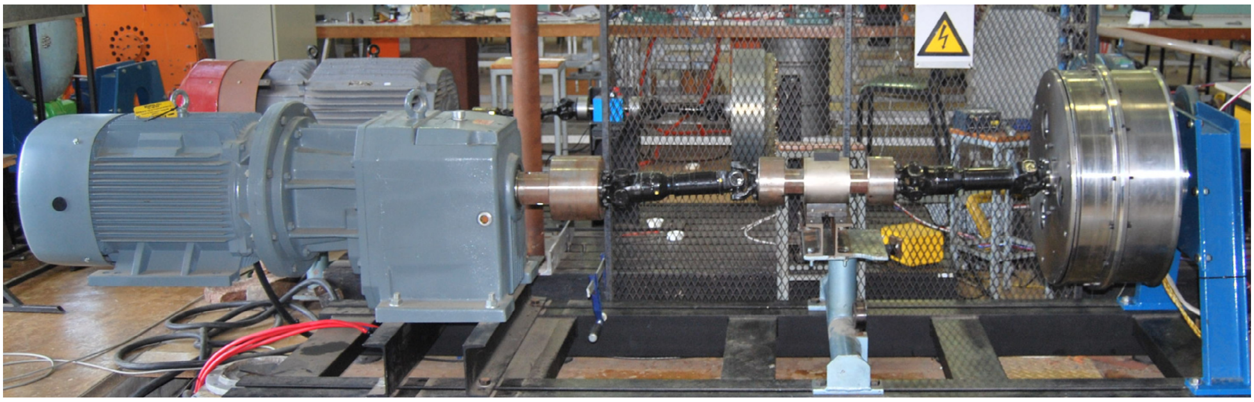

Figure 7.1: Prototype 15 kW SS-PMG 1 on the testbench connected to a driving motor on the right through a torque sensor shown in the middle.

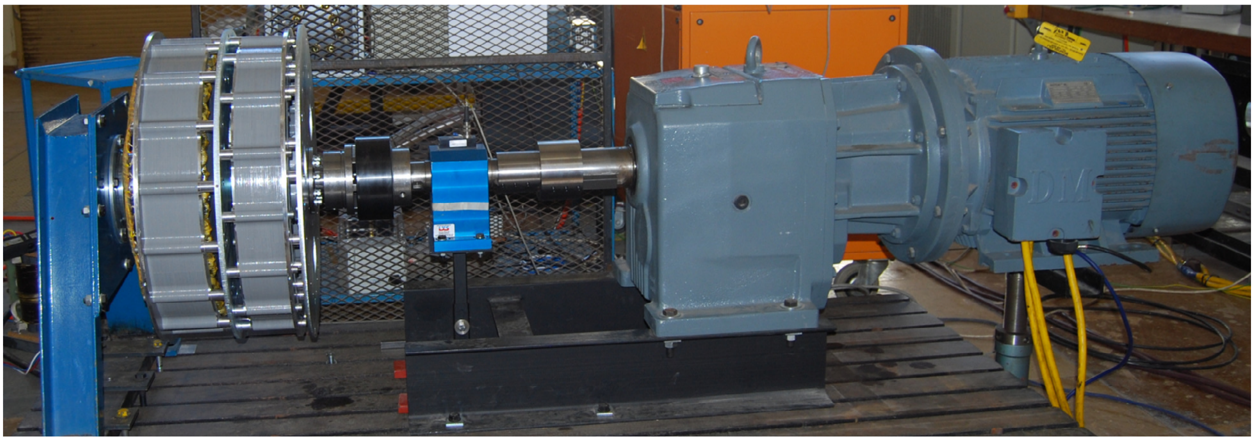

Figure 7.2: Prototype 15 kW SS-PMG 2 on the testbench connected to a driving motor on the left through a torque sensor shown in the middle.

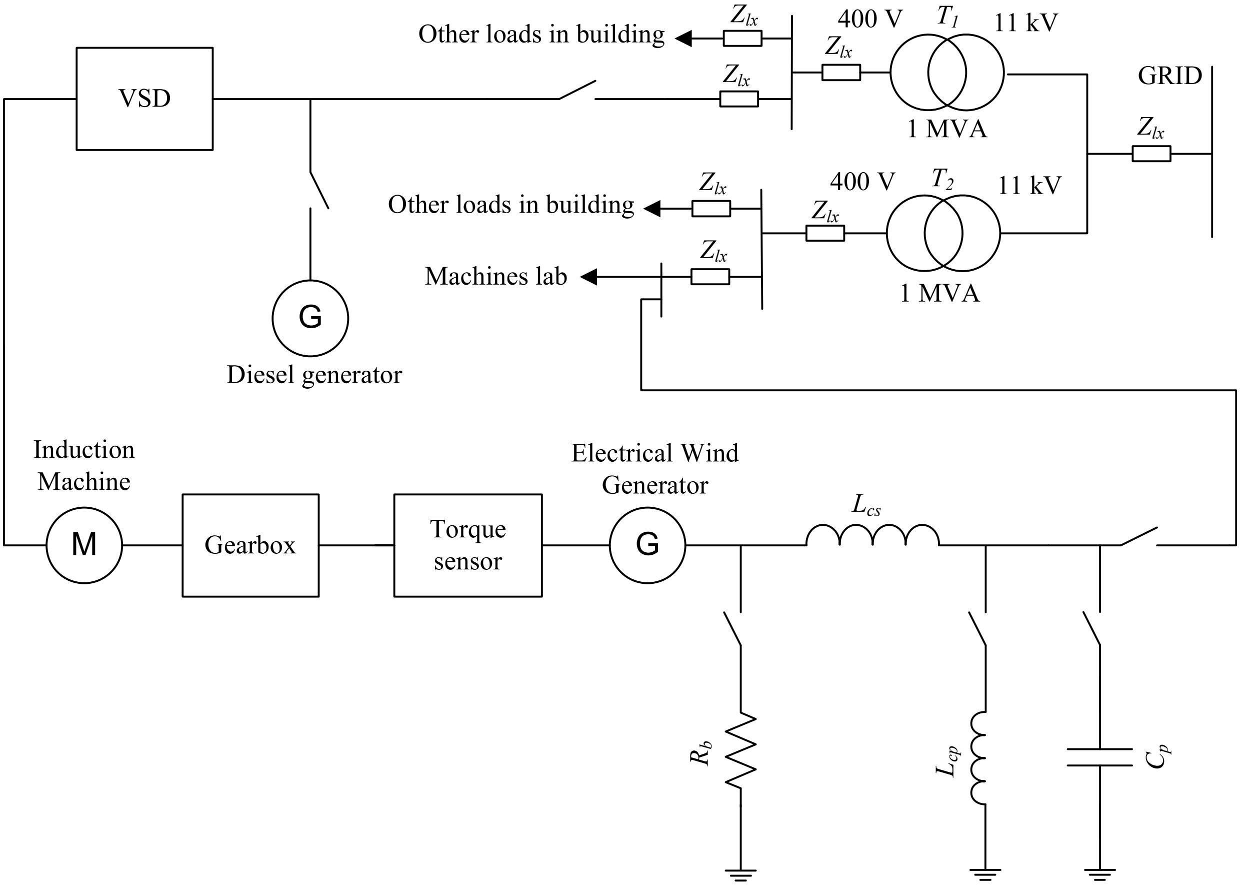

Figure 7.3: Top level schematic of the SS-PMG laboratory measuring setup.

grid connection point of the SS-PMG. As will be shown later on in this chapter, it is also found that the effective line impedance seen by the generator is different by connecting at the different grid connection points. This will affect the dynamic response of the SS-PMG as discussed in Chapter 2.

For this reason the diesel generator as shown in Fig. 7.3 is also utilised for some of the tests.

The induction motor used as a prime mover for the electrical wind generator is a 4 pole machine rated at 90 kW and is connected to the SS-PMG via a gearbox with a 15.2:1 gearing ratio. A smaller induction motor with a lower gearing ratio is also used in order to provide faster load steps as will be discussed. This is possible due to the much lower inertia, because of the lower gearing ratio of 7.6, of the smaller system. Furthermore, as will also be shown the type of coupling used to transfer the power from the driving system to the SS-PMG can significantly influence the dynamic stability of the system. The universal shaft couplings as used in Fig. 7.1 is, thus, replaced by the more rigid coupling used in Fig. 7.2.

7.2 Direct Grid Performance Evaluation

Fig. 7.4(a) and (b) show the electrical output power versus per unit load torque for the directly grid-connected SS-PMG 1 and SS-PMG 2 prototype generator systems respectively, with the rated electrical power 15 kW at 1000 Nm as shown. The line current with the rated current given as $I_s = 23$ A is shown in Fig. 7.5(a) and (b) for SS-PMG 1 and SS-PMG 2 respectively. For the direct-grid measurements, the laboratory grid voltage is measured as $V_s = 225$ V in most cases. As shown in Section 6.7 the induced voltage of SS-PMG 2 is slightly higher than the design voltage. This higher induced voltage of SS-PMG 2 explains the high current at low load values, as shown in Fig. 7.5(b), due to the large reactive power flow occurring from the voltage mismatch.

The efficiency versus load of the PMSG units of the two generator systems are shown in Fig. 7.6. Both PMSGs show a good efficiency in the region from 50 % to rated load, but a much poorer efficiency at low load values. This lower low load efficiency is due to the SS-PMG being operated at a fixed speed and grid frequency of 50 Hz. Furthermore, it is also shown that the FE calculated and measured values do not match very good at the lower load values. This is due to the underestimation of the no load losses of both PMSGs by FE, as shown in Fig. 6.7 in Section 6.3. The importance of reducing the frequency dependent losses of the direct grid PMSG is, thus, clear.

Figs. 7.7 and 7.8 show the reactive power flow and power factor of the two SS-PMGs versus load torque. Positive values for the reactive power flow indicates reactive power being delivered to the grid and negative values indicates reactive power being consumed. The grid code as given in [10] states that from 20 % power output, small scale systems need to operate between a power

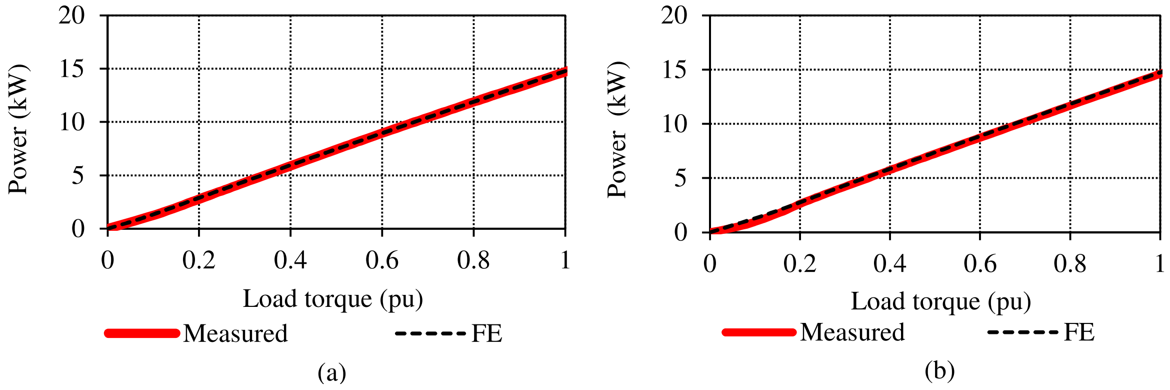

Figure 7.4: FE-predicted and measured electrical output power versus generator load for (a) SS-PMG 1 and (b) SS-PMG 2 connected directly to the power grid.

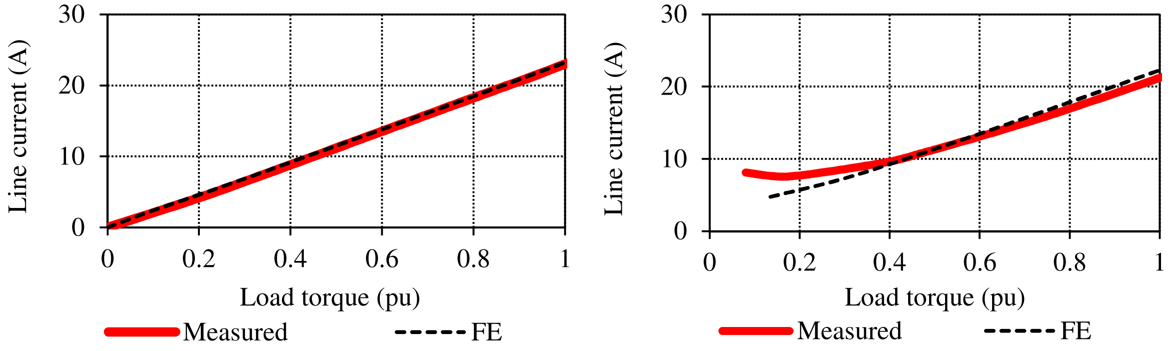

(a)

(b)

Figure 7.5: FE-predicted and measured grid current versus generator load for (a) SS-PMG 1 and (b) SS-PMG 2 connected directly to the power grid.

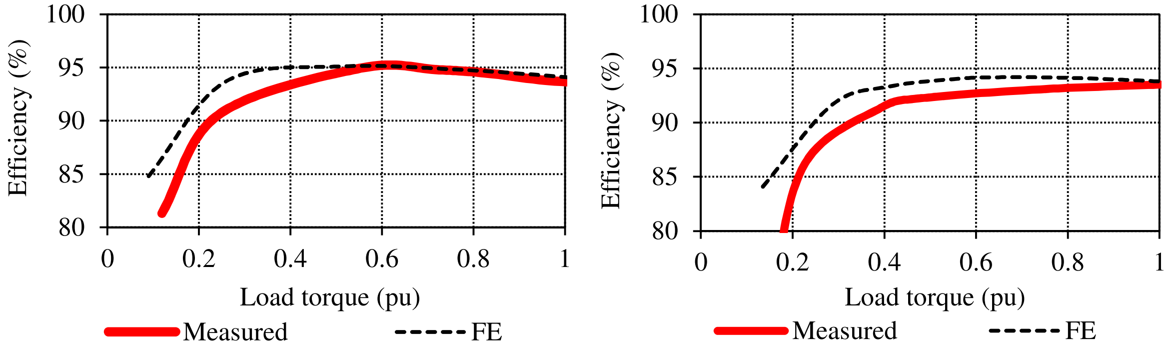

(a)

(b)

Figure 7.6: FE-predicted and measured efficiency versus generator load for (a) SS-PMG 1 and (b) SS-PMG 2 connected directly to the power grid.

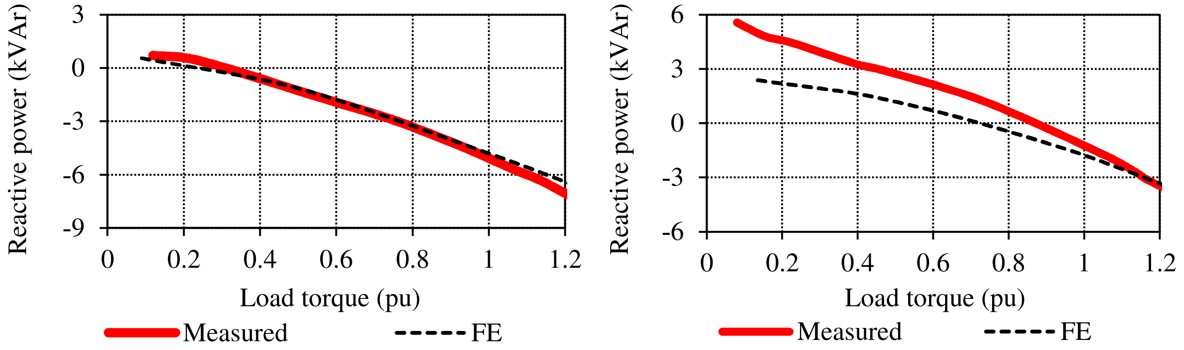

(a)

(b)

Figure 7.7: FE-predicted and measured reactive power versus generator load for (a) SS-PMG 1 and (b) SS-PMG 2 connected directly to the power grid.

factor of 0.95 leading or lagging. For small scale systems reactive power control is not required. It is seen that SS-PMG 1 complies with this limit for a RMS laboratory grid voltage of $V_s = 225$ V

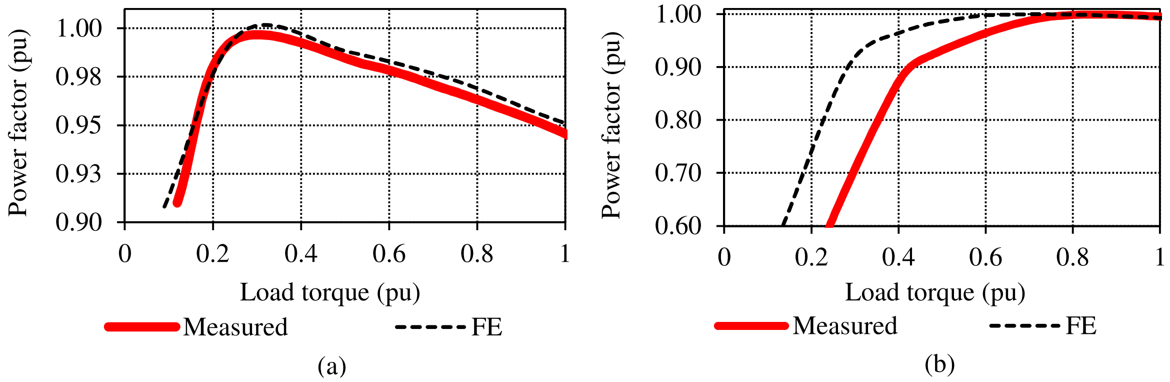

Figure 7.8: FE-predicted and measured power factor versus generator load for (a) SS-PMG 1 and (b) SS-PMG 2 connected directly to the power grid.

per phase. However, at low load values the power factor of SS-PMG 2 does not comply to the grid code specifications and a very poor power factor is observed. The reason for this poor power factor is that the induced voltage of SS-PMG 2 is too high, and due to the very low per unit impedance of this generator compared to SS-PMG 1 it is very sensitive to grid voltage variations.

7.3 SS-PMG versus Converter-fed PMSG Performance

In order to obtain some knowledge on the performance of the SS-PMG with regard to other wind generating systems the efficiencies versus wind speed of SS-PMG 1, and the PMSG-unit of SS-PMG 1 connected to the grid via a power electronic converter are evaluated. For small scale direct-drive wind turbine systems the generators usually have higher electrical frequencies due to the higher rotor speed as opposed to larger systems, which makes this comparison fair. The efficiency used for the converter is obtained for a small scale commercially available inverter as given in [180]. The data from [180] yield similar results as in [181] and [77] regarding the analysis of a small-scale PMSG and converter connected wind turbine system. For larger wind turbine systems higher efficiency values are given for the PMSG and converter systems, especially in the partially rated region.

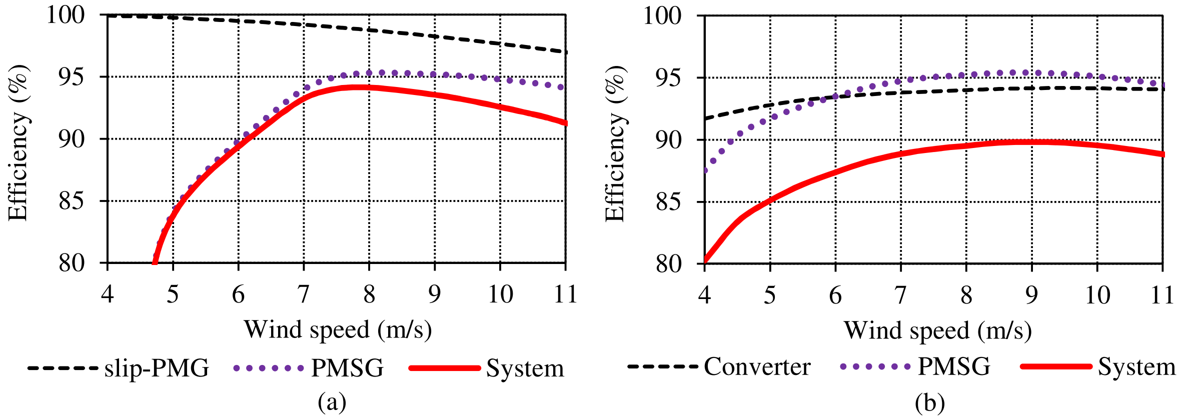

Figure 7.9: Efficiency versus wind speed for (a) SS-PMG 1 and (b) PMSG and converter connected wind turbine systems.

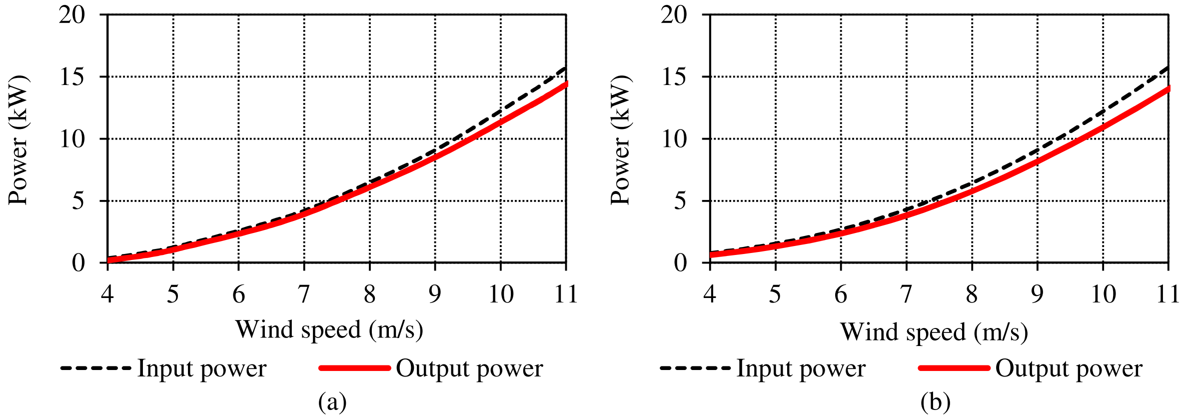

Figure 7.10: Mechanical turbine input and electrical output power versus wind speed for (a) the SS-PMG and (b) PMSG and converter connected wind turbine systems.

Fig. 7.9(a) show the efficiency of the slip-PMG and PMSG-units as well as the total SS-PMG system efficiency. In Fig. 7.9(b) the efficiencies of the converter and PMSG as well as the total efficiency of this system is shown. The fixed speed SS-PMG only have a disadvantage at very low wind speeds ($v_w < 5$ m/s) regarding generator efficiency. The high efficiency of the slip-PMG at low slip-speeds mitigates the low efficiency of the PMSG at low load values to some extent. Furthermore, power electronic converters also have lower efficiencies at low load values due to the fixed loss components such as the switching losses and the power consumed by the circuitry, which reduces the total system efficiency. Fig. 7.10(a) and (b) show the mechanical turbine input and electrical output power for the SS-PMG and the converter connected PMSG systems respectively. Due to the turbine only operating at fixed speed for the SS-PMG system, the turbine power will be less for the SS-PMG at lower wind speeds. However, in this case the SS-PMG compensates for this disadvantage to some extent by having a higher efficiency.

7.4 Grid Compliance

As explained in Chapter 5 it is specified in [10] that the generator needs to handle terminal voltage variations of +10 % and -15 % around the nominal voltage value of $V_s = 230$ V, which corresponds to V_s between 195.5 V and 253 V. For the evaluation of the harmonic content in the current waveforms the specifications from [160], where it is specified that the total harmonic distortion of the generator needs to be below 5 % are used. The generator needs to comply to these limits from a load > 0.2 pu.

7.4.1 Reactive Power

Fig. 7.12(a) and (b) show the reactive power and current at zero load versus a variation in terminal voltage. It is clear that the SS-PMG is sensitive to grid voltage variations, with undesirable reactive power flow occurring, especially for SS-PMG 2 due to its much lower per phase impedance as opposed to SS-PMG 1. As shown in Fig. 7.12(b) the reactive power flow can be curbed to some extent by adding an external impedance to the generator terminals ($X_{cs} = 2\pi L_{cs}$) as shown in Fig. 7.11. The reactive power and power factor of SS-PMG 2 are shown in Fig. 7.13 versus generator load for

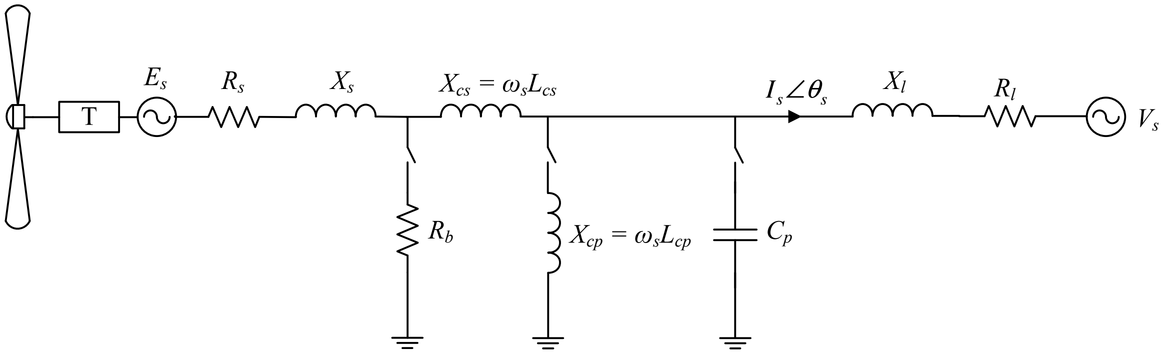

Figure 7.11: Diagram showing the SS-PMG interfaced to the network with compensation.

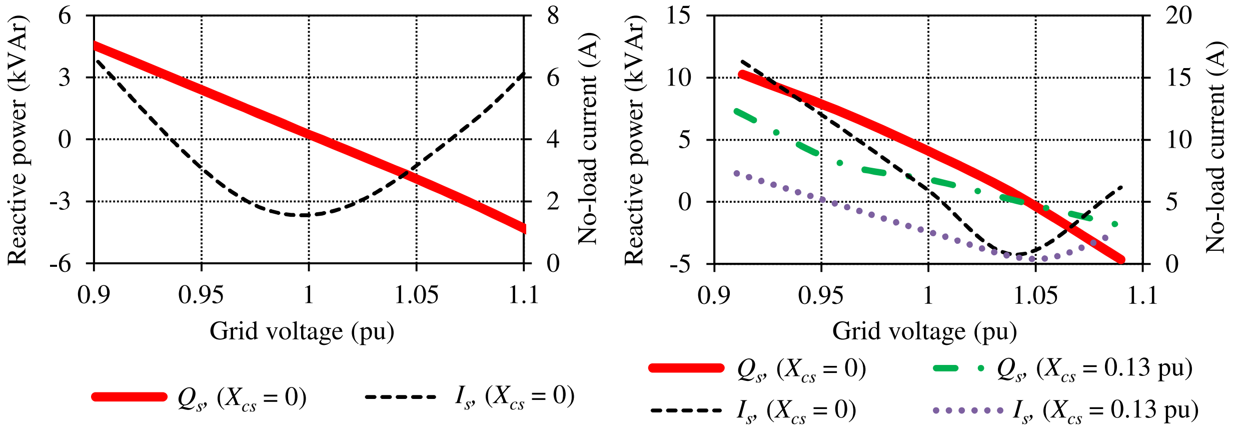

(a) (b)

Figure 7.12: Measured reactive power and current at zero load for (a) SS-PMG 1 and (b) SS-PMG 2 for $X_{cs} = 0$ and $X_{cs} = 0.13$ pu, versus grid voltage.

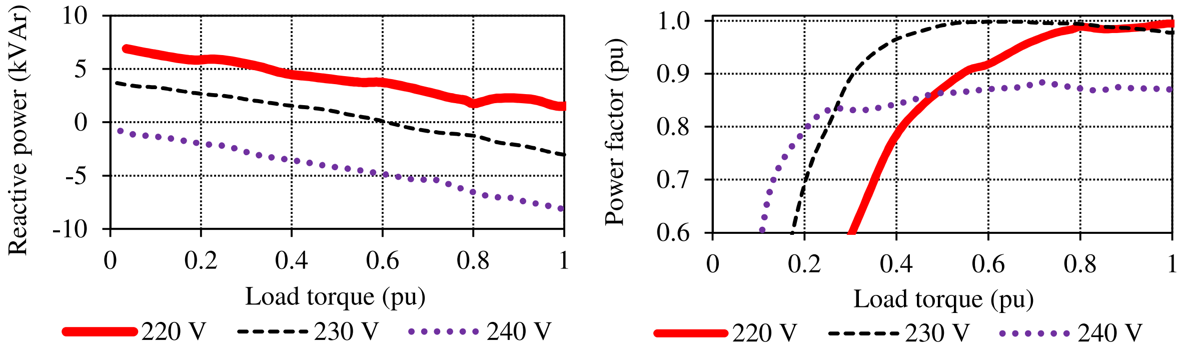

(a) (b)

Figure 7.13: FE-predicted and measured (a) power factor and (b) reactive power versus rotor speed for SS-PMG 2 connected directly to the power grid for different values of the terminal grid voltage.

different values of V_s with $X_{cs} = 0$ in this case. From Fig. 7.13 it is seen that even for variations as low as 5 % in V_s, SS-PMG 2 is unable to meet the grid code requirements.

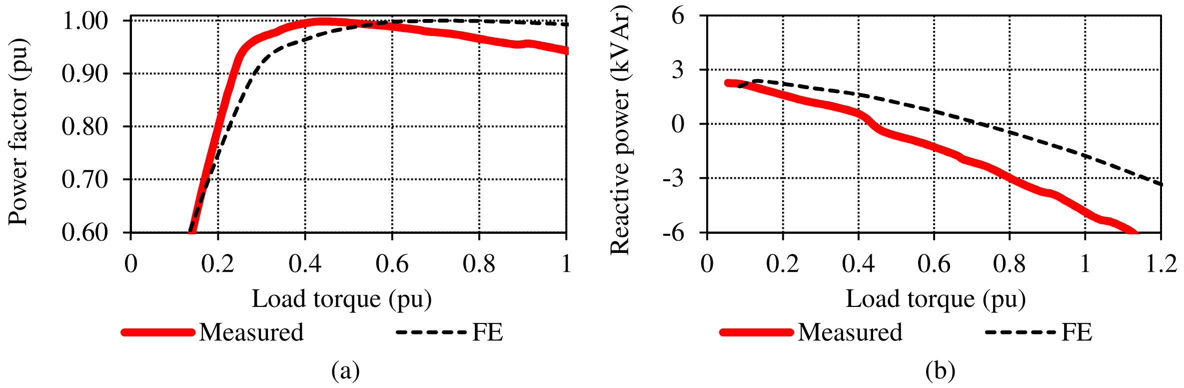

Figure 7.14: FE-predicted and measured (a) power factor and (b) reactive power versus load torque for SS-PMG 2 connected directly to the power grid with $X_{cs} = 0.13$ pu.

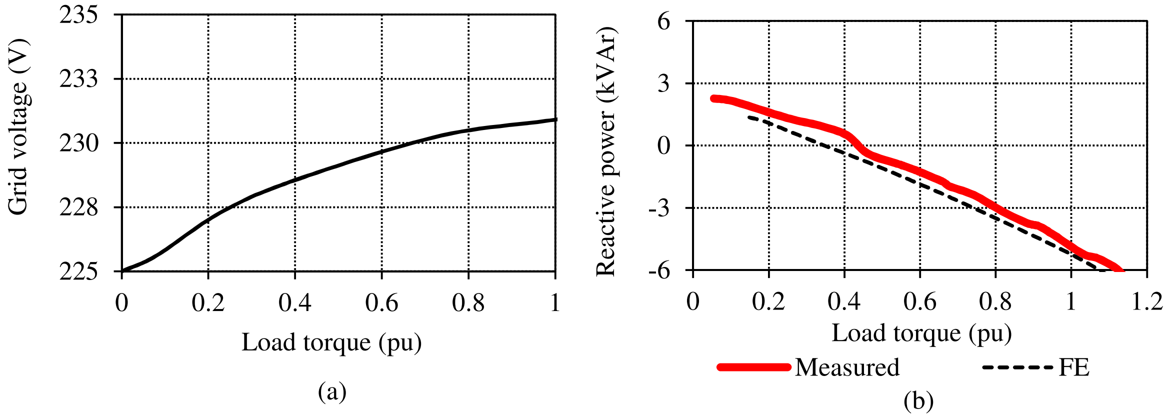

Figure 7.15: (a) Measured grid voltage versus load torque. (b) Reactive power versus versus load torque for SS-PMG 2 connected directly to the power grid with $X_{cs} = 0.13$ pu and the grid voltage made variable in the FE-analysis.

By adding the series line reactance as in Fig. 7.11 a clear improvement in the reactive power characteristics of SS-PMG 2 is observed as shown in Fig. 7.14(a) and (b) for the power factor and reactive power flow respectively. However, it is shown in Fig. 7.14 that the reactive power and power factor of the generator is not predicted accurately by FE analysis. An interesting observation is made regarding the grid voltage magnitude with an increase in generator load. As shown in Fig. 7.15(a) the grid voltage increases as the power delivered to the grid by the generator increases. As shown in Fig. 7.3 the SS-PMG being lab tested forms part of a distribution network feeding the laboratories and electrical engineering building in general. An effective line impedance ($Z_l = R_l + jX_l$) is situated between the voltage at the generator terminals and the effective grid voltage. Thus, as I_s being fed into the grid from the generator increases, it seems that the effective grid current entering this distribution network decreases as the generator starts feeding the other loads in the distribution network, which means that the voltage drop occurring over the line impedances as shown in Fig. 7.3 is mitigated to some extent. By making the voltage variable versus load current corresponding to Fig. 7.15(a) in the FE analysis a much better prediction of the reactive power flow of the generator is obtained in Fig. 7.15(b). However, depending on the magnitude of the incoming load current of the

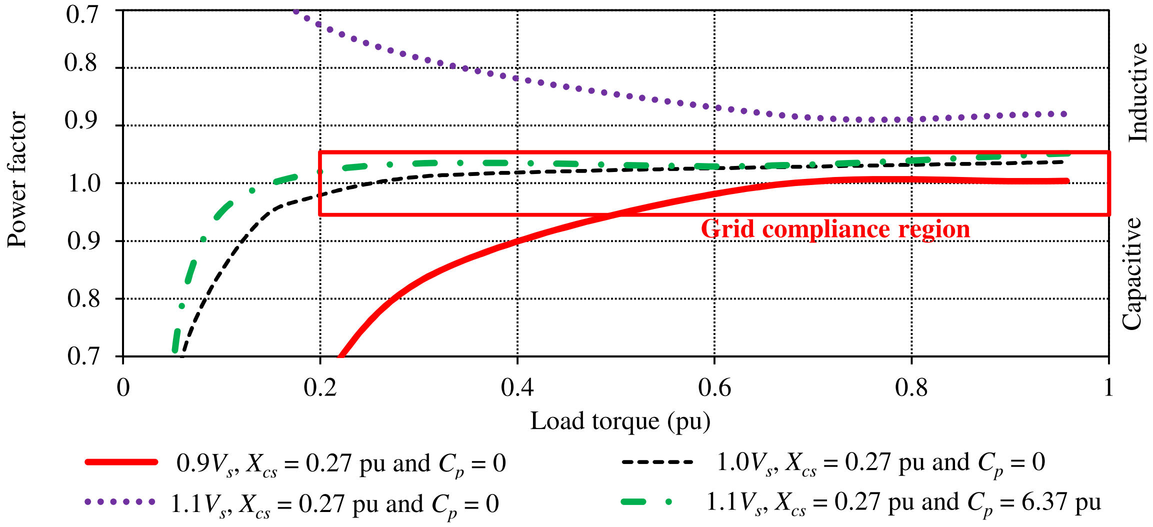

Figure 7.16: Measured power factor versus load torque at different values of V_s, X_{cs} and C_p for SS-PMG 2.

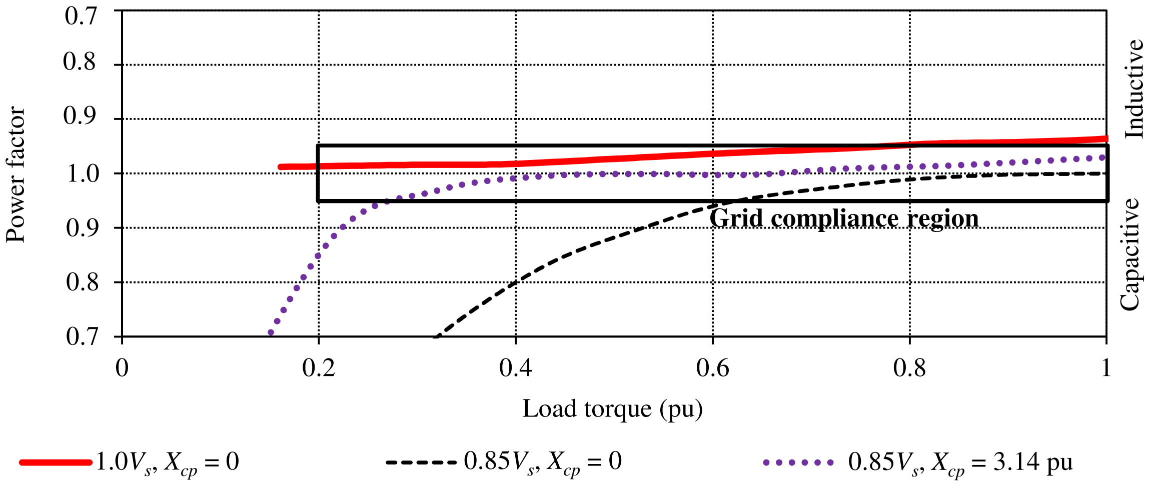

Figure 7.17: Measured power factor versus load torque at different values of V_s and X_{cp} for SS-PMG 1.

distribution network, this variation in V_s will not always correspond to Fig. 7.15(a). The stiffness of the grid connected to will, thus, also have a major effect on the performance of the SS-PMG.

It is seen that especially for lower grid voltages, compensation with $X_{cs} = 0.13$ pu is not adequate for grid code compliance. Fig. 7.16 shows the power factor versus generator load for different values of V_s and with X_{cs} increased to 0.27 pu with $L_{cs} = 8.5$ mH. For the case of $X_{cs} = 0.27$ pu it is seen that at the nominal grid voltage value the generator complies with the relevant grid code specification from 0.2 pu load. However, this value of X_{cs} is still not sufficient to achieve grid compliance for the lower grid voltage values as seen for the case, 0.9V_s. Furthermore, with $X_{cs} = 0.27$ pu, the case for 1.1V_s no longer complies with the grid code specifications. However, if power factor correcting capacitors, indicated by C_p in Fig. 7.11, similar as for conventional induction wind generators, are switched in for the higher grid voltages, it is seen that the generator complies with the grid code

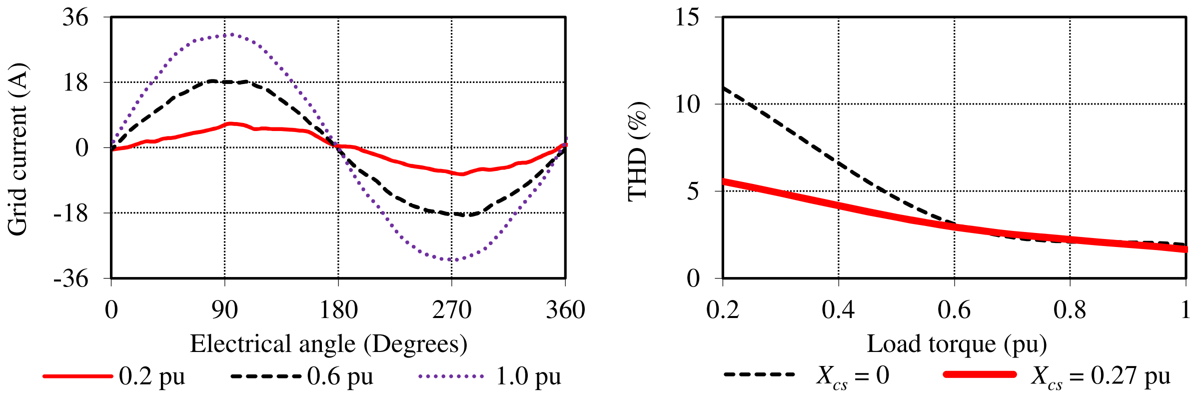

(a) (b)

Figure 7.18: (a) Measured current waveforms versus electrical angle for load torque values of 0.2 pu, 0.6 pu and 1.0 pu for SS-PMG 2 with $X_{cs} = 0$. (b) THD versus load torque for $X_{cs} = 0$ and $X_{cs} = 0.27$ pu for SS-PMG 2.

specifications. Furthermore, as shown in Fig. 7.17 that if the power factor correcting impedance of $X_{cp} = 3.14$ pu, with $L_{cp} = 100$ mH is switched in at low voltage levels for SS-PMG 1, the generator complies much closer with the grid code specifications.

7.4.2 Power Quality

Fig. 7.18(a) show the current waveforms of the DL-PMSG at 0.2, 0.6 and 1.0 pu generator load. It is clear that especially for the low load values a high harmonic content is prevalent in the current supplied to the grid. Fig. 7.18(b) show the THD in the grid current versus generator load with the THD limit specified < 5 % in [160] and defined as

$$\mathrm{THD} = \frac{\sqrt{\sum_{n=2}^{\infty} {I_n}^2}}{I_1}. \tag{7.1}$$

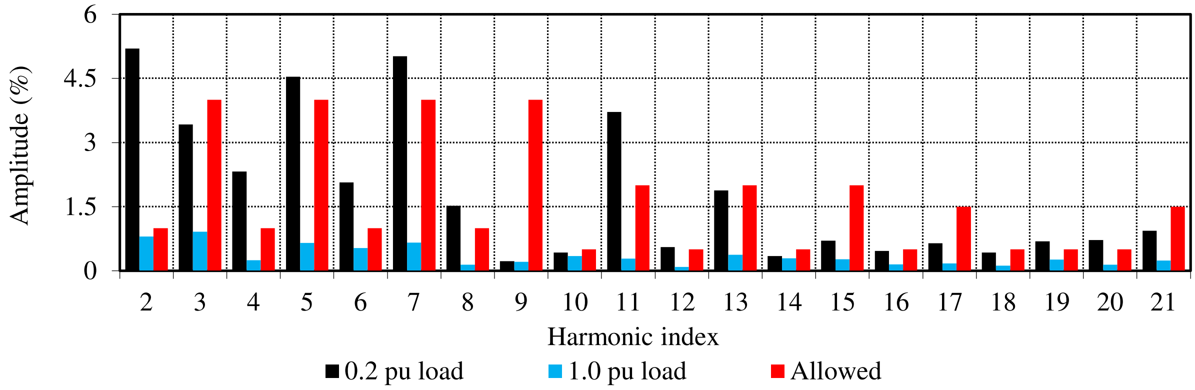

Figure 7.19: Harmonic components in the grid current for 0.2 pu and 1.0 pu load torque with $X_{cs} = 0$ for SS-PMG 2.

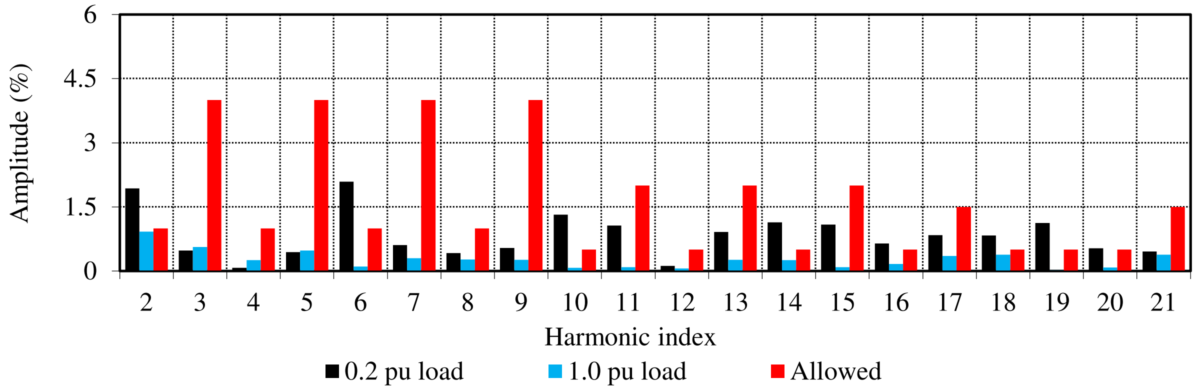

Figure 7.20: Harmonic components in the grid current for 0.2 pu and 1.0 pu load torque with $X_{cs} = 0.27$ pu for SS-PMG 2.

As seen in Fig. 7.18(b) the THD decreases with generator load as the per phase impedance of the generator begins to filter the harmonic components. Also shown in Fig. 7.18(b) is the effect of adding series compensation to the generator, with the THD clearly improved in this case. Figs. 7.19 and 7.20 show the harmonic components in the grid current for $X_{cs} = 0$ and $X_{cs} = 0.27$ pu at two different generator loads, with the allowable limit for each harmonic also shown as given in [160]. Again a clear difference is observed for the two cases, with and without compensation. For $X_{cs} = 0.27$ pu, the generator complies much closer to the specifications of [160].

7.5 Dynamic Measurements

As shown in Fig. 7.2 the SS-PMG is connected to the drive motor via a gearbox, with the torque sensor placed between the inertial components of the gearbox (J_g) and the slip-rotor (J_i). With the inertia of the gearbox much larger (in this case close to the value of J_t) than that of the slip-rotor, with $J_i + J_g = n_g^2 J_g' + J_i$, where J_g' is the inertia at the high speed side of the driving induction motor and $J_i + J_g$ the resulting inertia seen from the low speed side, with n_g the gearing ratio, the measurement on the torque sensor will, thus, reflect the torque interaction between the slip-rotor and common PM-rotor. Several problems were encountered with the dynamic measurements due to several unwanted dynamic effects caused by the driving system. An explanation is, thus, first given in this section on how this issue is resolved, which is followed by the rest of the dynamic measurements.

7.5.1 Oscillatory Test Bench Behaviour

Fig. 7.21 show the measured shaft torque versus time for different configurations in the test setup of the directly grid connected SS-PMG. In Fig. 7.21(a) the SS-PMG is connected as in Fig. 7.3 with the variable speed drive being supplied by one transformer (T_1) and the power developed by the SS-PMG fed to the grid through the other (T_2). A massive oscillation in the shaft torque is observed for this first test case. With the rated torque 1000 Nm it is seen that the torque is oscillating with an amplitude of 1400 Nm with a frequency of just over 12 Hz. The grid current corresponding to Fig. 7.21(a) is shown in Fig. 7.22(a), with the same severe oscillation observed as in the torque. It is evident that no utility will allow the connection of a system as unstable as this and continuous operation at this transient behaviour can damage the test system severely.

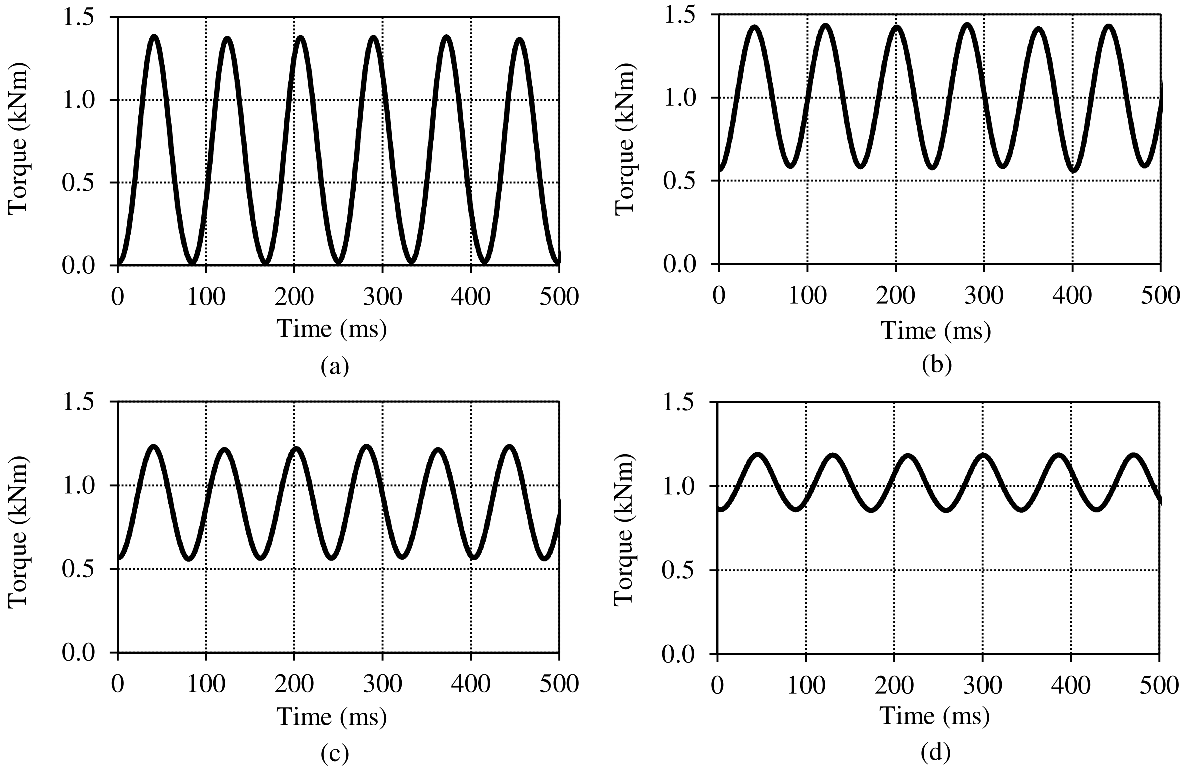

(a) (b) (c) (d)

Figure 7.21: Measured directly grid connected SS-PMG shaft torque versus time (T_{rated} = 1000 Nm), for SS-PMG 1 as in Fig. 7.1 with universal couplings, for the SS-PMG connected to (a) T_2, (b) T_1, (c) T_1 but in this case R_b added in parallel to the grid connection at the generator terminals, and (d) the VSD being fed by a diesel generator with the SS-PMG connected to T_1.

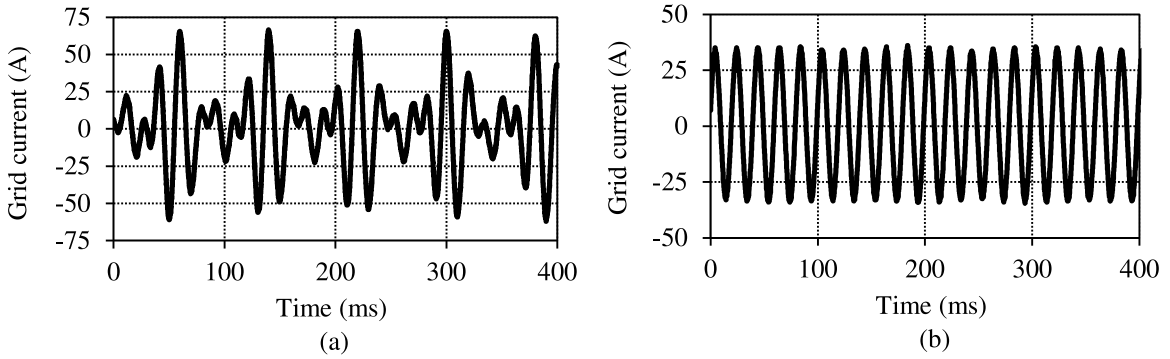

(a) (b)

Figure 7.22: Measured directly grid connected SS-PMG line current versus time with (a) corresponding to the measurement of Fig. 7.21(a) and (b) with one universal shaft and the torque sensor removed from the system.

To identify the source of this transient behaviour the grid connection point of the SS-PMG is moved to T_1. The resulting torque measurement is shown in Fig. 7.21(b), with the oscillation less severe in this case. A further reduction in the disturbance torque amplitude is observed by adding an external resistance at the generator terminals (R_b as in Figs. 7.3 and 7.11). It is, thus, clear that the dynamic behaviour of the generator is influenced by the grid parameters. Furthermore, as shown in Fig. 2.15 in Chapter 2 the resonance area is shifted in the frequency domain for a variation in L_s which explains the difference in dynamic behaviour for the different grid connection points. Shown in Fig. 7.21(d) is the measured torque versus time for the variable speed drive fed by a diesel generator. A further reduction in the disturbance torque amplitude is observed. The dynamic interaction between the SS-PMG and the variable speed drive is, thus, also shown to influence the dynamic behaviour of the system.

The most significant improvement in the transient behaviour of the SS-PMG is observed by modifying the mechanical coupling of the test bench. One universal coupling and the torque sensor is removed, with the remaining coupling better aligned. The measured grid current shown in Fig. 7.22(b) clearly indicate much better dynamic behaviour of the test system, with very little oscillation observed in the current amplitude. The importance of alignment and of using the correct couplings is, thus, clear. As explained in [182] a basic characteristic of universal couplings is the non-uniformity of the motion transferred, with the angular velocity ratio at the input and output of the coupling varying at two cycles per revolution. It is mentioned that the angular acceleration increases with an increase in offset angle with magnitudes as high as 15 % observed for offset angles of 30°. The disturbance frequency of the universal couplings can be calculated as $f_d = 2 \times n_s/60 = (150 \times 2)/60 = 5$ Hz, and with two universal couplings, $2 \times f_d = 10$ Hz, which is close to the disturbance frequency observed in Fig. 7.21. With the effective inertia between the couplings and the grid basically that of J_m, and with the disturbance frequency so close to the resonance area as shown in Figs. 2.14 and 2.15 in Chapter 2, it is clear that the universal couplings are unsuitable for the laboratory tests of the SS-PMG.

7.5.2 Dynamic Turbine Torque Emulation

Due to the high inertia value of $J_g + J_i = 205$ kg.m^2, even with the variable speed drive having a rating of 300 kVA the system is unable to emulate the sudden load changes as simulated in Chapter 2. Tests are, thus, conducted on a smaller test bench, with $J_g + J_i = 31$ kg.m^2 in this case. Fig. 7.23(a) show a step input in torque from 0 to rated torque and the resulting stator grid current response. This torque step input which is realised in 0.2 s clearly show that the SS-PMG is stable connected directly to the grid. This smaller test bench also make use of the universal couplings

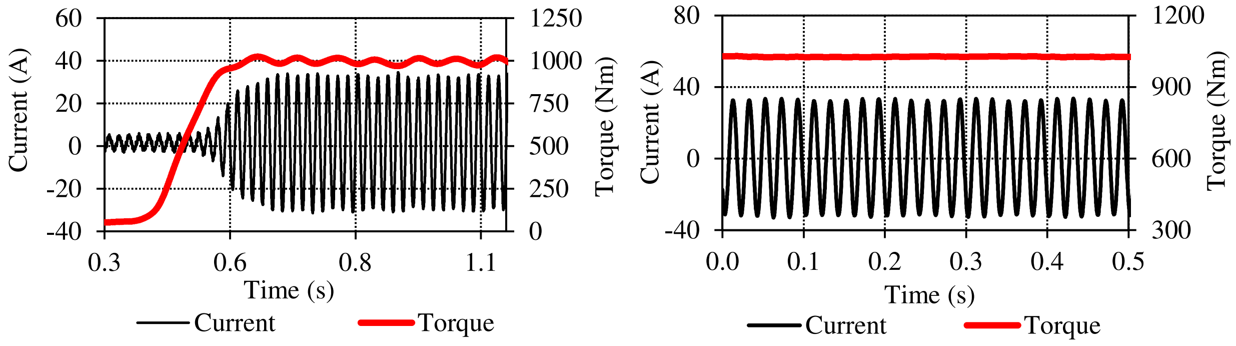

(a) (b)

Figure 7.23: (a) Measured stator current response and input torque for a step input from 0 to 1000 Nm for the SS-PMG on the smaller test bench. (b) Measured instantaneous stator current and torque at full load for the SS-PMG on the larger test bench with the new coupling configuration as in Fig. 7.2.

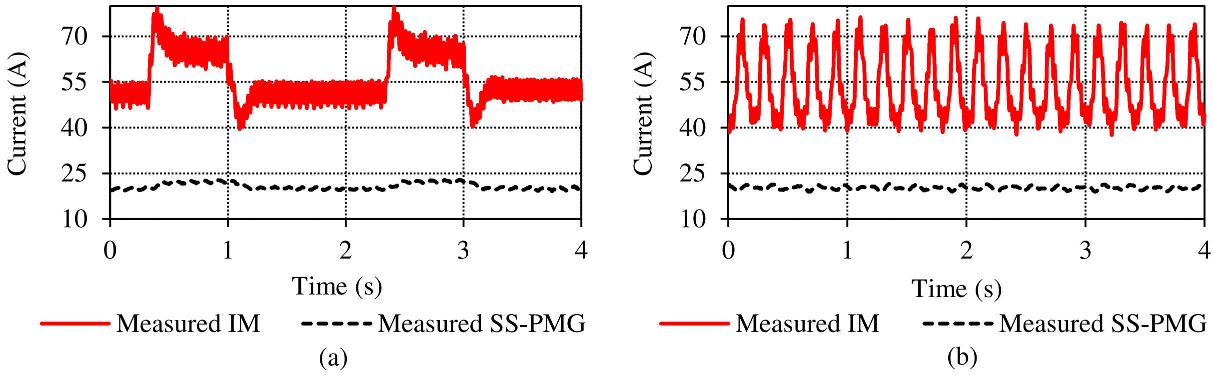

(a) (b)

Figure 7.24: Measured RMS current amplitude of the induction motor (IM) and corresponding response in the SS-PMG RMS grid current amplitude for a disturbance in the current amplitude of (a) $f_d = 0.5$ Hz and (b) $f_d = 5.0$ Hz.

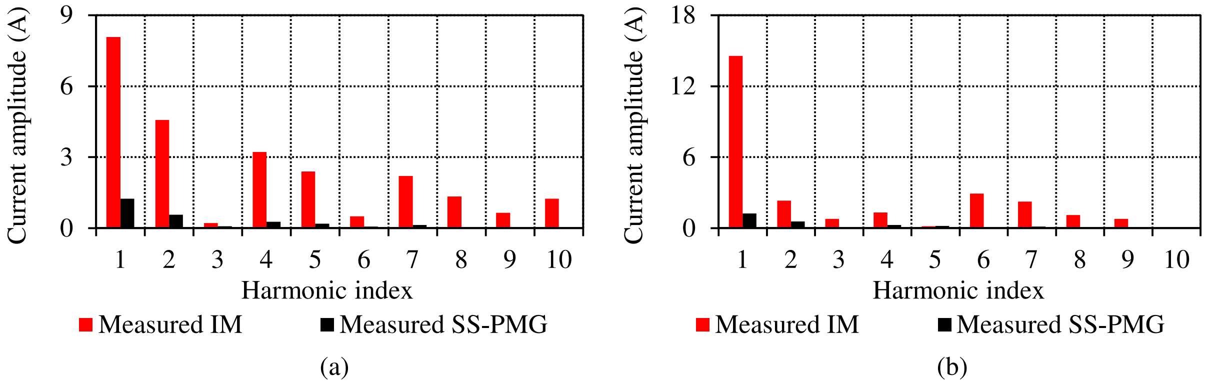

(a) (b)

Figure 7.25: Measured frequency spectrum of the RMS grid current amplitude of the induction motor (IM) and corresponding response in the SS-PMG RMS grid current amplitude for (a) $f_d = 0.5$ Hz and (b) $f_d = 5.0$ Hz.

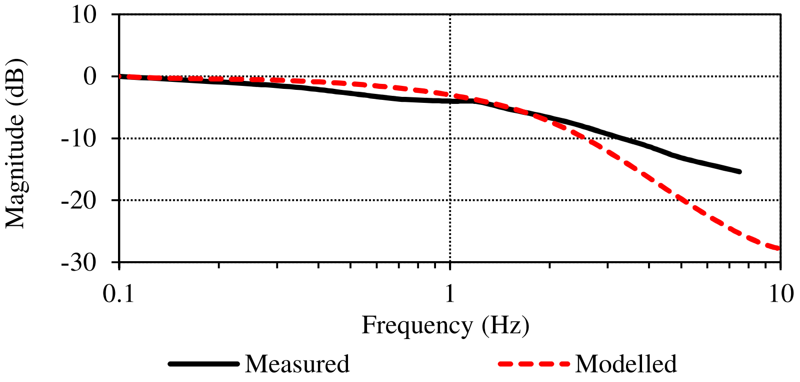

Figure 7.26: Measured and simulated frequency response of $\Delta\tau_s/\tau_{dt}$ for $J_t = J_g + J_i = 205$ kg.m^2 of the SS-PMG system.

as shown in Fig. 7.1. Furthermore, as shown in Fig. 2.11 in Chapter 2, disturbances added at the rotational frequency of this smaller testbench system, will be amplified as well. This explains the ripple component in the torque and current. In Fig. 7.23(b) the measured torque and grid current for the SS-PMG is shown at rated load with the new more rigid coupling configuration employed as shown in Fig. 7.2, with almost no dynamic disturbances observed in the system for this case.

To emulate the turbine torque disturbance inputs (tower oscillation, wind shear, yaw error and tower shadow as discussed in Chapter 2) a disturbance is generated in the RMS current amplitude of the induction motor driving the test system as shown in Fig. 7.24(a) for $f_d = 0.5$ Hz and (b) $f_d = 5$ Hz respectively, with the resulting SS-PMG grid current response also shown. The disturbance frequency f_d is varied form 0.1 to 7.5 Hz and the frequency spectrum is calculated in each case as shown in Fig 7.25(a) and (b). The ratio of the fundamental harmonic component of the induction motor current and the SS-PMG grid current is calculated in each case. Fig. 7.26 show the measured and simulated frequency response of the directly grid connected SS-PMG system on the large test bench to disturbances in the mechanical torque input. Even though there are still several other dynamic effects within the test setup as shown in Figs. 7.24 and 7.25 it is shown that the system's cut off frequency is closely predicted in the dynamic modelling of Chapter 2.

7.5.3 Torque Ripple Disturbances

Fig. 7.27(a), which correspond to Fig. 7.22(b) with one universal coupling removed, show the RMS grid current at rated load versus time, which clearly indicates a much lower disturbance in the grid current. In Fig. 7.27(b) the RMS grid current versus time is shown at about 0.8 pu load, with a clear oscillation observed in the grid current amplitude, which is shown to be much less in Fig. 7.27(a). From Fig. 2.14 in Chapter 2 it is known that this load point is more or less where the resonance area is situated if the dominant harmonic of $n = 12$ is considered for the non overlap DL slip-PMG torque ripple. Fig. 7.28(a) show the magnitude of the measured disturbance in the grid current amplitude versus load, and Fig. 7.28(b) show the bandwidth of $\Delta\tau_s/\tau_{dr}$ versus generator load, with the fundamental torque ripple component taken as $n = 12$. From Fig. 7.28 it is seen that the resonance area is very closely predicted by means of the modelling methods in Chapter 2. For this high torque ripple disturbance in the grid current the generator is still shown to be stable connected directly to the grid.

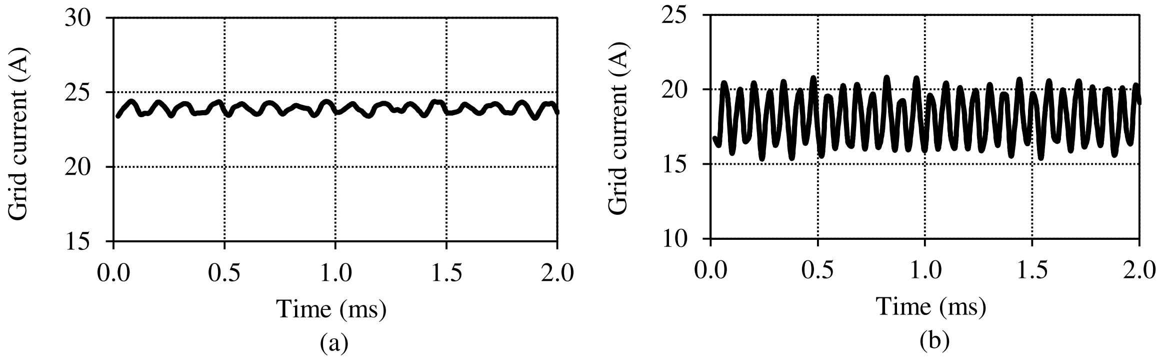

(a)

(b)

Figure 7.27: Measured directly grid connected SS-PMG RMS line current versus time at (a) rated load and (b) 0.8 pu load with one universal coupling and the torque sensor removed from the system.

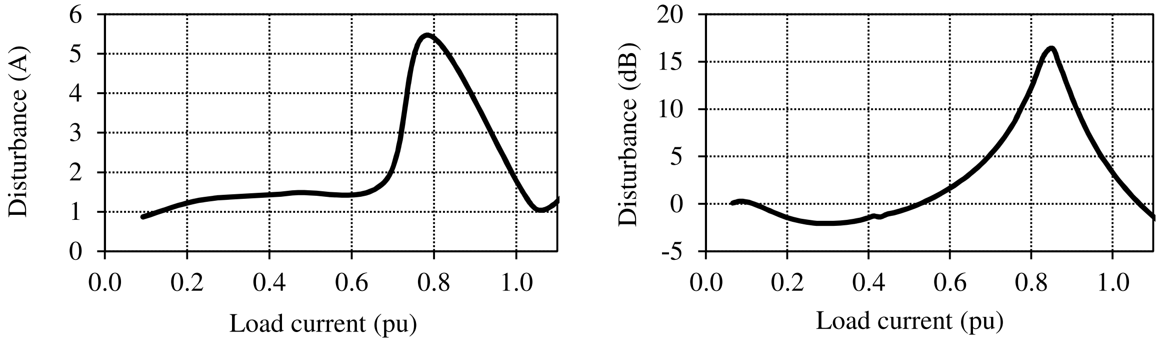

Figure 7.28: (a) Measured current disturbance amplitude versus generator load with one universal shaft and the torque sensor removed from the system. (b) The frequency response of $\Delta\tau_s/\tau_{dr}$ as simulated in Chapter 2 versus generator load.

7.5.4 Low Voltage Conditions

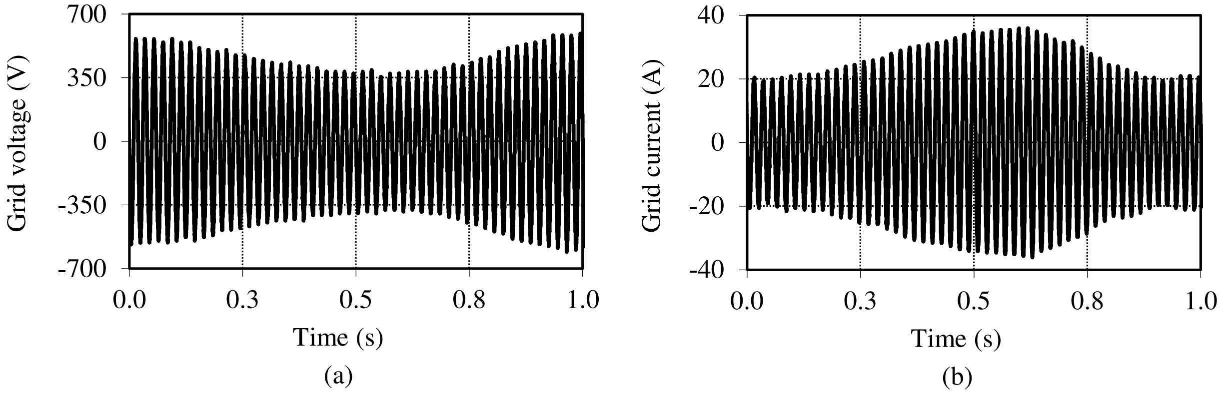

(a)

(b)

Figure 7.29: Measured (a) grid voltage and (b) grid current response for a voltage dip induced at the generator terminals.

Due to the possibility of damage to the lab test setup which could occur from the sudden voltage and current spikes, the LVRT specifications of Fig. 2.1 in Chapter 2 are not emulated in the laboratory. A less severe voltage dip is, thus, induced at the generator terminals as shown in Fig. 7.29(a). The current response of this voltage dip is shown in Fig. 7.29(b) with no oscillatory behaviour observed in the system. It is, thus, anticipated that the LVRT specifications as given in [10], poses no problem for the prototype case-study SS-PMG systems.

7.6 Field Test Setup

Several field tests, at different locations, with different wind conditions and with many of the test sites having a high turbulence intensity, have been conducted for the prototype SS-PMG systems. Although many of the field test sites would seem undesirable due to the turbulent wind conditions, this provides a clear insight into the stability and dynamic performance of the SS-PMG. Field test locations also include the South African National Antarctic Research Base (SANAE IV), where

Figure 7.30: SS-PMG 1 and SS-PMG 2 being field tested at the Stellenbosch University Mariendahl small wind turbine field testing facility.

SS-PMG 1 was interfaced with the SANAE IV diesel mini-grid. Two prototype SS-PMG systems, SS-PMG 1 and SS-PMG 2, are currently operating in the field at the Stellenbosch University Mariendahl small wind turbine field testing facility as shown in Fig. 7.30. All of the field test results shown were measured at this field test site.

7.7 Field Measurements

Fig. 7.31(a) show the load torque versus wind speed of the case study 15 kW wind turbine system as in Appendix B, with the rated load occurring at $v_w = 11$ m/s, the cut in wind speed at $v_w = 4$ m/s and the maximum operating wind speed at $v_w = 17$ m/s. For $v_w > 11$ m/s a passive furling

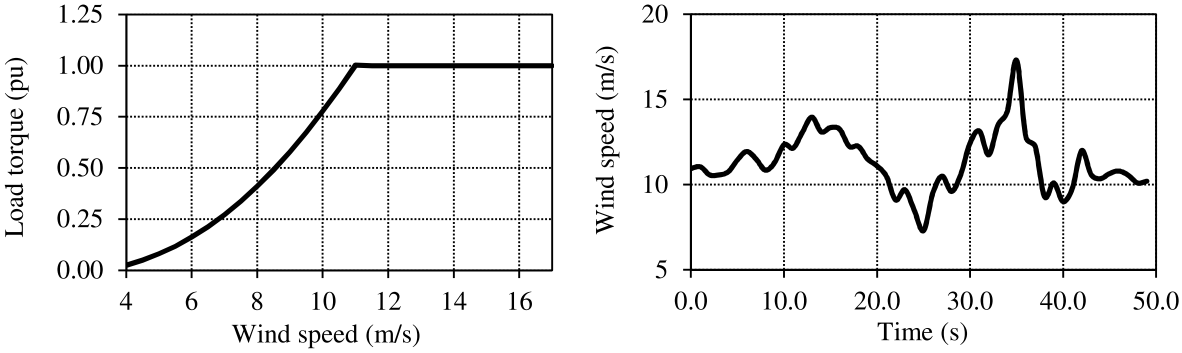

(a)

(b)

Figure 7.31: (a) Generator loading versus wind speed for the turbine used and (b) measured wind speed versus time at the field test site.

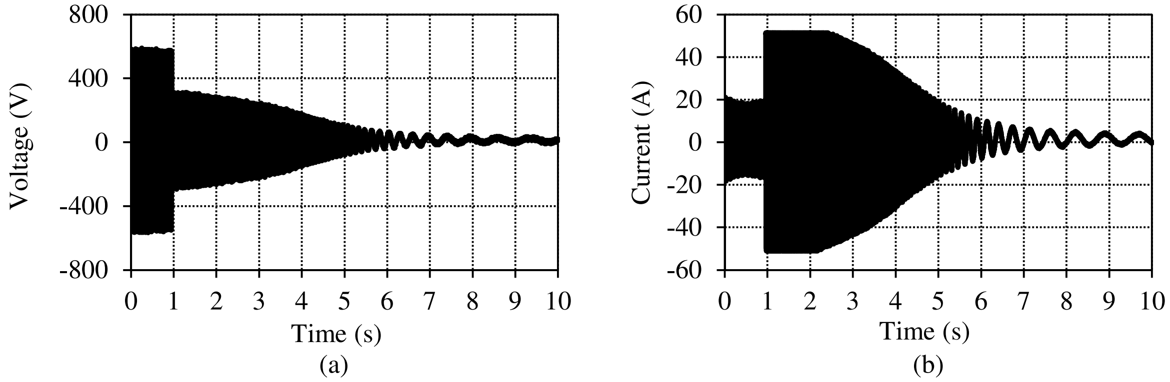

(a) (b)

Figure 7.32: (a) Voltage and (b) current versus time for the electromagnetic brake engaged at the field test site.

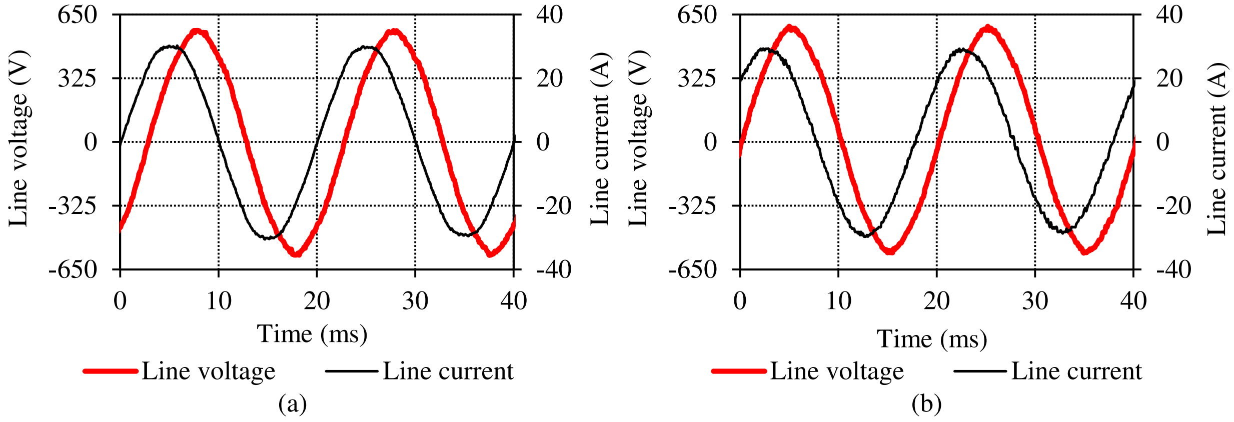

(a) (b)

Figure 7.33: Measured line voltage and current during field testing of (a) SS-PMG 1 and (b) SS-PMG 2 at almost rated wind speed.

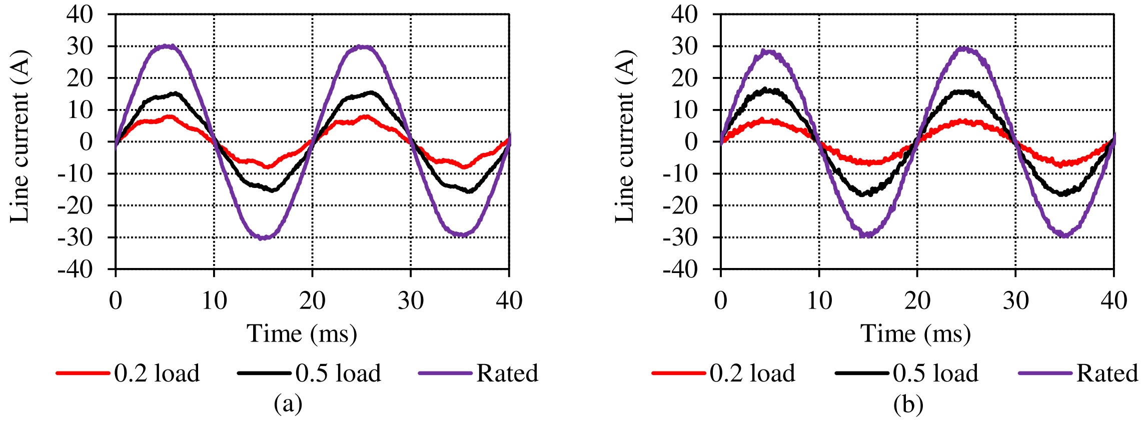

(a) (b)

Figure 7.34: Current waveforms at more or less 0.2, 0.5 and 1.0 pu load of (a) SS-PMG 1 and (b) SS-PMG 2.

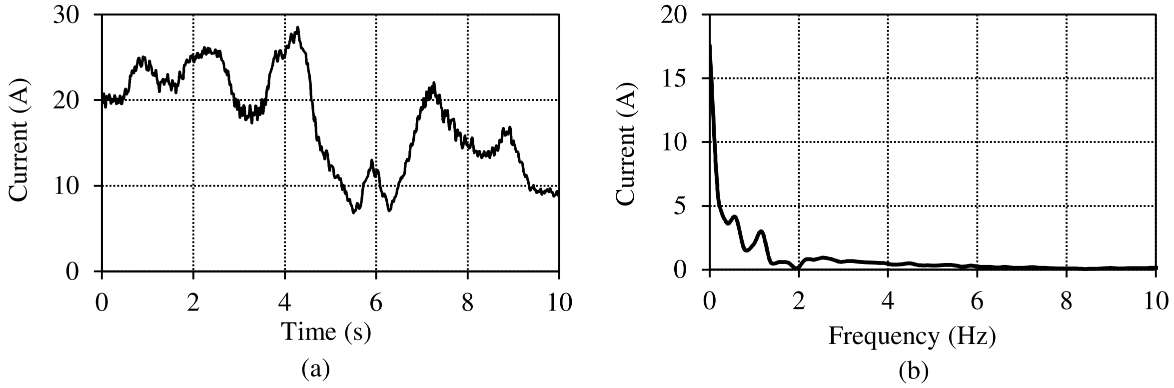

Figure 7.35: (a) Measured RMS grid current and (b) the RMS current oscillation frequency content of SS-PMG 1 during field testing to obtain the bandwidth of the system as in Chapter 2.

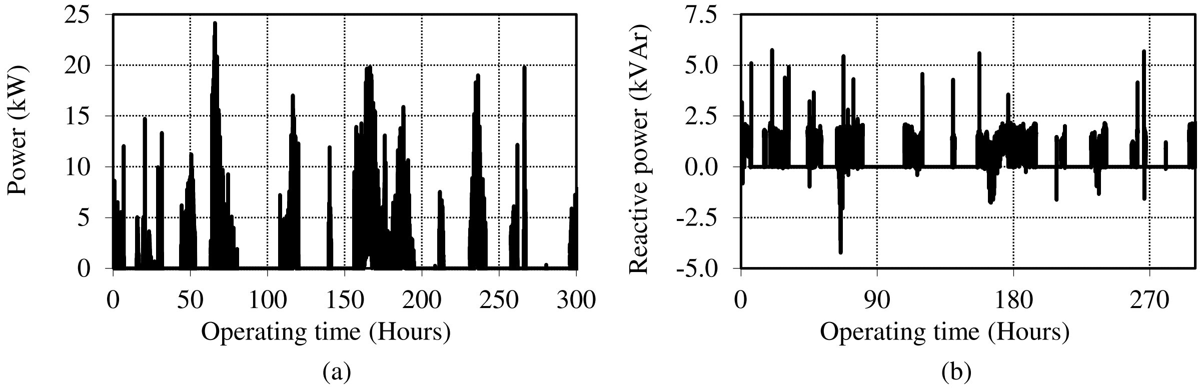

Figure 7.36: Measured (a) active power and (b) reactive power of SS-PMG 2 during field testing for a duration of about two weeks.

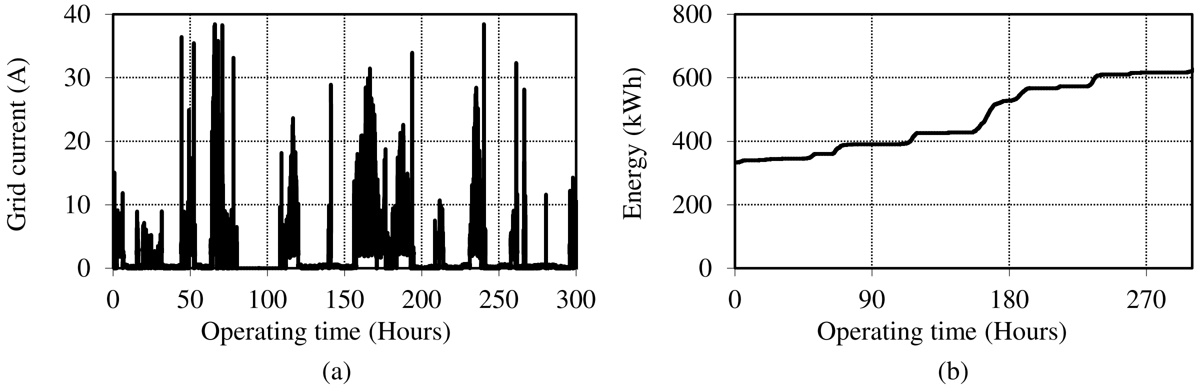

Figure 7.37: Measured (a) grid current and (b) cumulative energy in kWh delivered to the grid of SS-PMG 2 during field testing for a duration of about two weeks.

mechanism is enabled which furls the turbine out of the prevalent wind direction. With the turbine power curtailed the generator can continue operation at a more or less constant power of $P_s \approx 15$ kW.

Fig. 7.31(b) show the wind speed versus time at the field test site for a duration of almost one minute. The high turbulence intensity of the wind site can clearly be seen, with wind gusts occurring often. Not shown is the wind direction, which is found to change direction frequently for this test site. It is, thus, very difficult to match the wind speed with the generator power output, as it is difficult to accurately take into account the dynamics and time response of the furling system and the yawing mechanism. Fig. 7.32(a) and (b) show the generator voltage and current versus time respectively, for the electromagnetic brake engaged.

Fig. 7.33(a) and (b) show the measured grid voltage and current versus time of SS-PMG 1 and SS-PMG 2 respectively, at rated load. Fig. 7.34(a) and (b) show the grid currents of SS-PMG 1 and SS-PMG 2 respectively at different wind speeds. SS-PMG 2 is clearly shown to exhibit better current quality at the lower load values as opposed to SS-PMG 1, due to its higher induced voltage quality. Fig. 7.35(a) shows the measured RMS grid current for SS-PMG 1 during field testing for a 10 second measurement window. In Fig. 7.35(b) the oscillation frequency content in the RMS grid current of SS-PMG 1 in Fig. 7.35(a) is shown. In the oscillation frequency content of the measured RMS grid current, it is clearly seen that only the very low frequency components are transferred to the grid as predicted in Chapter 2.

Fig. 7.36(a) and (b) respectively show the measured active and reactive power components over a time period of about two weeks for SS-PMG 2 and the corresponding current injected into the grid is shown in Fig. 7.37(a). For this two week time period, Fig. 7.37(b) show the cumulative energy units in kWh delivered to the grid.

7.8 Summary

In this chapter two SS-PMG systems are practically evaluated, connected directly to the grid. Both SS-PMGs exhibit high efficiencies compared to a PMSG connected to the grid via a power electronic converter, except at low load values. The lower efficiency at low load values of the SS-PMG is offset to some extent by the very high efficiency of the slip-PMG unit at low loads. Furthermore, the reactive power flow magnitude is significantly influenced by the difference between the induced generator voltage and the grid voltage. For SS-PMG 2 with a very low per unit impedance this aspect is especially a factor. The reactive power flow is curbed to some extent by the addition of a series line reactance, which is also shown to reduce the harmonic current components injected into the grid. SS-PMG 2 is also shown to exhibit less harmonic content in the grid current as opposed to SS-PMG 1, due to the better induced voltage quality of the DL PMSG. In this chapter it is shown that both SS-PMGs do not comply to the grid code specifications, without compensation, if grid voltage variations occur in the range specified. However, grid compliance can easily be achieved, by switching in power factor correcting impedances if grid voltage variations do occur. Furthermore, it is also shown that the stiffness of the grid influences the reactive power flow characteristics due to the increase in generator terminal voltage.

It is also shown that careful attention should be given regarding the type of couplings used and the alignment of the test bench for the laboratory tests, as this aspect can significantly influence the dynamic behaviour of the SS-PMG. Misalignment and the use of incorrect couplings can lead to severe oscillations in the generator torque and grid current. The prediction of the behaviour of the SS-PMG regarding turbine disturbances and torque ripple disturbances in Chapter 2, are also practically verified in this chapter. Furthermore, the field measurements shown for both SS-PMGs clearly validate the dynamic stability and operational characteristics of the directly grid connected SS-PMG.

Chapter 8

Conclusion

In comparison with other types of wind generator technologies, the SS-PMG exhibits several advantages such as increased robustness, simplification of the drive-train, reduced maintenance and reduced operational costs. Other advantages of having a directly grid connected synchronous wind generator includes, the higher reactive power supporting capabilities during low voltage conditions and the addition of inertia to the grid. However, there are also several disadvantages for this type of wind generator, such as the increase in mass and cost by adding a second generator to the design, as well as the fact that the SS-PMG is a fixed speed wind generator which leads to a reduction in energy harvesting and due to the SS-PMG operating at a fixed grid frequency which reduces the efficiency at low wind speeds.

The benefits of the SS-PMG need to be quantified against the disadvantages of this type of wind generator, by obtaining an indication of the cost of energy generated by the SS-PMG over its lifetime. This cost calculation relates to the initial capital cost, operation and maintenance cost reduction, economic incentives due to higher reactive power compensation and contribution to grid inertia and the effect of income lost due to reduced energy harvesting. For good wind sites, however, it is observed that the loss in income due to the SS-PMG being fixed speed will be low. At current the SS-PMG seems to be a viable alternative at the small-scale wind power level and for rural and isolated applications where maintenance is a key issue. However, due to the current high price of PM material it is a question whether this generator is a viable alternative for direct drive, utility scale wind power systems.

8.1 General Conclusions

Before the feasibility of the SS-PMG on an economic basis can be quantified, several issues regarding the design, performance, implementation and dynamic behaviour of the SS-PMG needs to be addressed, which is the main focus of this study. Although, this thesis includes a very broad study on the SS-PMG, with several aspects requiring much more work, certain key findings are made regarding the design and implementation of the SS-PMG and wind generator design aspects in general as discussed below:

- It is shown that the directly grid connected SS-PMG offers a stable grid connection. The transfer function model developed for the SS-PMG in this study is shown to give a good indication of the dynamic characteristics of the system. From the simulated response of the case study 15 kW SS-PMG system, as well as measurements conducted both in the laboratory and the field it is shown that the system remains stable even for large step inputs in turbine torque. Care should, however, be taken regarding the SS-PMG parameters in the design as these can influence the damping ratio of the system as well as the bandwidth regarding torque ripple transients and the ability of the generator to stay connected to the grid during low voltage conditions.

- As shown in this study an incorrect calculation of the per phase inductance of both the PMSG and slip-PMG units, can have significant implications regarding the accurate prediction of the torque versus speed profiles of both machine units, as well as the short circuit current of the PMSG. An incorrect prediction in these performance parameters can have enormous implications regarding the final SS-PMG design. It is clearly shown that the end-effects of both the windings and the PMs cannot be ignored in the analysis, especially in the above rated region. This is especially true for PM machines with low aspect ratios typical for direct-drive PM wind generators. The new analytical approach in this thesis, to calculate the end-winding inductance of non overlap winding PM machines, is shown to give consistently good results compared to 3D-FE analysis and measurements. Furthermore, it is proposed that the end-flux fringing of the PMs are taken into account by reducing the PM strength with a certain factor instead of multiplying the output performance parameters of the machine simply by a constant fringing factor as proposed in literature.

- Due to the significant concern relating to the extra mass, cost and complexity of adding a second generator to the design a thorough design optimisation is done for the slip-PMG unit. Several new novel slip-PMG topologies, as well as new manufacturing methods for the slip-PMG are introduced and evaluated in this study. Surprisingly it is shown that aluminium can be used instead of copper without increasing the mass of the slip-PMG or by decreasing the machine performance, which have clear advantages regarding cost reduction. The slip-PMG can also be implemented as a slip permanent magnet coupling, which operates similarly to conventional eddy current couplings used in many industrial applications. It is shown that the mass and PM content of the slip-PMG can be substantially reduced, especially with regard to conventional eddy-current couplings. Furthermore, it is shown that with careful design and parameter selections the torque ripple amplitude and frequency of the slip-PMG can be designed to comply to the specifications given in the dynamic analysis of the SS-PMG.

- Although the PMSG design is similar to the design of conventional direct-drive PM generators, it is shown that a different design approach is needed for the directly grid connected PMSG, as the generator design needs to comply with all the requirements stipulated in the relevant grid codes. The design approach for the direct grid PMSG in this study is also applicable to all of the directly grid connected PM wind generator topologies discussed in this thesis. A parameter found to significantly influence the grid connection aspects, is the per phase impedance of the PMSG. A higher per unit impedance limits the flow of harmonic currents, acts as a buffer against reactive power flow if grid voltage variations occur and limits the short circuit current during grid faults. From the design optimisation of the PMSG the novel toroidally wound double rotor PMSG is shown to give the best performance regarding active mass and PM content especially for high pole number applications and higher wind power levels. Due to the much shorter end-windings and high fill factor of this generator it performs much better than the conventionally used three phase overlap winding PM generator. However, at the lower wind power levels the active mass and PM content of the DL non overlap winding PMSG will not be that much different, with this generator having the best induced voltage quality. Furthermore, an interesting observation made in this study, is that for higher fill factors the use of aluminium as winding material becomes more cost effective for direct drive wind generators.

- In the directly grid connected analysis of the two prototype SS-PMGs it is found that both SS-PMGs exhibit high efficiencies compared to a PMSG connected to the grid via a power electronic converter, except at low load values. The lower efficiency at low load values of the SS-PMG is offset to some extent by the very high efficiency of the slip-PMG unit at low loads. It is furthermore, shown that the generator can be made to comply to the relevant grid codes regarding reactive power flow, with the addition of very basic power factor correcting impedances. The addition of an additional series line reactance is also shown to reduce the reactive power flow due to grid voltage variations, and also to reduce the grid current harmonics injected into the grid. It is also shown that careful attention should be given regarding the type of couplings used and the alignment of the test bench for the laboratory tests, as this aspect can significantly influence the dynamic behaviour of the SS-PMG. Furthermore, the operating principles and grid connection aspects of the SS-PMG are practically verified, both in the laboratory and for the SS-PMG interfaced with a 15 kW wind turbine system in the field.

8.2 Future Work

From the work done in this study it is evident that there is large scope for additional studies to be carried out on this concept as this study only gives a very broad overview of the main SS-PMG design and implementation aspects. Recommendations for future work are listed below:

- Due to the work done in this study mostly focussing on the implementation of the SS-PMG at the small-scale wind power level, more work is required on the applicability of the SS-PMG for utility scale. A study is currently ongoing in this regard, with the mechanical aspects of the SS-PMG receiving much more interest in this case. Due to the current high price of PM material, direct-drive PMSG wind turbine systems are currently the most expensive solution as shown in Chapter 1. The application of the SS-PMG as a medium speed wind generator utilising a more reliable gearbox with fewer gearing stages could, thus, definitely be a consideration due to the mass and cost increase of using a SS-PMG in this case much less. Furthermore, the feasibility of replacing the PMSG with a wound synchronous generator can also be investigated, which could improve the grid connection characteristics of the SS-PMG.
- Future studies should also include a better quantification of the favourable grid connection aspects of the SS-PMG, regarding reactive power flow characteristics, grid voltage supporting capabilities and contribution to grid inertia if frequency variations occur.
- With reduced energy harvesting due to the fixed speed operation of the SS-PMG considered as a disadvantage, a thorough economic analysis is required to obtain an indication of the cost per energy unit produced by this system over its lifetime, compared to other wind generator solutions of similar size. The average wind speed of the specific wind site will obviously play a significant role.
- There are also some technical aspects of the work done in this study which requires further attention. For the slip-PMG, skin effects, the deep bar effect and the correct shape and size of the conductors need to be incorporated in future designs. These aspects can especially be

important for applications where it might be necessary to shape the torque versus slip profile according to certain specifications. The axial flux slip-PMG which is shown to give the lowest active and PM mass can also definitely be considered for future analysis.

- Regarding the PMSG design, further analysis of the toroidal winding, especially regarding the thermal and mechanical aspects of this machine type would be insightful. A very important aspect which should definitely be investigated further is the correct prediction of the no load machine losses as this is of extreme importance for the fixed speed SS-PMG efficiency at low load.

Appendices

Appendix A

Calculation of End-Winding Inductance Constants

For the calculation of the end winding inductance in Chapter 3 by means of the formula in [19], the constants k_1 and k_2 are required, with $K = k_1 - k_2$. Discussed below are the procedures to obtain the values of k_1 and k_2 from the theory in [19].

A.1 Calculation of Parameter $k1$

For the calculation of k_1 the following series formula as given in [19] can be used with

$$k_1 = \frac{2\beta}{\pi}\left[\left(\log_e\frac{4}{\beta} - \frac{1}{2}\right) + \frac{\beta^2}{8}\left(\log_e\frac{4}{\beta} + \frac{1}{8}\right) - \frac{\beta^2}{64}\left(\log_e\frac{4}{\beta} - \frac{2}{3}\right) + \frac{5\beta^6}{1024}\left(\log_e\frac{4}{\beta} - \frac{109}{120} - \right)..\right] \tag{A.1}$$

where $\beta = b/2a$, with a and b as defined for (3.1), (3.3) and (3.4) in Chapter 3. It is stated in [19] that for values of β as large as $1/4$, the first three terms in (A.1) will yield an accuracy of 0.001.

A.2 Calculation of Parameter $k2$.

The value of k_2 can be found in the lookup tables given in [19] as a function of c/b and $c/2a$, or as a function of b/c and $c/2a$, with a, b and c again as defined for (3.1), (3.3) and (3.4) in Chapter 3. However, in this study to simplify the end-winding inductance calculations, the value of k_2 is approximated by means of a curve fitting function with the help of the MATLAB package, for the two tables under consideration. If $b/c \leq 1$ then the following expression with $\delta = b/c$ and $\psi = c/2a$ can be used with

$$\begin{aligned} k_2 &= f_1 e^{f_2\psi} + f_3 e^{f_4\psi} \text{ where} \qquad \text{(A.2)}\\ f_1 &= -0.0638\delta^2 + 0.3298\delta - 0.001973,\\ f_2 &= -0.1165\delta^2 + 0.038898\delta - 0.3941,\\ f_3 &= 0.06118\delta^2 - 0.032218\delta + 0.001861 \text{ and}\\ f_4 &= -1.167\delta^2 + 0.3721\delta - 5.587. \end{aligned}$$

If $c/b \leq 1$ then the following expression can be used with $\delta = c/b$ and again $\psi = c/2a$ as

$$\begin{aligned}
k_2 &= f_1 e^{f_2 \psi} + f_3 e^{f_4 \psi} \quad \text{where} \qquad (A.3)\\
f_1 &= -0.2652\delta^2 + 0.6943\delta - 0.01944,\\
f_2 &= -8.246e^{-20.14\delta} - 0.2779e^{-0.3369\delta},\\
f_3 &= \frac{-0.001548\delta + 0.0003029}{\delta^4 - 2.211\delta^3 + 1.1485\delta^2 - 0.2759\delta + 0.01816} \quad \text{and}\\
f_4 &= \frac{-2.493\delta^2 + 0.8325\delta - 0.4384}{\delta^3 + 0.03686\delta^2 - 0.2928\delta + 0.05966}.
\end{aligned}$$

Appendix B

Case-Study Wind turbine System

Table B.1 gives some background on the case study 15 kW wind turbine system utilised in this study. This, turbine system is made as robust and simple as possible by utilising fixed pitch blades, passive yawing by means of a tail vane, passive auto furling by means of a tensioned spring system if the wind speed exceeds the rated value of $v_w = 11$ m/s and electromagnetic braking. It is, clear that if this small wind turbine is interfaced in conjunction with the SS-PMG, it will be a very robust wind turbine system, due to the components mostly considered in the reliability such as the pitching system, power electronic converter and gearbox not included within this system.

Figs. B.1 and B.2 respectively show the wind turbine power and torque versus wind speed and rotor speed as supplied by the turbine manufacturer. Fig. B.1 also show the power curves for the generator operated as a variable speed or fixed speed wind turbine system. The rated turbine speed is limited by the turbine supplier at 150 r/min. Fig. B.3(a) show the turbine nacelle and the furling spring system which is to be connected to the tail vane and Fig. B.3(b) show the wind turbine in

Table B.1: Parameters of the wind turbine system utilised.

Parameter	**Value**
Turbine diameter	7.2 m
Electrical generator	PMSG direct-drive
Maximum allowable generator diameter	≈ 0.67 m
Hub heights	10 m, 16 m and 24 m
Wind turbine tower	Lattice or tubular
Rated power	15 kW
Rated torque	1000 Nm
Suggested generator braking torque	> 2000 Nm
Rated turbine speed	150 r/min
Turbine speed limit	< 150 r/min
Cut-in wind speed	4 m/s
Rated wind speed	11 m/s
Maximum wind speed	17 m/s
Pitch	Fixed
Yaw	Passive with tail vane.
Over-speed protection	Passive auto-furling above rated wind speed.
Brake	Electromagnetic with resistor bank.

the furling position. The braking resistor bank is shown in Fig. B.4 with a capacitor bank mounted to its side, which can either be used for power factor correction or to increase the generator braking torque.

Fig. B.5(a) show the wind turbine being field tested on the Stellenbosch University grounds. Due to the vicinity of several buildings and trees this was also found to be a very turbulent wind site, which gives an adequate indication of the stability of the SS-PMG. Fig. B.5(b) show the wind turbine being field tested at the SANAE IV Antarctic research base, where extreme wind conditions frequently occur. Fig. B.6 show the field testing of SS-PMG 1 as discussed in Chapter 7 at the Stellenbosch University Mariendahl small wind turbine field testing facility.

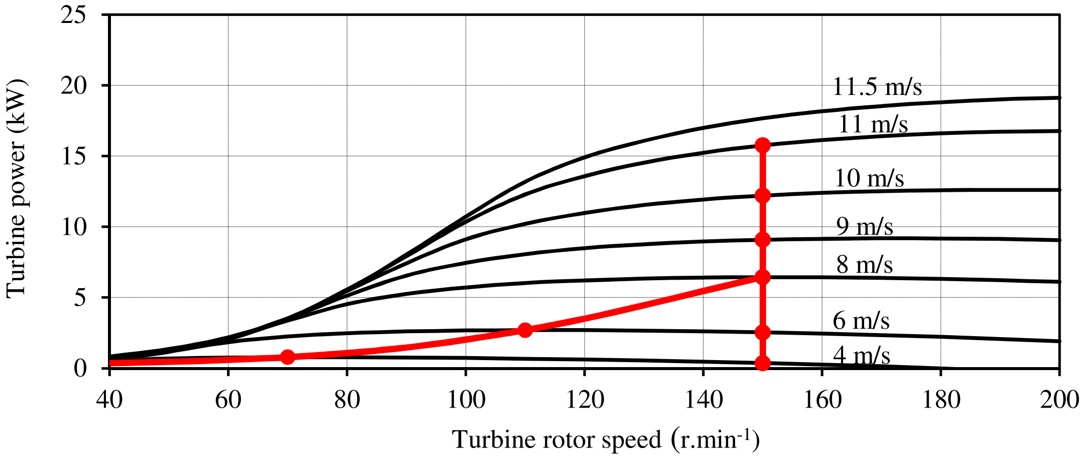

Figure B.1: Wind turbine power versus turbine speed and wind speed.

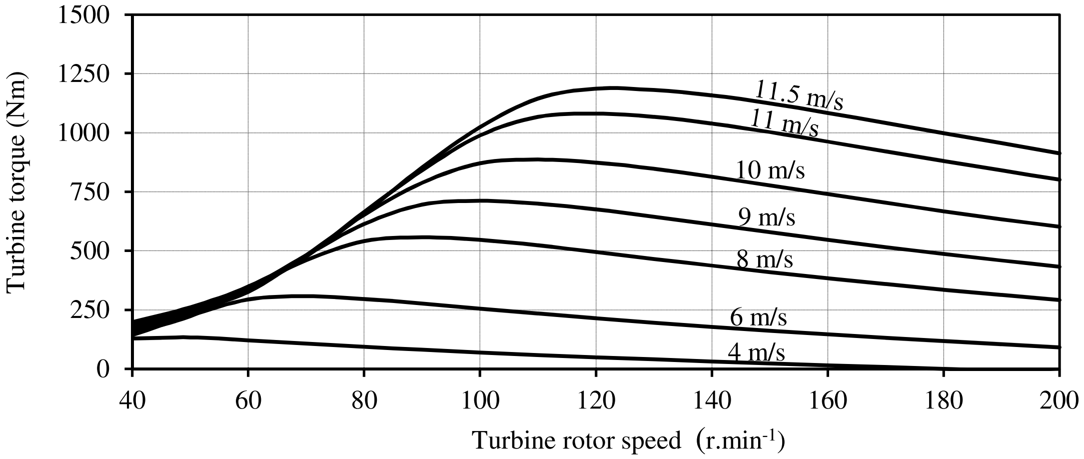

Figure B.2: Wind turbine torque versus turbine speed and wind speed.

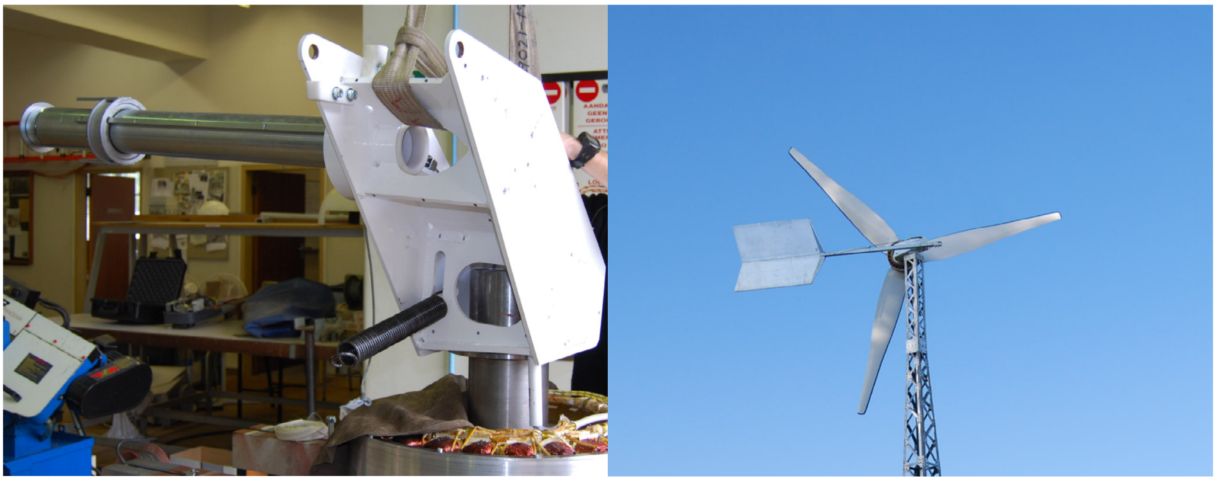

(a) (b)

Figure B.3: (a) Wind generator mounted to nacelle and (b) wind turbine in the furling position.

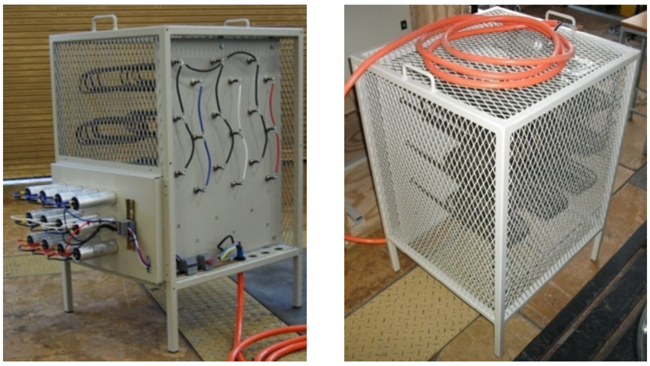

Figure B.4: Braking resistor bank with a capacitor bank mounted to its side.

(a) (b)

Figure B.5: (a) Wind turbine being field tested on the Stellenbosch University grounds and (b) at the SANAE IV Antarctic research base.

Figure B.6: SS-PMG 1 being field tested at the Stellenbosch University Mariendahl small wind turbine field testing facility.

Appendix C

Wind Site Evaluation

Some background is given in this section on the wind conditions of two of the wind sites, where the SS-PMG is field tested. Fig. C.1 show the wind speed distribution for the Stellenbosch University Mariendahl small wind turbine field testing facility. Due to field testing only very recently started at this site, the wind speed data of Fig. C.1 is only shown for a few months and not for a full year as usually required for the evaluation of a wind site. Fig. C.2 show the calculated energy harvest for this period for both a fixed speed SS-PMG, and a variable speed PMSG and power electronic converter system. Fig. C.3 show the wind speed distribution for the SANAE IV Antarctic wind site as obtained from [183], with Fig. C.4 showing the same energy harvesting calculation as in Fig. C.2.

For the lower annual wind speed site of Fig. C.1 the difference in annual energy yield for the fixed speed versus variable speed system is 10 %. For the wind site of Fig. C.3 with an average wind speed of 10.5 m/s, the difference is calculated as 2.5 %, with the fixed speed SS-PMG actually yielding more energy in this case due to its higher efficiency at the higher wind speeds as shown in Chapter 7.

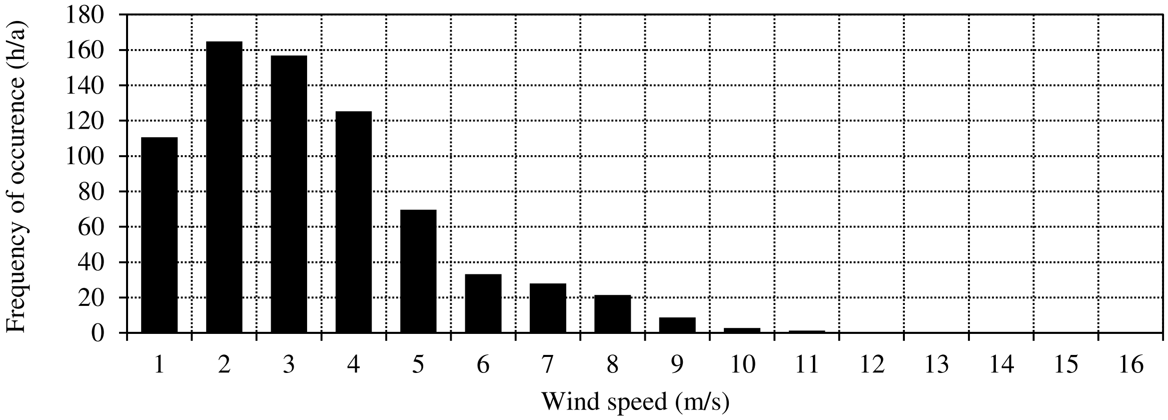

Figure C.1: Wind speed distribution for the Stellenbosch University Mariendahl field test site.

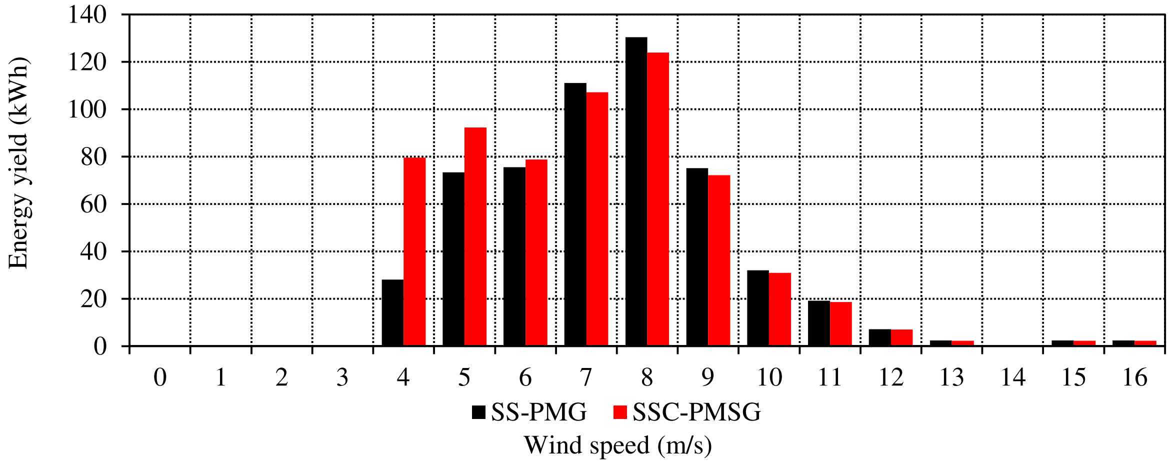

Figure C.2: Annual energy yield calculated for the wind site of Fig. C.1 for fixed speed and variable speed operation.

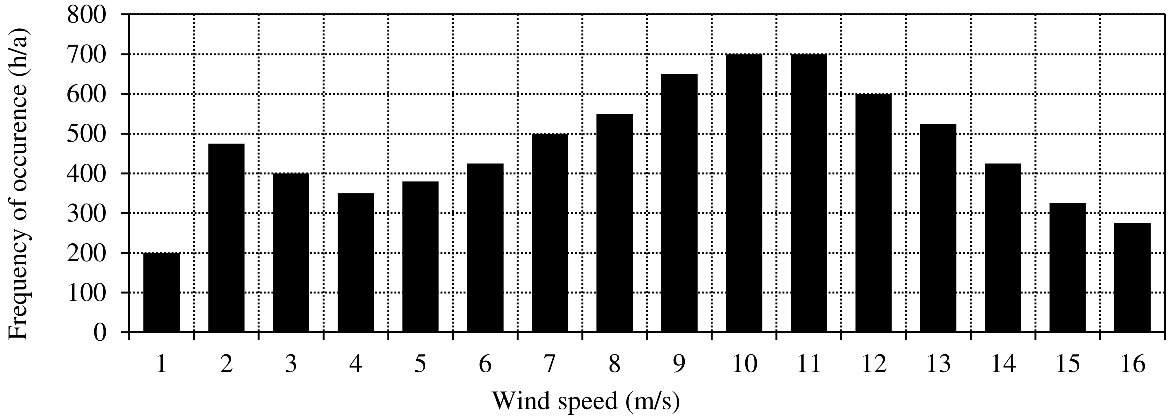

Figure C.3: Wind speed distribution for the SANAE IV Antarctic wind site.

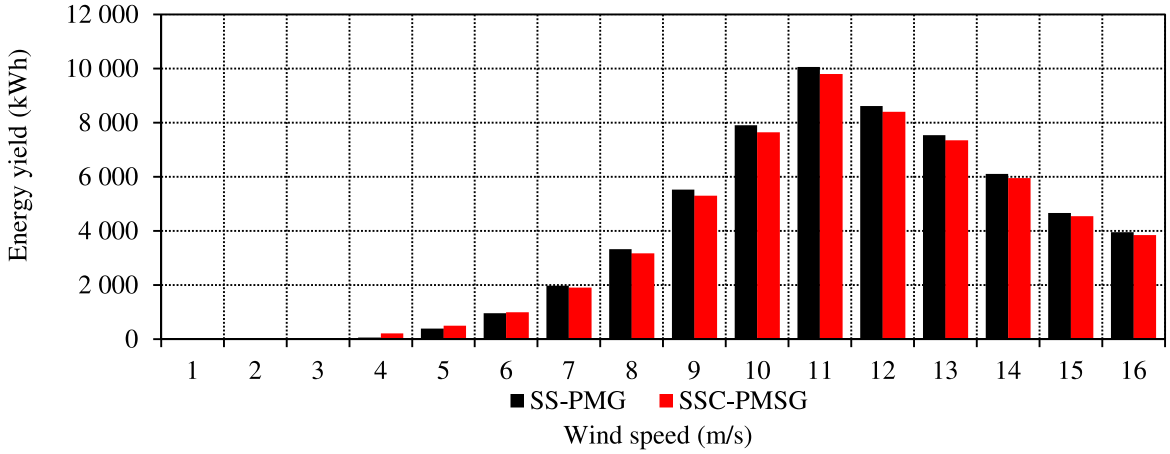

Figure C.4: Annual energy yield calculated for the wind site of Fig. C.3 for fixed speed and variable speed operation.

Bibliography

[1] (2014, Feb. 12) Global Wind Energy Coucil (GWEC) [Online]. Available: `http://www.gwec.net/`.

[2] (2014, Feb. 12) European Wind Energy Association (EWEA) [Online]. Available: `http://www.ewea.org/`.

[3] (2014, Feb. 12) *Small Wind World Report 2013*, World Wind Energy Association (WWEA) [Online]. Available: `www.wwindea.org`.

[4] J. K. Kaldellis and M. Kapsali. Shifting towards offshore wind energy–Recent activity and future development. *Journal of Energy Policy, Elsevier*, (53):136–148, 2013.

[5] Renewable energy technologies: Cost analysis series, Volume 1 Power Sector, Issue 5/5, Wind Power. International Renewable Energy Agency (IRENA), 2012.

[6] D. Bang, H. Polinder, G. Shrestha, and J. A. Fereira. Promising direct-drive generator system for large wind turbines. In *Wind Power to the Grid - EPE Wind Energy Chapter 1st Seminar, EPE-WECS*, Delft, Netherlands, 2008.

[7] F. Besnard. *On maintenance optimization for offshore wind farms.* PhD thesis, Chalmers University of Technology, Gothenburg, Sweden, 2013.

[8] Md. Arifujjaman, M. T. Iqbal, and J. E. Quaicoe. Reliability analysis of grid connected small wind turbine power electronics. *Journal of Applied Energy, Elsevier*, (86):1617–1623, 2009.

[9] M. Wilkinson and G. Hendriks. Report on wind turbine reliability profiles. Technical report, Reliawind, 2011. Deliverable D.1.3.

[10] Grid connection code for renewable power plants (RPPs) connected to the electricity transmission system (TS) or the distribution system (DS) in South Africa. The RSA Grid Code Secretariat, Version 2.6, November, 2012.

[11] J. H. J. Potgieter and M. J. Kamper. Torque and voltage quality in design optimisation of low cost non-overlap single layer winding permanent magnet wind generator. *IEEE Trans. on Industrial Electronics*, 59(5):2147–2156, 2012.

[12] J. H. J. Potgieter and M. J. Kamper. Design of new concept gearless direct-grid connected slip-synchronous permanent magnet wind generator. *IEEE Trans. on Industry Applications*, 48(3):913–922, 2012.

[13] J. H. van Wijk and M. J Kamper. Double-sided rotor technology for iron-cored permanent magnet wind generators: An evaluation. In *Proc. IEEE International Conference on Industrial Technology (ICIT 2013)*, Cape Town, South Africa, 2013.

[14] M. J. Kamper. Development and test results of South Africa's first 300 kW permanent magnet direct drive grid connected wind generator system. presented at the 18th Southern African Universities Power Engineering Conference, 2009.

[15] Arnold Magnetic Technologies, Rochester, NY, USA. *Sintered Neodymium-Iron-Boron Magnets N48H*, 2013.

[16] S. Sprague. *Lamination steels third edition A compendium of lamination steel alloys commonly used in electric motors.* The Electric Motor Education and Research Foundation, South Dartmourth, MA, USA, 3^{rd} edition, 2007.

[17] Z. Mouton and M. J. Kamper. Modelling and optimal design of an eddy current coupling for slip-synchronous permanent magnet wind generators. *in print IEEE Trans. on Industrial Electronics*, PP(PP):1–1, 2013.

[18] J. Pyrhönen, T. Jokinen, and Hrabovcová. *Design of Rotating Electrical Machines.* John Wiley & Sons, Ltd, 1^{st} edition, 2008.

[19] Frederick W. Grover. *Inductance calculations: Working formulas and tables.* Dover Publications, New York USA, 1^{st} edition, 1946.

[20] H. Polinder, F. F. A. van der Pijl, G. J. de Vilder, and P. Tavner. Comparison of direct-drive and geared generator concepts for wind turbines. *IEEE Transactions on Energy Conversion*, 21(3):725–733, 2006.

[21] Hybrid mini-grids for rural electrification: Lessons learned. Aliance for Rural Electrification (ARE), 2011.

[22] The potential of small and medium wind energy in developing countries A guide for energy sector decision-makers. Aliance for Rural Electrification (ARE), 2012.

[23] (2014, Feb. 12) *Enercon E-126 / 7 580 kW*, Enercon [Online].
Available: `http://www.enercon.de/en-en/66.htm`.

[24] E. Muljadi, T. Forsyth, and C. P. Butterfield. Soft-stall control versus furling control for small wind turbine power regulation. In *Windpower'98*, Bakersfield, CA, USA, 1998.

[25] H. Polinder, J. A. Ferreira, B. B. Jensen, A. B. Abrahamsen, K. Atallah, and R. A. McMahon. Trends in wind turbine generator systems. *IEEE Journal of Emerging and Selected Topics In Power Electronics*, 1(3):174–185, 2013.

[26] P. Gardner, A. Garrad, L. F. Hansen, P. Jamieson, C. Morgan, F. Murray, A. Tindal, J. I. Cruz, L. Arribas, and N. Fichaux. Wind Energy - The Facts, Part I, Technology , 2009. Wind Energy - The Facts (WindFacts) was a European project financed by the Intelligent Energy - Europe programme of the Executive Agency for Competitiveness and Innovation that ran from November 2007 to October 2009.

[27] E. Muljadi, C. P. Butterfield, and D. Handman. Dual-speed wind turbine generation. In *AWEA Windpower*, Denver, CO, USA, 1996.

[28] H. Li, Z. Chen, and H. Polinder. Optimization of multibrid permanent-magnet wind generator systems. *IEEE Transactions on Energy Conversion*, 24(1):82–92, 2009.

[29] S. Schmidt and A. Vath. Comparison of existing medium-speed drive train concepts with a differential gearbox approach. In *European Wind Energy Association Annual Event (EWEA)*, Copenhagen, Denmark, 2012.

[30] M. Ragheb. Safety of wind systems. Technical report, 2012.

[31] N. Boccard. Capacity factor of wind power realized values vs. estimates. *Journal of Energy Policy, Elsevier*, (37):2679–2688, 2009.

[32] R. Carriveau. Advances in windpower. Technical report, InTech, 2012.

[33] M. Wilkinson, B. Hendriks, F. Spinato, K. Harman, E. Gomez, H. Bulacio, J. Roca, P. Tavner, Y. Feng, and H. Long. Methodology and results of the reliawind reliability field study. In *European Wind Energy Conference (EWEC)*, Warsaw, Poland, 2010.

[34] H. Arabian-Hoseynabadi, P. J. Tavner, and H. Oraee. Reliability comparison of direct-drive and geared-drive wind turbine concepts. *Wind Energ.*, 13(1):62–73, 2010.

[35] F. Blaabjerg, K. Ma, and D. Zhou. Power electronics and reliability in renewable energy systems. In *IEEE International Symposium on Industrial Electronics (ISIE)*, Hangzhou, China, 2012.

[36] K. Ma, M. Liserre, and F. Blaabjerg. Lifetime estimation for the power semiconductors considering mission profiles in wind power converter. In *Energy Conversion Congress and Exposition (ECCE2013)*, Denver, CO, USA, 2013.

[37] R. Grinberg, G. Riedel, A. Korn, P. Steimer, and E. Bjornstad. On reliability of medium voltage multilevel converters. In *Energy Conversion Congress and Exposition (ECCE2013)*, Denver, CO, USA, 2013.

[38] S. Nababan, E. Muljadi, and F. Blaabjerg. An overview of power topologies for micro-hydro turbines. In *3rd IEEE International Symposium on Power Electronics for Distributed Generation Systems (PEDG)*, Aalborg, Denmark, 2012.

[39] A. J. G. Westlake, J. R. Bumby, and E. Spooner. Damping the power-angle oscillations of a permanent-magnet synchronous generator with particular reference to wind turbine applications. *IEE Proc. Electric Power Applications*, 143(3):269, 1996.

[40] S. Grabic, N. Celanovic, and V. A. Katic. Permanent magnet synchronous generator cascade for wind turbine application. *IEEE Trans. on Power Electronics*, 23(3):1136–1142, 2008.

[41] J. F. Hall. *Design and Control of a Variable Ratio Gearbox for Distributed Wind Turbine Systems.* PhD thesis, The University of Texas at Austin, Austin, TX, USA, 2012.

[42] C. Rossi, P. Corbelli, and G. Grandi. W-CVT continuously variable transmission for wind energy conversion system. In *Power Electronics and Machines in Wind Applications (PEMWA)*, Lincoln, NE, USA, 2009.

[43] (2014, Feb. 12) VMT technologies [Online]. Available: `http://www.moongears.com/`.

[44] V. Miltenović, M. Velimirović, M. Banić, and A Miltenović. Design of windturbines drive train based on CVT. *Balkan J. Mech. Transmiss.*, 1(1):45–56, 2011.

[45] (2014, Feb. 12) Integrated Quantam Wind (IQWind) [Online]. Available: `http://www.youtube.com/watch?v=bZOFs6IgUA4`.

[46] H. Müller, M. Pöller, A Basteck, M. Tilshcher, and J Pfister. Grid compatibility of variable speed wind turbines with directly coupled synchronous generator and hydro-dynamically controlled gearbox. In *Sixth International Workshop on Largescale integration of wind power and transmission networks for offshore wind farms*, Delft, Netherlands, 2006.

[47] (2014, Feb. 12) *DeWind D 8.2 2000 kW Wind Turbine*, DeWind [Online]. Available: `http://www.dewindco.com/eng/product/prod02_01.asp`.

[48] (2014, Feb. 12) Artemis Intelligent Power LTD [Online]. Available: `http://www.artemisip.com/applications/wind-turbines`.

[49] S. H. Salter and M. Rea. Hydraulics for wind. In *European Wind Energy Conference (EWEC)*, Hamburg, Germany, 1985.

[50] B. Skaare, B. Hörnsten, and F. G. Nielsen. Modeling, simulation and control of a wind turbine with a hydraulic transmission system. *Wind Energy*, pages 1–19, 2012.

[51] N. F. B. Diepeveen. *On the Application of Fluid Power Transmission in Offshore Wind Turbines*. PhD thesis, Delft University of Technology, Delft, Netherlands, 2013.

[52] M. Deldar, A. Izadian, and S. Anwar. Modeling of a hydraulic wind power transfer system utilizing a proportional valve. In *Energy Conversion Congress and Exposition (ECCE2013)*, Denver, CO, USA, 2013.

[53] A. Izadian, S. Hamzehlouia, M. Deldar, and S. Anwar. A hydraulic wind power transfer system: Operation and modeling. *IEEE Trans. on Sustainable Energy*, PP(99):1–1, 2014.

[54] F. Punga and L Schon. Der neue kollektorlose Einphasenmotor der Firma Krupp. *Elektrotechnische Zeitschrift*, 47(29):877–881, 1926.

[55] John F. H. Douglas. Characteristics of induction motors with permanent-magnet excitation. *AIEE Trans. Part III: Power Apparatus and Systems*, 78(3):221–225, 1959.

[56] Jan K. Sedivy. Induction motor with free-rotating DC excitation. *IEEE Trans. Power Apparatus and Systems*, 86(4):463–469, 1967.

[57] W. F. Low and N. Schofield. Design of a permanent magnet excited induction generator. In *Proc. of Int. Conf. on Electrical Machines (ICEM'92)*, Manchester, United Kingdom, 1992.

[58] Yoshiyuki Shibata, Nuio Tsuchida, and Koji Imai. High torque induction motor with rotating magnets in the rotor. *Electrical Engineering in Japan*, 117(3):102–109, 1996.

[59] Yoshiyuki Shibata, Nuio Tsuchida, and Koji Imai. Performance of induction motor with free-rotating magnets inside its rotor. *IEEE Trans on Industrial Electronics*, 46(3):646–652, 1999.

[60] Tadashi Fukami, Kenichi Nakagawa, Ryoichi Hanaoka, Shinzo Takata, and Toshio Miyamoto. Non-linear modeling of a permanent-magnet induction machine. *Electrical Engineering in Japan*, 144(1):58–67, 2003.

[61] Tadashi Fukami, M. Yokoi, Y. Kanamaru, and T Miyamoto. Performance evaluation of a permanent magnet induction generator. *Electrical Engineering in Japan*, 123(9):1065–1070, 2003.

[62] T. Fukami, K. Nakagawa, Y. Kanamaru, and T. Miyamoto. A technique for the steady-state analysis of a grid-connected permanent-magnet induction generator. *IEEE Trans. on Energy Conversion*, 19(2):318–324, 2004.

[63] T. Tsuda, T. Fukami, Y. Kanamaru, and T Miyamoto. Experimental study on the inrush current in a permanent magnet induction generator. In *Natl. Conv. Rec. IEEJ*, 2006.

[64] Toshihiro Tsuda, Tadashi Fukami, Yasunori Kanamaru, and Toshio Miyamoto. Effects of the built-in permanent magnet rotor on the equivalent circuit parameters of a permanent magnet induction generator. *IEEE Trans. on Energy Conversion*, 22(3):798–799, 2007.

[65] Toshihiro Tsuda, Tadashi Fukami, Yasunori Kanamaru, and Toshio Miyamoto. Performance analysis of the permanent-magnet induction generator under unbalanced grid voltages. *Elect. Eng. Jpn.*, 161(4):60–69, 2007.

[66] J. H. J. Potgieter, A. N. Lombard, R-J Wang, and M. J. Kamper. Evaluation of a permanent magnet excited induction generator for renewable energy applications. In *Southern African Universities Power Engineering Conference (SAUPEC)*, Stellenbosch, South Africa, 2009.

[67] P. Sharma, T. S. Bhatti, and K. S. S. Ramakrishnan. Permanent-magnet induction generators: An overview. *Journal of Engineering Science and Technology*, 6(3):332–338, 2011.

[68] A. M. Gazdac, A. M. Mabwe, C. S. Martis, F. Betin, and K. Biro. Analytical design algorithm and FEM analysis of the dual-rotor permanent magnet induction machine. In *Proc. of Int. Conf. on Electrical Machines (ICEM)*, Marseille, France, 2012.

[69] T. Epskamp, B. Hagenkort, T. Hartkopf, and S. Jöckel. No gearing, no converter: assessing the idea of highly reliable permanent-magnet induction generators. In *Proc. of European Wind Energy Conf. (EWEC'99)*, Nice, France, 1999.

[70] B. Hagenkort, T. Hartkopf, A. Binder, and S. Jöckel. Modelling a direct drive permanent magnet induction machine. In *Proc. of Int. Conf. on Electrical Machines (ICEM'00)*, Espoo, Finland, 2000.

[71] Gabriele Gail, T. Hartkopf, E. Tröster, M. Höffling, M. Henschel, and H. Schneider. Static and dynamic measurements of a permanent magnet induction generator: test results of a new wind generator concept. In *Proc. of Int. Conf. on Electrical Machines (ICEM'04)*, Cracow, Poland, 2004.

[72] E. Tröster, T. Hartkopf, H. Schneider, Gabriele Gail, and M. Henschel. Analysis of the equivalent circuit diagram of a permanent magnet induction machine. In *Proc. of Int. Conf. on Electrical Machines (ICEM'04)*, Cracow, Poland, 2004.

[73] E. Tröster, M. Sperling, and T. Hartkopf. Finite element analysis of a permanent magnet induction machine. In *International Symposium on Power Electronics, Electrical Drives, Automation and Motion, (SPEEDAM 2006)*, Taormina (Sicily), Italy, 2006.

[74] P. Sharma, T. S. Bhatti, and K. S. S. Ramakrishnan. Study of an isolated wind-diesel hybrid power system with STATCOM by incorporating a new mathematical model of PMIG. *Euro. Trans. Electr. Power*, 3(22):351–363, 2012.

[75] P. Sharma and T. S. Bhatti. Performance investigation of isolated wind-diesel hybrid power systems with WECS having PMIG. *IEEE Trans. on Industrial Electronics*, 60(4):1630–1637, 2013.

[76] P. Sharma, W. Sulkowski, and B. Hoff. Dynamic stability study of an isolated wind-diesel hybrid power system with wind power generation using IG, PMIG and PMSG: A comparison. *International Journal of Electrical Power & Energy Systems*, 53(0):857–866, 2013.

[77] J. H. J. Potgieter. Design and analysis of a gearless direct grid permanent magnet induction generator. Master's thesis, University of Stellenbosch, Stellenbosch, South Africa, 2011.

[78] Andrew J. Thomas. A doubly-fed permanent magnet generator for wind turbines. Master's thesis, Massachusetts Institute of Technology, Cambridge, MA, USA, 2004.

[79] Sivananda Kumjula Reddy. Operational behavior of a doubly-fed, permanent magnet generator for wind turbines. Master's thesis, Massachusetts Institute of Technology, Cambridge, MA, USA, 2005.

[80] Bin Lu. Operational behavior of a doubly-fed, permanent magnet generator for wind turbines. Master's thesis, Massachusetts Institute of Technology, Cambridge, MA, USA, 2007.

[81] U. Hoffmann, P. Bouwer, and M. J. Kamper. Direct grid connection of a slip-permanent magnet wind turbine generator. In *Energy Conversion Congress and Expo (ECCE2011)*, Phoenix, AZ, USA, 2011.

[82] U. Hoffmann and M. J. Kamper. Low voltage ride-through compensation for a slip-permanent magnet wind turbine generator. In *Southern African Universities Power Engineering Conference (SAUPEC)*, Cape Town, South Africa, 2011.

[83] A. T. Spies and M. J. Kamper. Reactive power control of a direct grid connected slip synchronous permanent magnet wind generator. In *IEEE International Conference on Industrial Technology (ICIT)*, Cape Town, South Africa, 2013.

[84] L. P. Lazaridis. Economic comparison of HVAC and HVDC solutions for large offshore wind farms under special consideration of reliability. Master's thesis, Royal Institute of Technology, Stockholm, Sweden, 2005.

[85] (2014, Feb. 12) *High performance small wind turbines*, Gaia-Wind [Online]. Available: `http://www.gaia-wind.com/`.

[86] S. Sharma, S-H. Huang, and N. D. R. Sarma. System inertial frequency response estimation and impact of renewable resources in ercot interconnection. In *2011 IEEE Power and Energy Society General Meeting*, San Diego, CA, USA, 2011.

[87] I. F. Moore. *Inertial Response from Wind Turbines.* PhD thesis, Cardiff University, Cardiff, United Kingdom, 2012.

[88] P. Tielens and D. van Hertem. Grid inertia and frequency control in power systems with high penetration of renewables. In *Young Researchers Symposium in Electrical Power Engineering Edition 6*, Delft, Netherlands, 2012.

[89] E. Muljadi, V. Gevorgian, M. Singh, and S. Santoso. Understanding inertial and frequency response of wind power plants. In *IEEE Symposium on Power Electronics and Machines in Wind Applications*, Denver, CO, USA, 2012.

[90] E. Muljadi, M. Singh, and V. Gevorgian. Fixed-speed and variable-slip wind turbines providing spinning reserves to the grid. In *IEEE Power and Energy Society General Meeting*, Vancouver, Canada, 2013.

[91] M. Singh, V. Gevorgian, E. Muljadi, and E. Ela. Variable-speed wind power plant operating with reserve power capability. In *Energy Conversion Congress and Exposition (ECCE2013)*, Denver, CO, USA, 2013.

[92] J. D. Glover and M. S. Sarma. *Power System Analysis and Design.* Brooks/Cole Thomson Learning, Pacific Grove, CA, USA, 3 edition, 2002.

[93] A. G. González Rodríquez, A. González Rodríquez, and M. Burgos Payán. Estimating wind turbines mechanical constants. In *International Conference on Renewable Energies and Power Quality (ICREPQ)*, Sevilla, Spain, 2007.

[94] J. A. Stegmann and M. J. Kamper. Economic and efficiency evaluation of different battery charging wind generator systems. In *Southern African Universities Power Engineering Conference (SAUPEC)*, Johannesburg, South Africa, 2010.

[95] G. C. Venkatesh and S. V. Kulkarni. Energy yield of passive stall regulated fixed speed wind turbine with optimal rotor speed. *Electric Power Systems Research, Elsevier*, (76):1019–1026, 2006.

[96] Lin Wang, Xinzi Tang, and Xiongwei Liu. Blade design optimisation for fixed-pitch fixed-speed wind turbines. *International Scholarity Research Network (ISRN), Renewable Energy*, pages 1–8, 2012.

[97] M. Davies, M. Dommaschk, J. Dorn, J. Lang, D. Retzmann, and D. Soerangr. HVDC PLUS - Basics and principle of operation. Technical report, SIEMENS, 2008.

[98] (2014, Feb. 12) *HVDC-Light® It's time to connect*, ABB [Online].
Available: `http://www.abb.com/`.

[99] R. Vermaak, J. H. J. Potgieter, and M. J. Kamper. Grid-connected VSC-HVDC wind farm system and control using permanent magnet induction generators. In *IEEE International Conference on Power Electronics and Drive Sytems (PEDS)*, Tapei, Taiwan, 2009.

[100] C. Meyer, M. Höing, and R. W. De Doncker. Control and design of DC grids for offshore wind farms. *IEEE Trans. on Industry Applications*, 43(6):1475–1482, 2007.

[101] T. Shimizu. Pole change type salient-pole a-c generator. *Fuji Denki Review*, 4(4):99–106, 1958.

[102] W. Fong, J. R. French, and G. H. Rawcliffe. Two-speed single-winding salient-pole synchronous machines. *Proc. IEE*, 112(2):351–358, 1965.

[103] J.J. Gutierrez, J. Ruiz, P. Saiz, I. Azcarate, L. A. Leturiondo, and A. Lazkano. Power quality in grid-connected wind turbines. *Wind Turbines, InTech*, pages 547–570, 2011.

[104] T. Thiringer and J. Dahlberg. Periodic pulsations from a three-bladed wind turbine. *IEEE Trans. on Energy Conversion*, 16(2):128–133, 2001.

[105] D. S. L. Dolan and P. W. Lehn. Simulation model of wind turbine 3p torque oscillations due to wind shear and tower shadow. *IEEE Trans. on Energy Conversion*, 21(3):717–724, 2006.

[106] W. A. A. M. Bierbooms. *Constrained stochastic simulation of wind gusts for wind turbine design.* PhD thesis, Delft University of Technology, Delft, Netherlands, 2009.

[107] M. Pöller and S. Achilles. Aggregated wind park models for analyzing power system dynamics. In *Fourth International Workshop on Large-scale Integration of Wind Power and Transmission Networks for Offshore Wind Farms*, Billund, Denmark, 2003.

[108] J. Sopanen, V. Ruuskanen, J. Nerg, and J. Pyrhönen. Dynamic torque analysis of a wind turbine drive train including a direct-driven permanent magnet generator. *IEEE Trans. on Industrial Electronics*, 58(9):3859–3867, 2011.

[109] ELECTRICITY SUPPLY - QUALITY OF SUPPLY, part 4: Application guidelines for utilities. South African Bureau of Standards, NRS 048-4:1999, South Africa, 1999.

[110] B. Espinar and D. Mayer. The role of energy storage for mini-grid stabilization. Technical report, International Energy Agency (IEA), Photovoltaic Power Systems Programme, 2011. IEA-PVPS T11-02:2011.

[111] L. A. C. Lopes, F. Katiraei, K. Mauch, M. Vandenbergh, and L. Arribas. PV hybrid mini-grids: Applicable control methods for various situations. Technical report, International Energy Agency (IEA), Photovoltaic Power Systems Programme, 2012. IEA-PVPS T11-07:2012.

[112] J. H. J. Potgieter and M. J. Kamper. Design considerations in the implementation of an electromagnetic brake for a 15 kW PM wind generator. In *Southern African Universities Power Engineering Conference (SAUPEC)*, Potchefstroom, South Africa, 2013.

[113] S. A. Hossain and E. R. Oliveira. Braking torque analysis of PMSM motor under stator winding failures. In *Proc. Int. Conf. on Electrical Machines*, Marseille, France, 2012.

[114] Y. Wang, J. Zhu, S. Wang, Y. Guo, and X. Wei. Nonlinear magnetic model of surface mounted PM machines incorporating saturation saliency. *IEEE Trans. on Magnetics*, 45(10):4684–4687, 2009.

[115] F. Ma, L. Fu, X. Fan, Z. Ye, J. Kang, and G. Wang. Large signal mathematical modeling of three-phase synchronous generator-rectifier systems. In *International Conference on Electrical Machines and Systems (ICEMS)*, Beijing, China, 2011.

[116] J. Salomäki, M. Hinkkanen, and J. Luomi. Cost-effective design of inverter output filters for AC drives. In *Annual Conference of the IEEE Industrial Electronics Society (IECON)*, Taipei, Taiwan, 2007.

[117] M. F. Hsieh, Y. C. Hsu, D. G. Dorell, and K. H. Hu. Investigation on end winding inductance in motor stator windings. *IEEE Trans. on Magnetics*, 43(6):2513–2515, 2007.

[118] A. M. El-Refaie, Z. Q. Zhu, T. M. Jahns, and D. Howe. Winding inductances of fractional slot surface-mounted permanent magnet brushless machines. In *Proc. Industry Applications Society Annual Meeting, 2008. IAS '08. IEEE*, Edmonton, Alberta, Canada, 2008.

[119] T. Cox, F. Eastham, and J. Proverbs. End turn leakage reactance of concentrated modular winding stators. *IEEE Trans. on Magnetics*, 44(11):4057–4061, 2008.

[120] A. J. Rix. *Design, comparison and experimental evaluation of non-overlap winding radial flux permanent magnet hub drives for electric vehicles.* PhD thesis, University of Stellenbosch, Stellenbosch, South Africa, 2011.

[121] P. J. Lawrenson. Calculation of machine end-winding inductances with special reference to turbogenerators. *PROC. IEE*, 117(6):1129–1134, 1970.

[122] M. J. Kamper and F. S. van der Merwe. Influence of laminations on axially directed flux in induction motors. In *Proc. International Conference on Electrical Machines (ICEM'88)*, Pisa, Italy, 1988.

[123] D. Žarko, D. Ban, and R. Klarić. Finite element approach to calculation of parameters of an interior permanent magnet motor. *AUTOMATIKA*, 46(3-4):113–122, 2005.

[124] A. Tounzi, T. Henneron, Y. Le Menach, R. Askour, E. Dumetz, and F. Piriou. 3-D Approaches to determine the end winding inductances of a permanent magnet linear synchronous motor. *IEEE Trans. on Magnetics*, 40(2):758–761, 2004.

[125] R. Lin and A. Arkkio. Calculation and analysis of stator end-winding leakage inductance of an induction machine. *IEEE Trans. on Magnetics*, 45(4):2009–2014, 2009.

[126] R. De Weerdt and R. Belmans. Squirrel cage induction motor end effects using 2-D and 3-D finite elements. In *Proc. 7th international conference on Electrical Machines and Drives*, Durham, USA, 1995.

[127] B. Funieru and A. Binder. Simulation of electrical machines end effects with reduced length 3D FEM models. In *Proc. Int. Conf. on Electrical Machines*, Marseille, France, 2012.

[128] Q. Gu and Q. Hao. Three-dimensional analytic model for permanent magnet electric machines with finite core length. *Electrical Engineering, Springer-Verlag*, 87(6):305–314, 2005.

[129] J. Wang, D. Howe, and G. W. Jewell. Fringing in tubular permanent-magnet machines: Part I. Magnetic field distribution, flux linkage, and thrust force. *IEEE Trans. on Magnetics*, 39(6):3507–3516, 2003.

[130] H. Polinder, J. G. Slootweg, M. J. Hoeijmakers, and J. C. Compter. Modeling of a linear PM machine including magnetic saturation and end effects: Maximum force-to-current ratio. *IEEE Trans. on Industry applications*, 39(6):1681–1688, 2003.

[131] W. Hua, M. Cheng, X. Zhu, and J. Zhang. Investigation of end-effects in brushless machines having magnets in the stator with doubly salient structure. In *IEEE International Magnetics Conference (INTERMAG)*, San Diego, California, USA, 2006.

[132] T. F. Chan and L. L. Lai. An axial-flux permanent-magnet synchronous generator for a direct-coupled wind-turbine system. *IEEE Trans. on Energy Conversion*, 22(1):86–94, 2007.

[133] H. VuXuan, D. Lahaye, H. Polinder, and J. A. Ferreira. Improved model for design of permanent magnet machines with concentrated windings. In *IEEE International Electric Machines & Drives Conference (IEMDC)*, Niagara Falls, ON, Canada, 2011.

[134] S. D. Umans. *Fitzgerald & Kingsley's Electric Machinery.* McGraw-Hill, New York, NY, USA, 7^{th} edition, 2014.

[135] S. Ruoho. *Modelling demagnetization of sintered NdFeB magnet material in time-discretized finite element analysis.* PhD thesis, Aalto University, Espoo, Finland, 2011.

[136] D. Hanselman. *Brushless Permanent Magnet Motor Design.* Magna Physics Publishing, Lebanon, OH, USA, 2^{nd} edition, 2006.

[137] S. Sprague. An examination of magnetic property variation of specification-acceptable electrical steel. In *Proc. Int. Conf. on Electrical Machines (ICEM)*, Marseille, France, 2012.

[138] Z. Cheng, N. Takahashi, B. Forghani, Y. Du, Y. Fan, and H. Wang. Effect of variation of B-H properties on loss and flux inside silicon steel lamination. *IEEE Trans. on Magnetics*, 47(5):1346–1349, 2011.

[139] B. Lequesne, B. Liu, and T. W. Nehl. Eddy-current machines with permanent magnets and solid rotors. *IEEE Trans. on Industry Applications*, 33(5):1289–1294, 1997.

[140] A. Canova and B. Vusini. Design of axial eddy-current couplers. *IEEE Trans. on Industry Applications*, 39(3):725–733, 2003.

[141] S. E. Gay and M. Ehsani. Parametric analysis of eddy-current brake performance by 3-D finite-element analysis. *IEEE Trans. on Magnetics*, 42(2):319–328, 2006.

[142] B. Zheng and S. Anwar. An antilock-braking algorithm for an eddy-current-based brake-by-wire system. *IEEE Trans. on Vehicular Technology*, 56(3):1100–1107, 2007.

[143] N. Amati, A. Canova, F. Cavalli, and M. Padovani. Dynamic behaviour of torsional eddy-current dampers: Sensitivity of the design parameters. *IEEE Trans. on Magnetics*, 43(7):3266–3277, 2007.

[144] L. Ye, D. Li, Y. Ma, and B. Jiao. Design and performance of a water-cooled permanent magnet retarder for heavy vehicles. *IEEE Trans. on Magnetics*, 26(3):953–958, 2011.

[145] J. F. Gieras, R-J Wang, and M. J. Kamper. *Axial Flux Permanent Magnet Brushless Machines.* Springer, 2^{nd} edition, 2008.

[146] M. A. Mueller and A. S. McDonald. A lightweight low-speed permanent magnet electrical generator for direct-drive wind turbines. *Wind Energy*, 12(8):768–780, 2009.

[147] J. A. Stegmann and M. J. Kamper. Design aspects of double-sided rotor radial flux air-cored permanent-magnet wind generator. *IEEE Trans. Industry Applications*, 47(2):767–778, 2011.

[148] M. J. Kamper, J. H. J. Potgieter, J. A. Stegmann, and P. Bouwer. Comparison of air-cored and iron-cored non-overlap winding radial flux permanent magnet direct drive wind generators. In *Energy Conversion Congress and Expo (ECCE2011)*, Phoenix, AZ, USA, 2011.

[149] Vanderplaats Research & Development, Inc., Colorado Springs, CO, USA. *VisualDOC Users Manual*, 2006. Version 6.

[150] N. Bianchi and S. Bolognani. Design techniques for reducing the cogging torque in surface-mounted PM motors. *IEEE Trans. Industry Applications*, 38(5):1259–1265, 2002.

[151] W. Fei and P. C. K. Luk. Torque ripple reduction of axial flux permanent magnet synchronous machine with segmented and laminated stator. *IEEE Trans. Magn.*, 45(10):132–138, 2009.

[152] M. Aydin, Z. Q. Zhu, T. A. Lipo, and D. Howe. Minimization of cogging torque in axial-flux permanent-magnet machines: Design concepts. *IEEE Trans. Magn.*, 43(9):3614–3622, 2007.

[153] M. S. Islam, S. Mir, and T. Sebastian. Issues in reducing the cogging torque of mass-produced permanent-magnet brushless DC motor. *IEEE Trans. Ind. Appl.*, 40(3):813–820, 2004.

[154] P. Salminen, J. Pyrhönen, F. Libert, and J. Soulard. Torque ripple of permanent magnet machines with concentrated windings. In *XII Int. Symp. Electromagnetic Fields Mechatronics, Electrical Electronic Engineering (ISEF)*, Baiona, Spain, 2005.

[155] C. C. Hwang, M. H. Wu, and S. P. Cheng. Influence of pole and slot combinations on cogging torque in fractional slot pm motors. *J. Magn. Mater.*, 304(1):e430–e432, 2006.

[156] Z. Q. Zhu and D. Howe. Influence of design parameters on cogging torque in permanent magnet machines. *IEEE Trans. Energy Convers.*, 15(4):407–412, 2000.

[157] S. A. Saied, S. Abbaszadeh, S. Hemmati, and M. Fadaie. A new approach to cogging torque reduction in surface-mounted permanent-magnet motors. *Eur. J. Sci. Res.*, 26(4):499–509, 2009.

[158] L. Gasparin, A. Cernigoj, S. Markic, and R. Fiser. Prediction of cogging torque level in PM motors due to assembly tolerances in mass-production. *Eur. J. Sci. Res.*, 27(4):911–918, 2008.

[159] ELECTRICITY SUPPLY - QUALITY OF SUPPLY, part 2: Voltage characteristics, compatibility levels, limits and assessment methods. Technology Standardization Department (TSD), ESKOM, NRS 048-2:2004, South Africa, 2004.

[160] GRID INTERCONNECTION OF EMBEDDED GENERATION, Part 2: Small-scale embedded generation. Technology Standardization Department (TSD), ESKOM, NRS 097-2-1:2010, South Africa, 2010.

[161] D. Bang, H. Polinder, G. Shrestha, and J. A. Fereira. Review of generator systems for direct-drive wind turbines. In *European Wind Energy Conference (EWEC)*, Brussels, Belgium, 2008.

[162] H. Li and Z. Chen. Overview of different wind generator systems and their comparisons. *IET Renew. Power Gener.*, 2(2):123–138, 2008.

[163] R. Scott Semken, M. Polikarpova, P. Röyttä, J. Alexandrova, J Pyrhönen, J. Nerg, A. Mikkola, and J. Backman. Direct-drive permanent magnet generators for high power wind turbines: benefits and limiting factors. *IET Renew. Power Gener.*, 6(1):1–8, 2012.

[164] J. N. Stander, G. Venter, and M. J. Kamper. Review of direct drive radial flux wind turbine generator mechanical design. *Wind Energy*, 15(3):459–472, 2012.

[165] M. A. Khan and P. Pillay. Design of a PM wind generator, optimised for energy capture over a wide operating range. In *IEEE International Conference on Electric Machines and Drives (IEMDC)*, San Antonio, TX, USA, 2005.

[166] D. G. Dorrell. Design requirements for brushless permanent magnet generators for use in small renewable energy systems. In *33rd Annual Conference of the IEEE Industrial Electronics Society (IECON)*, Taipei, Taiwan, 2007.

[167] F. Meier. *Permanent-Magnet Synchronous Machines with Non-Overlapping Concentrated Windings for Low-Speed Direct-Drive Applications.* PhD thesis, Royal Institute of Technology, Stockholm, Sweden, 2008.

[168] S. E. Skaar, O. Krovel, and R. Nilsen. Distribution, coil-span and winding factor factors for PM machines with concentrated windings. In *Int. Conf. On Electrical Machines (ICEM)*, Chania, Crete Island, Greece, 2006.

[169] M. J. Kamper, A. J. Rix, D. A. Wills, and R-J Wang. Formulation, finite-element modelling and winding factors of non-overlap winding permanent magnet machines. In *Int. Conf. On Electrical Machines (ICEM)*, Vilamoura, Portugal, 2008.

[170] R. Qu and T. Lipo. Dual-rotor, radial-flux, toroidally wound permanent-magnet machines. *IEEE Trans. on Industry Applications*, 39(6):1665–1673, 2003.

[171] Y. Yeh, M. Hsieh, and D. Dorell. Different arrangements for dual-rotor dual-output radial-flux motors. *IEEE Trans. on Industry Applications*, 48(2):612–622, 2012.

[172] P. Xu, X. Liu, K. Shi, and Y. Du. Design of dual-rotor radial flux permanent-magnet generator for wind power applications. *Applied Mechanics and Materials*, 416–417:9–14, 2013.

[173] D. Dama, D. Muftic, and R. Vajeth. Conductor optimisation for overhead transmission lines. In *Inaugural IEEE PES 2005 Conference and Exposition in Africa*, Durban, South Africa, 2005.

[174] J. C. Olivares-Galvaán, F. de León, P. S. Georgilakis, and R. Escarela-Pérez. Selection of copper against aluminium windings for distribution transformers. *IET Electr. Power Appl.*, 4(6):474–485, 2009.

[175] L. Pryor, R. Schlobohm, and B. Brownell. A comparison of aluminium vs. copper as used in electrical equipment. Technical report, GE Industrial Solutions, 2008.

[176] P-W. Han, Y-D. Chun, J. Choi, M-J. Kim, D-H. Koo, and J. Lee. The study to substitute aluminum for copper as a winding material in induction machine. In *31st International Telecommunications Energy Conference (INTELEC)*, Incheon, South Korea, 2009.

[177] E. Groendahl, M. Kimiabeigi, and H. Stiesdal. Generator with aluminium winding and wind turbine. Patent Application, November 2011. US 2011/0285141 A1.

[178] W. T. Benecki. The permanent magnet market - 2015. In *Magnetics 2013*, Orlando, FL, USA, 2013.

[179] Z. Q. Zhu. A simple method for measuring cogging torque in permanent magnet machines. In *IEEE Power & Energy Society General Meeting (PES)*, Calgary, AB, Canada, 2009.

[180] SMA Solar Technology. *WINDY BOY 3000TL / 3600TL / 4000TL / 5000TL with reactive power control*, 2012.

[181] Md. Arifujjaman, M. T. Iqbal, and J. E. Quaicoe. Analysis of conversion losses in grid connected small wind turbine systems. *The Open Renewable Energy Journal.*, 2:59–69, 2009.

[182] Stock Drive Products / Sterling Instrument. *D757 Data Book - Couplings and Universal joints*, 2013.

[183] J. N. Stander. The specification of a small wind energy conversion system for the South African Antarctic research base SANAE IV. Master's thesis, Stellenbosch University, Stellenbosch, South Africa, 2008.